

City Research Online

City St George's, University of London

Citation: Clark, R. P. (1973). The role of the human micro-environment in heat transfer and particle transport. (Unpublished Doctoral thesis, The City University)

This is the accepted version of the paper.

This version of the publication may differ from the final published version. To cite this item please consult the publisher's version.

Permanent repository link: https://openaccess.city.ac.uk/id/eprint/38425/

Copyright and Reuse: Copyright and Moral Rights remain with the author(s) and/or copyright holders. Copies of full items can be used for personal research or study, educational, or not-for-profit purposes without prior permission or charge, unless otherwise indicated, provided that the authors, title and full bibliographic details are credited, a hyperlink and/or URL is given for the original metadata page and the content is not changed in any way. For full details of reuse please refer to City Research Online policy.

City Research Online: http://openaccess.city.ac.uk/ publications@citystgeorges.ac.uk

The Role of the Human Micro-Environment in Heat Transfer and Particle Transport

by Raymond Peter Clark

A thesis submitted for the Degree of Doctor of Philosophy

THE CITY UNIVERSITY LIBRARY
ST. JOHN STREET, LONDON, E.C.1.

Department of Aeronautics,
The City University, London.

March 1973

Dedicated to the memory of the late Harold E. Lewis of The National Institute for Medical Research, without whose constant enthusiasm and encouragement this study could not have been made.

ACKNOWLEDGEMENTS

The work reported in this thesis was carried out at The City University, London, and the National Institute for Medical Research, Hampstead, London, between 1967 and 1972

I gratefully acknowledge the help given to me in various ways during this study by the following :

Professor G. A. Tokaty, who as Head of the Department of Aeronautics at The City University supported this work whilst I was in his Department.

The Late Dr. H. E. Lewis of the N.I.M.R., who co-supervised this work until his untimely death in 1971.

Professor R. N. Cox, who has acted as co-supervisor at The City University.

Dr. O. G. Edholm of the Division of Human Physiology at the N.I.M.R., who acted as co-supervisor of the work after the death of H. E. Lewis.

[redacted], who as Experimental Officer at The City University provided the technical services for much of this work.

[redacted] of the N.I.M.R., who typed the manuscript.

CONTENTS

1. Introduction.

2. Visualisation of the convective flow around a human subject.

2.1. The fluid dynamic characteristics of the flow.

3. Heat loss from the body surface.

3.1. Analysis of natural convection from a flat plate.

3.1.1. The boundary layer equations for laminar flow.

3.1.2. The application of the boundary layer equations to heat transfer from the human body.

3.2. The human body as a series of cylinders.

3.2.1. Radiant heat output.

3.2.2. Effect of radiation on convective heat output.

3.3. Discussion of the calculated heat transfer rates.

3.3.1. The effect of water vapour within the boundary layer.

4. A cylindrical heated model.

4.1. Description of the flow over the heated cylindrical model.

4.2. The sensitivity of the schlieren system.

5. Temperature and velocity profiles within the micro-environment.

5.1. The hot wire anemometer.

5.1.1. The hot wire probe.

5.1.2. Probe calibration.

5.1.3. Heat losses from the anemometer wire.

5.1.4. Time averaging of anemometer readings.

5.2. Use of the hot wire anemometer and thermocouple to measure velocity and temperature profiles.

6. The transport of particles by the natural convection boundary layer.

6.1. The motion of particles in a viscous flow.

6.1.1. Particle size and terminal velocity.

6.1.2. The acceleration of small particles in air.

6.1.3. Motion of a rotating particle in a velocity gradient.

6.1.4. Lift on a small sphere in a slow shear flow.

6.1.5. Thermal precipitation - radiometric forces.

6.1.6. Brownian motion of particles.

6.1.7. Aerodynamic lift force.

6.1.8. Summary of magnitudes of forces acting on particles.

6.2. The theory of electrostatic effects on particle motions.

6.3. Floor deposition in channel flow under gravity.

7. Particle transport experiments - introduction.

7.1. Surface shear stresses.

7.1.1. Van der Waals forces.

7.2. Size distribution of particles used in channel experiments.

7.2.1. Method of injecting particles into flow channel.

7.2.2. Method of counting deposited particles.

7.3. Channel deposition results.

7.3.1. Changes in channel wall material.

7.3.2. Extra experimental precautions.

7.3.3. The landing of particles on the channel walls.

7.4. The motions of particles in laminar channel flow.

7.5. Particle deposition when an electric field was applied to the channel.

7.6. Discussion of particle motions in flow channel experiments.

7.7. Particle deposition from a turbulant flow.

7.8. Aerobiological implications.

8. Particle sensing anemometer.

8.1. Efficiency of the particle sensing anemometer.

8.1.1. Sensitivity of the particle sensing anemometer.

8.2. Use of the particle sampler.

9. A full sized heated model of the human form.

9.1. Observations on particles moving in the convective flow over the heated model.

9.1.1. Observations with the model breathing.

9.1.2. Experiments on the release of particles from the surface of the heated model.

10. The movement of particles through fabric and the bellows action of clothing.

11. Some experiments concerning dust sampling.

11.1. The sampling and sizing of airborne particles.

12. Concluding remarks.

Appendix 1 - Remarks on the effect of clothing on heat transfer.

Appendix 2 - Lift and drag on a particle in viscous flow.

Appendix 3 - Particle deposition in vacuo.

Appendix 4 - Flow patterns and particle deposition in a glass model of the trachea and bronchi.

SUMMARY

The convective boundary layer flow over the human body that forms part of the human micro-environment has been investigated.

This flow has been visualised over the whole body surface using a schlieren optical system. Techniques are described for measuring the velocity and temperature profiles within the convective flow over models designed to simulate the boundary layer over the human body.

The human body has been considered as a series of heated cylinders and convective boundary layer theory has been used to determine the flow profiles and the heat output from these cylinders. These results have been shown to agree with the measured profiles and with the heat transfer data obtained by physiological methods. The way in which clothing modifies the convective flow patterns and the heat transfer is discussed.

The proposition that the human convective flow may transport particles from one site to another has been investigated using tracer particles in the flow of heated models and in a small laminar flow wind tunnel. The convective boundary layer has been shown to be a powerful mechanism for the dispersal of particles from the body.

Some air sampling techniques are described and the results of the sizing and identification of particles from various environments with special reference to the recovery of particles of skin shed from the body surface are reported.

The development of an electronic particle sampling device based on a hot wire anemometer probe is described.

The bellows action of garments in displacing air from non-occluded openings has been visualised. This effect is discussed in relation to the way in which garments used in operating theatres may enhance the dispersal of skin particles to contaminate the surrounding air.

GENERAL NOTATION FOR SYMBOLS OTHER THAN SPECIFICALLY DEFINED IN THE TEXT

Heat Transfer

Gr	Grashof number = $g x^3/\nu^2 (T_w - T_\infty)/T_\infty$
g	Acceleration due to gravity.
x	Vertical height along a flat plate.
ν	Kinematic velocity.
T	Local temperature.
Tw	Temperature of plate surface.
T_∞	Temperature of air a large distance from heated plate.
U	Flow velocity in x direction.
y	Horizontal distance from heated surface.
v	Flow velocity in y direction.
β	Coefficient of expansion of air (= 1/T).
K	Thermal conductivity of air.
Pr	Prandtl number $(C_p \mu/K) = (\nu/\alpha)$
μ	Viscosity of air.
Cp	Specific heat of air.
Re	Reynolds number = ul/ν
l	Characteristic dimension of system, i.e. anemometer wire diameter.
q(x)	Local heat transfer rate.
Nu	Nusselt number.
σ	Stefan-Boltzman constant.
ε	Surface emissivity.
ρ_a	Air density
Le	Lewis number = D/α
Sc	Schmidt number = D/ν
D	Mass diffusion coefficient.
α	Thermal diffusion coefficient.

Particle Transport

μm	Micron.

d	Particle diameter.
χ	Particle dynamic shape factor.
D'	Drag force on particle.
L'	Lift force on particle.
Cd	Particle drag coefficient.
Cl	Particle lift coefficient.
Ut	Particle terminal velocity.
U_τ	Shear velocity.
ρ_p	Particle density.
D	Flow channel depth.
Uo	Maximum velocity in flow channel.
Ue	Drift velocity due to electric charge.
η	Collection efficiency of particles landing on a wire.
γ	Particle glideangle - $\tan\gamma = Cl/Cd$.

INTRODUCTION

The skin surface, which is the boundary between man and his environment, is usually at a different temperature to the surroundings. It is this temperature difference that permits the body to exchange heat with the ambient air by conduction, convection and radiation and so help to maintain a thermal balance. There is a large amount of literature concerning heat transfer from the human body which involves measurements using physical and physiological techniques and much of it is explained and summarised in references 1, 2, 3 and 4. The ways in which the body may lose heat are radiation, conduction, convection and evaporation and the work reported in this thesis begins by considering heat transfer by convection in situations where the body is warmer than the surroundings, where convection normally accounts for some 30% of the total heat output.

Although the convection heat loss from the body has been calculated for many years, the formulae used for these calculations have been mainly derived from empirical methods used in engineering heat transfer work. These calculations provide values for the overall convective heat transfer from body and model surfaces but give no detailed information on the fluid flow fields that form the basis for heat transfer by convection. Lewis (5) showed that the convection currents that surround the body could be made visable by using a schlieren optical system. The work reported in this thesis started after this demonstration of the moving air currents, and the first step was to make detailed observations of the convective flow systematically over the entire body. The results of this work are reported in (6) and the observations were recorded on ciné film. Following this it was decided to try to describe the convective flow fields mathematically, to compute the convective heat transfer and to perform experiments to measure the velocity and temperature profiles found in the flow near to the body surface. These measurements and calculations form the first part of this thesis and show that the temperature gradient

between the body and the surroundings may produce a vigorous upward convective boundary layer flow. Constant temperature hot wire anemometers have been used for velocity measurements, and small thermocouples have measured temperature profiles within the boundary layer. Because of the many difficulties of performing experiments in the flows surrounding human subjects, models which simulated these convective flows have been used and a simple cylindrical model was constructed for heat transfer measurements.

The human body is then considered as a series of cylinders for the analysis of velocity profiles and heat output rates using boundary layer theory. These results are compared to those obtained by methods of partitional calorimetry.

Following the realisation of the vigour of this convective flow, it was considered that small particles could become entrained in this boundary layer to be transported by the air streams from one site to another. Of particular importance is the proposition that the small particles of skin that are constantly being shed from the human skin could be dispersed into the surrounding air. In this way, the convective flow could provide a link in the chain of airborne infection.

Some preliminary measurements of the bacterial concentration have shown that there are as many as 4 times the number of micro-organisms in the human boundary layer than in the ambient air. This is only possible if particles are shed from the surface or acquired from the surroundings. It is also possible that there may be dispersal of particles from the boundary layer to the surroundings. Particles may also be presented to the nose or mouth and then to the respiratory tract. Droplets which are dispersed in the expiratory flow to the boundary layer may also enter the surroundings from the plume of heated air above the head. It was also found from bacterial counts that when the skin surface just distal to a sampling nozzle is gently scratched, there can be as much as a tenfold increase in the number of micro-organisms as in the ambient air.

The transport of skin fragments and other particles of biological interest in the human convective flow is the subject of the second part of this thesis. The physical processes involved in the flight of small particles in air streams are investigated both theoretically and experimentally. The experimental part of the work involves the investigation of particle motions in air streams by ciné-photography and by the observation of particle deposition patterns on solid surfaces.

For particle transport studies a full-sized plastic model of the human form having an artificial respiratory system was constructed to investigate particle dispersion and deposition by the micro-environment. In addition, in order to study the motions of these particles in an air stream, a small wind tunnel was constructed to simulate the inner part of the laminar natural convection boundary layer flow.

Following these experiments in controlled flow conditions, which showed that the convective boundary layer could be a powerful mechanism for taking particles away from the body surface, it was decided to investigate and identify typical airborne particles. Consequently, air samples have been taken both in enclosed spaces and in the outside environment, and the last part of the thesis reports some of the results of particle sizing and identification that have been obtained. Neither the convective boundary layer flow nor the transport of particles by this layer appear to have been investigated previously.

2. VISUALISATION OF THE CONVECTIVE FLOW AROUND A HUMAN SUBJECT

The surface of the body is usually at a higher temperature than the ambient air and consequently there is a temperature gradient from the skin to the surroundings. This means that the air next to the skin becomes heated by conduction, becomes less dense and increases its buoyancy to rise; with cooler denser air taking its place. The refractive index gradient due to the temperature gradient creating the natural convective

boundary layer flow enabled a schlieren optical system to be used to visualise the flow patterns around the body. Figure 1 shows a diagram of the particular system that was used at the N.I.M.R. It consists of light from a bulb focussed with a spherical lens on to a vertical slit. This slit provides a vertical light source at the focus of a 45 cm diameter parabolic mirror of high optical quality. The light from this first mirror is reflected as a parallel beam to a second parabolic mirror some 6 m away. The light from this second mirror is brought to a focus at a cut-off and the light is finally focussed by a spherical lens to produce an image at a camera. As long as there are no refractive index changes within the region of the parallel beam - or the working area of the system - the light rays travel in straight lines to pass through the central portion of the cut-off. This cut-off consists of a narrow central band of gelatin on either side of which is gelatin of a different colour. If, however, a change of refractive index occurs within the working space, the light will be bent. The effect of such bending is to cause the light at the cut-off to be deflected from the central band and to pass through the contrasting coloured gelatin strips. If the central band of the cut-off is made of yellow gelatin and the other bands are of red gelatin, then undisturbed light rays in the working area show up as yellow, and rays that are bent due to refractive index changes show up as red. If a human subject is placed in the working section, then the refractive index changes within the human micro-environment allow the movement of the natural convective boundary layer flow to be recorded. In the N.I.M.R. schlieren system, the mirrors are positioned at a height of some 2 m from the ground and there is a hydraulic lift in the working space. In this way, the whole of the convective flow over a standing person may be visualised by raising and lowering the subject on the lift. At the highest lift position, the feet will be in the schlieren beam and the face area is in view with the lift lowered. The starting point for the present

investigation is a colour ciné schlieren film which traces the convective flow systematically over the body surface (7). The schlieren photography shows that the boundary layer, starting at the feet, detaches itself from the dorsa and rises vertically. Part of the flow, however, remains attached to join the flow at the ankle, from where it travels along the front of the leg, accelerating and becoming thicker as it rises.

As the layer of air, 1-2 cms thick, rises, it passes over the knee and thigh to the groin. The outer parts of the layer become partially detached at the convexities. Regions of reversed flow in the outer part of the layer are also seen. This general flow pattern persists up to the chest level until, in the region of the shoulder, where the surface is horizontal, most of the boundary layer breaks away upwards. Stagnation regions, where the flow is brought to rest, are found in the perineum, the axilla and under the nasal septum. Figure 2 shows a drawing of this flow over the vertical body and contrasts this with the horizontal case. When the flow meets the chin, some air is deflected and crosses the face just in front of the eye area. The ear deflects some of the air away from the side of the head to form a small plume. Air that is not deflected at the chin travels to the nose where part of it is inhaled. From the schlieren visualisation, the convective air velocity over the face of a naked standing man can be seen to reach 50 cm/sec and the boundary layer thickness at this position is some 15 cm. The total quantity of air passing over the head is over 10 litres/sec.

2.1. The Fluid Dynamic Characteristics of the Flow.

The parameter governing the characteristics of the convective boundary layer flow is the Grashof number $Gr = gx/\nu^2(Tw - T_\infty)$ which is the ratio of buoyancy forces to viscous forces. Cheesewright (8) gives the value of Gr for the onset of transition from the laminar flow on a vertical flat plate as 10^9 the flow becomes fully turbulent when $Gr > 10^{10}$.

For a temperature difference of 18°C between the body and the ambient air, the flow remains laminar up to a vertical height of 100 cms from the ground. The next 50 cms are the subject of a transitional flow and fully turbulent flow is developed at a height of 150 cms. Figure 3 shows the 3 flow regimes defined in terms of the Nusselt and Grashof numbers, and Figure 4 shows the variation of Gr with vertical height. For a naked standing man, the flow is seen to change from a laminar to a transitional flow at about the level of the navel (100 cms). On a clothed man, the temperature on the outside of the clothes may have dropped to 27°C and the flow over the whole body would then be laminar.

3. HEAT LOSS FROM THE BODY SURFACE

In man's thermal environment, radiation, conduction, convection and evaporation are balanced against an individual's own metabolic heat production to achieve a constant internal body temperature of 37°C and a skin surface temperature of from 30° to 33°C. For a naked man standing at rest in a room temperature of 15°C, the total heat output is about 100 watts. Radiation accounts for 60% of this; water loss from the skin and by insensible evaporation together with conduction at surfaces in contact with the skin is responsible for a further 10% and the rest, some 30%, of the heat is lost by convection.

Thermal regulation depends on the maintenance of a balance between heat production and heat loss. Such a balance occurs in any physical system if a steady state is attained and the human body may be regarded as such a system. In this study, the body skin temperature is taken to be 33°C and no account is taken of the local variations in this temperature which occur at various sites on the body. In the human body, the heat balance is maintained to some extent by control of heat production but for the most part is attained by the regulation of heat loss. The following table gives values for heat loss by convection, radiation and evaporation

for an adult man averaged over 24 hours. These values for the different fractions of heat loss by their respective means have been arrived at by a method of partitional calorimetry. By altering the temperature of the air and of the walls of an experimental chamber independently of each other, it was possible to study the parts played by convection and radiation under varying environmental conditions.

Table 1 :

	Kcals	% Total
Insensible water loss 1) By breath	255	11.5
2) By skin	336	15.0
Radiation	890	41.0
Convection	711	32.5
Total	2192	100

Typical Heat Loss for Adult Man in 24 hrs in an Ambient Temperature of 20°C (From 9)

Conduction from the skin to the surrounding air is sometimes considered as an independent method of heat transfer. With the realisation that a boundary layer type flow forms part of the human micro-environment, it is now seen that conduction is an intrinsic part of the convective heat loss.

3.1. Analysis of Natural Convection from a Flat Plate

Fluid motions that are caused by density gradients created by temperature gradients are termed natural convection flows as distinct from forced convection flows in which the fluid flow is maintained mechanically. Problems in free convection have mainly been solved by 2 methods : a) a similarity solution of the partial differential equations governing the flow is sought, which reduces them to ordinary differential equations in the similarity variables; b) boundary layer equations are satisfied on the average by replacing them by their integrals across the boundary layer.

For a flat plate, body forces are in equilibrium with the hydrostatic pressure when there is no temperature difference between the plate and the ambient air. If the plate is heated, the resultant temperature rise in the fluid produces a change of body force because of decreased density. The fluid nearer to the plate is therefore subject to a buoyancy force which is balanced by the viscous forces and the inertia of the moving fluid. Some early visualisation experiments on free convection flow under gravity about an isothermal flat plate were made using a schlieren method by Schmidt and Beckman (10) in 1930. Ostrach in 1953 (11) considered a viscous heat conducting fluid and developed asymptotic forms of the basic equations in laminar flow, and these are outlined in the following section. For turbulent natural convection from a vertical flate plate there is not a great deal of reliable, theoretical and experimental data. Griffiths and Davies(12) measured the local heat transfer rates and temperature and velocity profiles. These results only agree partially with the semi-theoretical result of Eckert and Jackson (13 and 14) and the analysis of Bayley (15). More recently, Cheesewright (16) has presented experimental temperature and velocity profiles for Grashof numbers between 10^{10} and 10^{11} which are in reasonable agreement with the existing experimental results. In the following sections, it is these profiles from Cheesewright that are used to determine the boundary layer parameters for turbulent flow over the body.

3.1.1. The Boundary Layer Equations for Laminar Flow.

In the case of the vertical hot plate, the pressure in each horizontal plane is equal to the gravitational pressure and is thus constant. The only cause of motion is furnished by the difference between weight and buoyancy in the gravitational field of the earth. The equations expressing the conservation of mass, momentum, and heat energy for a steady laminar flow in the boundary layer reduce to :

$$\frac{\partial u}{\partial x} + \frac{\partial u}{\partial y} = 0$$

$$u\frac{\partial u}{\partial x} + v\frac{\partial u}{\partial y} = g\beta(T - T_\infty) + \nu\frac{\partial^2 u}{\partial y^2}$$

$$u\frac{\partial T}{\partial x} + u\frac{\partial T}{\partial y} = k\frac{\partial^2 T}{\partial y^2}$$

With the associated boundary conditions :

$$\left.\begin{array}{l} u = 0 \\ v = 0 \\ T = T \\ \frac{\partial T}{\partial y} = 0 \end{array}\right] \text{at the wall} \qquad \left.\begin{array}{l} u = 0 \\ T = T \\ \quad = 0 \\ \frac{\partial T}{\partial y} = 0 \end{array}\right] \text{at infinity}$$

Where g is the acceleration due to gravity, β the coefficient of cubical expansion ($=\frac{1}{T_\infty}$ for a gas), T the temperature of the air, T_∞ the temperature at a large distance from the body and T_w the temperature at the wall.

Ostrach defined similarity variables of the form :

$$\eta = \left(\frac{Gr}{4}\right)^{1/4}\frac{y}{x}$$

$$H(\eta) = \frac{T - T_\infty}{T_w - T_\infty} \quad \text{and} \quad \psi = 4\nu\left(\frac{Gr}{4}\right)^{1/4} F(\eta)$$

where $Gr = g\beta(T_w - T_\infty)\frac{x^3}{\nu^2}$ = Grashof number

and ψ is the stream function defined by $u = \partial\psi/\partial y$ and $v = -\partial\psi/\partial x$

The substitution of these similarity parameters in the governing equations lead to the ordinary differential equations in the similarity variable η

$$F''' + 3FF'' - 2F'^2 + H = 0$$

$$H'' + 3Pr.FH' = 0$$

where $Pr = \nu/k$

The boundary conditions now become :

$$F'(0) = 0 = F(0)$$

$$F'(\infty) = 0 = H(\infty)$$

These equations have been solved to give the non-dimensional velocity and temperature profiles for various values of Pr. and are shown in Figures 5 and 6

3.1.2. The Application of the Solutions of the Equations to Heat Transfer from the Human Body.

The convective heat transfer from the body to the surroundings is proportional to the gradient of the temperature curve of the body ie $q(x) = -k(\partial T/\partial y)_0$ = heat transferred per unit time and area from a plate to the air. At a vertical height x this becomes, from the solutions for the velocity and temperature profiles in laminar natural convection flow, $q(x) = -Kcx^{-1/4}(\partial\theta/\partial\eta)_0(T_w - T_\infty)$

where $c = \sqrt{g/4\nu^2 \frac{T_w - T_\infty}{T_\infty}}$

For air having Prandtl No. 0.733, $(\partial\theta/\partial\eta)_0 = 0.478$

The total heat transferred by a plate of length l and width b is

$$Q = 0.508 \cdot 4/3 \; b \cdot l^{3/4} c k (T_w - T_\infty)$$

The mean Nusselt number defined by $Q = b.k.N_m(T_w - T_\infty)$

becomes $N_m = 0.478 \, c \, l^{3/4}$ or with the value of c from above

$$N_m = 0.478 \, Gr^{1/4}$$

Where Gr: Grashof Number = $\frac{g l^3}{\nu^2}\left(\frac{T_w - T_\infty}{T_\infty}\right)$

Above a vertical height of 153 cms with the temperature difference between the man and his environment of 18°C the Grashof number exceeds 10^{10} and the flow is fully turbulent. It is therefore important to know the velocity and temperature profiles together with the heat transfer rates in such a turbulent flow.

The velocity and temperature profiles as measured by Cheesewright for turbulent flow seen in Figure 7, starting with these profiles, an analysis similar to the laminar flow case above gives a value for the heat loss from a vertical plate in turbulent flow of

$$Q_T = b.k.(T_w - T_\infty)\; 12 \left[g \frac{x^3}{\nu^2} \left(\frac{T_w - T_\infty}{T_\infty} \right) \right]^{0.1}$$

and the mean Nusselt number may be defined as $N = 0{\cdot}12\ Gx^{0.3}$

From these expressions for heat transfer from laminar and turbulent flow it is seen that in the laminar case the total heat transfer Q_L varies with $x^{0.75}$ and that in the turbulent case Q_T is proportional to $x^{0.9}$. In laminar flow, the heat loss from body elements of height l and breadth b at room temperature is expressed as $Q_L = 0.01\ bl^{3/4}$ watts and for turbulent flow $Q_T = 0.02\ bl^{0.5}$ watts. Further, it is seen from the velocity profiles that the boundary layer thickness varies with $x^{0.25}$ for laminar flow and $x^{0.7}$ for turbulent flow.

An estimate of the convectional and viscous terms in the energy equation gives the thickness of the velocity boundary layer proportional to $1/\sqrt{Pr}$. In laminar flow (17), the ratio of the velocity and temperature profile thicknesses $\left(\frac{\delta v}{\delta T}\right)$ is found to be proportional to $1/\sqrt{Pr}$ This gives a good physical interpretation of the Prandtl number, and it is noted that for gases, where Pr. is about 1, the velocity and temperature thicknesses are nearly the same. For liquids, the thermal boundary layer is smaller than the velocity boundary layer.

3.2. The Human Body as a Series of Cylinders.

In order that boundary layer theory may be applied to the determination of the convective heat loss from the body surface, it is useful to consider the body as composed of a series of separate cylinders. Figure 8 shows how the body may most obviously be considered as broken down into six cylinders so as to represent the head, the torso, 2 arms and 2 legs.

The dimension shown as those taken from a typical subject. The total surface area for this model is 1.89 m^2 which compares well with the average value of 1.8 m^2 for the skin surface area of a man (1.6 m^2 for a woman). The body is further simplified by opening the cylinders to flat plates and by considering the torso and legs together as one flat

plate. The final set of plates together with their dimensions is shown below.

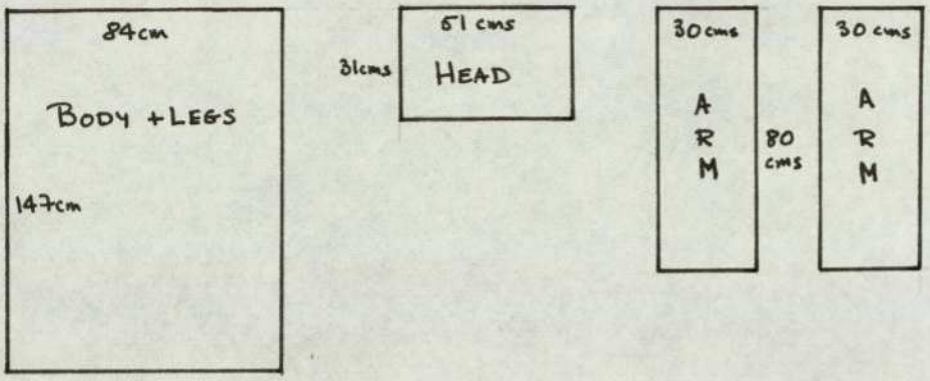


Table 2 shows the convective heat output from the various parts of the body as computed from section 3.1.2. for T_w = 33°C and T_∞ = 15°C.

Table 2 :

	Watts	% Total
Arm	7.9	13.8
Arm	7.9	13.8
Body	35.0	61.0
Head	6.6	11.4
Total	57.4	100

Convective Heat Loss from Body Cylinders

3.2.1. Radiant Heat Output.

Having simplified the human form into 4 plates, it is now possible to calculate the radiant heat loss to the surrounding air and to examine the effects of radiation on the convective heat transfer equations.

Using the Stefan Boltzmann equation for radiative heat transfer, we have the heat output from each body element given by $Q = \varepsilon \sigma A\left[\left(\frac{T_1}{100}\right)^4 - \left(\frac{T_2}{100}\right)^4\right]$ where ε = emissivity = 0.9. (The human skin, whatever its colour, may be regarded as having an emissity of 0.9 in these calculations), A = area of plate; σ = Stefan Boltzmann Constant; T_1 = surface temperature = 33°C; T_2 = temperature of surroundings = 15°C.

The results for the radiation loss from each body element are shown in Table 3, and these are discussed later

Table 3 :

	Watts	% Total
Arm	22.4	12.7
Arm	22.4	12.7
Body	116	66.0
Head	14.8	8.6
Total	176	100

Radiation Heat Loss from Body Cylinders

3.2.2. Effect of Radiation on Convective Heat Output.

In the convective heat transfer analysis, no account was taken of the modification to the boundary conditions for the flow equations that radiation losses at the wall (18). To consider these effects on the convective heat transfer, we shall assume (a) that radiation losses form part of an optically thin process, i.e. that the radiation penetration length is long compared to the boundary layer thickness, and (b) that air is transparent to radiation. The complete boundary layer equations are the same as in section 3.1.1., but the boundary conditions now become :

$q(x)_{wall} = -K\left(\frac{\partial T}{\partial y}\right)_{y=0}$ where $q(x)_{wall}$ is the heat flux from the body to the fluid and $q(x) = (q_w - q_{wr})$ where q_{wr} is the radiation heat loss

$$\therefore \frac{\partial T}{\partial y} = -\frac{q_w}{K} + \frac{\sigma \varepsilon}{K}\left(T^4 - T_\infty^4\right) \quad \text{at} \quad y = 0$$

also $u = v = 0$, $T \to T_\infty$ and $u \to 0$ as $y \to \infty$

The boundary layer equations with these boundary conditions have been solved for Pr = 0.72 to give

$$\frac{Nu}{(Gr)^{1/4}} = \left[0.407 - 0.161\,\xi' + \ldots\right]$$

$$\xi' = \frac{\sigma\,\varepsilon}{k}\,T_\infty^3\left(\frac{5\,k\,\nu^2 x}{g\beta q_w}\right)^{1/5} \quad \text{when } x_c = 153\text{cm (onset of turbulence)}$$

$$\xi' = 0.0436 \quad \text{giving} \quad \frac{Nu}{(Gr)^{1/4}} = 0.400$$

$$\xi' \text{ at } x_c = 29.5\,\text{cm} = 0.0321\,, \quad \frac{Nu}{(Gr)^{1/4}} = 0.402$$

Comparing these values to $Nu/(Gr)^{1/4} = 0.407$ (from ignoring radiation) we over-estimate the convective heat transfer by 1.7% at 153 cms and 1.3% at 29.5 cms.

An average value for the overestimation of convective heat transfer by ignoring radiation effects is therefore 1.5%.

3.3. Discussion of the Calculated Heat Transfer Rates.

The disadvantage in using theoretical methods to calculate the heat loss from an idealised set of cylinders representing the body is that the surface area available in radiation and the vertical height which is important in convection, both change markedly with body posture. Consequently, any attempt at a theoretical assessment of heat output over a long period when changes in the body posture may occur is rendered difficult. This is because of the need to determine the effective body area available for heat transfer in the various postures and then determining the dimensions of a representative cylinder. Therefore in these analyses only the 'extended' body position is used to demonstrate the heat transfer calculations and compare these results with physiological data.

In the convective heat loss analysis, it is seen in section 3.2. that the total convective heat output may be about 57 watts. When the resting convective heat loss of 57 watts is converted to an average heat loss for 24 hrs and is expressed in Kcals/24 hrs, we find that the value of 1066 Kcals/24 hrs compares extremely well with the heat loss in 24 hrs due to convection and insensible evaporation obtained from the partitional calorimetry methods of 1047 Kcals/24 hrs (19).

Here it should be mentioned that the calculation of convective heat loss for the various body cylinders was made for the laminar natural convection flow, where analysis leads to an expression for the mean Nusselt number given by $N_m = \cdot 478\ Gx^{1/4}$. As previously stated, laminar flow exists to a vertical height of 100 cms and fully developed turbulent flow only from a height of 153 cms. It might be more appropriate therefore to consider the head cylinder when it is subject to turbulent convective flow. In this case it has been shown that the mean Nusselt number can now be expressed as $N_m = .12\ Gx^{0.3}$ (20) and if the cylinder representing the head is considered as having such a flow starting from its leading edge, it can

be seen that the expression for the heat loss becomes $Qt = 6.6\ b(x)^{0.3}$ and the heat loss from the head now takes the value of 11 watts (compared to 7 watts in the laminar case). In view of the fact that the face and head are well endowed with sweat glands and discrete regions of varying temperature, it is doubtful whether such a distinction in the theoretical analysis is important, since the local temperature variations (and evaporation) could change the heat output to a greater extent.

When we consider the results for the radiant heat output from the cylinders, it is important to note that in Table 3 it is assumed that the whole of the plate surface area is effective in contributing to the heat loss by radiation. In reality, areas of skin between the fingers, under the arms, between the legs and under the chin radiate to adjacent skin areas and not to the environment. The physiological formulas which exist for the calculation of the entire surface area of the human subject (as functions of body height and weight) recognise that only a portion of this area is completely effective in losing heat by radiation. Various studies in partitional calorimetry show that in the normal 'extended' position of the body the effective radiating area will be somewhere between 70% and 85% of the total surface area. Any change from this posture will result in radiative area reduction.

A more valid comparison between these calculations and the results achieved by physiological methods is seen when we compare the plate results with the work of Herrington (21). In this study, a dry heated model of the human body was used in place of a real subject. Comparison between these results and those of the flat plates is more realistic than comparison with the calorimetry results with the human subject because evaporative losses are absent. The flat plate results are re-calculated in the correct units for air temperatures of 26.7°C (60°F) and 32.8°C (80°F). (The ambient temperature used by Herrington was 32.8°C and the following table shows them to be in reasonable accord with Herrington's

values.)

Table 4 :

Total Plate Area m^2	Total Heat Input watts	Surface Temp ^oC	Air Temp ^oC	Hr + Hc watts/m^2
1.80	84	32.1	26.7	43.3
Herrington's data				
1.89	118	32.8	26.7	66
1.89	252	32.8	15.6	129
Present data for 2 ambient temperatures				

The results of radiation heat loss from the flat plate analysis agree well with the radiation heat loss obtained experimentally on cylinders by Herrington (also reported in reference 21). From the above Table, it is seen that a 10^oC change in ambient air temperature results in nearly a twofold increase of the body heat output by convection and radiation. Since the main object of this work is to consider convective phenomena no more detailed study of radiation losses have been made here. The importance of evaporation in thermal regulation is demonstrated in the following Table. At all energy levels greater than the resting energy output rate, evaporation is by the far the most important heat transfer mechanism capable of increasing heat loss from the body and its dramatic effect is seen in this Table.

Table 5 :

Resting Rate	40 Kcal/M^2/hr
Awake and Resting	55 Kcal/M^2/hr
Light Work	75 Kcal/M^2/hr
Walking 4 mph	190 Kcal/M^2/hr
Strenuous Work	300-600 Kcal/M^2/hr

Typical Values for the Total Heat Loss from the Body

The results calculated for the flat plates give the total heat output as 102 Kcal/M^2/hr from convection and radiation alone in an ambient temperature of 15^{o}C. This correlates with physiological data for the output in light work and may be considered in reasonable agreement when account is taken of the fact that varying postures in light work may exclude much radiative and convective heat transfer areas, which may change with time.

In concluding this section, it is mentioned that the idealised model of the equivalent cylinder simply demonstrates that the theoretical analysis gives the same orders of magnitude as physiological methods in the extended position but due to the complex and variable geometry of other body postures, this form of analysis is not appropriate for detailed heat loss prediction.

3.3.1. The Effect of Water Vapour Within the Boundary Layer.

It is important to assess the change in boundary layer parameters when water vapour is introduced into the flow from the skin surface by the mechanism of sweating or insensible evaporation. If we consider the air surrounding the body to be dry, then in order for the convective boundary layer to become saturated with water vapour it is necessary that the secretion rate be such as to saturate the total mass of the air being convected upwards. For a convective up-flow of 10 litres/sec the maximum quantity of water vapour that the boundary layer is able to absorb is 0.228 gm/sec (0.82 litres/hr). If we consider a typical rate of insensible evaporation to be 0.01 gm/sec (i.e. about 1 litre/24 hr period) then it is seen that this is about 1/20th the quantity of water that the boundary layer is able to absorb before it becomes saturated.

When water is lost from the body surface, 0.58 Kcals of heat is lost for each gram that evaporates. This means that in a dry atmosphere, in

the absence of forced convection, the heat output of a person may increase by as much as (0.58 x 0.228 x 3600) Kcal/hr, i.e. 475 Kcal/hr, before the boundary layer is saturated. Thus the micro-environment has capacity to absorb evaporated sweat up to very severe exercise rates without the aid of forced convection if the surrounding air is dry.

If we consider the way in which the boundary layer flow could be modified by the introduction of water vapour, it is necessary to estimate the change that this water vapour within the air stream produces in the value of the Prandtl number. The value of Pr for saturated water vapour at room temperature is 0.96. However, the quantity of water that the air is able to absorb before it is saturated with the vapour is 0.082 litres water/litre dry air. That is 8.2% by volume of water in the air/water mixture. From this an estimate of the value of the Prandtl number for the saturated air gives the value of 0.74.

In the solutions for the boundary layer equations as outlined in section 3.1. profiles are only presented for discrete values of the Prandtl number of 0.73, 1.0 and 10. From these profiles, it may be seen that a change in value from Pr of 0.73 to 0.74 (a change of 1.4%) produces a negligible change in the flow parameters (a change of 0.5% in maximum velocity and of 0.7% in the boundary layer thickness). In all normal environments, the boundary layer flow may be considered similar in both dry and humid conditions, and that the flow may be analysed by considering the Prandtl number to be that for dry air.

In a turbulent boundary layer, the transport of heat is effected by conduction at the solid surfaces as well as by turbulent mixing; and the transport of mass is by diffusion and turbulent mixing. The diffusion and heat-conduction processes are dominant close to the interface and the turbulent mixing process dominates in the outer regions.

The dimensionless group which is the ratio of the diffusion coefficient of water vapour into air to the thermal diffusion coefficient is defined

as the Lewis number Le (= D/α).

It may be shown that a number of 2 component gas mixtures including humid air have a Lewis number nearly equal to 1. For the description of a mass transfer process, a parameter is often used which is the ratio of the diffusion coefficient and kinematic viscosity. It is called the Schmidt number, Sc = D/ν. A Lewis number of 1 is equivalent to a Schmidt number equal in value to the Prandtl number. The usefulness of these dimensionless groups is summarised as follows : Any relation for a heat transfer process can be changed over to a relation for a mass transfer process simply be replacing the Prandtl number in the heat transfer relation by the Schmidt number and replacing the Nusselt number for heat transfer by the Nusselt number for mass transfer. The relation for mass transfer obtained in this way holds for zero or small mass transfer rates.

4. A CYLINDRICAL HEATED MODEL

In order to investigate the micro-environment flow parameters, a model was designed and constructed to simulate the convective flow conditions likely to be encountered around the human body.

Figure 9 shows this model which consists of a 5" dia by 5' long aluminium cylinder mounted below a hollow aluminium casting of the human head. A long immersion heater was fitted into the base of the cylinder and the whole model filled with water. The heater was used to raise the surface temperature of the model to 33°C. To ensure a uniform surface temperature a small water pump allowed the heated water to circulate freely. The aluminium surface was painted matt black so that the model could be regarded as a black body radiator.

The model was used to fulfil 3 functions :

a) To assess the sensitivity of the N.I.M.R. schlieren system.

b) To generate a natural convection boundary layer so that the velocity and temperature measuring devices could be evaluated.

c) To provide the model head at the top of the cylinder with a known flow pattern and thus to observe the flow around the head.

In order that the thickness of the boundary layer approaching the head could be controlled, the model was provided with varying size sheets of cork lagging so that the boundary layer could be made to establish itself at any position along the cylinder.

When considering the cylinder as a boundary layer generator at a temperature of $33^{o}C$, the flow remains laminar until $Gr = 2 \times 10^{9}$ that is until x = 100 cms from the leading edge. The transitional flow remains until $Gr = 10^{10}$ when x = 153 cms, that is to the top of the neck. By varying the length of lagging on the cylinder, the flow over the whole model could be made laminar; a condition that simulated the effect of clothing.

4.1. Description of the Flow over the Heated Cylindrical Model.

The heated cylindrical model was observed using the schlieren system, and a colour ciné film of the natural convective flow was produced. Measurements in the boundary layer flow with the thermocouples and anemometers were also made.

From the schlieren visualisation film the flow along the vertical cylinder at low Grashof numbers ($< 2 \times 10^{9}$) where the boundary layer flow was laminar was observed. Although great care was taken to ensure as little ambient air movement as possible, the natural convective laminar flow was almost always observed to be unsteady. Large and small eddies were continually being shed from the cylinder and the extent of the visable boundary layer was constantly varying. This observation (which coincides with those of Cheesewright) was confirmed by the presence of an anemometer probe in the flow. Even when the wire was very near to the hot surface, unsteadiness was continuously seen on a cathode ray display. As a consequence of this unsteadiness, any precise observation of the transition

from laminar to turbulent flow using the schlieren system was not practicable.

When observing the flow near the neck and over the head of the model, large eddies were often seen. The outer part of such an eddy would move in a downward direction and give the appearance of reversed flow.

With no insulation on the model, the flow at head level was seen to extend some 20 to 25 cms from the model surface.

For both the laminar and turbulent flows, the inner part of the boundary layer was always very well defined and could be closely observed as it negotiated the various contours of the head. Only at near horizontal surfaces (i.e. shoulder, forehead, bridge of nose) did the local curvature cause breakaway and secondary flows. At all other places the flow followed very closely the contours of the face. The breakaway for the vertical plume began to be seen on the model surface at the hairline on the upper forehead.

The Sensitivity of the Schlieren System

Although the schlieren system is a very elegant way of making the convective air flow around the human body visible, it is important to know how much of the flow field may be visualised in any schlieren system.

The sensitivity of the schlieren system and consequently the part of the boundary layer appearing on a schlieren photograph depends mainly on the local refractive index gradient at the point of observation together with the path length travelled by the light beam (22). See figure below.

If we consider a very small segment AB of the wave front of a light wave which makes an angle Θ with the y axis. If now at A the refractive index is n and at B is (n + dn) then after a time Δt the wave will move to A'B' then

$$AA' = \Delta\ell/n \qquad \text{and} \qquad BB' = \Delta\ell/n+dn$$

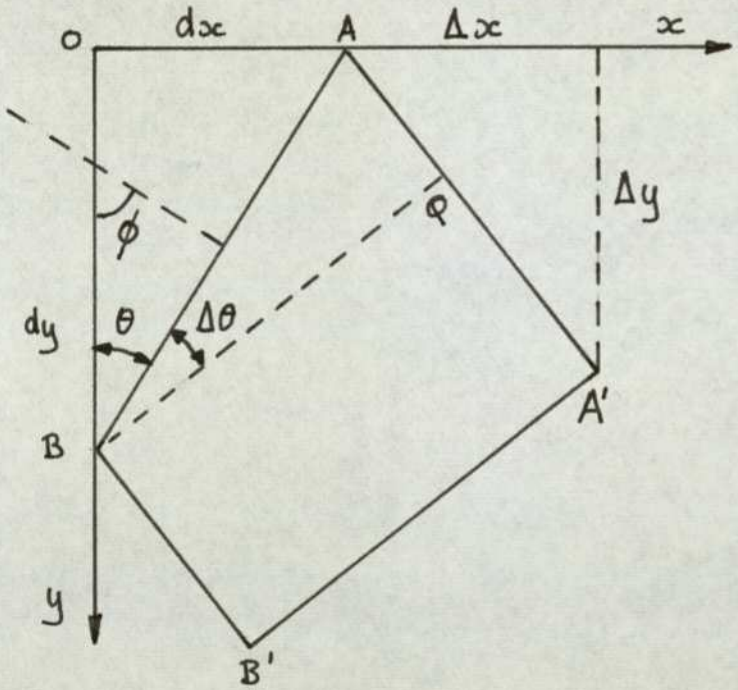
where Δ l is the optical path of the wavefront. Consequently,

$$\Delta\Theta = \frac{AB}{AB} = \frac{\Delta\ell}{n} \cdot \frac{1}{n} \cdot \frac{dn}{dy} \cos\Theta = \frac{1}{n}\frac{dn}{dy}\Delta x$$

$$\text{or} \quad \varepsilon = \int_0^{\ell} \frac{1}{n}\frac{dn}{dy} \cdot d\ell \cdot \sin\phi$$

where ε is the angle through which the light ray is bent by the disturbance and ϕ is the angle between the direction of the ray and dn/dy. Therefore, the schlieren method measures the gradient of the refractive index. A temperature gradient is equivalent to a refractive index gradient since $(n - 1)\,T = \text{const.}$ (law of Biot and Arago) and $dn/dy = (n - 1)/T$. dT/dy may be substituted in the above equation for ε

There is a limiting value for this temperature gradient, below which a given system will not register air movement. Schlieren photographs for laminar and turbulent flow were made. The value for the vertical height, x, is the distance from the cork insulation to the position on the cylinder where the boundary layer thickness is measured. The model surface temperature was $33^{\circ}C$ and the value of x for the laminar case was 10 cms



giving a $Gr = 2.7 \times 10^{6}$ and for the turbulent flow x = 153 cms gave $Gr = 10^{10}$ The extent of the visible air movement was noted on the photographs for both cases. From the theoretical temperature profiles and a photograph of the moving layer the mean limiting value of $^{\partial T}/_{\partial y}$ for this system was found to be $0.74^{\circ}/cm$ corresponding to the observed extent of the layer.

In turbulent flow air movement may still be seen even when the value for the temperature gradient is lower than this limiting value.

Such movement is seen each time the limiting value of $^{\partial T}/_{\partial y}$ is exceeded in the turbulent eddies in the outer regions of the boundary layer.

5. TEMPERATURE AND VELOCITY PROFILES WITHIN THE MICRO-ENVIRONMENT

The human natural convection boundary flow having been observed with a schlieren system, and boundary layer theory having been used on idealised models of the human form to determine convective and radiative heat losses together with the various boundary layer parameters, the next stage of the investigation was to develop techniques to measure the flow parameters on fully contoured human models and on human subjects. The 2 quantities to be measured were velocity and temperature within the boundary layer. Small thermocouple thermometers with one junction electronically maintained at a constant temperature were used for temperature profile measurements. The welded joint of the thermocouple was made small compared to the boundary layer thickness so as to obtain a large number of points in traversing a thin boundary layer.

For velocity measurements 3 instruments were considered. The first was a fluid jet anemometer that measured the displacement of an air jet by means of 2 total head tubes placed in the jet with their axes parallel to the jet nozzle. The assumption being that the total head profile would simply be displaced by the unknown fluid cross flow (23). The device has an output of 0.7 ins differential water gauge per foot per second of the unknown air velocity and is therefore suitable for measuring very small flow rates. However, the anemometer proved too bulky for a detailed exploration of the natural convection boundary layer. This instrument would prove useful for field work where mean flow rates were required.

A method of flow measurement making use of the displacement of a fine quartz fibre as measured through a reading telescope was considered (24). This fibre anemometer is suitable for very low flow rates but the telescope reading apparatus limits the use of this instrument where a direct line of sight to the fibre is not available. The orbit of the eye is an instance of an anatomical site where the measurement of the deflection of the fibre would be inhibited.

The instrument chosen for the velocity measurement was the constant temperature hot wire anemometer (25). The bridge circuits and amplifiers used were DISA 55D05 battery operated anemometers. Because of the high cost and delay in repairing the wire probes, a probe moulding and welding system was developed to enable probes of different shapes and sizes to be made.

5.1. The Hot Wire Anemometer.

The circuit for the constant temperature hot wire anemometer bridge circuit and amplifier is shown in Figure 10. A Wheatstone bridge circuit with the hot wire probe as one arm of the bridge forms the basis of the device. When the wire is cooled by being placed in a moving fluid stream, the resistance changes and the bridge becomes unbalanced. This unbalance is sensed by the amplifier which allows the bridge to receive a greater voltage across it and causes the probe to be heated until its resistance returns to the original value where the bridge is once again in balance. Since the response of the amplifier is many thousands of Hertz the practical limit to the response of the hot wire to velocity fluctuations is the thermal capacity of the wire itself.

Using 5μm dia tungsten wire approximately 2 mm in length on the probe element and keeping the wire at a temperature of 150^{o}C, the frequency response of the wire is O(30 KHz).

5.1.1. The Hot Wire Probe.

The probe itself (Figure 11) consists of a moulded epoxy-resin body, fitted at the end with a small jack plug. Figure 12 shows the mould from which these bodies were made together with probes at various stages of manufacture. The prongs of the probe are made of workhardened nichrome wire, and are approximately 2 mm apart. The 5μm dia tungsten wire is spot welded to the ends of the prongs using a specially designed micromanipulator (Figure 13) which allows delicate alignment of the probe

prongs with the wire. Figure 14 shows the circuit diagram of the capacitor discharge unit which was constructed for welding these small wires.

5.1.2. Probe Calibration.

Because of small differences in characteristics from probe to probe, it was essential that each probe be calibrated during the course of an experiment. In order to do this a small calibration rig was constructed and is shown diagramatically in Figure 15. This consists essentially of a vertical tube sufficiently long to ensure a fully developed parabolic velocity profile (100 tube diameters in this case) with air being drawn through the tube and past an anemometer placed in the flow. The volume flow rate of the air was determined by a rotameter placed in series with the calibration tube. With this apparatus, the hot wire anemometer may be calibrated to velocities as low as 0.5 cm/sec. Figure 16 shows a typical calibration curve for one of these anemometers.

5.1.3. Heat Losses from the Anemometer Wire.

The heat losses from a hot wire in a moving fluid are -

a) Radiation losses,

b) Conduction losses along the probe prongs,

c) Heat losses near a solid surface,

d) Forced convection losses to the fluid - these being a measure of the fluid velocity.

In a boundary layer velocity traverse any alteration in these losses as the wire moves towards the solid wall must be considered in the anemometer calibration.

Radiation Losses

Since air is optically thin there is a large radiation penetration length with respect to the boundary layer thickness. Since also the absorbtion coefficient = 0 the radiant heat loss follows the Stefan Boltzman law and is proportional to $(T_{wall}^4 - T_\infty^4)$. Heat loss due to radiation is

therefore constant as the wire approaches a solid wall and the calibration will not be affected.

End Losses Along the Probe Prongs

The hot wire is constantly losing heat to the probe prongs. These end losses were calculated by King (26) who showed that the temperature distribution could be represented by a hyperbolic cosine function. For the constant temperature wire used in these experiments, the prongs were made of ni-chrome having a high thermal conductivity. The end losses should remain constant and independent of the distance of the wire from the wall, except very near to the wall.

Effect of Changing Ambient Temperature

As the constant temperature wire approaches the heated skin surface, the temperature of the fluid flowing passed the wire is increasing and the temperature difference between the wire and the fluid decreases. As a consequence, the heat transfer from the wire due to forced convection falls. It is therefore necessary to determine the temperature sensitivity of the wire by measuring the 'no-flow' output from the wire at different ambient temperatures in order to correct the velocity output. The assumption is made here that the calibration curves for different air temperatures over the range of velocities that we are considering are similar in shape. The changes in no-flow voltage due to ambient temperature changes is simply an off-set on the calibration curve and is equivalent to a slightly different anemometer wire overheat ratio. Figure 17 shows the effect of different ambient temperatures on the heat loss rate for a typical probe.

Heat Loss When the Wire Approaches a Solid Wall

When the wire is very close to the solid wall, conduction directly across the air gap will predominate over the natural convective heat loss of the wire to cause a variation in the anemometer calibration. Figure 18 shows the wire heat loss as the wall is approached. It is seen that at distances closer than 300μm the heat loss rate rises steeply. If velocity

measurements were to be made on a human subject, it would be very difficult to measure closer to the skin due to involuntary body movements. Therefore it was not considered necessary to measure closer to the wall from the limiting value of $Y/\ell = 60$ shown on Figure 18 (where l is the diameter of the heated wire).

5.1.4. Time-Averaging of Anemometer Readings.

Cheesewright (16) has reported experiments to measure laminar natural convection velocity and temperature profiles in which the laminar boundary layer is almost always unsteady. This unsteadiness, which may be attributed to vertical temperature gradients and velocity disturbances within the laboratory, was the cause of some observed reversals of flow. In the present experiments, when the hot wire anemometer output from a laminar convection boundary layer flow was displayed on a cathode ray screen, the unsteady nature of the flow was clearly seen. The introduction of artificial disturbances into the laboratory, outside the boundary layer, did not appear to affect this unsteadiness. In order to obtain mean values for the velocity in this unsteady flow, the experimental technique was adapted so that the hot wire anemometer output could be sampled 100 times in 200 secs and the resulting outputs averaged to give the mean output voltage at any point in the boundary layer traverse.

An example of such a time averaged anemometer output is shown in Figure 19 which is plotted so as to show the frequency of recurring output voltages over a 200 sec period. From this figure it is seen that the majority of readings from the output voltage lie in the range (in this example) 0.720 - 0.705 volts (i.e. maximum change in output of 2%). This voltage range represents a velocity fluctuation of some 3 cm/sec. However, this range on the calibration curve (Figure 16) is very nearly represented by a straight line, and the assumption is made that the anemometer calibration curve is sufficiently linear over these small voltage output changes to enable the output voltage rather than the

equivalent velocity to be averaged. This simplification enabled the automatically obtained voltage readings to be averaged directly.

In order to estimate the effectiveness of this form of time averaging a statistical degree of confidence test was applied to the sample.

An estimate of the population variance $\hat{\sigma}^2$ from the sample variance S^2 (sum of squares of sample difference from sample average) (27) is given by the relation $\hat{\sigma}^2 = \frac{n}{n-1} S^2$ where n is the number in the sample, i.e. 10 in this test.

The value of $\hat{\sigma}^2$ was 107.7×10^{-6}.

In order to carry out a 5% significance test that the population has a mean value μ_o given by the mean of 100 readings (i.e. 0.714), it is necessary to compute a value for z given by $\frac{\bar{x} - \mu_o}{\sigma/\sqrt{n}}$ where $\bar{x}$ is the sample mean of 0.707.

For this test z = 2.13. From statistical tables $|z| > 1.96$ for 5% significance, which is the case in this example.

The conclusion from this test is that the probability that the true value μ for the mean of the output voltage lying in the range $\mu = (\mu_o \pm .05\mu_o)$ is 95%. This acceptable probability led to the adoption of the simple time averaging process to determine the bridge output voltage for the results in these experiments.

5.2. Use of the Hot Wire Anemometer and Thermocouples to Measure Velocity and Temperature profiles.

Figures 20, 21, 22 and 23 show velocity and temperature profiles measured in both the laminar and turbulent natural convection boundary layer on the heated model at various values of the Grashof number. In the case of the velocity profiles, 100 anemometer readings were time averaged and the calibration corrected for the temperature variation across the boundary layer.

Agreement with the theoretical profiles in laminar flow and the data of Cheesewright for turbulent flow are seen to be good for both the temperature

and velocity distributions and these 4 typical experimental curves demonstrate the viability of the measuring techniques that the first part of this work set out to establish. Also indicated on Figures 20 and 21 are the limits of the schlieren visualisation as determined from photographs using the heated cylindrical model. It is seen that if the boundary layer is considered to extend to a position where the air velocity is 0.1 that of the maximum, then the schlieren system allows visualisation of just over half of the boundary layer thickness.

These results for the temperature and velocity distributions around the heated model complement the schlieren visualisation of the flow and confirm the theoretical calculations from boundary layer theory for laminar flow.

The maximum velocities that occur within the flow at face level are shown to be some 50 cm/sec and the extent of the boundary layer at this level is measured to be around 20 cm. Because the flow becomes turbulent at 150 cm height, the head is generally in a region of transitional flow and consequently the flow parameters are difficult to predict. In laminar flow the velocity and thickness of the layer increase steadily with height. However, when the flow goes turbulent its nature changes so that the velocity does not increase so markedly. The energy becomes redistributed and the layer becomes much thicker with height with only a small change in velocity.

From these measurements of the boundary layer extent the volume flow over the head is calculated to be some 10 litres/sec.

6. THE TRANSPORT OF PARTICLES BY THE NATURAL CONVECTION BOUNDARY LAYER

The second part of this thesis sets out to consider the potential of the natural convection boundary layer as a transport mechanism for bacteria, industrial dusts, pollens, skin scales and other particulate debris. The main area of interest in the application of this work is the role of the

boundary layer in the transmission of airborne infection by the transport of particles that may be detached from the skin surface.

Davies and Noble (28) have shown that staphylococci are transmitted on small rafts of skin shed from the body and report the most common size for the raft was 13 μm dia; each raft may carry about 4 viable microbial units (29). As the body moves and is rubbed by clothing during exercise, fragments of skin are constantly being shed from the body with a consequent continuous dispersal of micro-organisms. These may find their way into the convective boundary layer and thence to some other body site, to the respiratory tract or to the surrounding air.

It has been found that a complete layer of skin from a man may be desquamated during the course of one or 2 days (30). It may therefore be calculated that the number of skin particles of about 13 μm dia dispersed per day is of the order of 10^{10} and the number of bacteria 'riding' on these particles can be as high as 4×10^{10} per day.

An important factor in the determination of the role of the natural convection boundary layer in autogenous infection and bacterial desimination from the body is an estimate of the bacterial density population of the skin. Among ecologists engaged on this problem there are great variations in methods of measurement with largely varying estimates for the population of the skin surface. However, it is clear that various body areas differ significantly in the densities of the populations they support. Marples (31 and 32) described these differences as "the sparsely inhabited desert of the forearm, the more heavily populated tropical forest of the axilla, and the cool dark woods of the scalp". The densest bacterial populations are found on the face and the neck and in the axilla and groin. The trunk and upper arms have much sparser populations. Numerical figures for these regions give the axilla a mean population of 2.41 million bacteria per square cm. of epidermis. The mean count for the scalp and forehead being 1.46 million and 200,000 respectively. Counts on the back

averaged only about 314 per sq cm.

Figures for the number of bacteria per unit weight of scurf, which is the surface of the epidermis, indicate an average value of about 530 million per gm.

Many methods for spore liberation are encountered in the plant world (33) which rely on the release of stored energy due to the elastic properties of plant tissues or of pressure differences within capilliaries, and it is interesting to speculate whether such mechanisms exist on the skin. Scanning electron micrographs of the skin (Figure 24) surface do reveal fibres that appear to be in tension. It has been thought that the energy release by rupture of such fibres could 'catapult' keratin flakes away from the skin surface. The results of experiments reported by Heldman et al (1967)(34) do suggest a spontaneous release of particles from arms that were exposed to an air stream in an isolation chamber. Although such a mechanism may exist, we have not been able to observe such a release by microscopic observation of the skin surface. The method of detachment that seems to dominate the release of skin particles is the abrasive action of clothes and the rubbing of one part of the body surface against another. This effect may be demonstrated by placing an arm in a perspex tube and gently rubbing the skin surface. With the use of a collimated light beam, detached particles may be seen to leave the skin and travel to the perspex surface by electrostatic attraction. Continuous gentle rubbing produces a stream of particles that does not seem to diminish in concentration even after some minutes. Figure 25 shows some more skin flakes that are nearly detached from the body surface.

To investigate the motions of particles moving in the boundary layer flow, experiments were carried out in a laminar flow channel which was used to simulate the velocity profile found in the inner part of the laminar natural convection boundary layer. Glass dust particles were injected into this flow and the numbers that deposited out of the streamline flow,

together with the numbers travelling the whole channel distance were counted. The various forces acting on the particles are considered separately and attempts at particle trajectory analysis are compared to the experimental results.

Since the natural convection boundary layer is very often laminar over large body lengths, an analogy is made between these channel experiments and analysis and the way that particulate debris may be expected to behave in the microenvironment. The numbers of particles $O(10^8)$ injected into the channel in any experiment was representative of the numbers of skin flakes that could be present around the body. As is shown further on, the shear stresses exerted on the skin by the natural convective flow over the body is not capable of dislodging skin particles or other small particles. Particles entering the boundary layer flow from the skin surface may therefore be dislodged by mechanical friction caused by the rubbing actions of limbs and clothes.

When the mass flow rate of upward moving convective air above a naked standing man is considered, the flow is seen to be of the order of 10L/sec with a maximum velocity of up to 50 cm/sec. An application of this work is found in operating theatre ventilation systems where the total room air is changed many times each hour, with the sterile make-up air often flowing downwards from the ceiling. The ventilating air velocity will depend on the volume of the theatre and the particular geometry of the ventilating system, but a local downwards velocity of around 20 cm/sec may be encountered at specific sites. The local downward flow velocity and the upward convective flow can therefore have comparable magnitudes and the consequent mixing of these two airflows can be important when considering the local flow conditions over, say, an operating theatre table.

6.1. The Motion of Particles in a Viscous Flow.

In the study of particle motion in viscous flow, Jeffrey (35) has

suggested that particles travelling in a fluid stream "..... will tend to adopt that motion, which of all the motions possible under the approximated equations corresponds to the least dissipation of energy." He follows with the proposition that "for motion in a capilliary tube the particles will tend to concentrate along the axis of the tube." Goldsmith and Mason (36) in carefully controlled experiments observed no axial migration with rigid rods and discs in viscous flow. For deformable particles (blood cells, oil droplets, etc.) the axial migration suggested by Jeffrey has been observed and analysed.

Owen (37) when considering the axial movement for solid particles in an air stream, suggests that the only forces tending to displace a particle from a streamline, in laminar flow, are Brownian diffusion, Magnus forces due to spin and differential shear forces. He suggests that all of these forces can only be of significance for particles less than 0.1 μm equivalent diameter. The nett conclusions from previous studies suggests that in a laminar flow, in the absence of gravity of electrostatic forces (also in the absence of particle collisions and interactions) particles will not deviate from their initial streamline motion.

In the following sections, an attempt is made to examine the trajectories of particles in a laminar flow. The application of this is to estimate the capacity of the natural convection boundary layer around the human body for dispersing particles from the streamlines into the surroundings, or transport such particles over the body.

The maximum velocities encountered in the human natural convection boundary layer are about 50 cm/sec, and over typical body lengths of up to a metre or so (e.g. leg, arm and body dimensions) the flow may be laminar. Any particle will be in suspension when the flow velocity is greater than the terminal fall velocity of the particle. Thus particles greater than about 80 μm equivalent diameter will fall to the ground and will not concern us in this analysis. Any particles entrained in the flow where the velocity

is very nearly equal to the particle fall velocity will have a small nett vertical velocity. For such particles the time of flight to traverse body lengths will be significant (smallest time will be about 1 sec) with the result that any forces tending to displace the particle from the streamline will have an appreciable time in which to act.

6.1.1. Particle Size and Terminal Velocity.

It is fortuitous that many particles of biological interest fall into the size range, that when subjected to the velocities found in the human natural convection boundary layer, have the times of flight across body surfaces that are outlined above. These particles are mainly dusts, pollens, skin scales and bacteria and the following table shows their size, terminal velocity, and Reynolds number (ratio of inertia to viscous forces) based on this terminal velocity.

When considering the boundary layer as a transport vehicle for dusts and micro-organisms, it is possible for particles up to 70 μm equivalent diameter to be suspended and to travel with the flow. Particles greater than this size have terminal velocities greater than any flow velocity found over the body and will fall to the ground. However, this size range contains all bacteria, pollens and many of the skin particles that the body is constantly losing.

Particle	Size	Terminal Velocity	Particle Re
Bacteria	1 μm - 5 μm	0.5×10^{-2} - 10^{-1} cm/sec	3.5×10^{-6} - 3.5×10^{-4}
Skin Scales	5 μm - 15 μm	10^{-1} - 1 cm/sec	3.5×10^{-4} - 1×10^{-2}
Pollens	15 μm - 70 μm	1 - 25 cm/sec	1×10^{-2} - 1.25
Dusts	> 100 μm	> 50 cm/sec	> 1.35

The ratio χ of the resistance of a particle to that of a spherical particle the same volume is called the dynamic shape factor of the particle.

The equivalent particle radius r_e is the radius of the sphere with the same volume as the given particle, and the Stokes or sedimentation radius r_s is the radius of a sphere with the same density and rate of settling. For spherical particles $r_e = r_s$ but for non-spherical particles χ may be shown to be r_e^2/r_s^2 . The value of χ for oblate and prolate ellipsoids is respectively 0.69 and 3.42 (39). Thus the values of r_e/r_s in these two cases are 1.85 and 0.83. These values are for ellipsoids having an aspect ratio of 10. This aspect ratio is the largest that is liable to be encountered in particles of biological interest considered here. In the above table, it is seen that even if the equivalent particle diameter changed by a factor of 2 the size range that describes the particle is still valid.

There are a number of practical difficulties in the determination of particle size in 3 dimensions under the microscope. The particle sizes measured in this work is quoted as the average size of the particle projection in the field of view taking two mutually perpendicular directions.

It is appropriate to mention here the effect of particle density on terminal velocity, and in this section the calculation of the terminal velocity for spherical particles with various densities is demonstrated.

A particle reaches its terminal velocity when the air resistance plus the buoyancy of the particle is equal to its weight. For flow at low Reynolds numbers the Stokes equation for the drag D on a sphere is given by

$$D = 3\pi\mu U d$$

and the corresponding expression using the drag coefficient becomes

$$C_D = 24/Re$$

Consequently, the 3 component forces acting on the particle are as follows :

$$\text{Drag force} = C_D \times \tfrac{1}{2} \rho_a U_t^2 \pi d^2/4$$

$$\text{Weight} = \rho_p g \pi d^3/6$$

$$\text{Upthrust} = \rho_a g \pi d^3/6$$

and the particle is in equilibrium when

$$C_D \times \tfrac{1}{2} \rho_a u_t^2 \pi d^2/4 = g \pi d^3/6 (\rho_p - \rho_a)$$

When the particle is heavy compared with air, the buoyancy forces may be neglected and the expression for the terminal velocity then becomes

$$u_t = g d^2/18\nu \cdot (\rho_p/\rho_a)$$

Considering 3 different values for (ρ_p/ρ_a) of 250, 500 and 1000 we have

for : ρ_p/ρ_a = 250 the particle density is .33 that of water

ρ_p/ρ_a = 500 the particle density is .65 that of water

ρ_p/ρ_a =1000 the particle density is 1.3 that of water.

The following table gives the terminal velocities for particles with these density ratios in the size range 0.1 to 100 μm and this is shown plotted in Figure 26.

Table 6

Particle Diameter μm	mm	cm/sec ρ_p/ρ_a = 250	cm/sec ρ_p/ρ_a = 500	cm/sec ρ_p/ρ_a = 1000
100	10^{-1}	9.35	18.7	37.4
10	10^{-2}	9.35×10^{-2}	18.7×10^{-2}	37.4×10^{-2}
1	10^{-3}	9.35×10^{-4}	18.7×10^{-4}	37.4×10^{-4}
0.1	10^{-4}	9.35×10^{-6}	18.7×10^{-6}	37.4×10^{-6}

From Figure 26, it is seen that in the particle size range 5 μm to 50 μm (which includes skin scales) that the terminal velocity for a 5 μm dia particle varies from 0.3 to 0.1 cm/sec as the density ratio goes from 1000 to 250.

In calculations of particle terminal velocity for glass particles used in flow channel experiments reported further on where the density ratio ρ_p/ρ_a = 1200, a good approximation to the terminal velocity is given by $U_t = d^2/200$ cm/sec, where d is the diameter of the particle in microns.

In the following section an attempt is made to estimate the magnitudes

of various forces that may act on small particles in viscous flow.

6.1.2. The Acceleration of Small Particles in Air.

When considering the motion of particles in laminar channel flow, it is important to know whether the distance in which a particle is accelerated to its final velocity relative to the fluid flow, is appreciable with respect to the distance that the particle may travel along the channel before impact with the side wall occurs. As an example we may consider a spherical particle of diameter d cms in an air flow of U cm/sec, with the density of the air being ρ_a and the density of the particle being ρ_p. The particle has a mass m gms, and let the particle accelerate from rest to $(U - u_t)$ cm/sec at a uniform 'a' cm/sec^2 in a distance S cm. The drag on a particle in a viscous flow is assumed to be given by $30/Re$, where Re is the particle Reynolds number. Consequently, the accelerating force on the particle is given by $F = 30/Re \cdot \frac{1}{2} \rho_a U^2 \pi d^2/4$

Equating this force F to the (mass x acceleration) of the particle, where the acceleration 'a' is given by $U^2 = 2aS$ we have $30/Re \cdot \frac{1}{2} \rho_a U^2 \pi d^2/4 = \rho_p \frac{\pi d^3}{8 \times 3} \cdot U^2/2S$

where ρ_p is given by $6m/\pi d^3$

$$\text{from which} \quad S = \rho_p/\rho_a \cdot d/45 \cdot Re$$

As a typical example of this distance S, we consider a 15 μm dia particle with $\rho_p/\rho_a = 1600$ (i.e. having twice the density of water) in an air flow of 20 cm/sec. The value for Re therefore is 0.2 and S = 100 μm. Consequently it is seen that the accelerating distances for such particles is negligible compared to distances travelled along the channel.

6.1.3. Motion of a Rotating Particle in a Velocity Gradient.

Rotation of a particle may arise due to a velocity gradient such as a shear layer near to a wall. At small particle Reynolds numbers, rotation causes fluid entrainment adding to the velocity on one side of the particle and lowering the velocity on the other side. This Magnus effect

tends to move the particle towards the region of higher velocity. An experimental effort to assess this Magnus effect by measuring the lift, drag and rotating speed of small spheres was made by Eichorn and Small (40) and the following relation between lift and drag was obtained $L/D = d^2\omega/6\nu$ where ω is the rotational speed and ν the fluid viscosity. Hence for small particles (rotating once in 1 sec), the lift force due to their passage through a shear layer can be neglected when ω is small, since for a 30 μm dia particle, say, the $L/D \simeq 10^{-5}\omega$

6.1.4. Lift on a Small Sphere in a Slow Shear Flow.

Saffman (41) has derived an expression for the transverse force on a sphere entrained in a fluid moving with uniform simple shear. He found that this force was independent of the rotation of the sphere and was given by $F_\ell = K\mu 4u \cdot d^2/\nu^{1/2} \cdot (du/dy)^{1/2}$ where u = velocity difference between the particle and fluid $= u_t$. du/dy = velocity gradient in the fluid and K = 6.46 -a constant from numerical integration. We may consider the effect of this force on particles in the laminar flow channel where the velocity profile is given by $U = U_{max.} \times (1 - 4\, y^2/d^2)$; and therefore $du/dy = U_{max}\ 8\ y/d^2$. At a typical position say d/4 from the channel wall, $(du/dy) = 2u_{max}/d$ and for a channel Re = 200, Umax = 20 cm/sec. For lycopodium spores 30 μm dia, Ut = 4 cm/sec then L = 6.46 x $(30/2 \times 10)^2 \sqrt{210}\rho$ where ρ is the air density. The Stokes drag Fs of the particle is given by $6\pi\mu u_t d$ and the ratio lift force/drag force = L/D = 3.7×10^{-3}. From the analysis of the photographic motions of particles in a following section, it is seen that this force is too small by about an order of magnitude to sustain the observed motions and is therefore regarded to be of second order importance.

6.1.5. Thermal Precipitation - Radiometric Forces.

Small particles in air where there is a temperature gradient tend to move in the direction of the lower temperature. The

precipitating force results from the decrease in concentration and velocity of the gas molecules along a temperature gradient. Thermal precipitation accounts in part for the blackening of cold walls above radiators and for the pattern of dust deposits on ceilings. This kind of precipitation is employed in some particle sampling apparatus.

A number of thermal force equations have been proposed and an idea of the order of magnitude of the velocity associated with a temperature gradient may be obtained (42) from $U = \frac{.04}{T} \, dT/dx$ where U is in cm/sec and the temperature gradient dT/dx is in degrees absolute/cm. In the human natural convection boundary layer the maximum value of the temperature gradient is about $4^{o}C$/cm and the maximum velocity of a small particle down this gradient U is 5×10^{-4} cm/sec. This velocity is negligible when correlated to the time of flight of particles, either in the following channel experiments or in the natural convective flow and only becomes significant for particles in the submicron range.

6.1.6. Brownian Motion of Particles.

The mass of microscopic particles is so small that they are driven about in air by the buffeting action of the gas molecules. Under equilibrium conditions, the vectorial sum of the molecular impacts are zero; it is the oscillating motion that these impacts cause that is known as Brownian motion.

The Einstein equation relating the mean square displacement of a particle undergoing Brownian motion and the time interval between 2 successive observations is $\bar{x}^2 = \frac{RTt}{3\pi\eta r N}$

R = gas constant — N = Avagadro number = 6.06×10^{23} mole/gm molecule

T = absolute temperature — t = time interval

r = particle radius — η = air viscosity.

If we consider the displacement due to Brownian motion of a freely falling stream of particles of minimum size 15 μm dia, then particles down to this

size would be expected to land within a circle of diameter 2x in falling through vertical distance h. Then from the Einstein equation $x = K\sqrt{h}$ where $k = 0.704 \times 10^{-4}$. This small value for k shows that deviation of such particles in free fall due to Brownian motion would be very difficult to detect experimentally as the horizontal distances moved are very small.

6.1.7. Aerodynamic Lift Force.

The force on an irregular shaped particle resulting from the motion of the particle through the air may be inclined to the path direction. Imai (43) has produced an expression for the ratio of Cl/Cd for a 2-dimensional inclined elliptic cylinder of several aspect ratios. The magnitude of this ratio Cl/Cd for a particle of aspect ratio 10 and having an equivalent diameter of 30 μm (giving a value of Re based on the terminal velocity of 0.08) may reach a maximum value of 0.1. This 2-dimensional analysis is applied as it gives similar values for Cl/Cd as available estimates for the 3-dimensional case (56)
The derivation of these values for Cl/Cd is indicated in Appendix 2 for the 2-dimensional case and expressions are developed for the trajectory of such a particle in a laminar channel flow. The deposition concentration of particles along the laminar flow channel walls have been evaluated for various flow rates. These calculations are also outlined in Appendix 2 and the results are shown in Figures 27, 28 and 29.

It is known (39) that non-spherical particles may move at an angle θ from the line of action of resistance of the fluid. For ellipsoids of revolution (44) it has been calculated that the angle θ increases as the ratio β of the major and minor axes of the ellipsoid increases. For oblate spheroids the maximum value of θ is 4.6 at $\beta = 2$ and 9.4 at $\beta = 10$ and for prolate ellipsoids it is 3.9 at $\beta = 2$ and 10.4 at $\beta = 10$. When the value of $Re > 0.05 - 0.1$ the motion changes. Elongated particles try to align themselves to balance the fluid resistance and the nett

gravitational force. This tends to be the position where longest edges are perpendicular to the direction of the motion.

As the Re increases, the trajectory of a freely falling particle deviates further from the vertical the larger the particle. Experiments with coal ash in still air conditions (45) gave the average deviation for 800 μm dia particles in falling 100 cms of 0.45 cms. At higher Re, the path of the particles becomes spiral or zig-zag.

As particles orient themselves across the flow direction their mobility (vel/force) parallel to the flow direction becomes less than in the perpendicular direction, so that while settling they slip sideways or glide (46). For Re $<$ .1, i.e. dia d $<$ 20 μm this lifting phenomenon was not observed.

6.1.8. Summary of the Magnitudes of Forces on Particles.

The magnitudes of the forces discussed in the previous sections is expressed by the ratio of the sideways force (L) to the weight or drag (D) of the particle.

For example used in the calculation of the following table is for 30 um dia particle having a density equal to that of water and in a temperature and velocity gradient similar to those found in the human convective boundary layer.

Table 7.

Force	Ratio L/D
Magnus Force	10^{-5}
Force due to differential shear (Saffman)	3.7×10^{-3}
Thermal Precipitation	1.8×10^{-4}
Brownian Force	5×10^{-5}
Aerodynamic Lift Force	10^{-1}

6.2. The Theory of Electrostatic Effects on Particle Motions.

The existing theory and technology concerning the behaviour of particles in an electric field, derives in the main, from consideration of electrostatic precipitators used in the purification of contaminated gases (47). In these devices, 2 distinct physical processes take place: the charging of the particle and its subsequent transport to the collecting electrode. However, in considering the behaviour of particles due to electric processes in the natural convection boundary layer or in the laminar flow channel there was no active charging of the particles by a dominating electric field. The particles may be charged during their motion through the air, or be charged before beginning this motion. Consequently, any theoretical treatment based on precipitator theory can only be a guide to the processes in the physical phenomenon.

In an electric field, when a particle is uncharged, ions collide with it and charge it until the repulsive action exerted on approaching ions balances the force due to the field. Charging then ceases. It is assumed that diffusion of the ions and particles is neglected, and that the attractive 'mirror' force between a particle and an approaching ion, due to induction, is negligible. It has been shown that these assumptions are justified for sufficiently large particles for which the charging is very rapid. For small particles of less than .5 μm dia, the neglected factors become important. For large particles, the drift velocity of a charged particle of radius 'a' obeying Stoke's law is expressed as $U_e = K_e I I_o a / 6\pi\mu$ where K_e is a constant dependent on the particle dielectric constant, I_o is the field charge and I the particle charge. It is seen that for these particles the velocity is proportional to particle radius and to the product $I\ I_o$.

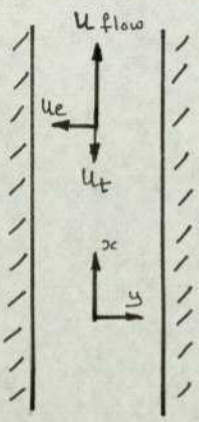
For a field strength $I = I_o = 10$ electrostatic units (3000 volts/cm) the theoretical particle velocities are shown below (48).

Table 8

Particle Radius μm	Velocity cm/sec
100	885
10	88.5
1	8.85
.1	.885
All sizes	2.8

The above discussion considered that the particles were spherical, and therefore that the charge could be assumed to be uniformly distributed over the particle surface area. In attempting to determine the motion of the irregular glass dust particles used in the following channel experiments, the fact that the particles can have very small radii of curvature can give rise to a high asymmetrical point charges and lead to unpredictable particle motions.

In the case of the vertical upward laminar channel flow, we may consider the deposition on a side wall due to an electrostatic field giving a particle a sideways drift velocity expressed as $U_e = Ke\ d$.



$u_t = kd^2$

$u_e = k_e d$

$$dx/dt = u - u_t$$

$$dy/dt = u_e$$

$dx/dy = u_e/u - u_t$ and for a parabolic profile velocity profile where $u = u_0(1 - 4y^2/D^2)$

$$dx/dy = \frac{u_e}{u_0(1-4y^2/D^2) - u_t} = \frac{k_e d}{u_0(1-4y^2/D^2) - kd^2}$$

The distance along the channel that a particle goes from the injection point before landing on a side wall.

$$X = \int_0^{D/2} \frac{u_o\left(1 - 4y^2/D^2\right) - kd^2}{k_e d}\, dy \quad \text{from whence}$$

$$X/D = \frac{1}{k_e d}\left[\frac{u_o}{3} - \frac{u_t}{2}\right]$$

Differentiating with respect to the particle diameter d

$$\frac{d\,X/D}{dd} = -\left[\frac{u_o}{3k_e d^2} + \frac{k}{k_e\, 2}\right]$$

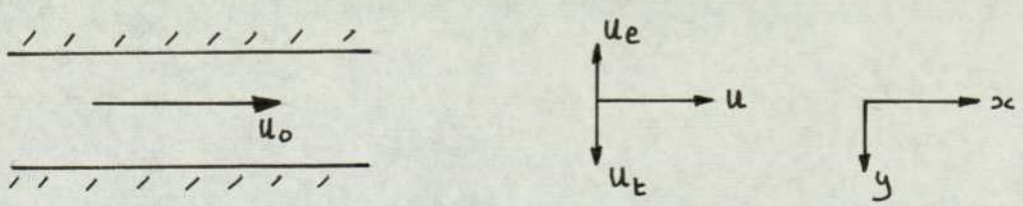
From an initial particle distribution N(d) given by $N(d) = Ae^{-Bd^2}$ the number of particles landing on unit area of a side wall is given by

$$\bar{N} = N(d)\,\delta(d)/\delta(X/D) = Ae^{-Bd^2} \frac{1}{\left[\frac{u_o}{3k_e d^2} + \frac{k}{2k_e}\right]}$$

$$= \frac{Ae^{-Bd^2} d^2}{(X/D)} \quad \text{or} \quad Ae^{-Bd^2}\left[\frac{6d^2 k_e}{2u_o + 3u_t}\right]$$

If we consider an electric field able to attract a 5 μm particle to the side wall a distance x/d = 50 from the injection point after a time of flight of 4 secs (corresponding to a channel Re of 105 as in the particle experiments) then the value of Ke to achieve this deposition should not be less than 400. Figure 30 shows the deposition concentration along a vertical side wall for this value of Ke. The maximum deposition is seen to occur at a value of x/D of 5.

Electrostatic + Gravity Effect in a Horizontal Channel



Consider roof deposition where Ue > Ut

dx/dt = U, dy/dt = (Ue - Ut) $\qquad$ $Ut = kd^2$ $\qquad$ $Ue = Ke\ d$

$$dx/dt = U_o\left(1 - 4y^2/D^2\right) \text{ for parabolic profile}$$

$$dy/dx = \frac{U_e - U_t}{U_o\left(1 - 4y^2/D^2\right)}$$

Distance to point of impact x on upper wall of channel is given by

$$X = \int_0^{D/2} \frac{U_o\left(1 - 4y^2/D^2\right)}{\left(U_e - U_t\right)}\, dy$$

$$\text{ie } X/D = U_o/3(U_e - U_t) \text{ From which}$$

$$\frac{d(X/D)}{d(d)} = \frac{1}{3d}\left[\frac{9U_t}{U_o}(X/D)^2 - 3(X/D)\right]$$

Number concentration of deposited glass dust particles per unit area on channel roof is given by

$$\bar{N} = N(d)\ \delta(d)/\delta(X/D)$$

$$\text{ie } \bar{N} = Ae^{-Bd^2}\frac{3d}{\left[\frac{9U_t}{U_o}(X/D)^2 - 3(X/D)\right]}$$

When applied to the following channel experiments without an impressed electric field and evaluated for a channel Re of 200 based on Uo, the value of Ke capable of causing the largest particle to move upwards is Ke = 3000. In this case X/D = 10.9 for a 2 μm dia particle and X/D = 1.59 for a 40 μm particle. Therefore in such a theory there is no roof deposition at

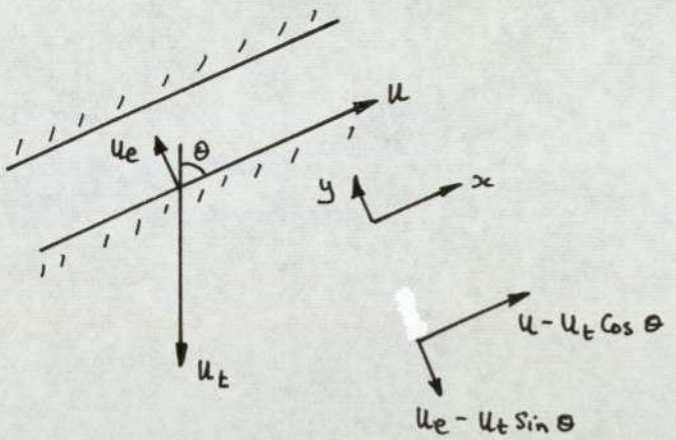
X/D > 10.9 if the largest particles are allowed to reach the roof.

Table 9

Particle Diameter μm	X/D for Deposition Position
2	10.9
5	4.64
10	2.54
20	1.64
30	1.72
40	1.59

Electrostatic - Gravity Effect + Channel Inclination

The following analysis is for roof deposition in the inclined channel.



$u_e > u_t \sin\theta$ for roof deposition

$$dx/dt = u - u_t \cos\theta$$

$$dy/dt = u_e - u_t \sin\theta$$

$$dy/dx = \frac{u_e - u_t \sin\theta}{u_o\left(1 - 4y^2/D^2\right) - u_t \cos\theta}$$

Distance X to impact on channel roof is given by

$$X = \int_0^{D/2} \frac{u_o\left(1 - 4y^2/D^2\right) - u_t \cos\theta}{(u_e - u_t \sin\theta)}$$

and

$$X/D = \frac{1}{u_e - u_t \sin\theta}\left[\frac{u_o}{3} - \frac{u_t}{2}\cos\theta\right]$$

From which $$\frac{d(X/D)}{d(d)} = \frac{k}{(Ke - kd\sin\theta)}\left[\frac{X}{D}\sin\theta - \cos\theta\right] - \frac{(X/D)}{d}$$

And the number deposition concentration $\bar{N}$ is given by

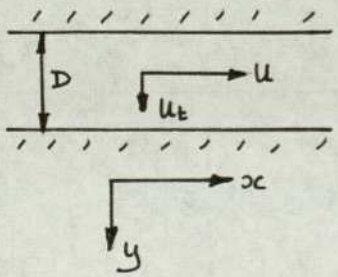
$$\bar{N} = Ae^{-Bd^2} \qquad \frac{1}{\frac{k}{(Ke - kd\sin\theta)}\left[\frac{X}{D}\sin\theta - \cos\theta\right] - \frac{(X/D)}{d}}$$

From the expression for X/D, it may be seen that the same small values for X/D occur for large particle sizes as in the horizontal channel. Thus the deposition patterns that would be expected if the electrostatic effect could simply be described as in this theory are seen to be different to those obtained in the flow channel. In the experiments, a size distribution showing both large and small particles deposited is observed for all values of X/D.

The following sections describe some experiments which attempt to assess the charges that the particles used in the flow channel experiments were carrying.

6.3. Floor Deposition in Channel Flow under Gravity.

In laminar channel flow, the depsition pattern on the bottom of the channel is considered for a parabolic velocity profile. If we consider a particle in such a flow, moving at the local horizontal fluid velocity U and falling vertically with terminal velocity Ut where Uo is the maximum velocity at the centre of the flow.



$$u = u_o\left(1 - 4y^2/D^2\right)$$

$$dy/dt = u_t$$

$$dx/dt = u_o\left(1 - 4y^2/D^2\right)$$

$$dy/dx = \frac{u_t}{u_o\left(1 - 4y^2/D^2\right)}$$

and the distance from injection to the position of the point of impact along the channel is given by :

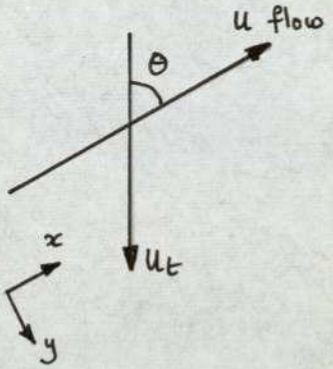
$$X = \int_0^{D/2} \frac{u_0}{u_t}\left(1 - 4y^2/D^2\right) dy \quad \text{and} \quad \frac{X}{D} = \frac{1}{3}\left(u_0/u_t\right)$$

Considering an interval $\delta(x/D)$ along the channel at a distance x/D from the injection point. The number of particles landing in this small distance $\delta(x/D)$ will have diameters between d and $(d + \delta d)$ When the number of the injected particles is given by Ae^{-Bd^2} then the number of particles of size interval δd landing on unit length in channel of unit width (number density/unit area) is given by

$$\bar{N} = N(d)\,\delta(d)/\delta(x/D) = Ae^{-Bd^2}\, d/2 \cdot 1/(x/D)$$

where $\delta(d)/\delta(x/D)$ is given by $-2u_0/3\,d u_t$ and $u_t = kd^2$

For the non-horizontal case when the flow is inclined at an angle θ to the vertical and the fluid flow is upwards.



$$dx/dt = u - u_t \cos\theta$$

$$dy/dt = \frac{u_t \sin\theta}{(u - u_t \cos\theta)} \quad \text{and in a parabolic velocity profile}$$

$$dy/dx = \frac{u_t \sin\theta}{\left[u_0(1 - 4y^2/D^2) - u_t \cos\theta\right]}$$

The distance x along the channel to the particle landing position is given by

$$X = \int_0^{D/2} \frac{u_0\left(1 - 4y^2/D^2\right) - u_t \cos\theta}{u_t \sin\theta}\, dy$$

From whence

$$x/D = 1/u_t \sin\theta \left[\frac{u_0}{3} - \frac{u_t \cos\theta}{2}\right]$$

Differentiating with respect to the particle diameter l

$$\frac{d(x/D)}{d(d)} = -\frac{2u_0}{3d u_t \sin\theta}$$

As before, the number of particles landing on unit area of the bottom channel wall is given by :

$$\bar{N} = N(d)\, \delta(d)/\delta(x/D)$$

$$\text{ie } \bar{N} = Ae^{-Bd^2}(d/2) \cdot \frac{1}{\left[x/D + \cot\theta/2\right]}$$

Figure 31 shows this distribution plotted for glass dust for the horizontal channel. The variation of distribution with channel inclination θ is also found from this relation for any fixed value of x/D. Figure 32 shows this distribution (together with an experimental result) for a channel x/d of 4 in a flow with Re of 105 based on the maximum velocity. For channel inclinations greater than 30°, the rate of deposition remains nearly constant with increasing inclination, whereas the floor deposition increases rapidly as θ goes from 0° to 20°.

7. PARTICLE TRANSPORT EXPERIMENTS - INTRODUCTION

Since the convective flow over a naked man generally remains laminar up to a height of 100 cms, and in the clothed condition may remain laminar over the whole body length, some experiments were made to determine the motions of small particles in such a laminar flow. To this end, a laminar flow channel was constructed and is shown in Figure 33 (49). This consists of 2 parallel glass sides and is fitted with a contoured aluminium entry section. The channel depth was 1.5 (but could be varied) cm so that the values of $(du/dy)_{wall}$ for fully developed Poiseuille flow could be of the same order as is encountered in the laminar natural convection boundary layer, i.e. $du/dy = O(100)\ sec^{-1}$. The Poiseuille flow was fully developed after a distance L' given by $L'/D = 0.058\ Re$ where Re = channel Reynolds

number and D the channel depth. Thus after about 25 cm for a channel Re of 300 the flow was fully developed (50). After about 25 cm the parabolic profile was fully developed to represent the inner part of the laminar natural convection boundary layer to a thickness just beyond the position where the maximum velocity occurs. By studying the behaviour of particles in this channel, some idea of how particles may behave in the thermal boundary layer can be inferred. At the top of the channel, a filter was arranged to collect particles that travelled the whole channel length without being deposited. Beyond this point a vacuum pump was fitted with a variable speed control so that a whole range of laminar flow rates could be studied.

Just below the filter, a hot wire anemometer was sited so that the velocity distributions across the channel could be measured. The developed parabolic profile was measured for 2 Reynolds numbers and is shown in Figure 34. The anemometer was situated 85 cms from the inlet to the channel and as a precaution against unsteadiness in the flow caused by fan motor fluctuations, the velocity readings were time averaged. In the event a thick paper filter placed at the top of the channel was used which completely eliminated these fluctuations.

7.1. Surface Shear Stresses.

In all particle transport phenomena studied here, both in the human natural convective flow and in the experimental flow channel, it is observed that whenever a particle lands on a surface it will not be removed again by any shear stresses arising from the fluid motion. It is possible to speak of a fluid threshold velocity and to define it by the wall shear velocity U_τ at which particle motion at a wall starts due only to the fluid shear stress.

Bagnold (51) performed experiments with sand grains to determine the value of U_τ at which the movements of various sizes of sand grain began.

Figure 35 shows this threshold velocity plotted against the grain diameter. The grain size is drawn on a square root scale, and it is seen that for large grains the threshold velocity is proportional to $\sqrt{d}$. As the particle size begins to fall, a critical diameter is reached where the shear velocity needed for movement becomes a minimum. For air, this critical diameter is seen to be 80 μm, and for particles smaller than this, fluid velocity has to be larger before movement may take place. The square root relation between the shear velocity and particle diameter holds for particles down to 80 μm dia. The shear velocity needed to initiate movement of such a particle is 15 cm/sec. For a 10 μm dia particle, this velocity is seen to have risen to 32 cm/sec. The density of soft keratin is 0.6048 gm/cc, but for hard desquamated keratin this rises to 1.325 gm/cc. However, the results of Bagnold's experiments may be used to give an idea of how skin scales as well as glass particles may behave on a solid surface, since the threshold velocity, proportional to the square root of the particle density, would be overestimated by a maximum of 1.4 times.

From the boundary layer analysis for convection along a vertical flat plate, it is found that the maximum values for $(du/dy)_{wall}$ in the flow about a human body will not exceed 100 sec^{-1}. The shear velocity is defined by $U_\tau = \sqrt{\tau/\rho}$ which may be written as $\sqrt{\nu\, du/dy}$ since $\tau = \mu(du/dy)$ and $\mu/\rho = \nu$ The corresponding maximum value of U_τ encountered in the natural convection flow will be about 4 cm/sec.

For the laminar flow channel in Poiseuille flow the value of (du/dy) at the wall is given by $4U_0/D$ where D is the channel depth, and once again the maximum value for (du/dy) is $O(100)sec^{-1}$ at U_{max} of 40 cm/sec (the criterion by which the channel described in the following sections was designed) and the values of the wall shear velocity are again about 4 cm/sec.

Since, from Bagnold's results, the minimum value for U_τ at which movement of 80 μm sand particles (with $\rho_p/\rho_a = 2600$) occurs is 15 cm/sec, it

is seen that the values of wall shear are too small to effect any movement of 5 μm to 50 μm diameter from surfaces on which they land. This conclusion is supported by observation in the following channel flow experiments, and also by the work of Corn and Stein (52) who found that air velocities of some 5 x 10^3 cm/sec were required to move 30 μm dia glass beads from a flat surface, and in these experiments the value of U_τ was about 60 cm/sec.

7.1.1. Van der Waals Forces.

Small particles are known to adhere firmly to any surface on which they land. Forces causing such adhesion to smooth clear surfaces (non-electric forces) are those which act between the molecules of the surfaces in contact. They are the same type as those involved in surface tension and the tensile strength of materials. Such attractive forces are known as Van der Waals forces. The magnitude of such a force between 2 molecules is given by $F = \lambda/r^7$ where λ is a constant and r is the separation of the centres. For 2 spheres effectively in contact (assumed to be separated by $h = 5\text{Å}$) the force of attraction has been found to be $F = \pi^2 \lambda q_v^2/24h^2 \left[\frac{d_1 d_2}{d_1+d_2}\right]$ where d_1 and d_2 are the sphere diameters, q_v the number of molecules/cc The term $\pi^2 \lambda q_v^2$ is of the order of 10^{-12} or 10^{-13}. For a sphere in contact with a plane surface, the equation becomes $F = A\,d$ dynes where A is a constant equal to 2π x the total surface energy of the sphere. If a quartz particle is suspended upside down from a plate, the gravity force W is $mg = 981 \times \frac{1}{6} \pi \rho d^3$ and the Van der Waals force has been found as 212d. The particle will stick to the plate if F is greater than W; that is, if d is less than 0.46 cms. For any natural particle of this size, contact between sphere and plate would be imperfect due to the roughness of the surface, so that in fact the sphere would fall off. However, as the particle sizes become measurable in microns, the irregularities become less important and better adhesion is possible.

The attractive force becomes so great that it is impossible to remove small particles from a plate even by vigorous shaking (53).

7.2. Size Distribution of Particles Used in the Flow Channel Experiments.

In a preliminary experiment in the flow channel, it was found that small glass dust fragments behaved in a similar way to skin scales and that their morphology and size were, in many respects, similar. Because skin scales are not easily obtained in usable quantities, it was decided to use the glass dust fragments for experiments within the flow channel. Ballotini were chosen because they would have similar physical characteristics to glass dust, except for their shape. Being spherical, they would not experience an aerodynamic lift force acting at right angles to the drag force (other than second order forces due to shear gradients as discussed in 6.1.8.) As a control shape, spherical glass ballotini were also used in the channel. These particles are shown in Figure 36. Within the flow channel, these particles did not produce a health hazard. However, for any particle experiments in free convection flows where the particles would be liberated into laboratory air, it was considered necessary to produce particles which would be non-toxic and non-antigenic. Such particles were subsequently produced by Lees and Brighton and the process is fully described in Reference (54). The particles they produced were harmless and behaved in a similar way within the flow channel to the glass dust and skin scales.

In order to estimate the numbers of sizes of the glass particles introduced into the flow, a particle size analysis was carried out on representative samples of the 2 materials. These analyses were performed on a Coulter counter by the manufacturers of the counter. Figures 37 and 38 give these results plotted as particle diameter versus cumulative percentage weight for the glass dust and the ballotini. For glass dust it is seen that 95% by weight of the particles lie in the 5 μm to 50 μm range

with only 5% larger than 50 μm which are not liable to be transported in the boundary layer. For the ballotini we see that only 6% are smaller than 25 μm.

Figures 39 and 40 are histograms showing the actual numbers of particles in 1 mg of the 2 samples of each size interval.

In this analysis, as previously discussed in section 4.1.1., the term 'equivalent diameter' for the particle is the diameter of a sphere of equal volume to that of the particle considered. Except in the case of the ballotini, this will not be exactly the same as an equivalent diameter based on a sphere having the same terminal velocity as the particle. The curve for the size distribution of the glass dust may be represented by

$N = 6000\, e^{-.0029\, d^2}$

This particle analysis enables us to determine the numbers of particles injected into the flow in the channel flow experiments. For all these tests, the length of powder in a capilliary tube was 8 cms and 13% by weight of the particles actually travelled in the flow. The analysis for glass dust gives the number per mg in the 5 μm to 50 μm range as 2.66×10^6 and for the glass ballotini 8.3×10^3.

From weighing the 8 cm length of capilliary tube filled with the 2 samples, the average numbers of particles 'flying' are as follows :

Glass Dust	1.2×10^8 particles
Glass Ballotini	4×10^5 particles.

The length of 8 cms of filled capilliary was chosen as it gave depositions that were not too great to be counted under the microscope. Also, these depositions were large enough to give densities of particles at various sites that allowed a reasonable number to be counted in traversing the channel wall with a microscope magnification capable of recognising particles as small as 5 μm equivalent diameter.

7.2.1. Method of Injecting Particles into the Flow.

In all of the channel experiments the method of particle injection was the same. The particles were injected at 3 equally spaced positions across the channel width. A capilliary tube was filled with a given length of glass powder (8 cms in most cases) and this quantity was injected at each of the 3 positions across the channel.

A preliminary test of weighing the particles in the tube before injection and of catching and weighing the powder that 'fell out' at the inlet to the channel gave a value for the weight of particles that entered the air stream. In all tests with the glass powder, it was found that 12-13% by weight of the total number of particles injected entered the air stream.

7.2.2. Method of Counting Deposited Particles.

Before each particle deposition experiment the 2 channel walls were thoroughly cleaned and examined under the microscope for any dust deposits. The side walls of the channel were marked on the outer surface with a longitudinal centre line and transverse lines for varying values of L/D along the channel. These values for L/D are shown along the abscissa in all the deposition graphs. At each counting position, the microscope was traversed from the centre line on the glass wall to the outer edge. The diameter of the circle in the field of view was 630 μm and the traverse distance across the channel side was 50 mm. The total area thus surveyed in one traverse across the wall was 31.5 mm^2. Consequently, the graphs of particle deposition versus wall site show the density of particle deposition scaled to 30 sq mm for convenience.

The microscrope was provided with a 16 mm focal length objective and a X10 magnification eyepiece. The microscope lighting and the speed of traverse of the wall surface were such as to make the identification and counting of particles smaller than about 5 μm equivalent diameter impracticable.

Therefore the observed and counted deposited particles fall in the size range 5 μm to 50 μm.

7.3. Channel Deposition Results.

The first experiments made with the laminar flow channel using glass dust particles gave the deposition on the near wall of the channel in the vertical case and floor deposition for angles of inclination down to 60° to the vertical. Figure 41 shows this deposition. The greatest number of particles land nearest to the injection point, and the numbers decrease with increasing values of x/D. Nearest to the injection point, the numbers counted, of O(2000) represent the practical limit of particle density observations with the microscope power available. Greater numbers were impracticable to count.

Figure 42 shows the deposition at various values of x/D for the bottom surface at different channel inclinations. There is a marked maximum deposition for angles of inclination varying from about 35° to 45° to the vertical. Once again the numbers deposited at any site are fairly large. The channel Re in these 2 experiments was 100 based on the maximum velocity in the channel, the flow direction was upwards, and the particles were injected at the base of the channel.

For experiments with the channel vertical, Figure 43 shows the glass dust deposition with upward flowing air for 2 values of the Re. Near to the injection a large number of particles deposit, this falls steadily to x/D of about 28 and then rises to maximum value, before falling again as the end of the channel and the filter are approached. It was in this experiment that a maximum deposition position was first noticed. The reasonably large numbers of particles that deposited near to the injection point is ascribed to the velocities imparted to the particles in the capilliary during injection with their consequent projection across the flow to the channel walls. This phenomenon is assumed to be more pronounced

with ballotini than with the glass dust because of their much greater exit velocity from the injection tube giving rise to an increased rate of injection. The change in Re from 150 to 500 only served to change the position of this maximum deposition from x/D of 40.2 to 44.4, with the numbers of particles remaining substantially the same. Figure 44 shows, for a Re of 140, the size distribution spectrum of dust particles deposited at 3 values of x/D along the channel. It is seen that this is essentially the same as the distribution of the injected particles. In all of these experiments, particles smaller than 5 μm equivalent diameter were not counted through the microscope at the magnification used, they were indistinguishable from dust and surface imperfections in the glass.

In order to assess the particle deposition that may have been caused by secondary flows within the channel, the aspect ratio of the channel section was changed. To do this, the channel depth was changed; Figure 45 shows deposition when a false bottom was fitted to the channel giving it a depth of 0.833 cms instead of the original 1.5 cms. Here it is seen that a maximum deposition occurs just before x/d = 34.4 with a flow Re of 170. The standard method of particle injection of 8 cms length of glass powder in a capilliary tube at each of 3 positions across the channel at mid-depth was modified, and Figure 46 shows the effect of having the capilliary tube offset from the centre of the channel depth by a distance D/4. The deposition of the wall remote from the injection position gives maximum deposition at x/D of 38, whereas a maximum occurs at x/D of 25 on the wall nearest to the capilliary tube. When injection is at 3 positions in a plane normal to the channel sides, the deposition on the wall opposite to injection is about twice as great as on the wall by the injection tube. Maximum deposition occurs in both these cases when x/D is 48. These results are shown in Figure 47.

Ballotini were used in the vertical channel at various values of Re for both upward and downward flow. In all these cases, very few ballotini

were deposited on the side walls (max. of 20 at any one station) and these were either clusters (and therefore non-round) which separated on impact or were deformed spheres. It appeared that no truly spherical single ballotini were deposited.

The experiment of changing the aspect ratio of the flow channel which produced little change in the deposition for glass dust indicates that secondary flows had little importance on the particle deposition pattern.

Following these experiments in the vertical flow, glass dust particles were used as the channel was tilted at an angle θ to the vertical for angles all the way down to the horizontal. In all of these tests the counts were made on the upper surface or roof of the channel. Figures 48 and 49 show this roof deposition for the 1.5 cm deep channel for 2 values of the Re with upward flow. It is seen that the maximum deposition position is rather better defined for the lower Re. The result in Figure 50 shows that on the roof of the channel there is maximum deposition at a given value of x/D at an angle varying between 20^{o} and 40^{o} to the vertical. Deposition on the roof and floor of the channel at inclination were therefore similar in this respect.

When the 0.833 cm deep channel is used at inclination, Figure 51 shows 2 values of x/D with high deposition, but these peaks are not so pronounced as in the deeper channel.

With downward flow, Figure 52 shows that no marked roof deposition with glass dust occurred at any angle when the channel depth was 1.5 cm, whereas with the narrower channel more marked maxima are seen at values of x/D between 40 and 44 as shown in Figure 53.

The results for the channel in the horizontal position are shown separately. Figure 54 shows the deposition for 2 values of Re with the 1.5 cm deep channel and Figure 55 the deposition with the narrower section. These 3 plots show a considerable reduction in the numbers of particles deposited from the cases with less inclination to the vertical, and there

is no very clear maximum, except in the test with the narrower channel.

Experiments with ballotini in both the upward and downward flow, and at the 2 channel depths showed that no deposition at all occurred on the channel roof at angles of inclination greater than 20^{o} to the vertical.

Deposition experiments on the channel floor with ballotini were made with the channel horizontal and inclined at 20^{o} to the vertical. Figures 56 and 57 show the total deposition of all sizes of particles plotted against X/D. The total number deposited is seen to fall with distance from the injection position. In these particular experiments, only truly spherical discrete particles were counted.

Figures 58 and 59 give the size spectrum of the deposited ballotini on the channel floor at several values of X/D and it is seen that there is a range of sizes that are deposited at each value of X/D.

In all the above experiments, the relative humidity in the test room was 35%; this value remained constant because of remoteness from the outside air, and the constant temperature maintained by the central heating.

Figure 60 shows the effect of change of humidity on particle deposition. The solid line on the graph shows deposition in the narrow channel with downward vertical flow at a R/H of 35% (this curve also completes the family of curves for dry air deposition). Wet blotting paper was put on both sides of the channel inlet section to increase the relative humidity of the air to some 70% to 80% (as determined from a rough evaporation rate based on the change in weight of the blotting paper with time) and the dotted line in this Figure shows this deposition. For the more humid air, there is a slight reduction in the numbers of deposited particles, but the maximum deposition position of x/D of 42 is not altered.

As an extension to the experiments with air moving in the channel, particles were dropped into it in the absence of any air flow both in the vertical case and at 20^{o} to the vertical. In the case of ballotini, no particles were deposited. For the glass dust, however, the numbers deposited

in the vertical case were of the same order as when the air was flowing in the channel (Figure 61). The maximum deposition point was displaced to a value of x/D of 28. At 20^{o} to the vertical, glass dust particles were still found on the roof of the channel, the counts being very low (of the order of 20 at any position). It must be emphasised here that such small counts of glass dust are not as reliable as those of O(100) because of the difficulty of distinguishing the glass particles from dust deposited from the air during counting (such a distinction is not difficult when using ballotini). In this experiment, the vertical falling distance was a maximum of 80 cms and the lateral displacement 0.75 cms. Particles of all sizes of irregular glass dust deposited on the vertical channel wall with the range of Re from 0.01 - 0.45 indicating that the mechanism of gliding and rotating can influence the trajectories of smaller particles than put forward in (46) and discussed in section 4.1.7.

The motions of a large number of glass dust particles (only a very small proportion of those injected) were observed as they moved in the air flow. For these particles their motions could be classified as either a) oscillatory, b) spiral, or c) vibrating.

One class of oscillating particles would move upwards with the stream then slightly sideways, to a region of lower velocity. This then allowed them to fall downwards whilst at the same time moving out again to a faster region of the flow and to begin to move upwards once more. The amplitude of this motion varied from a fraction of a centimetre to more than 20 cm, but appeared to be constant for any particular particle.

Spiral motion gave the impression of the particle screwing itself along in the flow direction but showing no deviation from the general flow direction. Many particles were seen to travel with the flow and at the same time to vibrate in a plane normal to the flow. The period for this vibration was as small as .02 sec and the amplitude was of the order of several particle diameters. The nett effect of this vibration did not

displace the particle towards either channel wall. With suitable adjustments to the flow rate, particles with any of these motions could be retained in the field of view for as long as 10 minutes. These particle motions were observed using lycopodium spores and other irregular shaped particles. These motions were not observed using spherical glass ballotini.

7.3.1. Changes in Channel Wall Material.

In order to estimate the possible electrostatic effects due to the channel wall material on particle deposition, various materials were substituted for the glass in one of the tunnel side walls. These materials were perspex, aluminium, and Fablon. Figure 62 shows the numbers of glass dust particles deposited at the various stations along the vertical channel for these different wall materials. The perspex wall gave rise to a deposition near to the injection point an order of magnitude greater than with any of the other materials and the deposition pattern at the other positions along the wall were not in accordance with the patterns nor the other materials. The perspex used in this test was not rubbed for several hours before the experiment; nevertheless, its electrostatic charge was obvious from the effect it had on body hairs after a few minutes with the air flowing through the tunnel. It is noted, when using the perspex wall, that the same deposition pattern was seen on the opposite glass wall. This suggests that electrostatic induction (the imparting of a charge to the moving particle, thus causing it to be attracted to the glass surface) as well as simple attraction by the perspex plays a part in this deposition mechanism.

Glass ballotini were used in a similar test (Figure 63) with the vertical channel. The total number of particles deposited a long way from the entry was much lower than with the irregular shaped glass dust. However, the same result of greatly increased deposition on the perspex

wall (with the attendant deposit on the glass wall opposite) was seen again.

7.3.2. Extra Experimental Procedures.

Following a discussion with C. N. Davies, 2 further experimental procedures were used. As a simple test as to whether or not glass dust and ballotini were differentially charged before being injected into the flow channel, the capilliary tube was filled with a mixture of the dust and ballotini. Equal weights of the 2 powders were thoroughly mixed together and this mixture was injected into the channel when it was vertical and when inclined at 20^{o} to the vertical. At 20^{o} inclination, no ballotini were deposited on the top channel wall. There was no noticeable change in the deposition patterns when the mixture or the dust alone are injected. The conclusion from this test must be that if electrostatic deposition is significant, then there is no 'charge sharing' between the glass dust and the ballotini before injection and dispersal in the fluid flow.

An investigation was also made into the possibility that some of the glass particles, especially the ballotini, were not adhering to the top surface on the channel on arrival but were bouncing away from it. According to N. A. Fuchs (39) a particle will stick to a surface if the component of its approach velocity normal to the surface does not exceed (30/d) cm/sec where d is the diameter of the particle in microns with a density close to that of water. For the larger glass particles, this normal velocity would have to exceed one cm/sec to allow the particle to bounce. The top wall of the channel was coated with a thin solution of oil in carbon tetrachloride so that any particles arriving at this surface would become embedded in it with no chance of any rebound. Tests were made with the channel vertical and then inclined at 20^{o} with both the dust and ballotini. No ballotini were deposited at 20^{o} and only the few deformed or clustered spheres deposited in the vertical position. With the glass

dust, the observed patterns of deposition were similar to those shown in Figures without the oiled surface. From this test, it is concluded that in all of the particle deposition experiments any particles that arrived at the upper channel surface,when it was clean and dry, adhered to it and that there was no loss of particles, either dust or ballotini, due to bounce.

7.3.3. The Landing of Particles on the Channel Walls.

When particles of glass dust were injected into the vertical channel with the air flowing upwards, it was possible to observe some particle motions with the microscope mounted halfway along the channel. The channel flow rate was reduced so that most of the larger particles moved upwards at only 1-2 cm/sec. Even this low velocity was too great to observe in detail the motions of particles that travelled straight to the filter under the microscope. However, observation with the naked eye could not reveal anything but straight line motion for such particles.

In all of these observations there was no evidence of any spin about either a horizontal or a vertical axis for any of the observed particles. No visual evidence is available for any motion, other than a straight line trajectory, for particles travelling straight to the filter (or to the side walls).

When the channel was horizontal, none of these 3 classes of motion could be observed and once again it was not possible to focus on to particles traversing the whole length of the channel. In the vertical case it was never possible to watch a particle land from the flow. The particles that did land appeared in the field of view so quickly as to give no time to focus on them as they approached the wall.

During the course of a long observation of the top channel wall in the horizontal case, not a single particle was observed during the final approach and landing on the wall despite the use of a number of different

microscope magnification combinations. Nevertheless, when the top channel was removed and a normal particle count made, the familiar deposition pattern was seen.

Using the vertical channel, a part of the wall in the field of view of the microscope was thoroughly cleaned. With a maximum channel flow velocity of 10 cm/sec a time of 4 secs elapsed after particle injection before particles deposited at 30 cm from the injection point were seen through the microscope. This simple test suggests that the deposited particles travel straight to their deposition site and are not those which perform any of the special motions described previously which would require a much longer time in which to deposit. (These oscillating particles were easily recognised and have never been observed to deposit).

An experiment was performed to try to make a number balance between the injected particles and those deposited on the side walls and at the filter for the channel inclined at 20^{o} to the vertical. The following results were obtained :

For the capilliary tube used

Weight of empty tube	6500 mg
Weight with 6.2 cm of powder	6620 mg
Weight of powder	120 mg

This gives a calibration for the capilliary tube, at the packing density used in all of these experiments of

19.4 mg of powder per cm of tube.

The total length of powder injected at the 3 positions in the channel was 22 cm, giving a weight of 425 mg.

Original weight of clean filter	1000 mg
Final weight of filter	1030 mg
Weight of particles on filter	30 mg

A graphical integration of the deposition of particles on both the upper

and lower channel walls taken from Figures 42 and 48, gives

Number of particles deposited on top surface	1.03×10^4
Number of particles deposited on bottom surface	5.8×10^5
Total number of particles deposited - approx.	6×10^5

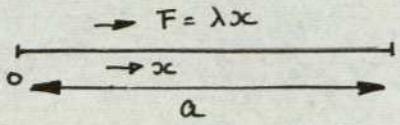
This represents a deposition of 0.5% of the particles entering the stream, and since from a previous experiment it was known that 13% of the injected particles actually 'fly' (the rest drop out of the inlet section) we should expect (13% - 0.50)%, i.e. 12.5% of the injected particles to reach the filter. That is, 12.5% of 425 mg = 52 mg deposit on the filter.

In the experiment to determine the particle balance, 30 mg of the powder reached the filter, and this was 0.58 times that which would be expected from subtracting a graphical integration of the numbers of deposited particles from the number that entered the flow. As there is less than a factor of 2 between the expected and actual weights on the filter, the experiment can be said to be reasonably satisfactory in confirming a particle balance since graphical integration is a relatively inexact method for particle number determination.

7.4. The Motions of Particles in Laminar Channel Flow.

The oscillatory and spiralling motions of lycopodium (Figure 64) particles in the flow channel have been recorded on ciné film. From this, a frame by frame analysis was made to give a plot of the serial positions of the particles. Typical results for this are shown diagramatically in Figure 65. These results were made with the channel vertical with a flow Re of 150, and the particle Re, based on the terminal fall velocity, was 0.1. A representative particle oscillating amplitude as taken from this diagram is 1500 μm for a particle of diameter 30 μm and density 0.621 gm/cc. The weight of the particle is then 8.63×10^{-7} gms wt and the frequency of the oscillation 2 cycles/sec. When the particle motion is assumed to be simple harmonic under the action of a force F (lift force say) that is

proportional to x, the distance from the central position of the motion, and equal to λx



If the weight of the particle is w, then the equation of motion is

$$w\ddot{x}/g = -\lambda x \quad \text{ie} \quad \ddot{x} + \lambda g/w \cdot x = 0$$

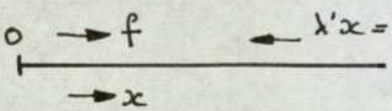
and the solution to this differential equation is given by

$x = A\cos nt + B\sin nt$ when $n^2 = \lambda g/w$ and the period of motion is $T = 2\pi/n$

The period for the particle motion was $\frac{1}{2}$ sec and hence $\lambda = 11 \times 10^{-8}$

The maximum force on the particle occurs when x = 750 μm and this force is then 8.25×10^{-9} gm wt. Hence the ratio of the sideways force F to the weight W was $L/W \simeq 10^{-2}$

If we take this analysis one stage further to consider the particle to be under the action of a constant force f (lift force) in the direction of x increasing, and of a force $\lambda' x = F'$ proportional to the distance of the particle from O, and acting in a direction towards x = 0



Then the equation of motion becomes $w\ddot{x}/g = F' - \lambda' x$

or $\ddot{x} + n^2(x - b) = 0$ where $b = F'/\lambda'$ and $n = \sqrt{\lambda' g/w}$

When the amplitude of the motion is 2a the body is in equilibrium at x = a, and oscillates about x = 0 with a period $2\pi/n = \frac{1}{2}$ sec, i.e. $n = 4\pi = \sqrt{g/w}$

and $\lambda' = 1.38 \times 10^{-7}$. When $a = 750\mu m$

$F' = 1.04 \times 10^{-8}$

The ratio of $\frac{\text{Max force } F'}{\text{Weight } W}$ is again $= 10^{-2}$

From this result, it is seen that the motion observed in the flow channel may be initiated and sustained by either a changing aerodynamic lift force (changing due to particle rotation say) where the ratio of the lift to drag

is $O(10^{-2})$ or by a constant (electrostatic) force with a second varying opposing force (aerodynamic, shear flow force,etc.) where this opposing force is again $O(10^{-2})$ x the weight of the particle.

7.5. Particle Deposition when an Electric Field was Applied to the Channel.

In order to assess the behaviour of glass dust particles in an electric field, some experiments were made in the laminar flow channel when inside sections of the walls were covered with a conducting layer which could have various voltages applied.

Both of the inside channel walls were covered with a 13.5 cm length of 30 μm thick plastic sheeting which was lightly coated with aluminium. This aluminium coating allowed the plastic sheet to be an electric conductor, but was thin enough to allow visual observation of the inside of the channel. Thin wires were taken from these conducting surfaces to the outside of the channel and were attached to an electrical power supply. In this way the plates were charged to various voltages to create an electrical field through which particles that were injected into the flow would pass. The particle deposition on the conducting part of the channel was determined by particle counts under the microscope as in the previous experiments. Glass dust particles and lycopodium spores were used in these experiments with the channel vertical.

Figure 66 shows the average particle (glass dust) deposition at various values of X/D when the wall under examination was subjected to an increasing positive and negative voltage.

Figure 67 shows the particle deposition concentration along the length of the channel for various voltages up to a maximum of ± 350 v and 250 v a/c, and Figure 68 is a similar curve for lycopodium spores. From these results the maximum deposition at any voltage was found when the plate voltage had a negative sign and that this deposition was fairly constant along the charged surface. The implication of this result is that the

predominant charge on any of the particles that were charged was positive.

The deposition for the maximum negative voltage attainable (350v) was some 60 x greater that when the plates were uncharged. Since some 0.5% of injected particles deposit with uncharged plates, this means that some 40% of the upward moving particles carry positive charges large enough to cause deposition in a field strength of 230 v/cm (i.e. channel depth 1.5 cm and applied voltage 350).

The deposition on the plate when it was negatively charged was about 20 x the zero charge deposition. From this it may be estimated that some 10% of the glass particles carried a negative charge sufficient to cause deposition in a field of 230 v/cm. This result implies that about 50% of the particles carry no charge, or one that requires a greater field strength to cause deposition on the channel walls. With the plates charged to $\pm$ 250 volts, a similar pattern of deposition occurred. In this case, only 7% carry a sufficiently large positive charge to cause deposition and some $3\frac{1}{2}$% a negative charge. In this case, some 90% of particles are undeflected in such a field strength of 167 v/cm.

When the particles in the channel were subjected to an alternating field of $\pm$ 167 v/cm of a frequency of 50 Hertz, the deposition is indistinguishable to that when the plates are uncharged. The application of an a/c voltage, if the time in which the voltage changes sign is of the same order or longer than the relaxation time of the particle ($O(10^{-3})$ sec for a 15 μm dia particle) means that the particle vibrates due to the electric field and this would not be expected to exert a nett deflection on the particle. The alternating field effectively cancels any electrostatic deflection and the experimental results in Figures 67 and 68 support this supposition. Visual observation of the particles when the plates were supplied with + and - voltage and an alternating voltage, showed that the spiralling and oscillating motions of the particles observed when the plates were uncharged still occurred.

The conclusion to the experiments in the channel flow must be that some deposition is caused by electrostatic forces (for instance in roof deposition when the channel is tilted past the glide angle of the particle) but that other forces including aerodynamic lift force contribute to the observed motions. These channel experiments enable us to visualise the effects of such aerodynamic forces that may cause deposition but are insensitive in completely distinguishing them from electrostatic effects which may be similar in magnitude in frequency of occurrence on the particles.

The results in Figure 68 for deposition of lycopodium spores in an electric field show similar patterns to the glass dust. The predominant charge found on the particles is positive (present on some 10% of the particles); negative charges appearing on only 2% of particles. Qualititavely this agrees with experiments carried out by Gregory (55) who found that over 80% of fresh spores of different kinds carried positive charge. The small numbers of spores carrying charge in these experiments may be due to the fact that the particles had been stored in a closed bottle for a long period, whereas the spores in Gregory's experiments were newly liberated from the sporating plants.

7.6. Discussion on Particle Motions Observed in Channel Experiments.

In trying to correlate the experimental channel deposition results with a theoretical analysis, a combination of forces causing particle motion is possible. Considering the floor deposition in a horizontal channel due to gravity alone, for glass dust, it is seen in Figure 69 that for a value of x/d greater than 5, the deposition falls rapidly. However, when this curve is compared to the experimental one for floor deposition, it is seen that at large values of x/D there are always more deposited particles than expected. Moreover, the theoretical deposition allows only a single particle size to deposit at any value of x/D; this size decreases with

increasing x/D. The experimental results give the distribution of particle sizes to be similar throughout the channel length.

When considering the directions and magnitudes of the various forces acting in the horizontal flow, it must be concluded that the only force powerful enough to cause roof deposition is some form of electrostatic force. The analysis for electrostatic deposition alone on the upper surface, on the assumption that the electrostatic drift velocity is proportional to the particle diameter, again does not allow for the deposition of large particles at large values of x/D. Although the dominating force for deposition on the roof must be electrostatic, the charging on irregular shaped particles is more likely a function of the small radii of curvature found, than on a mean equivalent diameter based on the terminal fall velocity. The results from the deposition in vacuo (see Appendix 3) suggest that such charges are acquired during motion through the air, and are not present on the particles at injection. Consequently, it is not possible to base a deposition analysis entirely on the assumption of a drift velocity as a function of the equivalent diameter. This idea is further borne out when we consider the analysis of roof deposition in the horizontal channel due to an electrostatic drift velocity great enough to allow the largest particle to reach the top surface. The electric field described by the value of Ke has to be so large that all but the very smallest particles (i.e. less than 1 μm) are deposited on the top surface when x/D = 10 and the larger particles deposit before x/D is 2.

In the vertical channel, where gravity effects provide a relative velocity, Ut, with respect to the particle, electrostatic deposition will again give maximum deposition for the largest particle at x/D of about 5. Once again, in such an analysis there is no possibility of large particles remaining in the flow for long channel lengths. In assessing the feasibility of aerodynamic lifting forces being responsible for the deposition in vertical flow, no such rigid size limitation along the channel

exists. This is because the value of x/D at which a particle lands, does not solely depend on its diameter (which determines Ut) but is also a function of the angle at which it enters the flow, which in its turn determines the glide path the particle assumes relative to the flow. This being the case, large particles may possibly take up a steep glide angle and deposit on the wall at large x/D; conversely, small particles could have a shallow glide angle and deposit near to the injection point. Assuming that equal proportions of the total numbers of particles entering the flow at all angles from 0 to $\pi/4$ the possibility of deposition at any wall site is dominated by the glide angles taken up by the particles and less by the size distribution of those injected. The proposition that lifting forces cause particle deposition is discussed in Appendix 2 to preclude roof deposition when the channel angle θ to the vertical exceeds (approx. 4^{o}), however experimental deposition occurs at all angles down to the horizontal.

Since the basis for aerodynamic lift force normal to the fluid flow relies on relative velocity between the particle and the fluid (the terminal velocity Ut in vertical flow) any phenomenon causing such a relative velocity will create lift forces to modify particle trajectories and create the observed deposition patterns. Although roof deposition due to aerodynamic lift forces is only possible for a small range of channel inclinations, floor deposition can be modified by this force for all angles down to the horizontal. This is because there will be a component of Ut acting parallel to the flow, and opposite to it for upward flow. The situation becomes further complicated by the action of any electrostatic forces transverse to the flow which can also cause relative velocity in the flow direction. Such an interaction of forces in similar or opposing directions could account for the roof deposition not correlating with a simple electrostatic drift velocity analysis.

A further complex motion that could modify the pattern of deposition

is apparent when the interaction between particles is considered. In the discussion,particle collisions are assumed not to occur since the suspension of injected particles is not sufficiently closely packed. However, in any injected cloud of particles, the interparticulate spacing could be of the order of a few particle diameters such that the particle wakes could interact. The result of this would be that the drag of the particle would be different to the Stoke's drag. If this drag changes at a faster rate than the particle relaxation time, then the local relative velocity between the particle and the fluid could cause aerodynamic lift affecting the deposition pattern.

In all of the particle experiments, only a very small proportion (0.5% of those injected for the experiment at 20^{o}) of particles deposited out of the flow in the channel lengths used.

Therefore, the efforts at analysis have been directed at looking at the relatively few particles that leave the streamline flow. The effects that cause particle deposition could also be regarded as those that allow the particles to remain for longer periods in the flow than would be expected by sedimentation alone. With the channel vertical, the spherical ballotini were not observed to cross the flow streamlines and with the channel inclined there was no ballotini deposition on the channel roof. However, the floor deposition of ballotini (Figures 57 - 59) shows that there is a similar size distribution amongst the deposited particles at several values of X/D. If the ballotini simply settled towards the floor under gravity with termal velocities proportional to their diameter, there would be single sized particles at each value of X/D; small particles would travel the longest distance and large particles would deposit at small values of X/D.

Aerodynamic lift forces cannot be responsible for determining the effective Ut of the floor deposited ballotini, and this effect could be due to electrostatic forces and a combination of rotation and shear forces.

However, this effect is not observed in vertical flow where the particle's drag and weight act in the same direction. The transport of particles in a laminar channel flow would seem to be a complex process involving aerodynamic lift due to particle drag and relative velocity together with electrostatic lift forces both playing a part in inhibiting as well as causing particle deposition.

7.7. Particle Deposition from a Turbulent Flow.

The human natural convection flow over a naked subject in room temperature remains laminar up to a height of 100 cms and only becomes turbulent after 150 cms. With a clothed subject, as has already been indicated, the flow may well be laminar over the whole body height. Because of the predominance of laminar flow conditions the work reported in this thesis mainly deals with laminar flows. Nevertheless in this work some account of the behaviour of particles in a turbulent flow is necessary. Owen (56) says that "..... in general the transport of fine solid particles from a turbulent gas stream to an adjoining surface is achieved principally by turbulent diffusion in which particles acquire a motion in response to the fluctuating gas velocities in their immediate neighbourhood. But very close to the wall, within the so called viscous sub-layer, the turbulent fluctuations are evanescent and some additional process is required to enable a particle to achieve the final motion needed to make impact with the wall."

The final part of this motion to the wall surface has been thought to have been caused by particles being 'convected' to the wall from the region of energetic turbulent motions outside the viscous sub-layer by the occasional eddy that encroaches on it. Added to this, all of the forces that have so far been considered for laminar flow will also influence the last part of the particle motion. To achieve an estimate of particle deposition from the turbulent convective boundary layer the expression given by Owen for the number of particles N deposited in unit time on unit

area of the wall from a stream in which the concentration of particles by number is ψ_0 of

$$N = k u_\tau \psi_0 \sigma^2$$

Here k is a constant estimated to be of the order of 10^{-4}

U_τ is the friction velocity and $\sigma = u_\tau^2 \tau^*/\nu$ which is a measure of the ratio of the relaxation time of a particle, τ^* is the characteristic time of an eddy in the viscous sub-layer and is related to the particles and flow properties by

$$\sigma = 1/18 \; \rho_p/\rho_a \left(u_\tau d/\nu\right)^2$$

in which ρ_a and ρ_p are respectively the densities of the gas and the particulate material and d is the particle diameter. Using the expression of $u_\tau = \sqrt{\nu \, du/dy}$ for the friction velocity

$$N = K/18^2 \left(\rho_p/\rho_a\right)^2 \left(d/\nu\right)^2 \psi_0 \left(du/dy\right)^{3/2} \quad cm^{-2} \, sec^{-1}$$

As an example, we consider the total volume flow over the face in 1 sec of 10 litres to contain 10^8 particles. This number is representative of the numbers of skin particles that may be found around the body and is also similar to the number of particles used in the flow channel experiments.

If $(\rho_p/\rho_a) = 1200$ and $du/dy = 30 \, sec^{-1}$ at 150 cm height and $\psi_0 = 10^4$ particles $/ cm^3$

The expression for N gives $N = 3.35 \times 10^{-2} \; cm^{-2} \, sec^{-1}$

or more generally $N/\psi_0 = 3.35 \times 10^{-6} \; cm \, sec^{-1}$

When the numbers of particles that would deposit from the flow on to an area equivalent to that of one of the flow channel walls is calculated (i.e. 500 sq cm) the total number deposited is seen to be extremely low at around 17.

This analysis for turbulent flow deposition is intended only to indicate the order of magnitude for particle deposition, and it is seen that such deposition due to turbulent diffusion is very small when compared to

deposition due to sedimentation or electrostatic attraction which has already been discussed. Fuchs (39), who reviews the literature on this process, which is rather limited, indicates that the work of Alexander and Coldren (57) for flow in horizontal ducts implies that diffusive deposition plays a small part in the wall deposition of particles.

7.8. Aerobiological Implications.

The results of studying the transport of particles in the laminar flow channel are useful in assessing the motion of particles in the human boundary layer. Bacteriological air samples show that human microenvironment contains more micro-organisms in a given volume than the ambient air. This is important in the consideration of the cross infection process associated with the convective boundary layer. This higher number of particles can result either from contamination from the skin surface or from the outside air. If particles are able to cross streamlines in the boundary layer flow, then the volume particle concentration of particles in the flow past the nose and mouth may be higher than the concentrations in the ambient air. The fact that particles are able to travel considerable distances, even when the flow is over an inclined surface, without being deposited is again a potential hazard to the respiratory system. Of particular interest in this respect is the flow under the chin. For a fully clothed man wearing a tie, schlieren visualisation shows that the horizontal velocity under the chin will probably not be lower than 4 cm/sec and any debris travelling in the flow at this point would have to move for some 5 cms horizontally before moving upwards again. The results from the particle experiments suggest that in this distance the gravity effect on the particles may be less than expected by sedimentation under gravity alone and hence the particles could remain in the flow until they are again able to travel upwards and subsequently reach the respiratory tract. Similarly, the same is true of regions such as the shoulder, where the convective flow tends

to break away upwards when reaching the horizontal surface, from the surface deposition could be less than expected.

In any particular channel experiment the number of particles injected into the flow was of $O(10^8)$ which compares well with the numbers of skin particles that may be present around the body. Although the numbers of particles depositing on the side walls of the channel (roof or floor deposition) were large and of the $O(10^5)$ to (10^6) they were a small proportion of the numbers injected. Since the numbers of pathogenic organisms required at any body site for infection to begin may vary in every case, this number of particles, if pathogenic and depositing from the convective flow, could prove significant bacteriologically.

In view of the large numbers of particles available for transport in the human boundary layer and the fact that they are able to move large distances in such a flow suggests that the boundary layer, ending in the plume with a mass flow of up to 10 L/sec with velocities up to 50 cm/sec, is a powerful mechanism for local environment contamination.

8. PARTICLE SENSING ANEMOMETER

The hot wire anemometer has been adapted for use as an instrument for detecting the presence of particles in the laminar flow channel, in the convective boundary layer of humans and heated models and in dusty environments (58, 59).

When a particle lands on the heated wire, the wire rapidly loses heat to the particle. The voltage output associated with this heat loss is distinguishable from that due to velocity fluctuations. The waveform has a very steep slope which reaches a peak and then dies away exponentially. The peak voltage associated with an impact from a 30 μm dia particle in a 10 cm/sec airstream is O(300 mv). When the particle hits the wire there may also be a 'strain gauge' effect on the wire but this is assumed to be small since the presence of particles has also been detected using a hot

film probe where this effect is negligible. With suitable electronic filters, the signals due to particle impacts can be discriminated from turbulence signals in the anemometer bridge and displayed on a storage CRO and an electronic counter. At the same time, a tone from a loudspeaker indicates a particle impact. Figure 70 shows the deposition of particles on a 5 μm dia wire and block diagrams and electronic circuits for the sampler are shown in Figures 71 and 72.

8.1. Efficiency of the Sensing Anemometer.

In order to assess the efficiency of this form of sampler, it is necessary to calculate the ratio of the number of particles deposited on the wire to the number of particles, the centres of which would have passed through it if they had moved all the time in straight lines. To find this efficiency, the outermost trajectories for which the centres of the particles still collide with the wire must be determined. Let h denote the distance from the outermost trajectory to the centre line of the flow at an infinitely large distance from the body, then for a cylinder $\eta = h/R$ where R is the cylinder radius. For purely inertial deposition η depends only on the particle stop distance. The ratio of this stop distance to a characteristic dimension of the system (wire radius) is called the Stokes number. The collection efficiency for particles on a cylinder (39) has been calculated, but no allowance is made for the interception (bounce) effect of the boundary layer. Figure 73 shows this collection efficiency plotted against the Stokes number. In the case of the sampler described here, and considering a 20 μm dia particle hitting a 5 μm dia wire, the efficiency is seen to be about 98%. The sampler may be calibrated by comparing the electronic counter output with the impacts seen on a ciné film made at the same time. This calibration gives an overall efficiency of some 40% which is accounted for by the interaction effect, the boundary layer, and the fact that there is a minimum electric signal required to

trigger the counter. This magnitude of the signal due to an impact will be a function of the geometry of the particle contact with the wire, and the thermal conductivity of the particle.

8.1.1. Sensitivity of the Sampler in an Unsteady Airstream.

The heat loss from the heated wire may be expressed by

$$I^2 R_w = (A + B\sqrt{U})\,(R_w - R_o)/R_o \quad - a$$

When the wire is in a turbulent or unsteady airstream with mean velocity $\bar{U}$ and fluctuating component u, the resulting wire current I will be similarly composed of mean value $\bar{I}$ and change, or offset i. These mean values will be related by

$$\bar{I}^2 R_w = (A + B\sqrt{\bar{u}})\,(R_w - R_o)/R_o \quad - b$$

To find the relation between u and i we use a) and b)

$$(\bar{I} + i)^2 R_w = (A + B\sqrt{\bar{u}+u})\,(R_w - R_o)/R_o$$

In addition to the cooling caused by the fluctuating turbulence, consider the impact of a droplet of mass m and specific heat Cp, then

$$(\bar{I} + i)^2 R_w = (A + B\sqrt{\bar{u}+u})(R_w - R_o)/R_o + \dot{m} C_p (\theta_w - \theta_o) \quad - c$$

where m is the mass of aerosol per unit time landing on the wire.

Using α = temperature coefficient of resistivity we have

$$\theta_w - \theta_o = (R_w - R_o)/\alpha R_o \quad \text{from c.}$$

$$(\bar{I} + i)^2 R_w = (A + B\sqrt{\bar{u}+u})(R_w - R_o)/R_o + \dot{m} C_p/\alpha\,(R_w - R_o)/R_o$$

$$\text{or } (\bar{I} + i)^2 R_w = \left[(A + B\sqrt{\bar{u}+u}) + \dot{m} C_p/\alpha\right]\left[\phi\right] \quad - d$$

where $\phi = \dfrac{R_w - R_o}{R_o}$ = wire overheat ratio

When $R_w - R_o \gg r_w$ and $\bar{u} \gg u$ equation d may be simplified to $(I^2 + i^2 + 2iI) R_w = \left[A + B\sqrt{\bar{u}+u} + \dot{m} C_p/\alpha\right]\left[\phi\right]$

$$\text{or } (A + B\sqrt{\bar{u}})[\phi] + i^2 R_\omega + 2i\bar{I}R_\omega = \left[A + B\sqrt{\bar{u}+u} + \dot{m}C_p/\alpha\right][\phi]$$

$$B\sqrt{\bar{u}}[\phi] + i^2 R_\omega + 2i\bar{I}R_\omega = [\phi]\left[\dot{m}C_p/\alpha + B\sqrt{\bar{u}+u}\right.$$

$$i^2 R_\omega = [\phi]\left[\dot{m}C_p/\alpha + B\left(\sqrt{\bar{u}+u} - \sqrt{\bar{u}}\right)\right]$$

$$= [\phi]\left[\dot{m}C_p/\alpha + B\left(u/2\sqrt{\bar{u}}\right)\right] \quad \text{——} \quad e$$

from binomial exparsion.

Let the voltage fluctuation, iR be expressed as $e = S_1 u + S_2 \dot{m}$ where S_1 and S_2 may be considered as sensitivities. It is desirable to make S_1 and S_2/S_1 large.

$$S_2 = \phi C_p/i\alpha \,, \quad S_1 = \phi/i \; B/2\sqrt{\bar{u}} \,, \quad S_2/S_1 = C_p/\alpha \; 2\sqrt{\bar{u}}/B$$

B is proportional to the wire diameter and length and indirectly proportional to α. Therefore for large overheat ratios, large stream velocities, small wire lengths l and low values of α the chances of discriminating particle impacts will increase.

8.2. Use of the Particle Sampler.

The sampler has been used to plot the particle distribution in the channel flow at various inclinations. Figure 74 shows a typical distribution using 30 μm dia aerosol droplets with the channel inclined at 20° to the vertical. The position of maximum particle concentration is seen to be displaced from the channel centre towards the channel floor due to the particles sedimenting under gravity.

The sampler has been incorporated into a sampling nozzle shown in

Figure 75 and Figure 76 shows particle counts in a reasonably clean environment with the sampling nozzle placed in the boundary layer of a heated cylindrical model. With the model at room temperature, the volume concentration of particles was about 2.9×10^3 per litre. When the model is heated this rises to around 6×10^3 particles per litre. The slopes of the curves over 3 hours were consistently different. This experiment indicates that either the boundary layer has a concentrating effect or that the concentration in the corridor changed between the 2 tests, but remained constant during each 3 hour period.

Figure 77 shows the decay in concentration of a cloud of aerosol particles O(30 μm dia) over a period of one hour. In this experiment, the sampler and pump were placed at floor level in a still room and the aerosol cloud was injected into the room air.

9. A FULL SIZED HEATED MODEL OF THE HUMAN FORM

It was decided to investigate movement of particles in the boundary layer flow over a full sized heated model of the human form (60). This model was made of glass reinforced plastic and was fitted with a water pump and heater, as shown in Figure 78. In order to assess the transport of particles to the respiratory tract, the model was made to 'breathe'. A detachable nose could be fixed to a series of pipes embedded into the head. At the end of these pipes was a reciprocating air pump that gave variable tidal volumes and breathing rates similar to those found in the human. Just inside the nose, a removable wire grid was arranged to capture particles. A hot wire anemometer was also incorporated to monitor the respiratory cycle and detect particles entering the nose. This breathing system is shown diagramatically in Figure 79 and Figure 80 shows the respiratory cycle as recorded by the hot wire anemometer and displayed on a storage CRO. In this figure, the tidal volume was 600 cc and the respiratory rate was 16 cycles/min. Figure 81 shows a schlieren picture

of the expiratory pattern at this tidal volume. This Figure also shows a 'hollow rake' positioned next to the nose. When carbon dioxide is passed through these tubes the stream deflections of the carbon dioxide can be noted. In this way, the breathing zones may be defined and the region from where the inspired air is drawn established. Using this technique, it may be seen that the whole of the inspired air is taken from the convective boundary layer. It is also seen that there is little chance that the expired air could be re-inspired.

9.1. Observations on Particles Moving in the Convective Flow of the Heated Model.

Preliminary flow visualisation experiments were made using lycopodium spores and with the nares of the model blocked. The particles were injected into the boundary layer flow using a small glass capilliary tube attached to a mechanical vibrator (Figure 82). The particle motions were recorded photographically. It was observed that at sites such as the abdomen and chest, some of the particles behaved very much as those in the laminar flow channel. They did not deposit but performed oscillating and spiralling motions for a considerable time (up to one minute) at distances the order of 200 μm away from the body surface.

Particles mainly deposited on the upper surfaces of inclined areas, i.e. the bridge of the nose, the forehead, shoulders, and crown of the head. Under the nose, where the nares were solid, the particles did not deposit but remained in the flow to move with the streamlines. This observation implies that in order for particles to enter the respiratory tract they have to be 'sucked' in during the inspiratory period of the respiratory cycle.

In the region of the orbit (with the model eyeball at the same temperature as the surroundings) no particles deposited.

9.1.1. Observations with the Model 'Breathing'.

From the observations of particle behaviour in the laminar flow channel and from the experiments in the previous section showing that the particles could cross streamlines in the convective boundary layer, it was important to determine whether there was any difference in particle concentration in inspired air with the model hot and cold. In order to assess environmental contamination level, experiments were made in a busy corridor at the NIMR. Sampling wires 100 μm dia were stretched across the nares and the respiration pump operated for consecutive periods of 3 hours, first with the model cold and then with it at skin temperature. At the end of the experiments, each wire was photographed under the Tessovar microscope and the particle deposition determined. This experiment was repeated several times with various levels of activity in the corridor (therefore with different degrees of air contamination), and the maximum value of the ratio $\frac{\text{Particles entering the nose - model hot}}{\text{Particles entering the nose - model cold}}$ was 2. In some experiments, this ratio was 1, with no measurable difference in deposition. This ratio was never found to be less than 1. The numbers of particles in the size range 5 - 50 μm that entered the nose in these preliminary experiments were between 100 - 200 particles/litre (2800 - 5600 particles/cu ft). A more complete understanding of the streamline crossing mechanism of the particles would be of help in any future work on this particular aspect of particle movement within the microenvironment.

9.1.2. Experiments on the Release of Particles from the Surface of the Heated Model.

In order to simulate the abrasive action of clothing, a system for liberating particles from the skin surface was devised. A large cotton 'bandage' was soaked in light magnesium carbonate solution and wrapped around the heated surface of the model man where the water evaporated to leave the bandage impregnated with the fine powder. A stiff

brush, attached to a reciprocating arm driven by a crank on an electric motor was positioned so that the bandage could be gently scratched. In this way, a controlled number of particles could be liberated into the convective boundary layer. Figure 83 shows this mechanism. Considerable concentrations of particles were collected in the nostrils and in the plume of the model when particles were liberated from the surface for periods up to 2 hours with the model breathing. This demonstrates that for particles to enter the respiratory tract rather than simply divert with the flow at the nares, it is necessary for them to be 'sucked' in during inspiration. When this experiment was repeated without the simulated breathing cycle, there was no deposition on the wires at the nares.

10. THE MOVEMENT OF PARTICLES THROUGH FABRIC AND THE BELLOWS ACTION OF CLOTHING

Although the insulating properties of ordinary clothing gives rise to a smaller temperature gradient between the outside of the garment and the surroundings, there is still a large enough temperature difference to create a convective boundary layer which is able to lift all but the largest particles within the flow. The way in which particles may move through fabric is demonstrated by placing an ordinary cotton surgical gown over the heated model that has the artificial skin attached, as in Figure 84. The temperature on the outer surface of the gown is about 24°C (a drop of 10°C from the body surface temperature). Figure 85 shows the weave of this cloth which has holes some 60 μm square. With gentle movement of the gown similar to that which may be caused by moving about, particles are seen to come through the cotton to be entrained and move upwards, in the convective boundary layer that establishes itself on the outer surface of the gown.

Efforts to identify, and methods of controlling, by specially designed clothing, sources of infection in operating theatres showed bacteriologically that organisms shed from the surgeon's body could penetrate gown materials and escape from the openings in the fabric. (Charnley 61). Bethune et al

1965 (62), Bernard et al, 1965 (63). It was shown by Blowers et al, 1965 (64) that when a subject was clothed in a one-piece polythene suit which was practically impermeable to particles, but which had the bottoms of the trousers open, then the resulting contamination reached half of that from a standard operating suit. In these experiments, the apertures at the waist, neck and arms were found to be less important sites for the escape of skin organisms.

Schlieren observation of the openings around clothing shows that any movement of the subject results in large quantities of air being 'pumped' out of these openings by the bellows actions of the clothes. Figure 86 shows a schlieren picture and a drawing of the way in which stagnant air may build up and spill over on to the outside of the gown surface. A similar pumping action is seen with loosely fitting surgical boots and trousers where particles may be blown out to be dispersed by the boundary layer, as shown in Figures 87 and 88. A general principle for protective clothing design therefore should be that all openings be occluded and that loose garments be 'tucked' in. In an operating theatre, the surgical gown would best be replaced by tight fitting occluded trousers. Schlieren photography shows that during respiration the expired air is expelled as a well defined jet of air which may reach as far as one metre from the body. The object of a surgical mask is to reduce the chance of expired droplets reaching a site where infection may be caused. When a subject wears a surgical mask in a schlieren beam, the expiratory pattern is completely changed. Expired air still penetrates the mask material, but on a much reduced scale (65 and 66). Violent expiration may still project air up to $\frac{1}{2}$ metre from the nose but in general, the 'zone' of expiration only extends some 10 - 15 cms in front of the mask, and because of the high filtration efficiency of the mask, this particular route for infective materials is restricted. Nevertheless, the expired air must be carried away from the nose and most of it is diverted upwards to leave the mask in

a nearly vertical direction through the openings next to the orbit. Figures 89 and 90 show diagramatically the differences in the expiratory air patterns. The jets of air that do escape through the mask openings are seen to join with and be carried away by the general convective upflow over the face.

11. SOME EXPERIMENTS CONCERNING DUST SAMPLING

Microscopic examination of house dust and dust found in corridors and laboratories revealed that the majority of the debris examined - some 70% to 80% - was decomposed organic material, mainly skin scales, many of them covered with micro-organisms. An Anderson mini-sampler was used to sample the dust in various environments. This device is shown dismantled in Figure 91. The instrument was clipped to a lapel so that the air sample could be taken in the micro-environment. In early summer, pollens as well as skin scales and grits were collected. The result of a particularly interesting experimental sample is shown in Figure 92. This sample was obtained during a journey on the London Underground Northern Line between Hampstead and Morden. Many of the stations on this line are hazy with dust which appears to be soot or carbon. The debris collected on the sample plates was examined under the microscope and about 80% found, once again, to be decomposing skin scales and other heavily contaminated organic material. The rest of the sample was composed of fine carbon and larger soot. Most of the organic material in the sample was black. This colouring is not explained by the particles landing on the tunnel side walls to become black and then re-entering the air due to the shear stresses acting when a train displaces air in the station, because the levels of shear stress are generally too small to dislodge settled particles. The most likely explanation of this colouring was suggested by P. H. Gregory at Rothamsted. This was that the particles attached to each other by electrostatic action to form filaments composed of skin scales and carbon particles, with the

skin becoming black by contact with the carbon. The filaments would grow out some distance from the wall surface and would therefore be able to be broken by air movements caused by trains and passengers.

11.1. The Sampling and Sizing of Airborne Particles.

During the early Summer of 1972, samples were collected with an Anderson Mini Sampler from the air of living rooms and a garden in a rural district. At the same time, a Royco Model 215 Particle Monitor was used to determine the concentration levels and particle size distributions.

Figure 93 shows a micrograph of some of the particles from the sample of garden air. Although there were a lot of pollens present and particles of soot and ash, many of the particles are identified as being pieces of skin, some having micro-organisms attached. The samples both indoors and outside were remarkably similar in composition (other than there being more pollens outside). At present it is not possible to identify skin squames as originating from humans or animals. There is no reason to suppose that much of the skin debris could not have come from animals. The concept that so much of the airborne contamination originates from humans and animals has implications in the field of plant pathology where these particles may land on plants or crops.

The results from the Royco particle monitor showed that there were consistently more particles in room air than in the outside air. Figure 94 shows the comparison between house and garden. It may be seen that the garden air was a little cleaner than a class 100,000 clean room. Figure 95 shows the consistency of the particle concentration levels in garden air on 4 different days. The largest change in concentration levels is seen to occur in particles greater than 5 μm dia and this size includes many of the pollens present in the air during the period of the test.

In an effort to measure the concentration of the larger particles

(around 10 μm and greater) and correlate this with the general pollen level as given daily by R.R. Davies, this size range of particles was monitored hourly on 2 occasions. Figure 96 shows the variation in concentration on a day when the pollen count was very high at 250. During the period of this test when the count reached a high peak in the evening, one of the occupants of the house reported a severe hay fever attack resulting in bed rest until the particle count reduced. This subject was unaware of the high particle counts during this 4 hour period. Figure 97 shows a similar experiment performed the following day. The general concentration level was much reduced and the pollen count, although high at 89, was lower than the day before.

The particle concentration level increase in a small enclosed room after the entry of a subject was measured. The subject first remained still and then began to walk around and figure 98 shows this change in concentration of several particle sizes during a half-hour period. The greatest increase in concentration is seen with the larger particles. During this period, the number of particles larger than 5 μm dia increased by 4 times, whereas the concentration of 0.5 μm dia particles just doubled.

Figure 99 shows a similar increase in concentration of the larger particles when the subject remained seated and removed and then replaced his clothes during a 40 minute period. In this case the larger particles increased in concentration between 3 and 5 times, and the smaller particles increased their concentration by less than 1.5 times.

Concluding Remarks

The convective boundary layer around the human body has been discussed and the way in which this flow gives rise to convective heat transfer has been investigated The use of hot wire anemometers and thermocouples to measure the convective boundary layer velocity and temperature profiles has been described. These boundary layer velocity and temperature profiles

have been measured around heated models that were designed to simulate the human convective boundary layer flow. Measurements in vivo have not been attempted in this study although the techniques for measuring velocity and temperature which have been developed would be suitable for this application with further development.

Measurements within the flow around the heated models have shown that the convective boundary layer flow in the extended position can have velocities of up to 50 cm/sec and a thickness at face height of some 15-20 cm. The plume of hot air above the head extends for some 1.5 metres, and the total mass flow over the head is about 10 litres/sec.

The convective boundary layer flow has been shown to be more vigorous than had generally been appreciated before these studies. Many textbooks concerned with the physiology of heat transfer have hitherto described the convective flow as a very thin layer or film of moving air, and the heat loss by convection has also been underestimated (by as much as 50%) in some texts (67). Change of posture modifies the convective flow and the boundary layer becomes less vigorous as the vertical height of the body decreases. Generally, the local convective heat transfer increases with descreasing boundary layer thickness. This is because the temperature gradient from the body to the surroundings becomes steeper in a thin air layer (with higher $q = kdT/dY$).

If the heat loss from the head alone is considered, then it is seen that in the 'extended' position the head may be surrounded by a thick boundary layer flow which affords a degree of thermal insulation because of the shallow temperature gradient and lower value of kdT/dY. Studies of the heat loss from the head have shown that this heat loss may be a surprisingly high proportion of the total heat loss from the body (up to 20% of the total). However, these results were obtained using a calorimeter which was placed over the head. Thus the head was isolated

from any convective influences from the lower body and this could account in some part for the high heat output rates measured. This configuration would be representative of the heat loss from the head in the lying down position when there is no flow from beneath the head.

The heat loss from the head by convection for various body postures is the subject of a continuing study.

The convecti ve flow remains laminar for a height of about 100 cm until the Grashof number reaches 2×10^9 and becomes turbulent after 150 cm when the Grashof number exceeds 10^{10}

The human body has been considered as a series of 5 cylinders and the heat loss by convection from these cylinders has been analysed using boundary layer theory. For the body in the extended position, these calculations are in reasonable agreement with convective heat output data from partitional calorimetry methods. The convective heat transfer for the naked body in a comfortably warm room at about $20^{o}C$ is about 30% of the total heat loss. The way in which clothing modifies the convective heat loss by reducing the temperature difference between the skin and surroundings is discussed in Appendix 1 . However, it is interesting to note that in the expression for the Grashof number, the temperature difference term appears to the first power, whereas the vertical height is to the third power. From this it may be seen that the convective flow parameters are not very sensitive to changes in the surrounding temperature. The heat transfer varies with $X^{\frac{3}{4}}$ but only with $(T_{\omega} - T_{\infty})^{\frac{1}{4}}$. Thus a doubling of the temperature difference, which is quite a drastic environmental change, only alters the Nusselt number by a factor of 1.2. If the vertical height of the subject halves, due to posture changes, this produces a change in Nusselt number of 1.7 times.

The proposition that the convective boundary layer flow can transport particles from one site to another has been validated. Particles up to about 70 μm equivalent diameter are able to be lifted upwards by this flow.

These particles may enter the flow either from the body or clothing surface or be entrained from the surrounding air. Once in the flow they may either be presented to the respiratory tract for inspiration or dispersed to the surroundings from the plume of air above the head.

The motions of small particles have been investigated in a flow channel. This channel simulated the velocity profile found in the convective flow next to the skin surface and allowed the particle motions to be studied over distances similar to those found on the body. Most of the particles were shown to travel large distances within the channel although some were shown to be deposited from the flow on to the channel walls. Once these particles landed it was shown that they would not be re-entrained by the shear stresses produced by the flowing air. The forces acting on such particles to cause deposition have been examined in detail and it has been shown that aerodynamic lift forces and electrostatic effects account for some of the observed phenomena.

Particles have been observed moving in the convective flow over a heated model of the human form and these observations coincide with those made in the channel flow. This heated model has also been used to visualise the way in which particles that are detached from the skin surface may pass through the weave of garments and travel upwards in the flow.

The way in which the bellows actions of garments may enhance the dispersion of particles from non-occluded openings has been visualised in the schlieren optical system, with special reference to garments used in operating theatres. It is hoped that this work will complement the bacteriological studies in this field by providing some understanding of the physics of particle dispersion by these garments.

The thickness of the boundary layer of some 15 cm at face height implies that interaction between the convective flows of 2 people will occur when their skin surfaces are as much as 30 cm apart. Such separation distances do not constitute crowded conditions and this interaction of flows provides

a possible mechanism for cross infection within enclosed areas.

The interaction of the convective flows around 2 heated models was observed in the schlieren system as the separation distance of the models was increased. The exchange of air between the 2 convective flows was clearly visible and was seen when large rolling eddies were present, up to a separation distance of 50 cms.

The desquamation of skin particles is the main source of contamination in industrial clean rooms and in operating theatres. The movement of such particles by the convective flow within the micro-environment must be taken into account in the design of protective clothing for use within such environments.

The boundary layer also provides a path for particles that could result in the start of autogenous infection downstream of a rubbed or scratched site. The last part of this thesis reports the recovery of skin particles from enclosed spaces such as houses, factories and the outside air even in rural areas.

Various air sampling techniques have been used in this study to sample airborne particles. Results are reported which show the spectrum size distribution of airborne particles in various environments. These experiments have shown that the contamination of enclosed living areas is about an order of magnitude higher than the contamination of outside air in rural areas. Microscopic observation of these particles indicates that the majority of particles in living areas are skin scales and that they are also found in large numbers in the outside air.

These results show that man is an important source of pollution within the environment. The proposition that skin particles and their associated micro-organisms form a normal constituent of the atmosphere will subsequently be investigated.

These results, together with a study of the micro-environmental flows of humans and animals have application in the study of the transmission

of general airborne infection and in the transmission of plant pathogens. The extension of the use of the hot wire anemometer as a particle sampler together with the associated electronic circuits has also been described. This device has found application in counting tracer particle concentration levels within enclosed areas and in testing the efficiency of ventilation systems.

For a still man almost all of the air that is inspired has been shown to have travelled over the body surface in the boundary layer and the humidity gained (although not sufficient to change the boundary layer parameters) may be such as to ensure efficient humidification of the lungs. Some aspects of humidification of the respiratory tract are discussed in(72) Of particular interest is the flow in the orbit. The eyeball may be pushed forward as a result of the inflammatory processes within the orbit, or as an associated feature of the disorder of exopthalmic goitre. This protrusion of the eyeball, which may be of the order of 2-3 mm would put the eyeball in the path of the fast moving air in the boundary layer. This, together with the disturbances associated with the eyelashes, puts the eyeball in a position where drying out of the eye's lubricating fluids becomes enhanced and possibly lead to sight degeneration and ultimate blindness. A simple prophylactic measure that suggests itself is to allow the patient to wear tight-fitting goggles in order to isolate the eyeball from the convective flow.

APPENDIX 1

Remarks on the Effects of Clothing

Although this study is mainly concerned with the convective flow over the naked body, a few remarks about clothing design and the convective flow are appropriate here. Any mechanism that slows down the convective boundary layer will consequently reduce the heat transfer rate. If this velocity reduction is carried to the extreme of stopping the flow altogether, then heat transfer will only occur across the air gap by conduction. The thermal conductivity of air is lower than any normal clothing and it is therefore warmer to wear several layers of a thin loose-fitting garment than something thick and tight-fitting. In this way, there will be layers of stationary air between the garments providing good thermal insulation. String vests are an example of boundary layer velocity inhibition. The coarse mesh of the vest provides pockets of local circulation cells and reduces the convective velocity. These unlikely looking garments thus prove to be very warm. As a corollary, anything which speeds up the flow of air past the skin surface (i.e. forced convection) will increase the heat loss rate. Desert tribesmen's robes are an example of garments providing this action. They act as bellows to drive air past the skin surface faster than the natural convection velocity. Consequently, the heat transfer rate is increased and these robes are very efficient cooling garments in hot climates.

Evaporation, being such an important method for heat loss from the naked body, the design of clothing must take account of this variable regulation process. The thermal conductivity of most clothing is low (although not as low as air alone) and hence any heat loss changes that the body metabolism requires must come from evaporation that must not be inhibited by the clothing. Thus, it is essential that the clothes next to the sweating skin surface are not impervious to water and do not stop the evaporation of the secreted sweat. The reason why plastic undergarments are not acceptable is that the sweat secretion creates a damp interface

between the garment and the skin with the attendant interruption of the heat regulation processes of convective and evaporative heat loss.

Normal indoor clothing may produce a temperature difference between the skin and the outer surface of the garment of from $5^{o}C$ to $8^{o}C$ depending on the tightness of the garment and the thermal conductivity of the material. It is interesting to note that if the temperature on the outer surface of the garment is reduced to $10^{o}C$, then the height at which the natural convective flow becomes fully turbulent, based on a Gx of 10^{10}, is 187 cms, compared to 153 cms for the naked man. Transition from the laminar begins at a Gx of 2×10^{9} when the height above the ground is 122 cms for the clothed man which is 22 cms greater than for the naked man. Thus it is seen that the boundary layer may remain laminar over the whole body surface. The heat loss by convection for a clothed person (ordinary 'indoor' clothing) when the temperature difference ($T_{\omega} - T_{\infty}$) is reduced to $5^{o}C$ is about 25% of the heat loss for the naked man, which reduces the convective heat output to 14-16 watts. The maximum velocity in the convective flow for the naked man at the transition height of 153 cms is 30 cm/sec; with clothing this reduces to a value close to 22 cm/sec. Thus the convective flow pattern may be established over a clothed body to produce velocities which may only be some 25% lower than for the naked man.

APPENDIX 2

Lift and Drag on a Particle in Viscous Flow

For a settling particle, any departure from sphericity may produce additional lift forces. Owen (56) guide by the analysis of slow flow about spheroids (Happel and Brenner 1965) gives an expression for this extra lift. When $U_t d/\nu \ll 1$ the extra lift on a particle with small eccentricity e and an incidence with respect to Ut is of the order of $\mu U_t d e^2$ The value for L/D in laminar flow is about $e^2(U_t^3/g\nu)$ The eccentricity of an oblate spheroid is $e = \left(1-(b/a)^2\right)^{1/2}$ where b and a are the polar and equatorial radii. For a particle with aspect ratio 5, in a laminar flow where U_t = 4 cm/sec this value L/D is about 0.4.

Imai, in presenting a method for solving Oseen's equation for the flow past an inclined 2-dimensional elliptic cylinder gives values of Cl/Cd of a similar magnitude to the estimates for the 3-dimensional case. This analysis for the 2-dimensional case is outlined below and the results are used to estimate the trajectory of a particle subjected to a lift and drag force.

For the flow past an inclined 2-dimensional elliptic cylinder at an angle of incidence α gives analytical expressions for the lift and drag coefficients as follows :

$$C_D = \frac{16}{\pi}\,\frac{2S-1-\cos 2\alpha}{D} - \frac{\pi R}{4D}\left[S^2+\frac{1}{2}(1-2\cos 2\alpha-\cos 4\alpha)S\right.$$

$$-\frac{1}{24}(9+8\cos 2\alpha-7\cos 4\alpha)+\frac{1}{D}\left\{\frac{1}{12}(30+23\cos 2\alpha\right.$$

$$\left.\left.-10\cos 4\alpha-3\cos 6\alpha)S-\frac{1}{12}(14+21\cos 2\alpha+6\cos 4\alpha-\cos 6\alpha)\right\}\right]$$

and

$$C_L = \frac{16\pi}{R}\,\frac{\sin 2\alpha}{D}\left[1-\frac{R^2}{64}\left(2S^2+(1+\cos 2\alpha)S+\frac{1}{3}(2-\cos 2\alpha)\right.\right.$$

$$\left.\left.+\frac{1}{D}\left\{\frac{1}{2}(5+4\cos 2\alpha+\cos 4\alpha)S+\frac{1}{3}(9+10\cos 2\alpha+\cos 4\alpha)\right\}\right]\right.$$

where $D = 4S^2 - 2(1+\cos 2\alpha)$

$S = \ln\left(\frac{16}{R}\right) - \gamma$

$\gamma = 0.57721$ for a flat plate.

APPENDIX 2 - (2)

Figure 100 shows from the results of Imai, values of Cl/Cd versus angle of incidence for 2 values of Re. If we assume the same form of solution for 3-dimensional particles using values for Re based on the terminal velocities of the particles, it is seen that for Re = 1, Cl/Cd varies from 0.25 to 0.18 for angles of inclination ranging from 18^{o} to 72^{o}. That is, a 28% variation in glide angle for 60% of all angles of particle inclination. We therefore define an AVERAGE particle to be one that has an angle of inclination (assumed constant throughout the trajectory) between 18^{o} and 72^{o} with an Re based on the terminal velocity of 0.01 to 1.0.

Taking a mean value for the inclination of the average particle of 45^{o} we have, to a first approximation, values for Cl and Cd as follows :

$$C_D = \frac{16\pi}{RD}(2s-1) - \frac{\pi R}{4D}\left[s^2 + \frac{1}{2}s - \frac{9}{24} + \frac{30s}{12D} - \frac{7s}{60}\right]$$

$$C_L = \sin 2\alpha \cdot \frac{16\pi}{RD}\left[1 - \frac{R^2}{64}\left(2s^2 + s + \frac{2}{3} + \frac{5s}{2D} + \frac{3}{D}\right)\right]$$

ie $$C_D \simeq \frac{16\pi}{RD}(2s-1)$$

$$C_L \simeq \frac{16\pi}{RD}\sin 2\alpha$$

giving $$C_L/C_D = \frac{16\pi}{RD} \cdot \frac{R.D}{16\pi} \cdot \frac{\sin 2\alpha}{(2s-1)} = \frac{\sin 2\alpha}{2s-1}$$

where s from before $= \ln\left(\frac{16}{R}\right) - \chi$

The following table shows some maximum values of the glide angle of the particle $= \tan^{-1} C_L/C_D$ for various particle sizes, and an angle of inclination of $\pi/4$ The particles in the flow move along the channel at an angle $\tan^{-1} C_L/C_D$ relative to the flow.

Particle Size	Re	Cl/Cd	Glide Angle γ
0.1 μm	3.50×10^{-8}	0.0266	$1^{o}31'$
1 μm	3.50×10^{-6}	0.0328	$1^{o}53'$
5 μm	4.37×10^{-4}	0.0534	$3^{o}\ 3'$
15 μm	1.18×10^{-2}	0.0825	$4^{o}43'$
70 μm	1.20	0.3318	$18^{o}21'$
90 μm	2.55	0.6652	$33^{o}38'$
100 μm	3.50	1.131	$48^{o}31'$

Trajectory of a Particle with Lift and Drag Forces

For a particle moving in a uniform laminar flow, its motion will be at an angle $\pi/2 - \gamma = \tan^{C_o}/_{C_L}$ to the flow, with a velocity (for vertical upward flow) of U_t in the flow direction. This assumes that the only forces affecting the particle motion are the stokes drag and an associated aerodynamic lift force. The assumption is also made that for any particle this glide angle γ remains constant during the time of flight of the particle.

In a small time dt the particle moves a distance dx in the flow direction, and a distance dy across the flow: where

$$dx/dt = (u - u_t) \quad \text{and} \quad dx/dy = \left(\frac{u - u_t}{u_t}\right) \tan\gamma$$

where U is the focal flow velocity.

If the particle is moving in a channel of width D, and begins its motion from the centre of the channel, then the total distance X_u moved along the channel in the flow direction before impact with a side wall is given by

$$\int_0^{D/2} \left(\frac{u - u_t}{u_t}\right) \tan\gamma \, dy \quad \text{ie} \quad X_u/D = \left(\frac{u - u_t}{u_t}\right) \cdot \frac{\tan\gamma}{2}$$

for uniform flow.

Similarly, if the channel flow has a parabolic velocity profile, with a maximum velocity U_o where $u_y = u_o(1 - 4y^2/D^2)$ we have

$$dx/dt = u_o(1 - 4u^2/D^2) - u_t \quad \text{and} \quad dy/dt = u_t/\tan\gamma$$

The distance X_p moved by the particle before impact in this case is

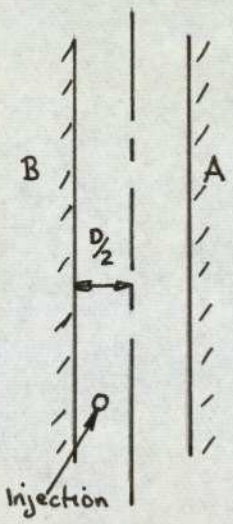
$$\int_0^{D/2} \left[\frac{u_0}{u_t} \tan\gamma \left(1 - \frac{4y^2}{D^2}\right) - \tan\gamma \right] dy$$

From which $$\frac{X_p}{D} = \frac{\tan\gamma}{3} \left[\frac{u_0}{u_t} - \frac{3}{2} \right]$$

If the particles are in an air stream moving vertically downwards, then the values for the distance moved before impact in uniform flow and in Poiseuille flow are respectively for uniform and parabolic flow;

$$\frac{X_{u_D}}{D} = \left(\frac{u + u_t}{u_t}\right) \frac{\tan\gamma}{2} \; ; \; \frac{X_{P_D}}{D} \left[\frac{u_0}{u_t} + \frac{3}{2} \right] \frac{\tan\gamma}{3}$$

A similar analysis can be applied to particles not injected in the centre of the channel, but at a point distant D/4 from one side wall.



For Poiseuille flow the distance a particle travels before hitting either wall A or B is given by

$$\frac{X_{P_A}}{D} = \frac{\tan\gamma}{4} \left(\frac{u_0}{u_t} \cdot \frac{9}{4} - 3 \right)$$

$$\frac{X_{P_B}}{D} = \frac{\tan\gamma}{4} \left(\frac{u_0}{u_t} \frac{5}{12} - 1 \right)$$

The Concentrations of Deposited Particles

It is now possible to begin to consider the deposition concentrations along the sides of a channel from a given initial number of injected particles with a known size distribution. We assume that the particles in this given size range are equally distributed, when injected, over angles of incidence between 0 and $\pm \pi/4$

Initially, we shall consider the motion of the particles injected into a Poiseuille flow at the centre of a channel of depth D. From above we have :

$$\frac{X_p}{D} = \frac{\tan\gamma}{3} \left[\frac{u_0}{u_t} \mp \frac{3}{2} \right]$$

where U_t is the terminal velocity of the particle, given by $U_t = kd^2$, k being a constant related to the density of the particle, and d being the particle diameter. The -ve sign denotes upward flow, and the +ve sign downward flow. The above equation (from Imai) can be re-written as

$$X_D/D = \frac{2s-1}{3 \sin 2\alpha}\left[\frac{u_0}{u_t} \mp \frac{3}{2}\right]$$

where α is the angle of incidence of the particle, $S = \ln \frac{16}{R} - \gamma_e$ where γ_e is the Euler constant.

The number of particles between diameters d & (d + δd) and having an angle of incidence between α and (α + $\delta\alpha$) is given by

$$\tfrac{1}{2}\, \bar{N}(d)\, \delta d .\, \delta\alpha/\pi/4$$

where N(d) is the number distribution of the injected particles.

Let $\delta\bar{n}$ be the number of particles landing on unit area of a wall of unit width. Then the number landing in a channel length $\delta(x/D)$ is given by :

$$\delta\bar{n} = \tfrac{1}{2}\, \bar{N}(d)\, \delta d/\delta(x/D) \cdot \delta\alpha/\pi/4$$

This may be integrated with respect to α to give $\bar{n}$ as $f(x/D)$ where $\bar{n}$ is the total number of particles landing on a wall. i.e.

$$\bar{n} = 8/\pi \int_0^{\pi/4} \frac{\bar{N}(d) .\, d .\, \sin 2\alpha}{(2s-1)u_0/u_t + 3\left(u_0/u_t \mp \frac{3}{2}\right)}\, d\alpha$$

where

$$\left(\frac{\delta(x/D)}{\delta(d)}\right)_{\alpha\,\text{const}} = \frac{2}{3d \sin 2\alpha}\left[(2s-1)\frac{u_0}{u_t} + 3\left(\frac{u_0}{u_t} \mp \frac{3}{2}\right)\right]$$

For a uniform velocity profile, as in the entry section of a flow channel a similar expression for the number concentration becomes

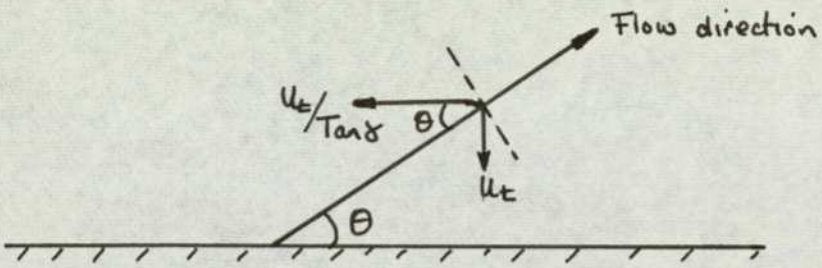
$$\bar{n} = \frac{8}{\pi} \int_0^{\pi/4} \frac{\bar{N}(d)\, d .\, \sin 2\alpha}{(2s-1)u_0/u_t + 2\left(u_0/u_t \mp 1\right)}\, d\alpha$$

These expressions have been numerically evaluated for a series of Re and for various flow configurations. (Figures 27, 28, 29) where the distribution of the particles is expressed by $6000\, e^{-.0029d^2}$ for the glass dust particles used in the flow channel experiments.

Limitation of the Theoretical Treatment

The deposition due to any lift forces acting on the particle has been

treated theoretically in the previous sections only for the cases where the flow is vertically upwards or downwards. If the flow is at an angle θ to the horizontal, then a falling particle will have a downward velocity of U_t and a horizontal velocity of $U_t/\tan\gamma$ relative to the flow as in the diagram below.



The particle will only move to the upper wall of an inclined channel if the normal component to the flow $U_t \cot\gamma \sin\theta > U_t \cos\theta$ ie if $\cot\gamma > \cot\theta$ ie $\gamma > \theta$

As an example; for a 15 μm dia particle ($\gamma = 85^\circ 29'$) there will be no deposition on the upper surface of the channel due to lift for particles of O(15 μm) when the inclination of the flow is greater than 4° to the vertical.

APPENDIX 3

Particle Deposition in Vacuo

In the discussion of the results from the channel deposition experiments, it is necessary to consider the effects of any electrostatic forces acting on the particles. G.M. Hidy, when considering the kinetic theory of aerosols (71) says "The capability of small particles for becoming charged is well known ..... The present theory for electrical effects in aerosols stems largely from classical electrostatics ..... many aspects of charging and electrical interaction in (atmospheric) clouds have not yet been explained. Because of many uncertainties in the details of this interaction, electrostatic influences have often been invoked arbitrarily to explain deviation in aerosol behaviour from expected observations. It may well be true that the electrical effects contribute to these deviations, but considerably more careful research usually is needed to verify such conclusions."

In the experiments with the vertical glass channel, it is necessary to try to determine the magnitude of any electrostatic effects leading to particle deposition so that the relative magnitude of any aerodynamic mechanism causing deposition on upper surfaces at channel inclinations less than δ to the horizontal may be assessed.

In an effort to determine the relative parts played by electrical and aerodynamic forces on particle deposition, some experiments were carried out in an evacuated vessel. A flat glass plate was suspended in a long evacuated glass tube, and glass dust and ballotini were allowed to fall past this plate from a horizontal distance away of one cm. The air pressure in the glass tube was reduced to around 3 mm mercury so that any aerodynamic effects were much reduced. Particle motion, other than in a vertically downward direction was then only possible by electrostatic forces or undamped sideways velocities given to the particles during the injection process. In order to minimise this latter effect, the particles were kept in a vertical rubber tube which was sealed with 2 clamps during the time of evacuation of

the vessel. When the bottom clamp was released, the particles fell through a vertical tube at the bottom of which a small hole allowed only a small proportion of the particles to pass into the glass vessel. This injection tube was designed as a screen to give a collimated beam of particles that could fall past the glass plate. In practice, perfect collimation was never achieved, since collisions between particles in the injection tube, together with slight vibrations of the whole system produced undamped sideways motions which would cause the beam of particles to fill the tube section at about $1\frac{1}{2}$ M from the injection level.

Figure 101 shows the deposition of particles on to the glass plate for the best attainable collimation in vacuo and this is contrasted to the deposition in the same system with the air present. For $X/D > 35$ in vacuo the effect of the beam spread is seen to be significant, whereas for $X/D < 35$ very few particles are seen to be deposited. The experiment for particles falling in air shows the same deposition pattern as in the channel experiments and correlates well with Figure 42; the values of X/D for maximum deposition in the 2 cases being about 25. When ballotini were used in this experiment, the beam spreading caused the same deposition as for the glass dust in vacuo, but as in the channel experiments with air, only clustered and deformed particles deposited.

The deposition pattern for glass dust is therefore seen to be different for vacuo and air, but the only definite conclusion to the experiment is that the deposition pattern exhibiting a maximum value in air relies on the presence of the air. It therefore seems probable that if the attraction of particles by the glass due to a residual charge on the glass particles alone is mainly responsible for the deposition process (as assumed by Owen in JFM 39,pt.2,pp.407-432) then the presence of air is essential to the charging phenomenon. This is supported by the result given in section 7.3.2. where glass dust and ballotini were mixed together and afterwards showed no change in their individual deposition patterns. Here it would seem that any electrostatic charge differences were brought about after injection and were therefore due to the passage of air past the particles.

APPENDIX 4

Flow Patterns and Particle Deposition in a Glass Model of the Trachea and Bronchi

Since the deposition pattern in the laminar flow channel has been studied with the air flow in a downward direction, it was considered of interest to look at the deposition pattern in a model trachea and first bronchi with the flow alternately upwards and downwards.

The flow in the respiratory system is being studied by other workers so that no more than a few pilot experiments have been carried out, and as a consequence the conclusions drawn are limited.

For breathing rates of up to about 30 L/min the flow in the trachea may be laminar, at greater flow rates it is always turbulent, at least as far as the first bronchi. Breathing rates in the resting state will give laminar flow in the trachea. A simple glass model of the trachea and first bronchi was constructed and is shown in Figure 102. Two anemometer positions are shown and a vacuum pump was arranged to achieve either upward or downward flow with the model in the vertical position. With downward flow (inspiration) the velocity profiles in both the trachea and first bronchi are shown in Figures 103, 104 and 105. The trachea profile is simply developing Poiseuille flow, but the flow in the bronchi is more complex. At the lower Re of 825 (based on velocity in the trachea) there is a fast moving jet near to the inner wall; at the higher Re of 1073 jets are seen at both walls with relatively low velocity in the centre of the bronchi. The mean velocity in the bronchi being half that in the trachea. Smoke tests showed the separation bubbles occurred on the outer wall at the bend and at the stagnation point in the region of the carina causing a complex and unstable 3-dimensional flow pattern. The flow could be seen at times crossing from the trachea walls to the inner walls of the bronchi just downstream of the carina.

These profiles and observations were subsequently confirmed by the work of Schroter & Sudlow (73) who are undertaking a complete flow description using a similar glass model. In view of this, no further work was undertaken

to establish a more complete picture of the flow.

Figure 106 shows the deposition of glass dust on the walls of the model for the vertical position in both upward and downward flow. For downward flow the particles were injected at the top of the trachea, and for upward flow the injection was at the base of one of the first bronchi. The inclined surfaces leading to the carina at the inlet to the bronchi were subject to the greatest deposition of the order of 3000 particles/mm^2 with both directions of the flow and also when ballotini were injected. There was once again no evidence of ballotini deposition on the upper surfaces of the bronchi, or in the vertical trachea in either flow direction except for a few deformed particles and some clusters. It should be added here that the particle counting method used for the flat glass channel sides was used in a modified form for this trachea model. However because of the curvature of the glass, and the need to track the microscope very near to the model to achieve adequate magnification, this simple method was far from ideal. For detailed work on particle deposition in such a model, a more sophisticated counting technique needs to be evolved that allows observation of the complete circumference of any cross-section through the model.

The only conclusion drawn from these experiments is that significant glass dust deposition was noted on the model walls in both the trachea and first bronchi in laminar flow with the model vertical and in both inspiratory and expiratory flow.

REFERENCES

1. Temperature and Human Life. Winslow, C-E.A. and Herrington, L.P., 1949. Princetown University Press.
2. Physiology of Heat Regulation and the Science of Clothing. L.E. Newburgh. 1968. Hafner Publishing Co. Inc.
3. The Stress of Hot Environments. D. McK. Kerslake. Cambridge University Press. 1972.
4. Principles of Human Physiology. Ed. H. Davson and M.G. Eggleton. Chaps. 33, 34. 14th Edition. 1968. Churchill Ltd.
5. Lewis, H.E. (1967). J. Physiol., Lond. 188, 6P.
6. Lewis, H.E., Foster, A.R., Mullan, B.J., Cox, R.N., Clark, R.P. The Lancet, June 28, 1969. pp. 1273-1277.
7. Film - Man's Natural Barrier to the Environment. (16 mm colour, sound, 6 mins). Film Library, Department of Audio-Visual Communication, British Medical Association, Tavistock Square, London WC1.
8. Cheesewright, R. Int. Jnl. Heat Mass Trans. (1967). Vol. 10.
9. Principles of Human Physiology. 11th Edition. 1952. by Evans, C.L. Churchill Ltd.
10. Schmidt, E. and Beckman, W. Forsch Ing-Wes. 1, 391 (1930).
11. Ostrach, S., N.A.C.A. Tech. Note 2635. (1952).
12. Griffith, E. and Davies, A.H. The Transmission of Heat by Radiation and Convection. Food Investigation Board, D.S.I.R. Special Report No. 9. H.M.S.O. (1922).
13. Eckert, E.R.G. and Jackson, T.W. Natl. Advisory Comm., Aeron. Rept. 1015 (1951).
14. Eckert, E.R.G. in Introduction to Heat and Mass Transfer (1963). McGraw Hill.
15. Bayley, F.J. (1955). Proc. Inst. Mech. Engrs. 169, Part 20.
16. Cheesewright, R. Trans. A.S.M.E. (1967). Paper 67 - HT - 17.
17. Schlichting, H. Boundary Layer Theory. McGraw Hill. 6th Ed. 1968.
18. Cess, R.D. Advances in Heat. Transfer 1, 1964. 1-50.
19. Principles of Human Physiology. 11th Edition by C.L. Evans (1952). Churchill Ltd.

20. Saunders, O.A. Proc. Roy. Soc. (London). A172: 55-71. (1939).

21. Herrington, L. A.S.M.E. Jnl. Heat Trans. August 1969.

22. Schlieren Methods: Holder, D.W. and North, R.J. (1963). H.M.S.O. Notes on Applied Science No. 31.

23. Tanney, J. Nat. Res. Council of Canada. Rep. 9587. 1967.

24. Tritton, D.J. J. Fluid Mech. 16 pt. 2. 1963.

25. Dryden, H.L. and Kuethe, A.M. NACA TR. No. 320. 1928.

26. King, L.V. (1914). Phil. Trans. Roy. Soc. A, 214.

27. Facts from Figures. Moroney, M.J. Penguin Books.

28. Davies, R.R. and Noble, W.C. The Lancet, December 22, 1962. p.1295.

29. Lidwell, O.M., Noble, W.C. and Dolphin, G.W. J. Hyg., Camb. (1959) 57, p.299.

30. Rothman, S. in Physiology and Biochemistry of the Skin (1954). p. 586. Chicago.

31. Marples, M. Br. J. Derm. 1969. 81, Supplement 1, 2.

32. Marples, M. Scientific American 220, 108 (1969).

33. Ingold, C.T. in Spore Liberation (1965). Clarendon Press, Oxford.

34. Heldman, D.R., Sunga, F.E.C.A., Hendrick, T.I. Contamination Control, August 1967, p.28.

35. Jeffrey, G. Proc. Roy. Soc. 1922. pp. 161-179.

36. Goldsmith, H.L. and Mason, S.G. (1962). J. Colloid Sci. 17. pp. 448-476.

37. Owen, P.R. in Circulatory and Respiratory Mass Transport (1960). London: Churchill.

39. The Mechanics of Aerosols (1964). Fuchs, N.A. Pergamon Press.

40. Eichhorn, R. and Small, S. J. Fluid Mech. 20 (3), 513 (1964).

41. Saffman, P.G. (1965). J. Fluid Mech. 22, 385 (Corrigendum 31, 3).

42. Industrial Dust. Drinker, P. and Hatch, T. (1954). McGraw-Hill.

43. Imai, I. (1954). Roc. Roy. Soc. A. 224, p.141.

44. Gans, Richard. Sonderdruck aus SitzunsBerichte der bayerischen Akademie der Wissenschaften, pp. 191-203. Wie fallen Stäbe und Scheiben in einer reibenden Flüssigkeit. München, 1911.

45. Kilb, A. Forsch. Ing. Wesen. 58, 6, 89 (1934).

46. Lyashchenko, P. Gostoptekhizdat Moscow (1940). p.40.

47. Soo, S.L. Fluid Dynamics of Multiphase Systems (1967). Blaisdell Publishing Company.

48. Davies, C.N. Proc. Inst. Mech. Engrs. (1952). IB. 185-213.

49. Clark, R.P., Cox, R.N. and Lewis, H.E. (1970). J. Physiol, 208, 43-45P.

50. Modern Developments in Fluid Dynamics. Vols. 1 and 2. Ed. S. Goldstein. Clarendon Press. 1950.

51. Bagnold, A. The Physics of Blown Sand and Desert Dunes. London 1941.

52. Corn, M. and Stein, F. in Surface Contamination. Ed. B. R. Fish (1967). Pergamon Press, Oxford.

53. Jordon, D. Brit. J. Appl. Phys. Suppl., No. 3. 194 (1954).

54. Lees, Julienne and Brighton, W.D. J. Hyg., Camb. (1972). 70, 557.

55. Gregory, P.H. Nature, 180, p. 330. Aug. 17, 1957.

56. Owen, P.R. J. Fluid Mech. (1969) 39, pt. 2, pp. 407-432.

57. Alexander, L.and Coldren, C. Ind. Eng. Chem., 43, 1325 (1951).

58. Goldschmidt, V.W. (1965). J. Colloid Sci. 20, 617-634.

59. Clark, R.P., Cox, R.N., Lewis, H.E. (1971). J. Physiol, 214, 3-4P.

60. Clark, R.P., Cox, R.N., Lewis, H.E. (1971). J. Physiol, 216, 19-20P.

61. Charnley, J. and Eftekhar, N. The Lancet, January 25 (1969), p. 172.

62. Bethune, D.W., Blowers, R., Parker, M., Pask, E.A. The Lancet, February 27, 1965, p. 480.

63. Bernard, H.R., Speers, R., O'Grady, F. and Shooter, R.A. The Lancet, September 4, 1965, p.458.

64. Blowers, R. and McClusky, M. The Lancet, October 2, 1965, p.681.

65. Jennison, M.W. in Aerobiology (1942). Ed. F. R. Moulton. American Association for the Advancement of Science. No. 17. Washington.

66. Shooter, R.A., Smith, M.A. and Hunter, C.J.W. Brit. J. Surg. 47, 1959.

67. Phyiology in Health and Disease, Wiggers, C.J. Pub. Henry Kimpton, London 1949.

68. Burton, A.C. and Froese, G. Defence Research Board, Canada (1957) E.P. Technical Report No. 6.

69. Burton, A.C. 6th Commonwealth Defence Conference on Clothing and General Stores, Australia (1959).

70. Low Reynolds number Hydrodynamics. Happel, J. and Brenner, H. Prentice-Hall.

71. In Surface and Colloid Science, Vol. 2. Ed. E. Majijevic. J. Wiley, 1969.

72. Altshuler, B. in Circulatory and Respiratory Mass Transport. CIBA (1969).

73. Schroter, R.C. and Sudlow, M.F. Resp. Physiol. (1969). 7, 341-355.

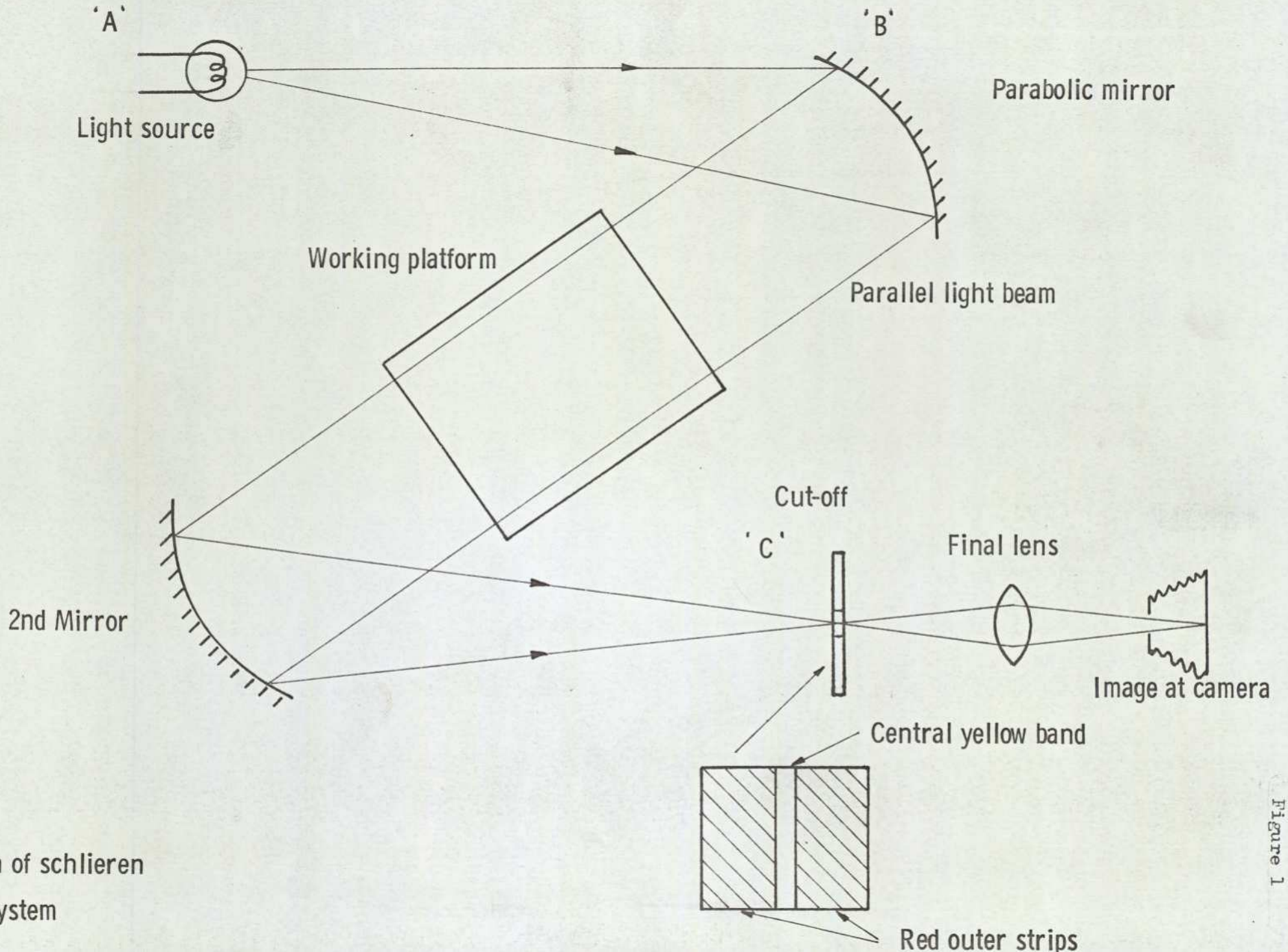
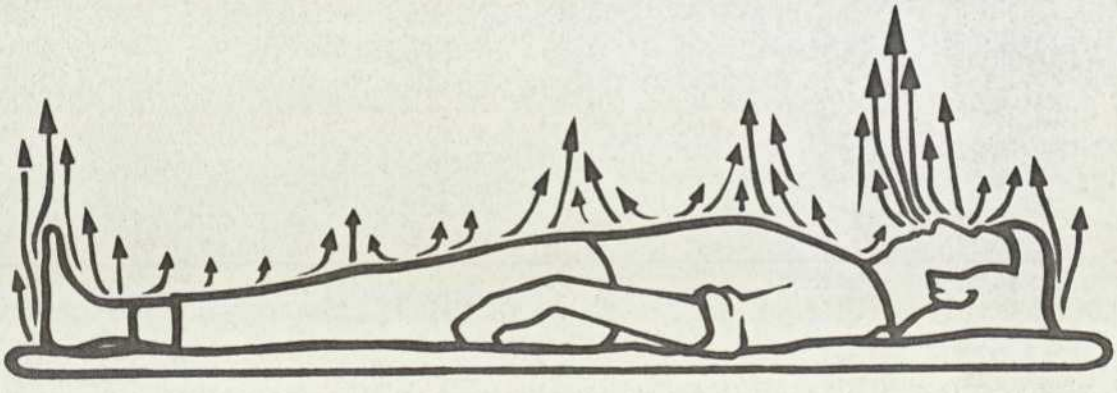
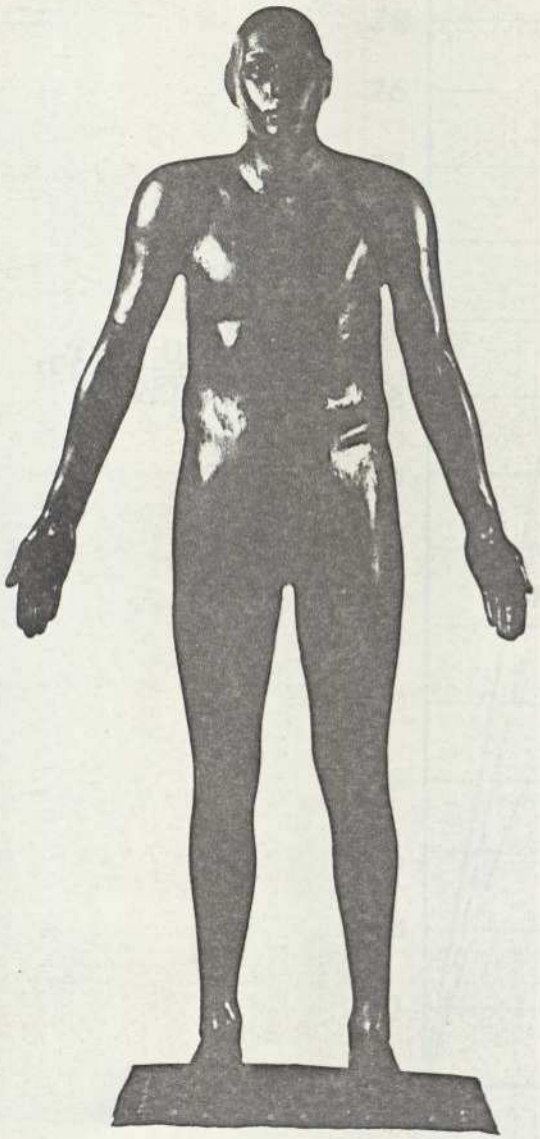


Diagram of schlieren optical system

Figure 1







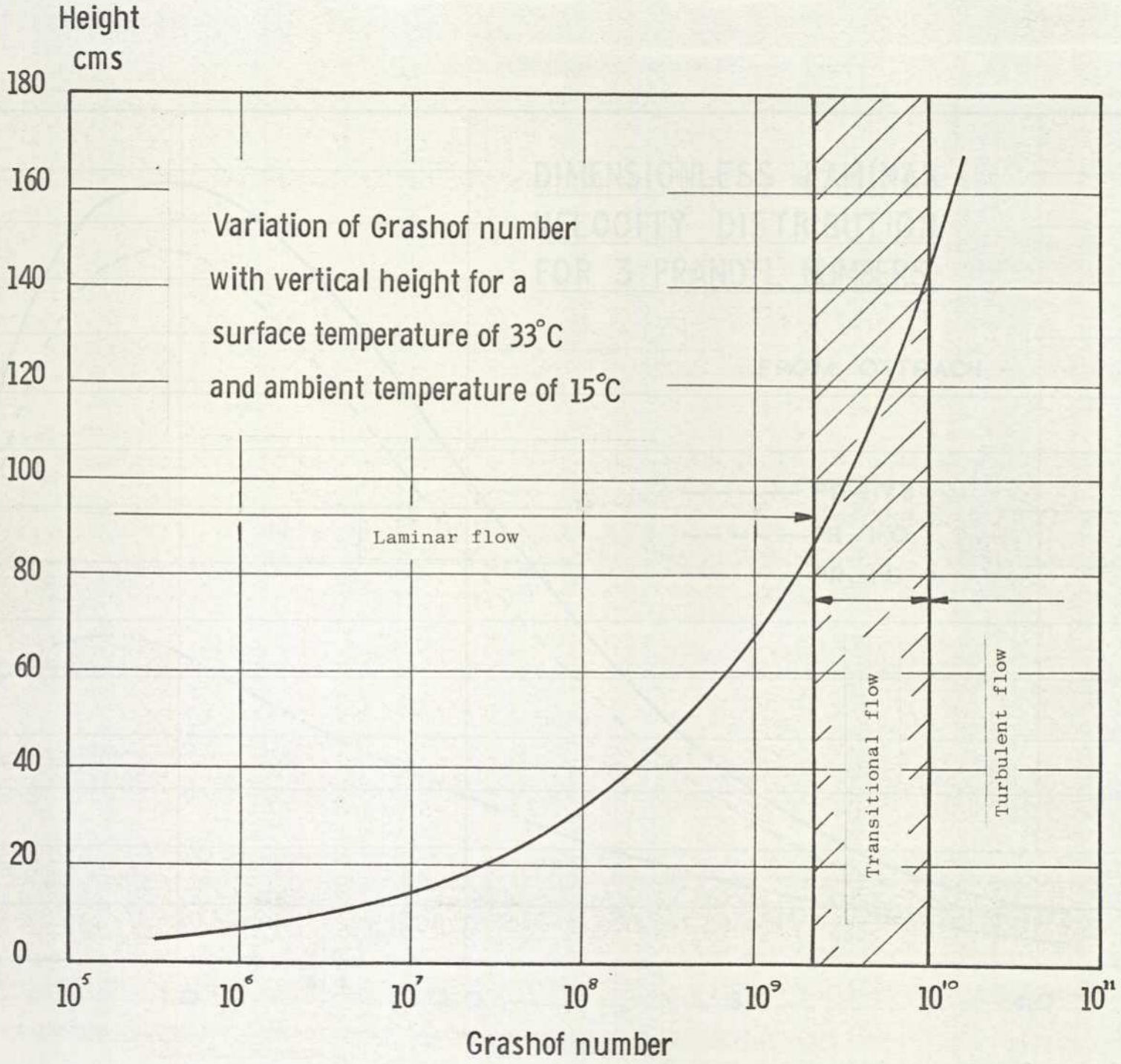
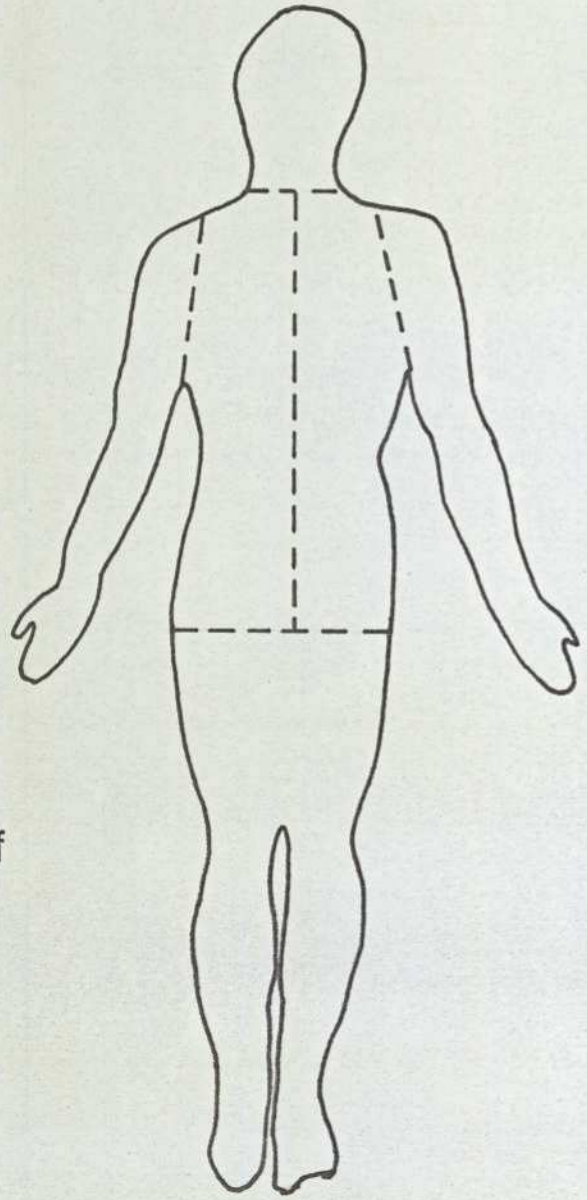

Height
cms
180
160
140
120
100
80
60
40
20
0
Variation of Grashof number
with vertical height for a
surface temperature of 33°C
and ambient temperature of 15°C
Laminar flow
Transitional flow
Turbulent flow
10^5
10^6
10^7
10^8
10^9
10^{10}
10^{11}
Grashof number

Figure 4

Division of human body for heat transfer analysis



Total surface area of cylinders 1.89 M²

c = circumference of cylinder

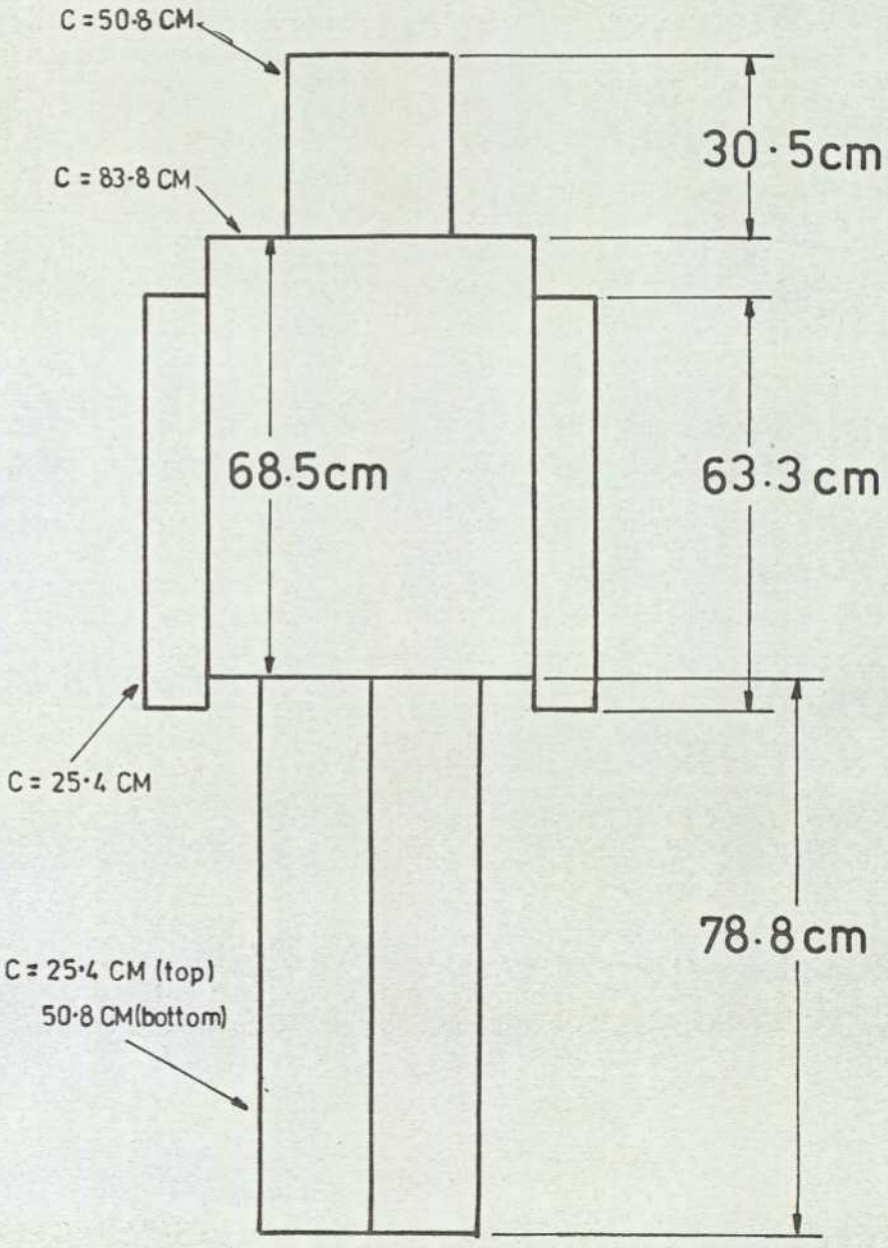
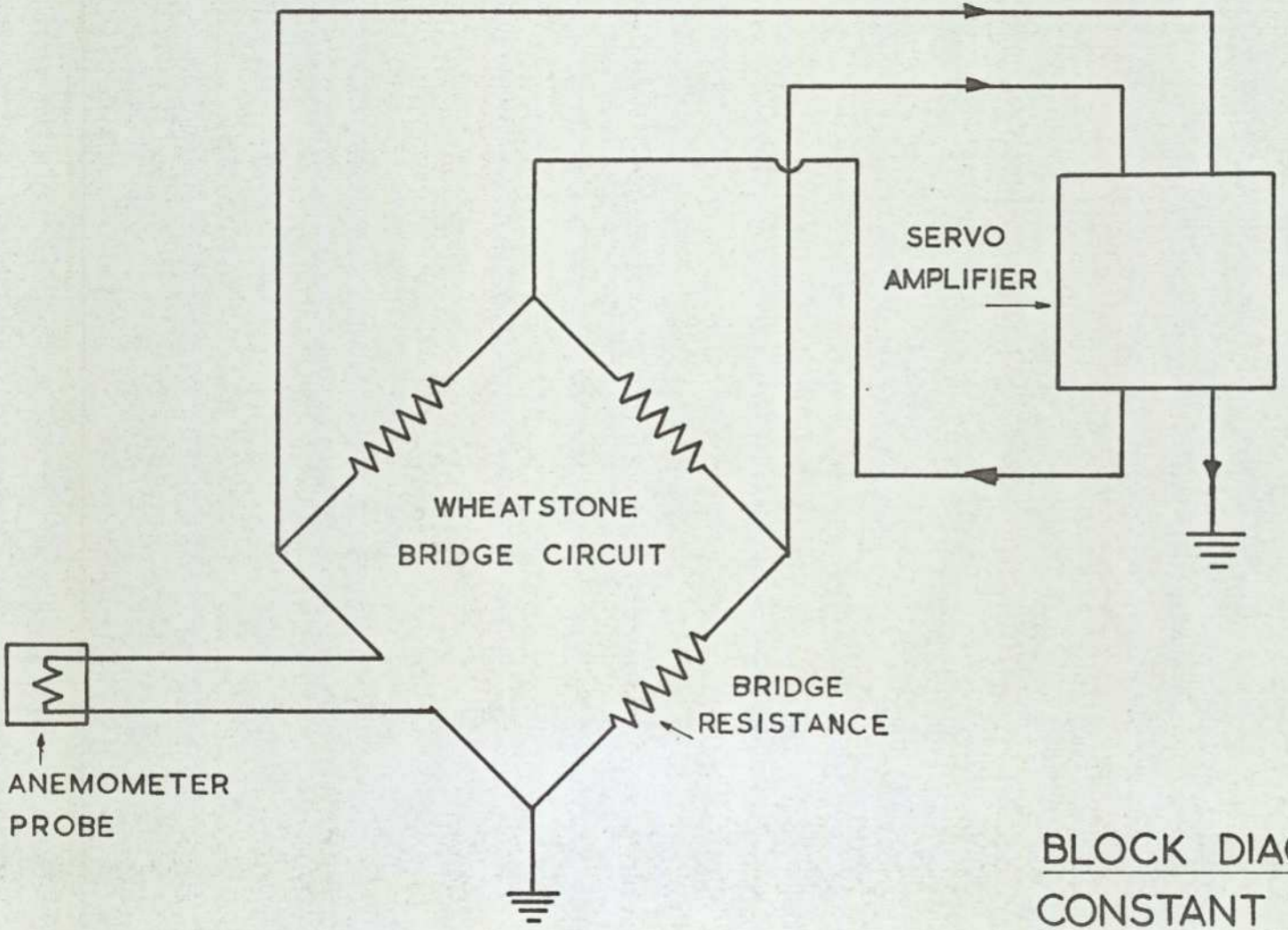


Figure 8

Figure 9

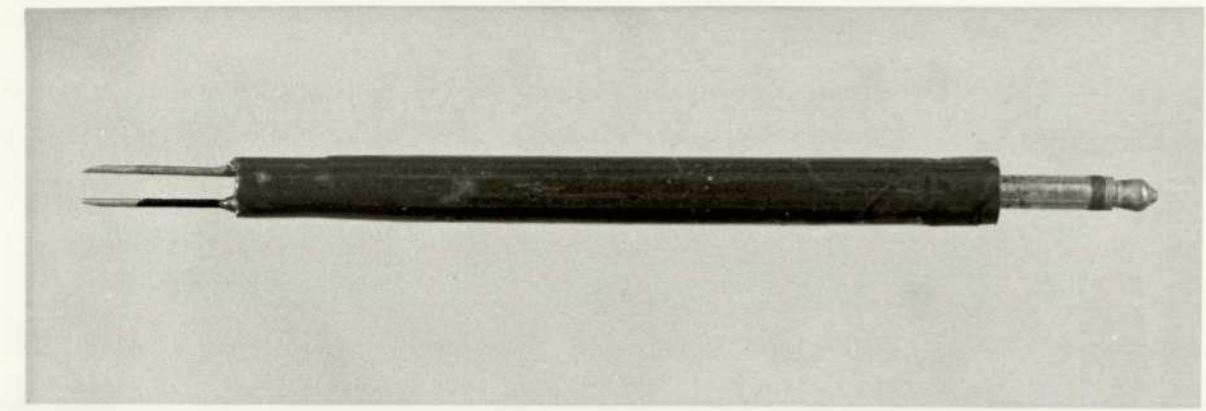


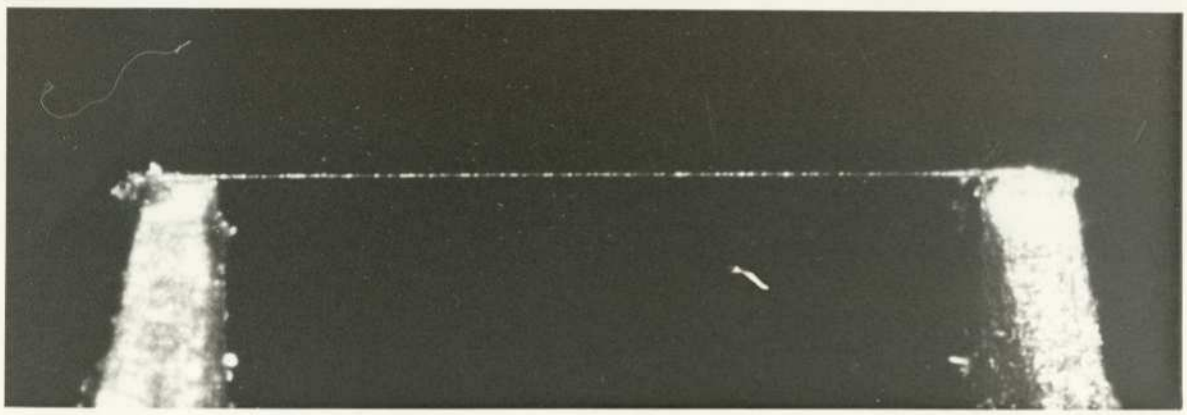


BLOCK DIAGRAM OF
CONSTANT TEMPERATURE
HOT WIRE ANEMOMETER

Figure 10

Figure 11





Hot wire probe
and mould

Figure 12

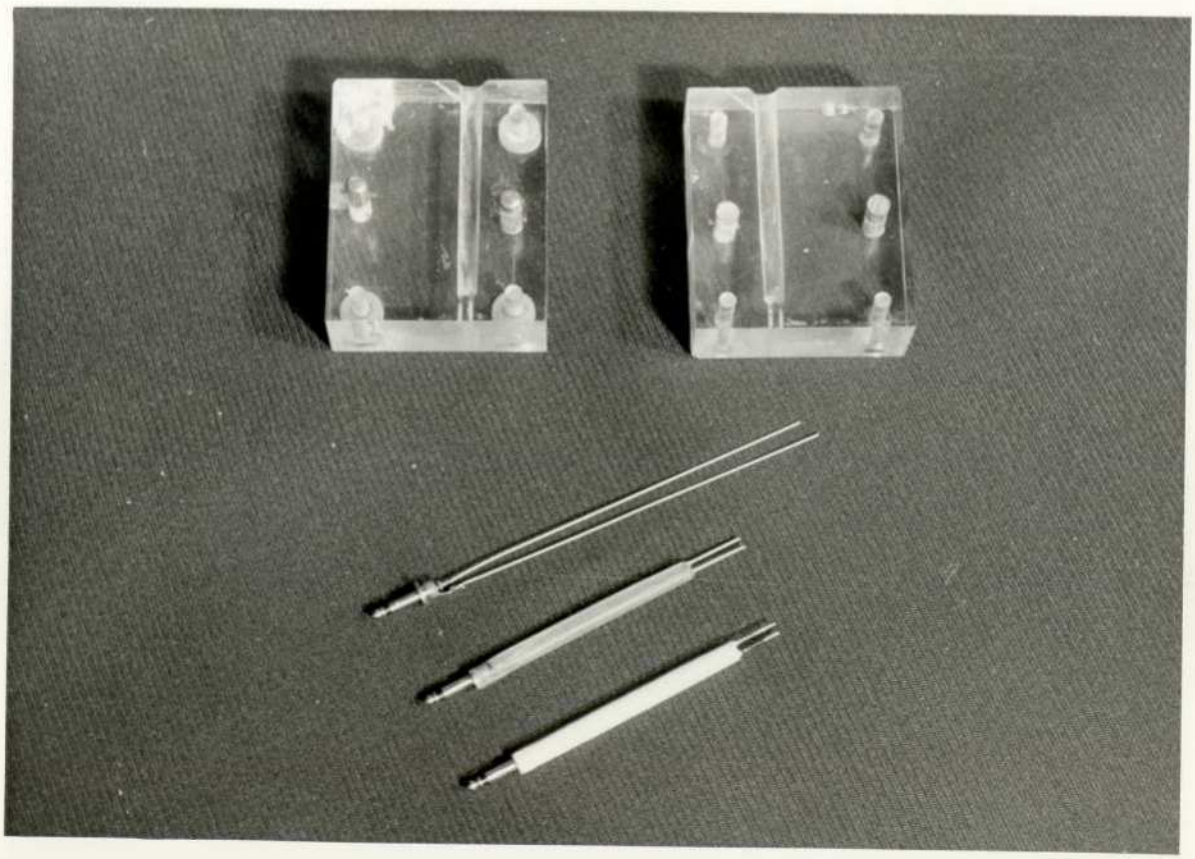
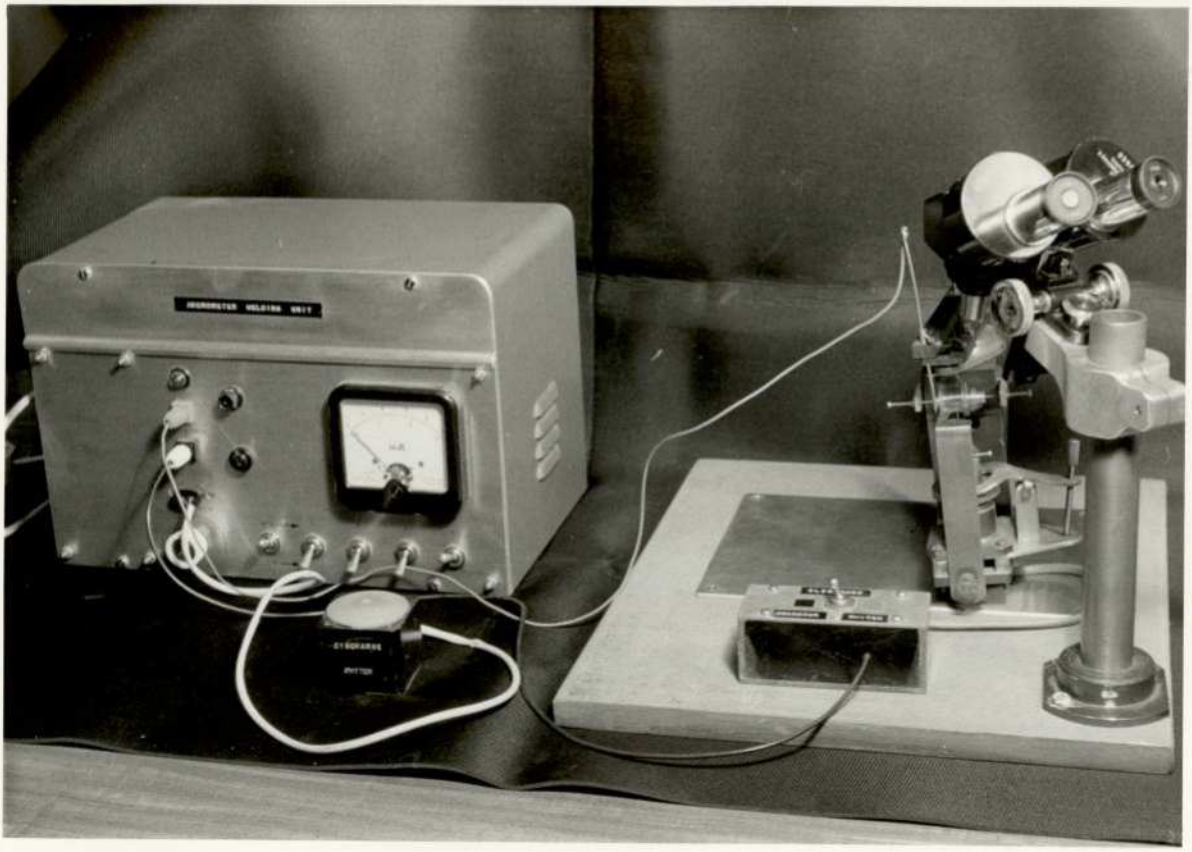
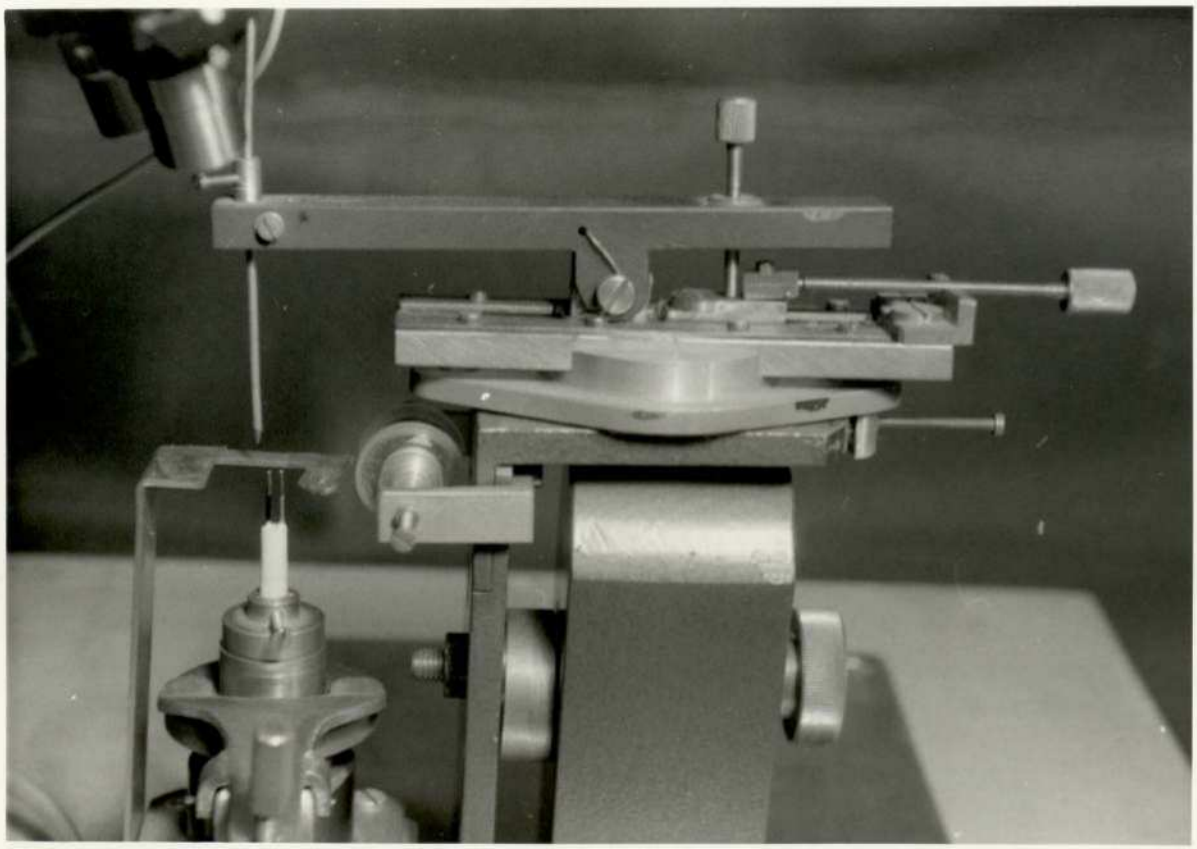
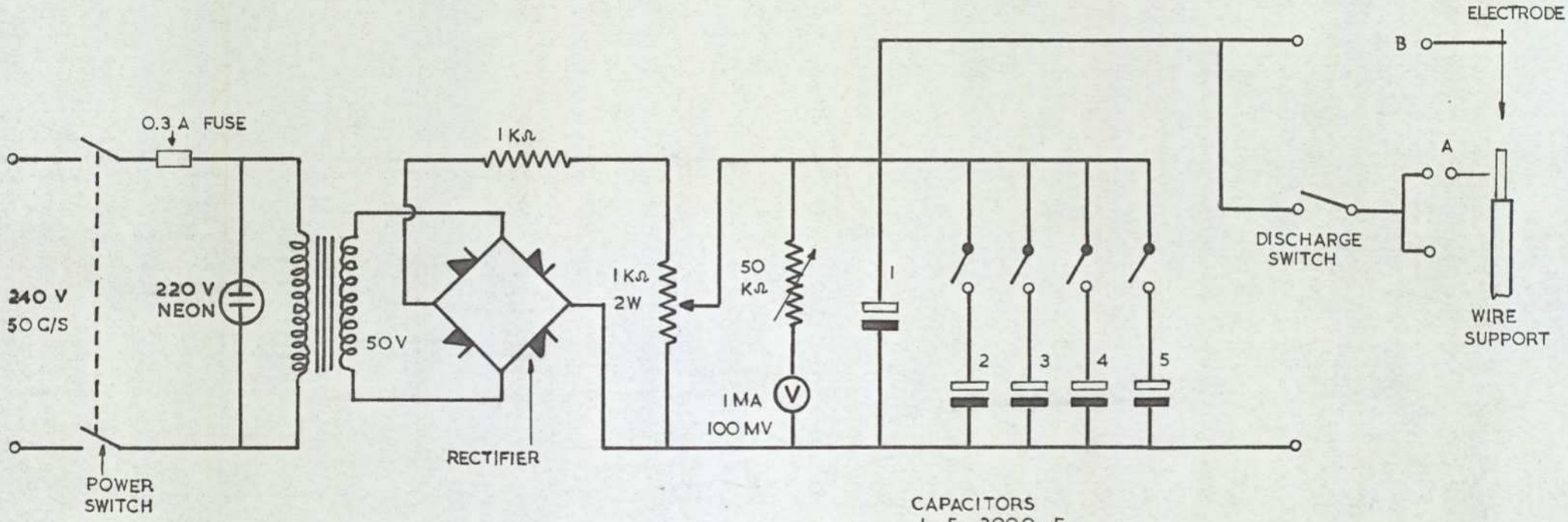


Figure 13



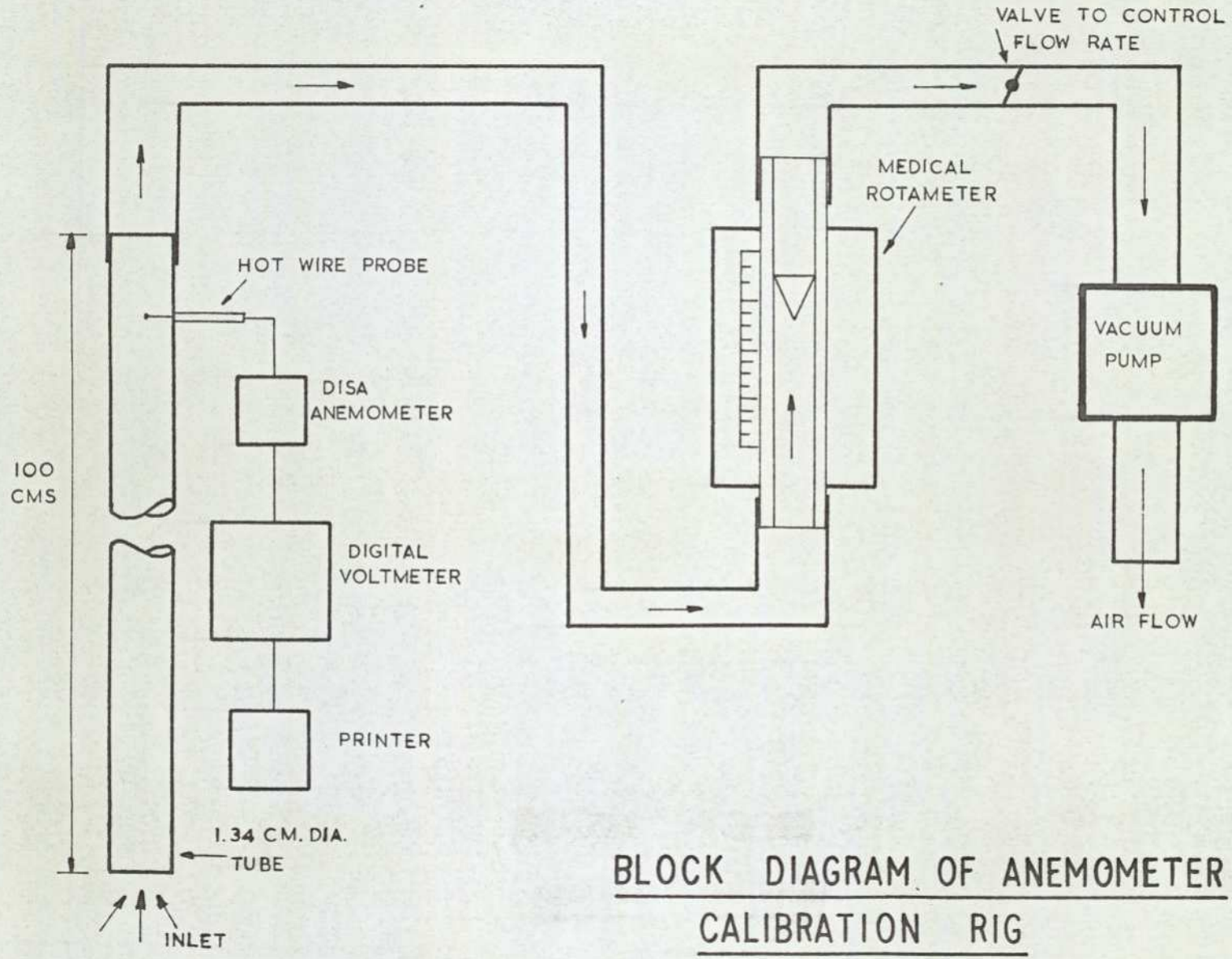
Micromanipulator
and
Welding Unit





CIRCUIT DIAGRAM OF ANEMOMETER WELDING UNIT

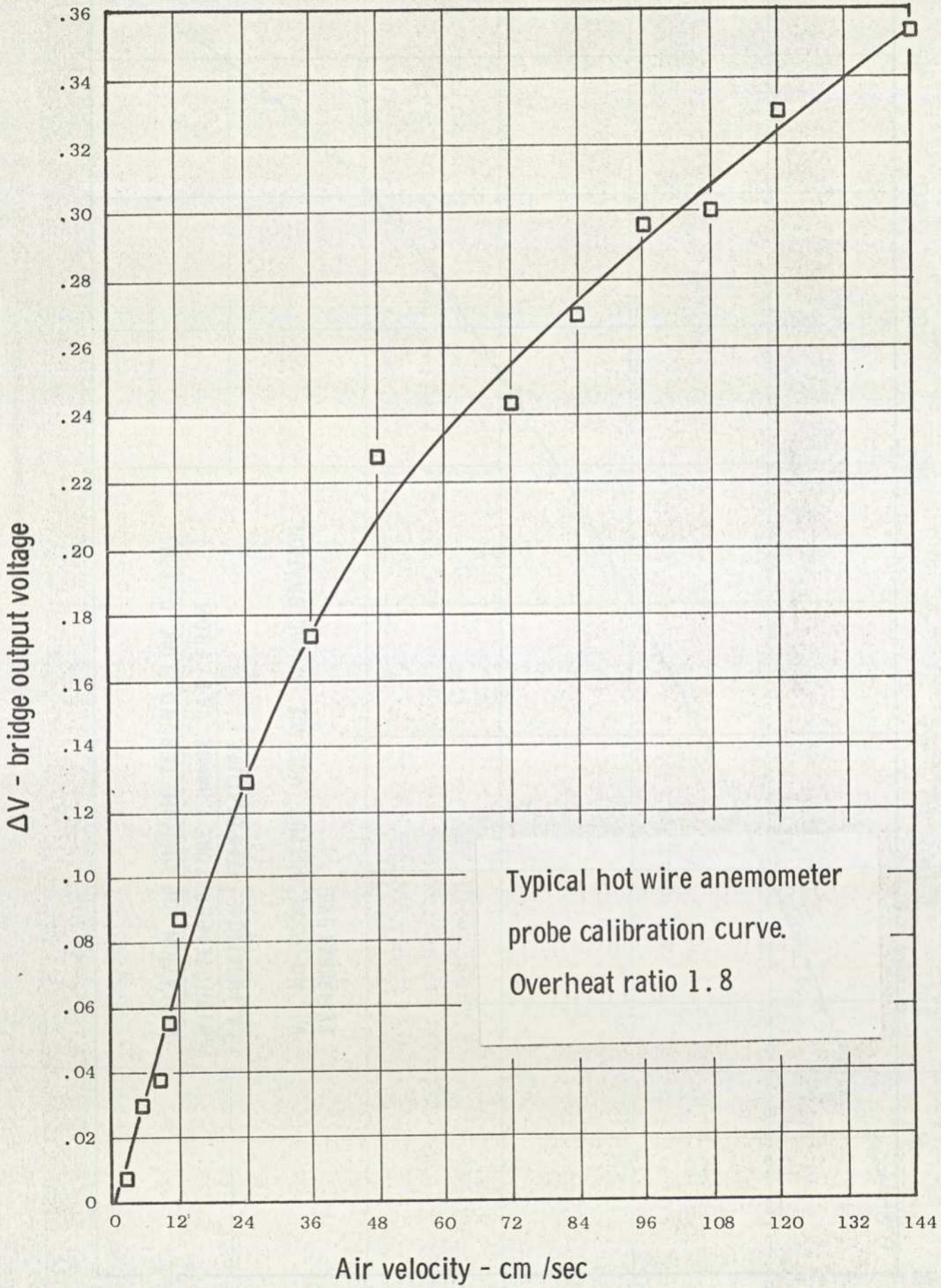
Figure 14



BLOCK DIAGRAM OF ANEMOMETER
CALIBRATION RIG

Figure 15

Figure 16


.36
.34
.32
.30
.28
.26
.24
.22
.20
.18
.16
.14
.12
.10
.08
.06
.04
.02
0
ΔV - bridge output voltage
0
12
24
36
48
60
72
84
96
108
120
132
144
Air velocity - cm /sec
Typical hot wire anemometer
probe calibration curve.
Overheat ratio 1.8

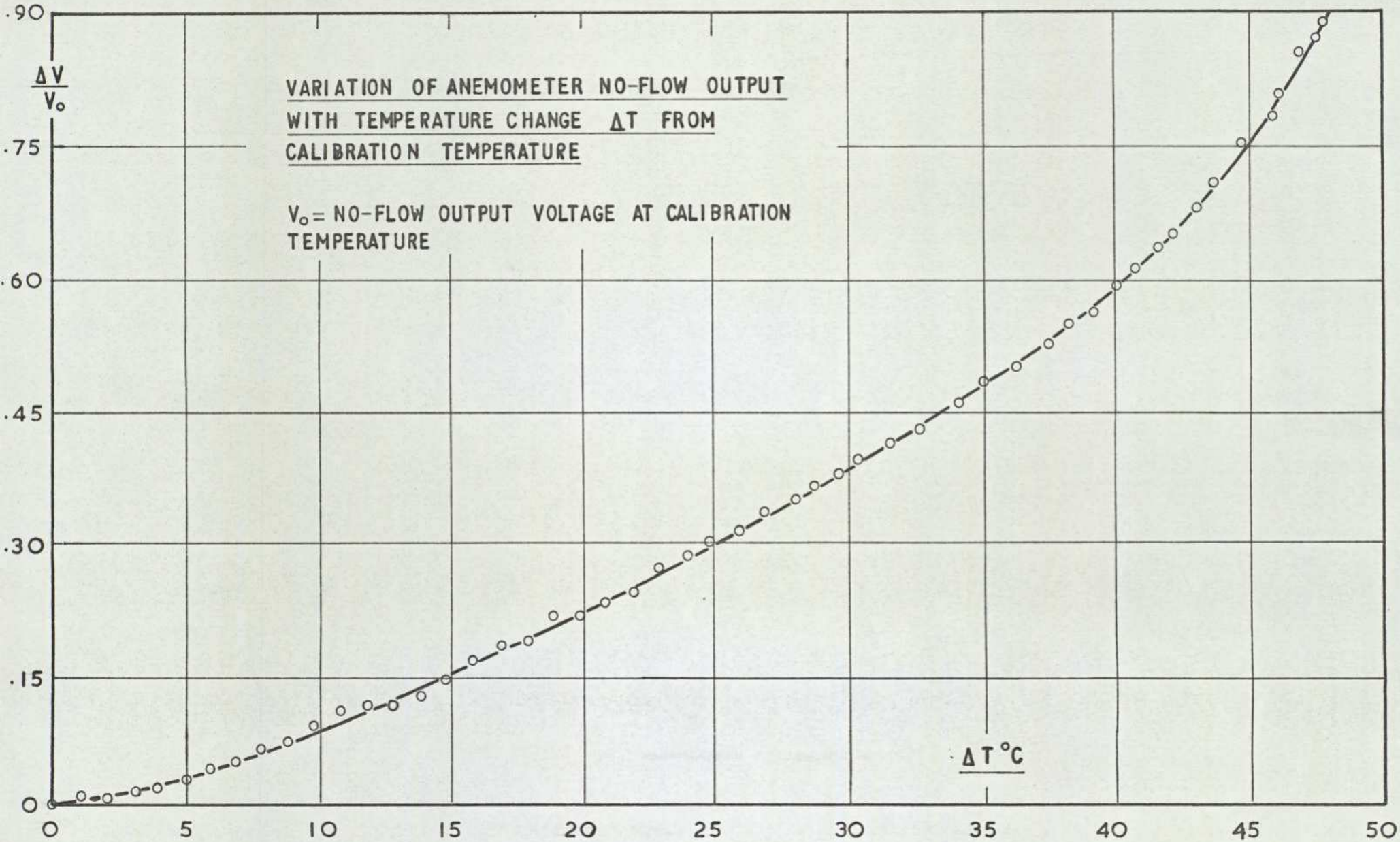
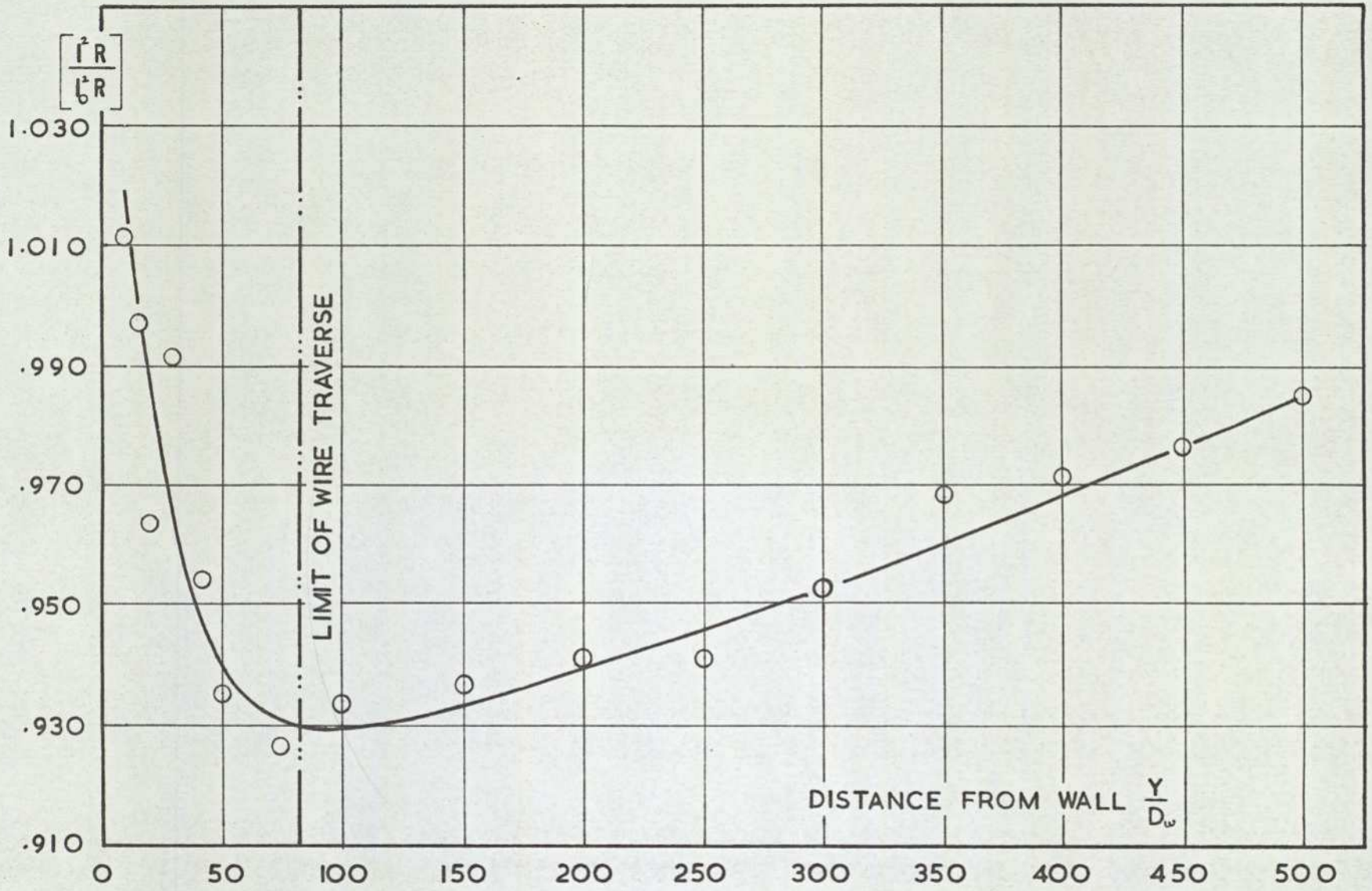

VARIATION OF ANEMOMETER NO-FLOW OUTPUT WITH TEMPERATURE CHANGE ΔT FROM CALIBRATION TEMPERATURE
V_o = NO-FLOW OUTPUT VOLTAGE AT CALIBRATION TEMPERATURE
$\frac{\Delta V}{V_o}$
.90
.75
.60
.45
.30
.15
0
0
5
10
15
20
25
30
35
40
45
50
ΔT °C

Figure 17

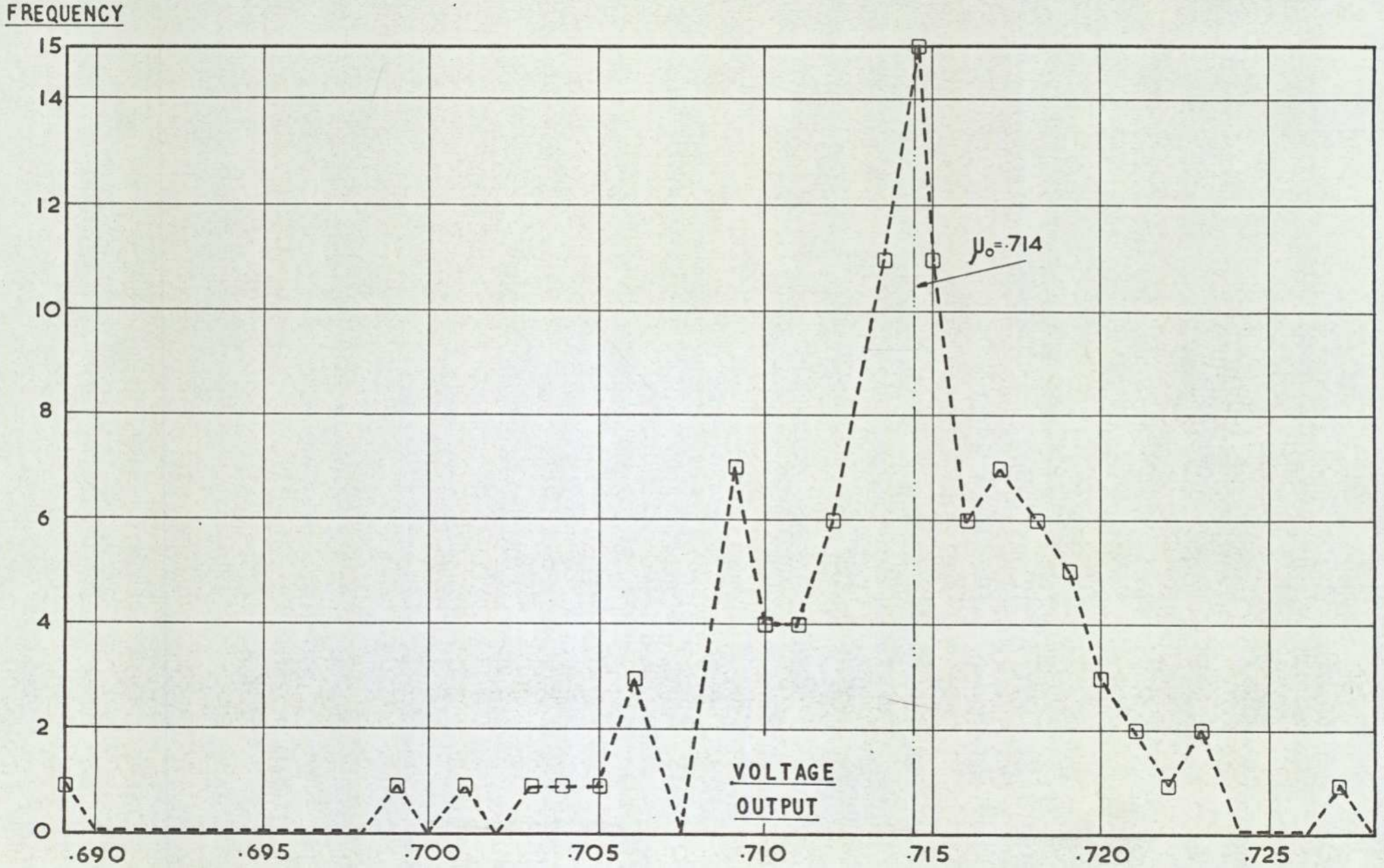


VARIATION OF WIRE HEAT LOSS WITH DISTANCE FROM HEATED WALL

I_o^2R BASED ON NO-FLOW VOLTAGE AT AMBIENT TEMPERATURE

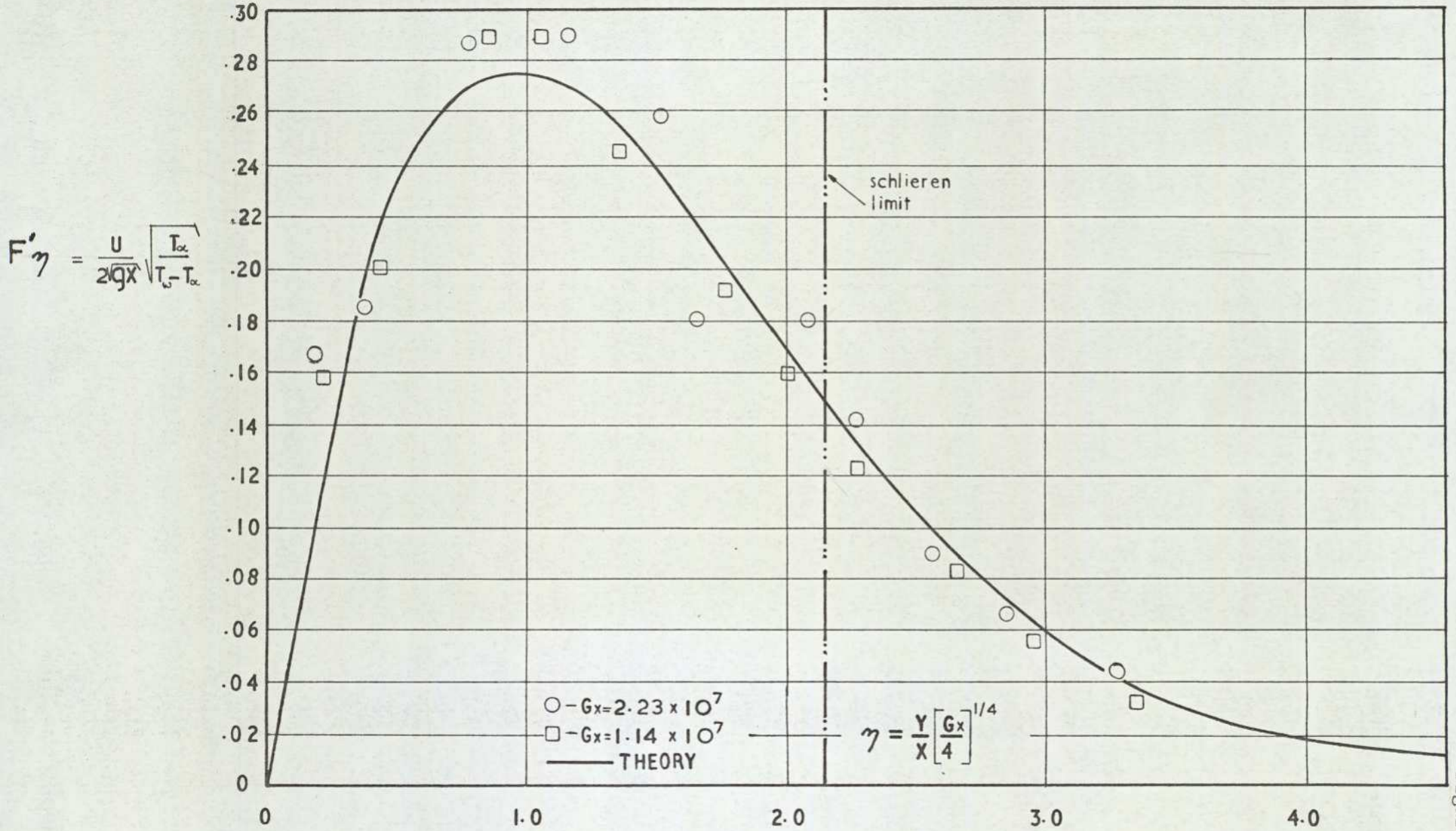
WIRE DIAMETER $D_3 = 5\mu$

Figure 18



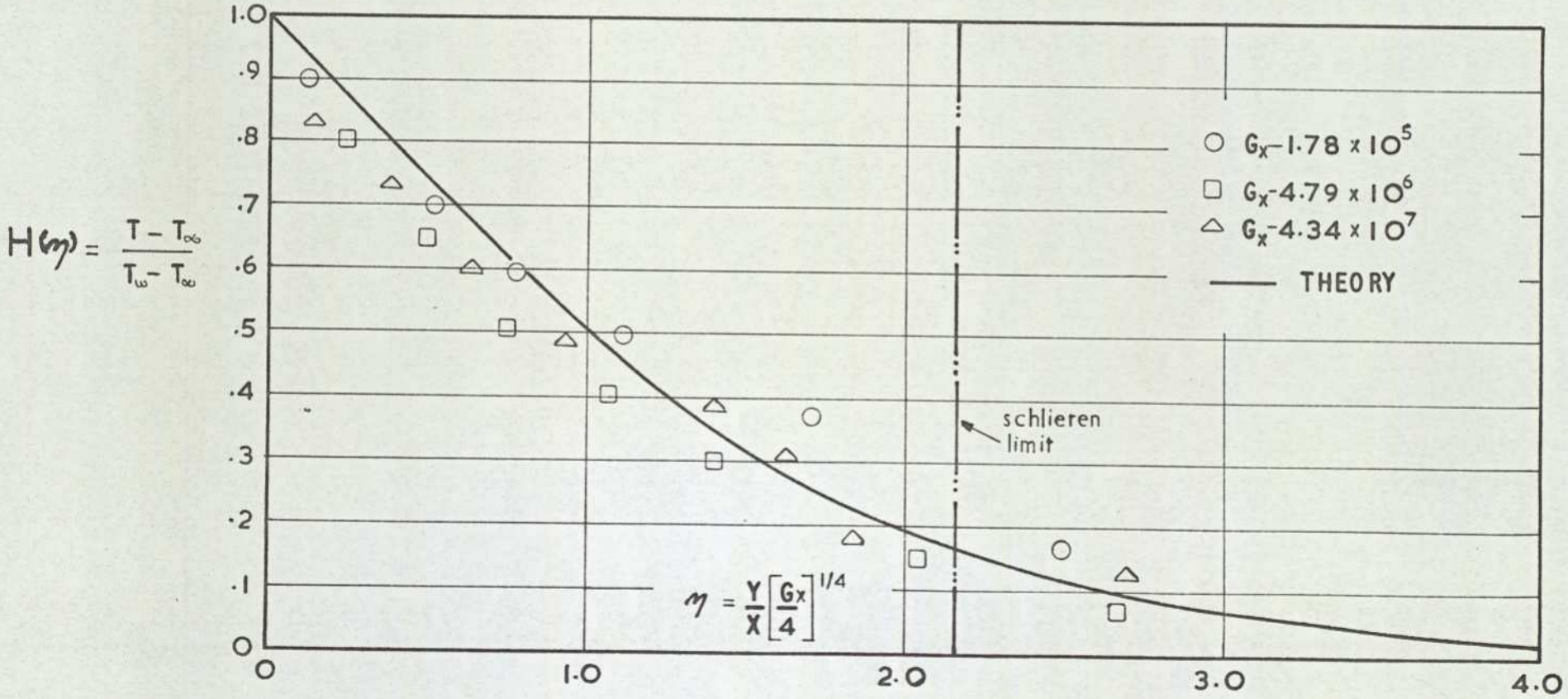
FREQUENCY DISTRIBUTION FOR 100 READINGS OF ANEMOMETER OUTPUT VOLTAGE TAKEN AT 2 SECOND INTERVALS TO ESTIMATE μ_o

Figure 19



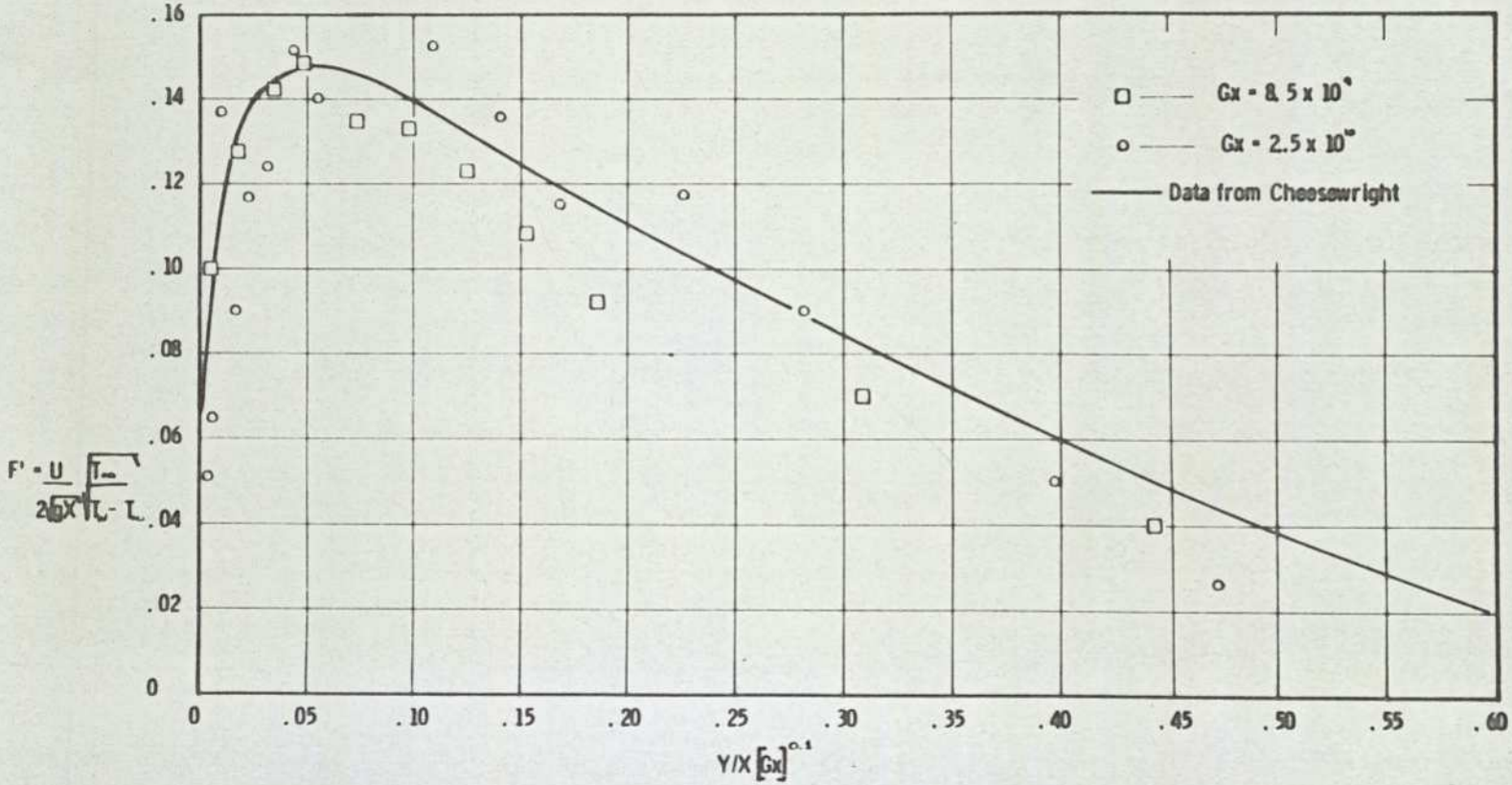
EXPERIMENTAL VELOCITY DISTRIBUTION IN NATURAL CONVECTION BOUNDARY LAYER

Figure 20



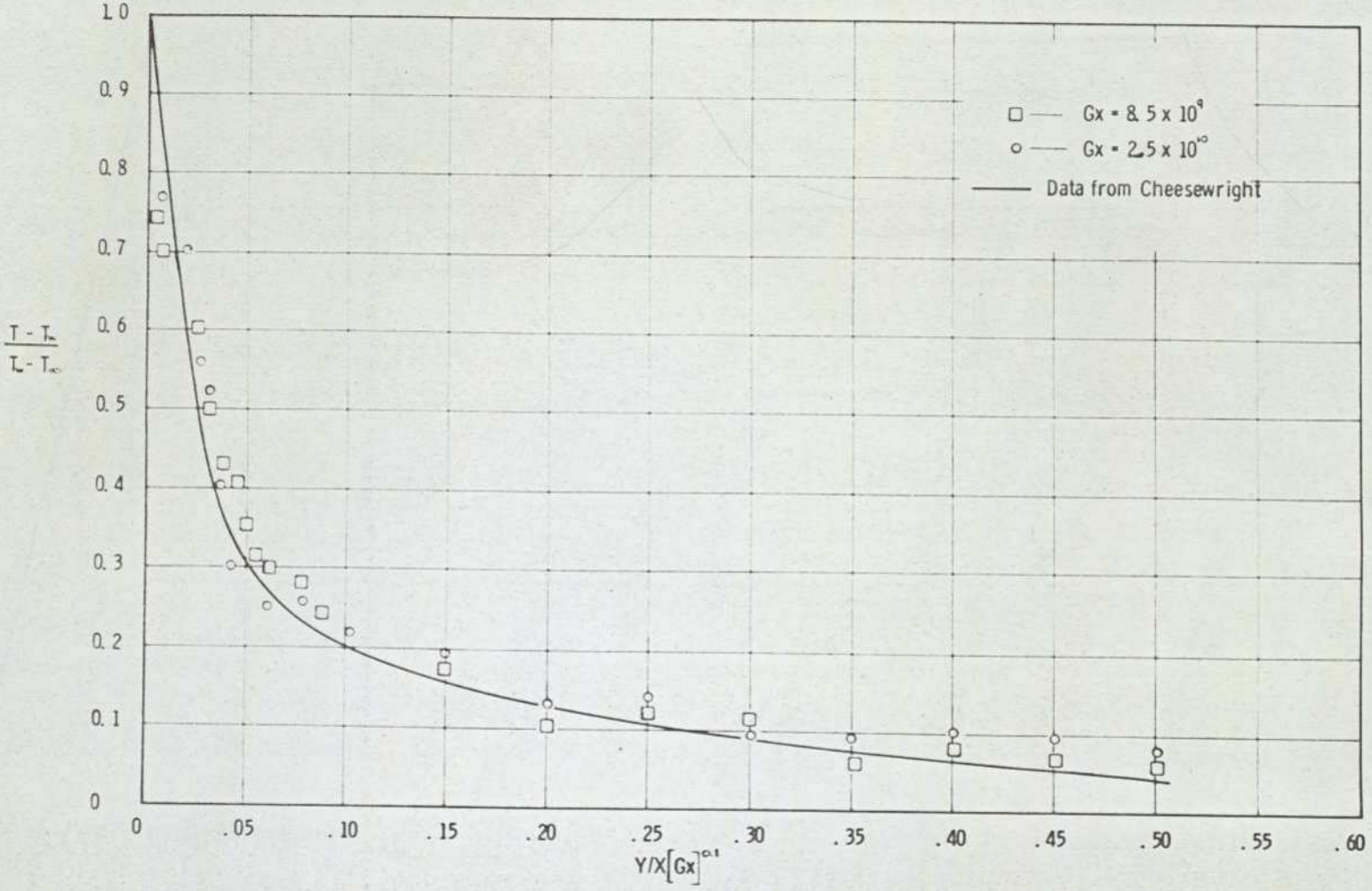
EXPERIMENTAL TEMPERATURE DISTRIBUTION IN THE NATURAL CONVECTION BOUNDARY LAYER

Figure 21



Experimental velocity distribution in turbulent flow

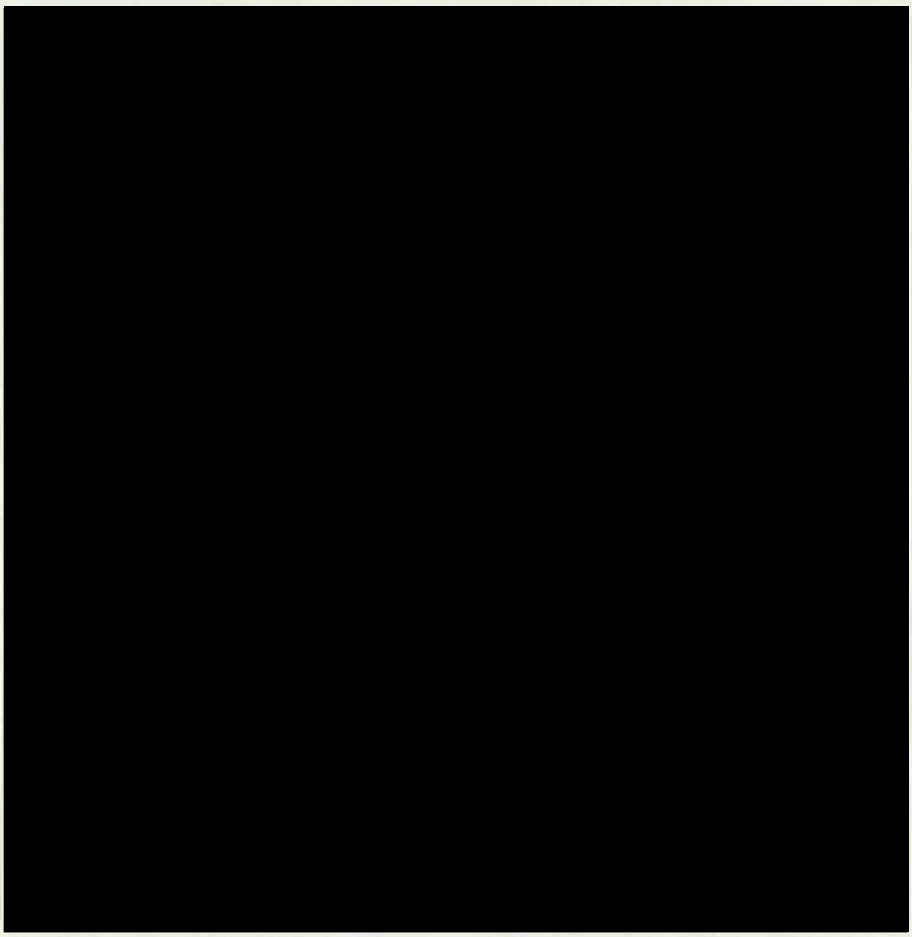
Figure 22



Experimental temperature distribution in turbulent flow

Figure 23

Figure 24



Stereoscan picture of skin fibres in tension

Figure 25



Skin scales on body surface that are nearly detached

Particle diameter vs terminal fall velocity for several particle densities

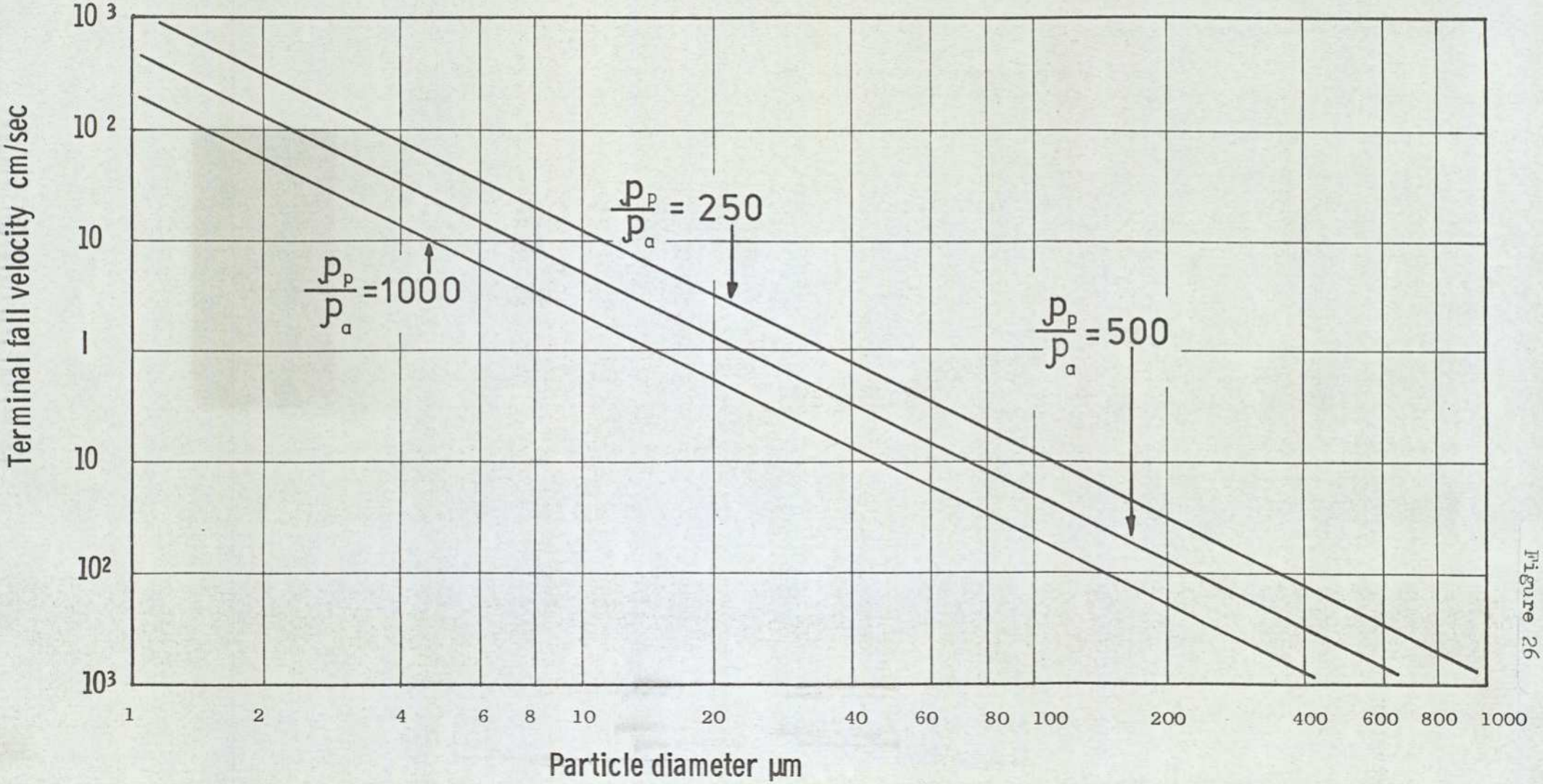
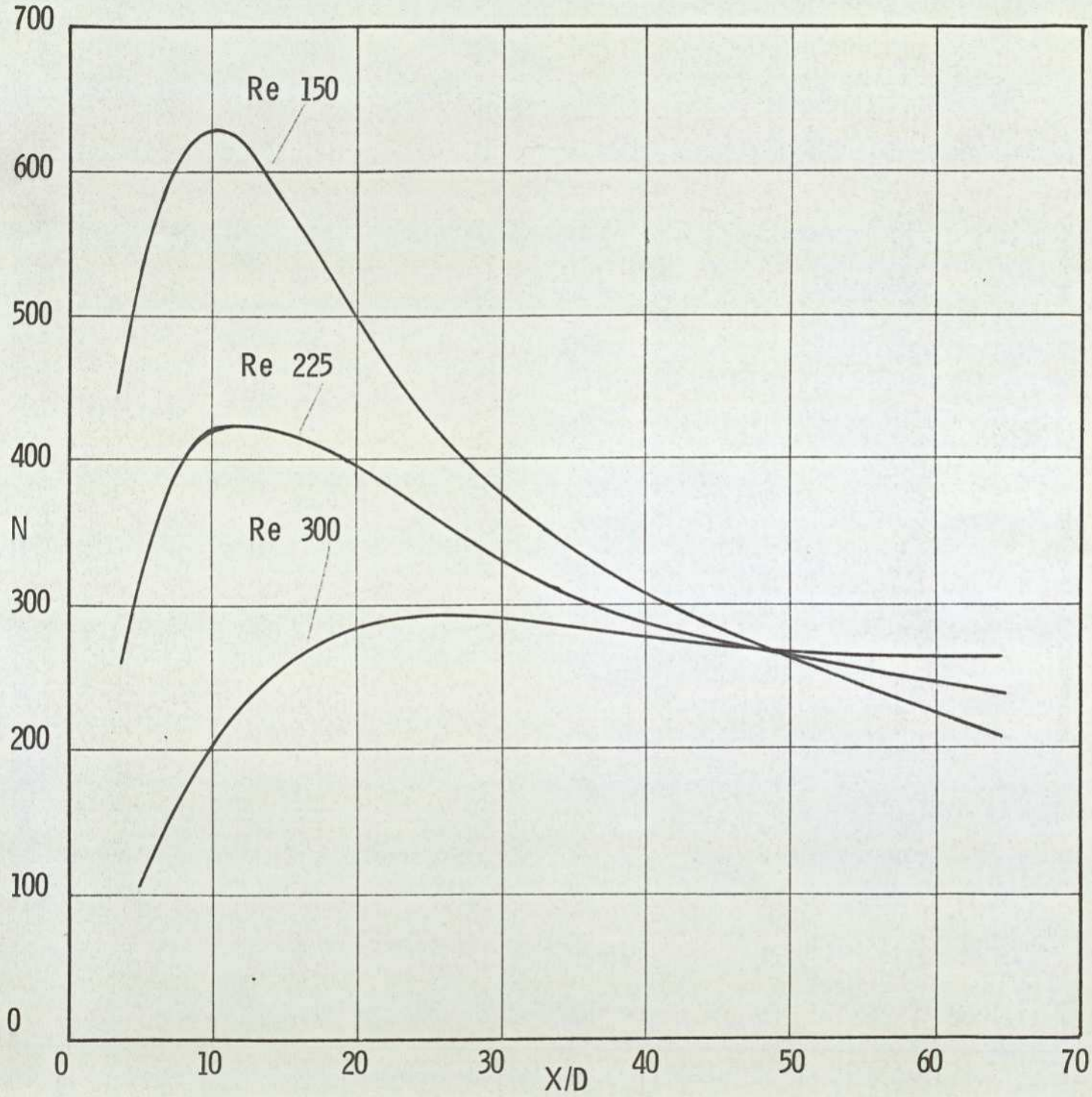
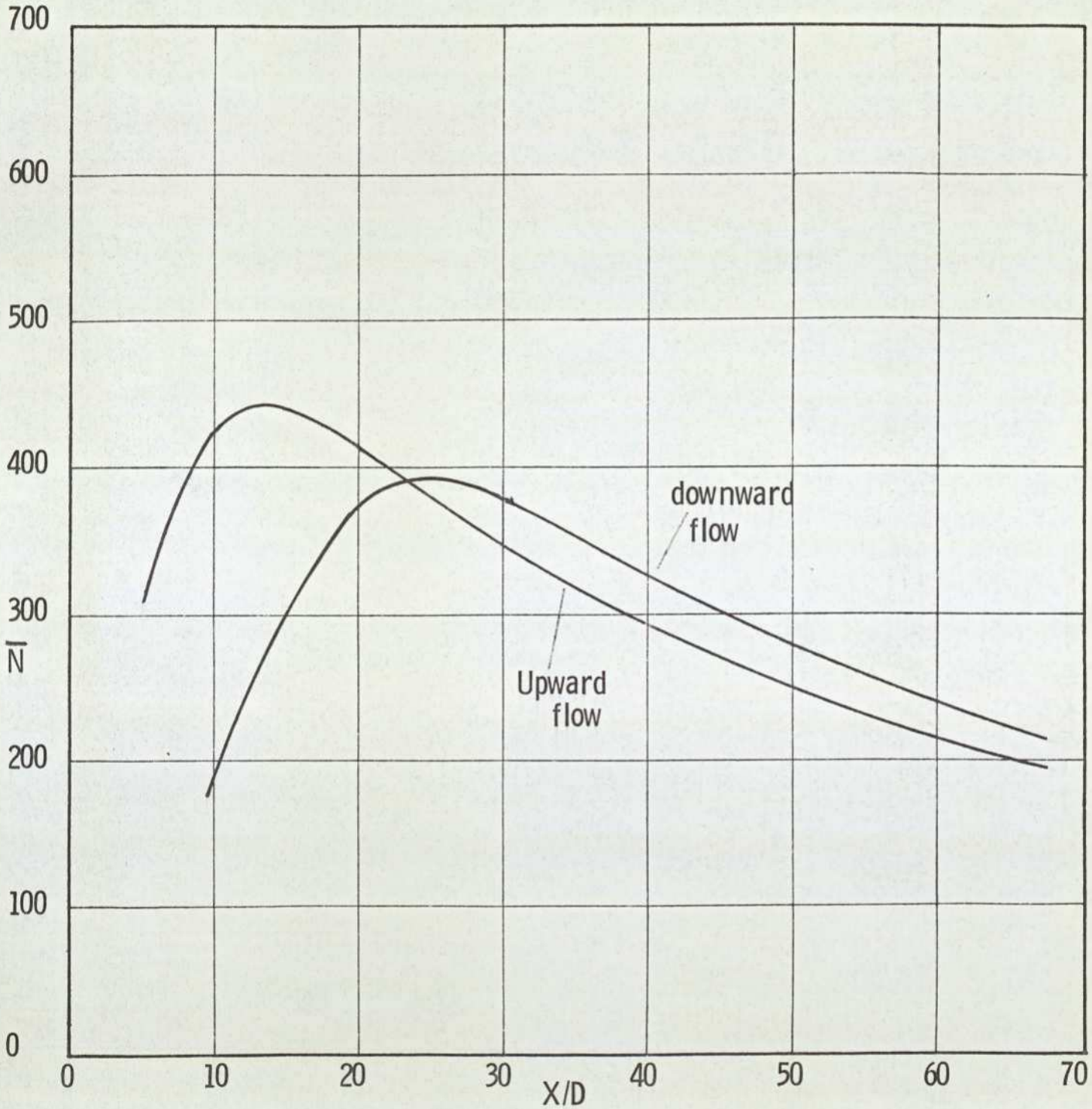


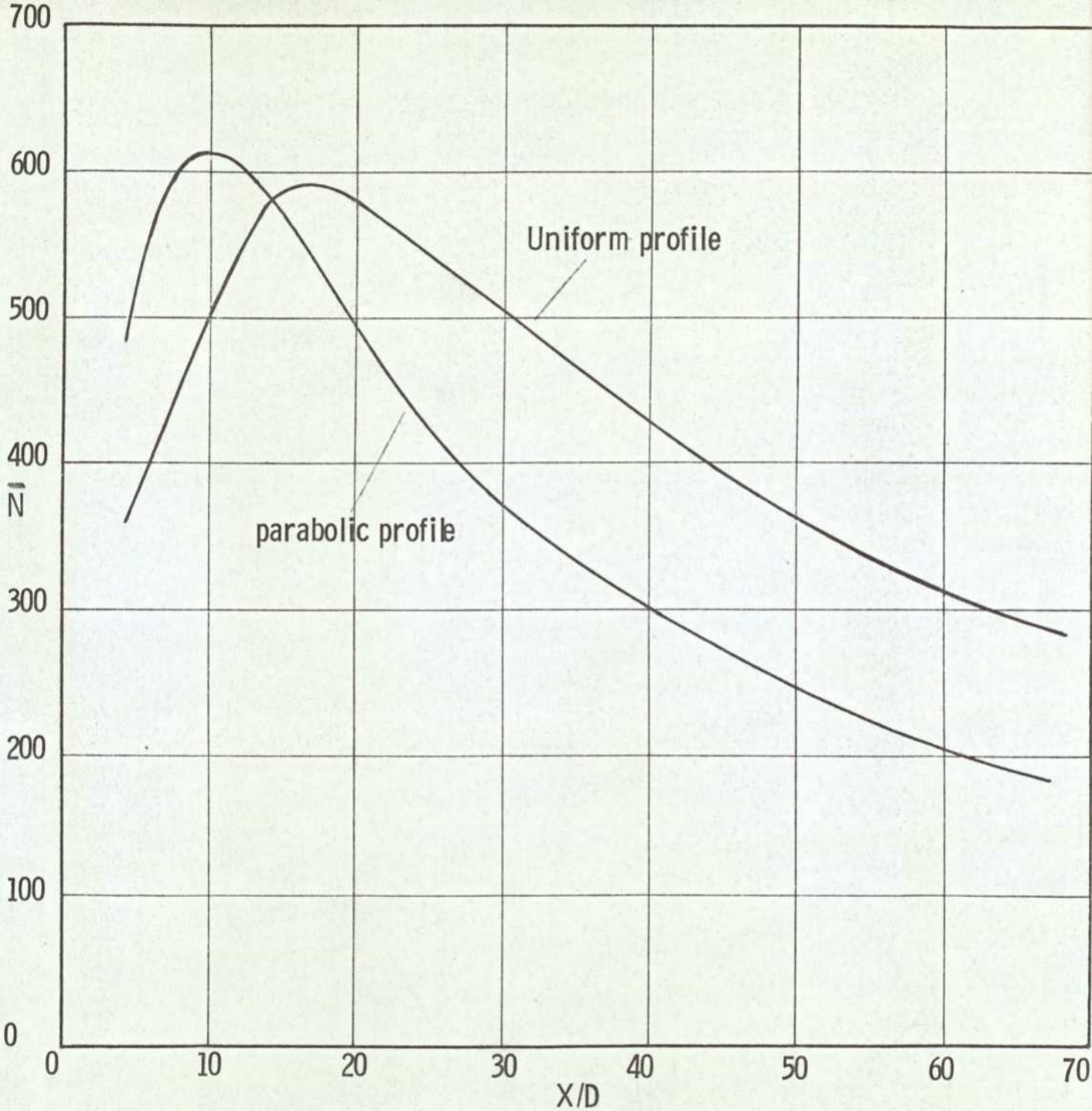
Figure 26



Particle deposition by aerodynamic lift force. Effect of channel Re.
Parabolic velocity profile.

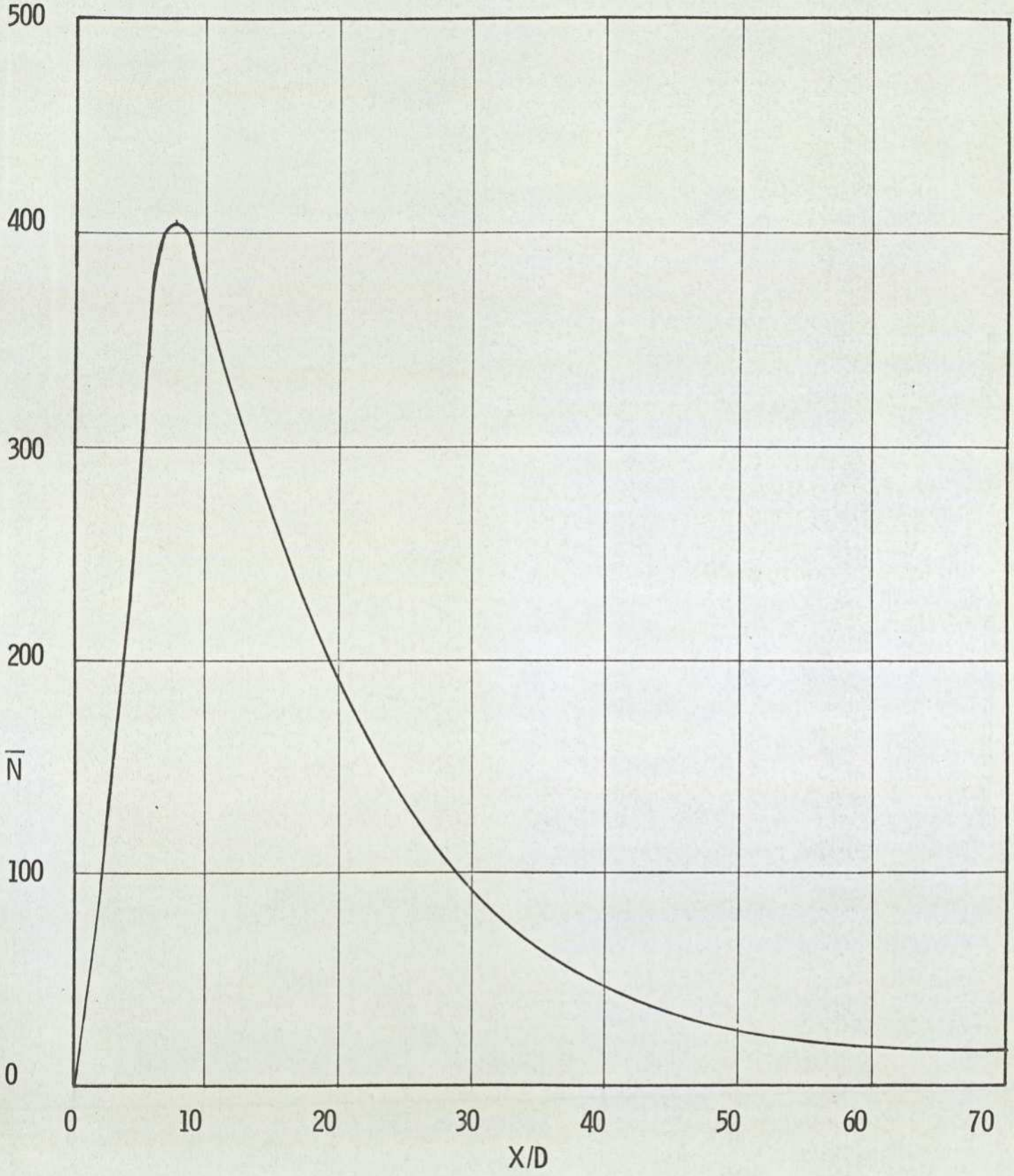


Particle deposition by aerodynamic lift force. Effect of main flow direction. Parabolic velocity profile. Channel Re = 225

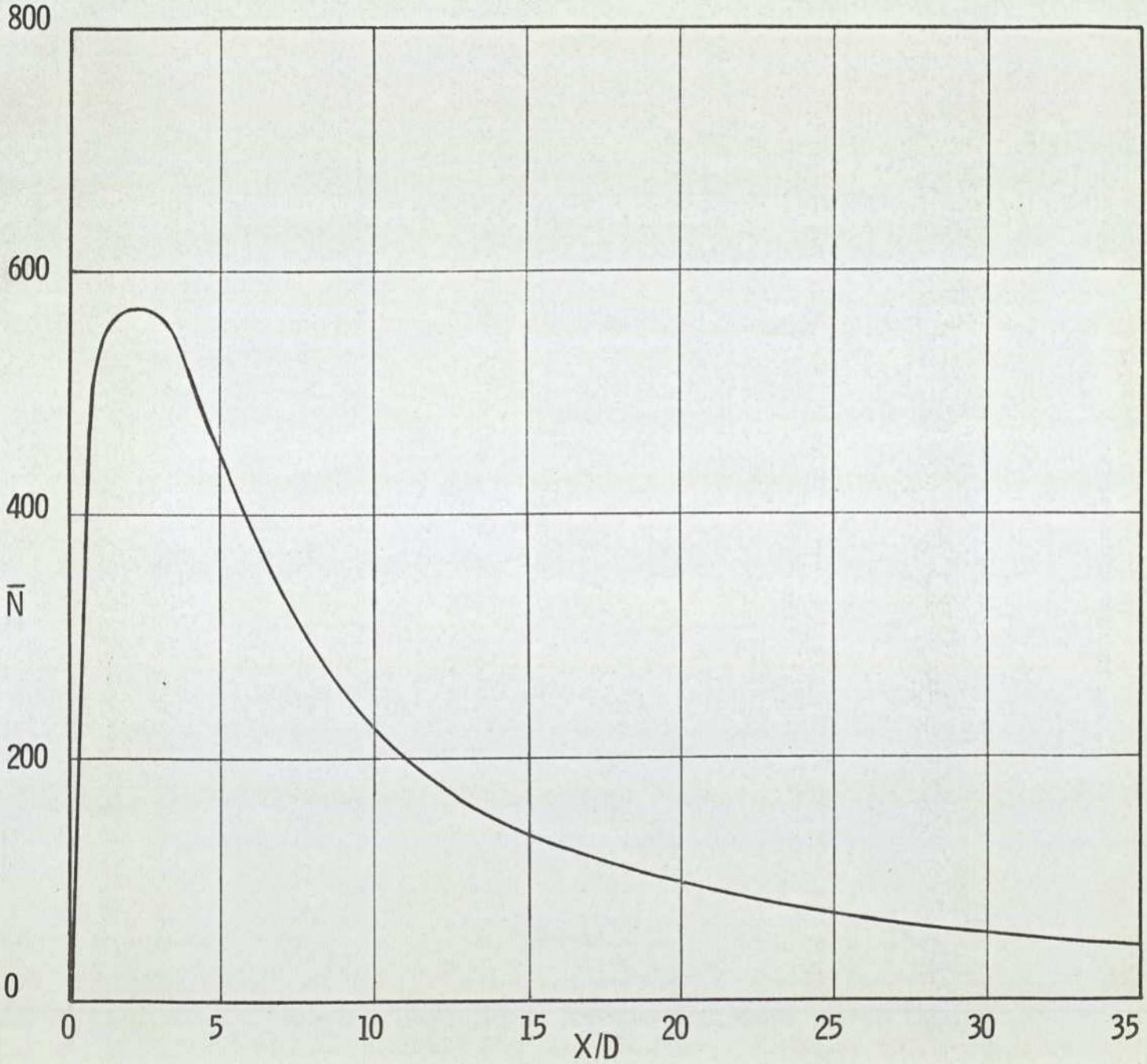


Particle deposition by aerodynamic lift force. Effect of channel velocity profile. Channel Re=150

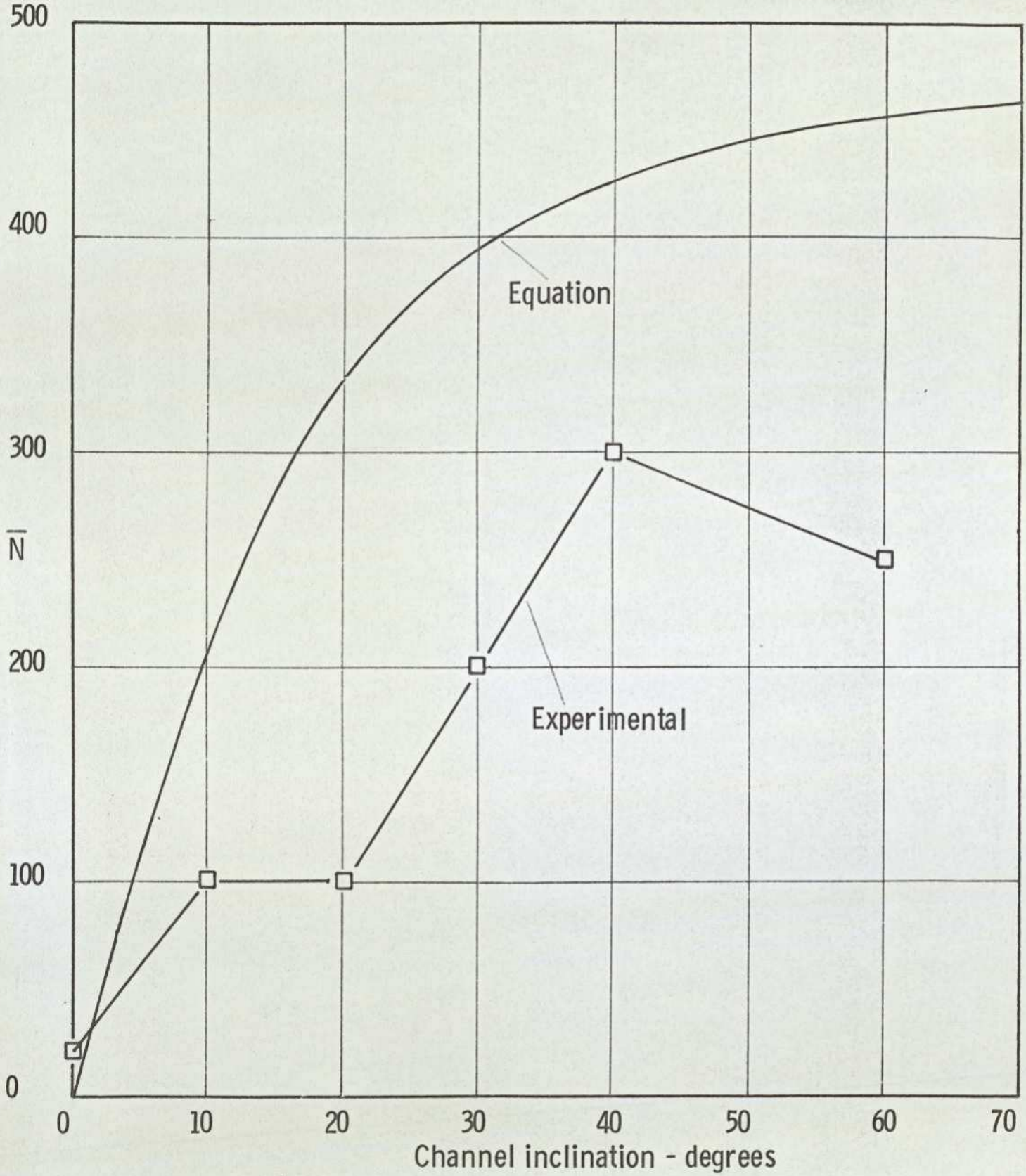
Figure 30



Deposition due to electrostatic field given by Ue = Ke d for vertical laminar channel flow where Ke = 400 Channel Re = 200

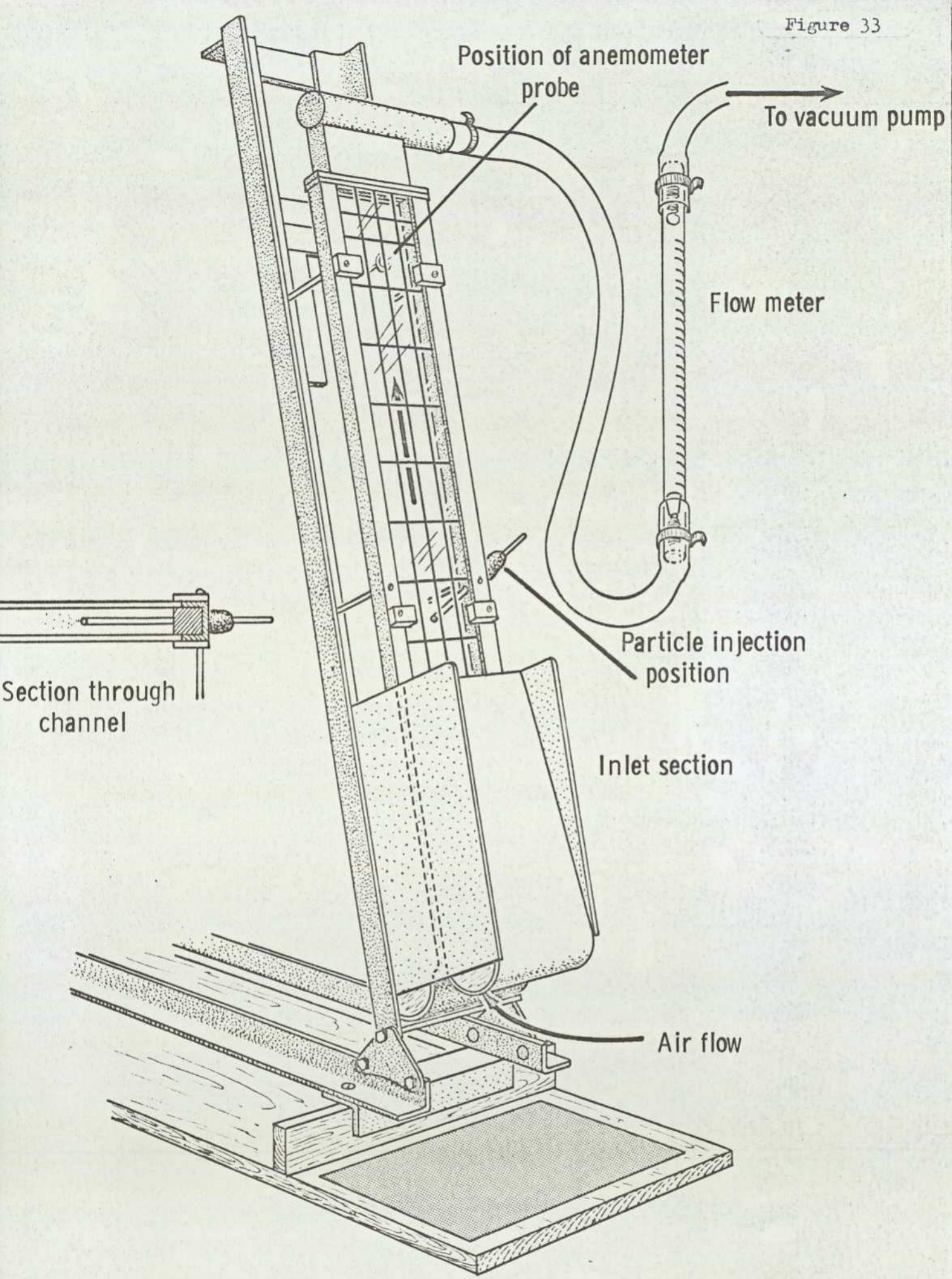


Floor deposition in horizontal channel under gravity alone. Re_{d^2} 105. Number distribution of injected particles given by $N = 6000\, e^{-0.0229 d^2}$ from equation

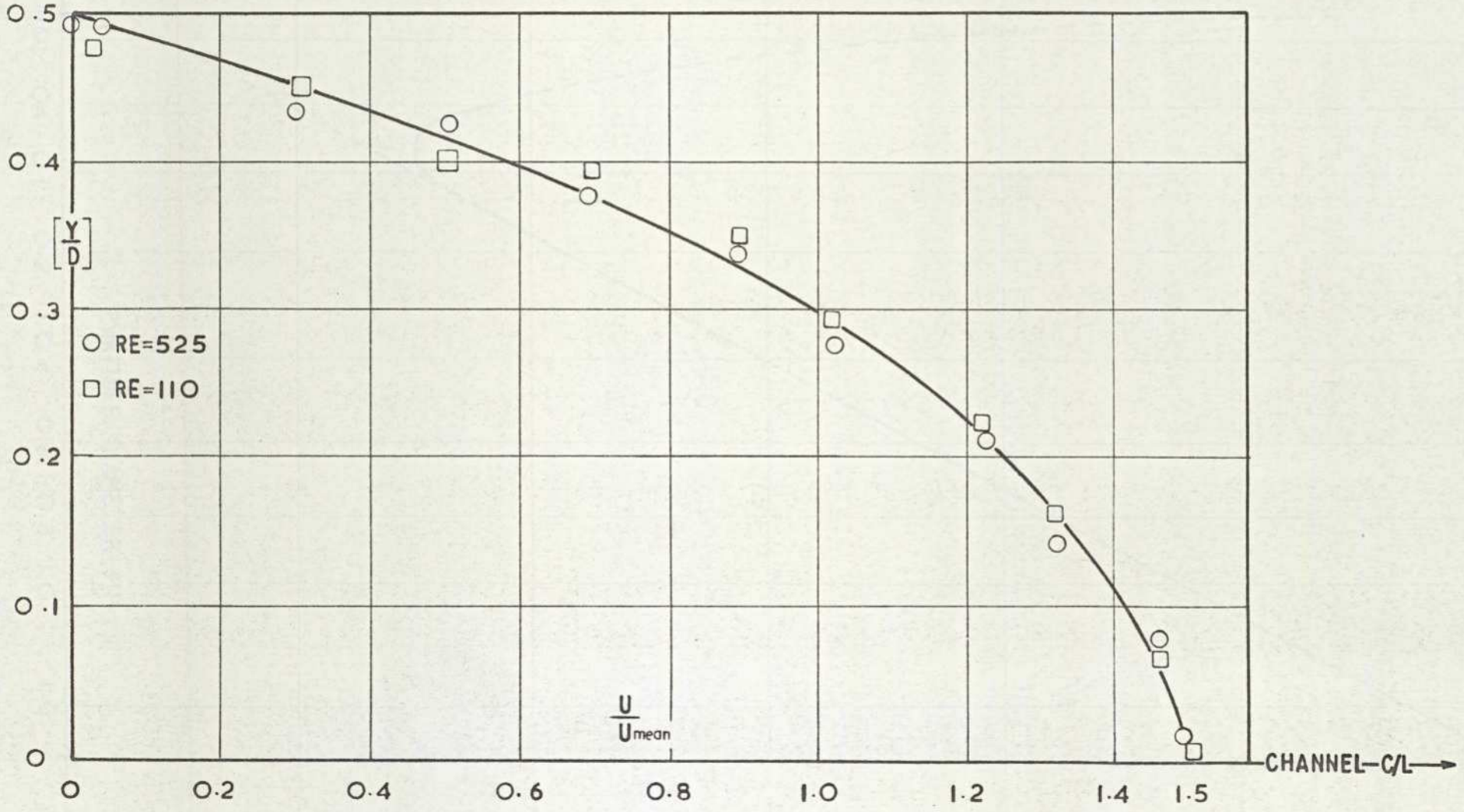


Gravity effect in inclined channel - flow upwards. Variation of channel inclination with deposition $\overline{N}$ from equation compared with experimental data at X/D=4

Figure 33



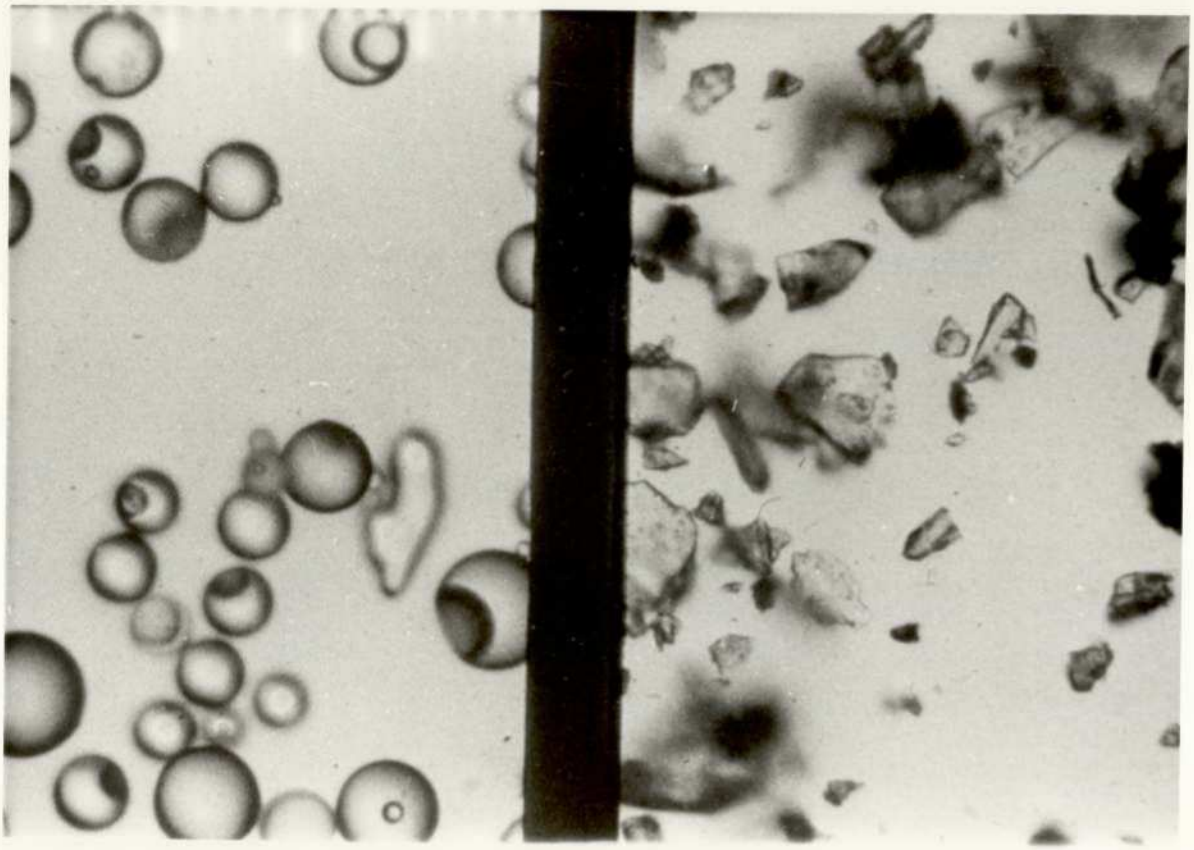
LAMINAR FLOW CHANNEL



VELOCITY PROFILE FOR LAMINAR FLOW CHANNEL

Figure 34

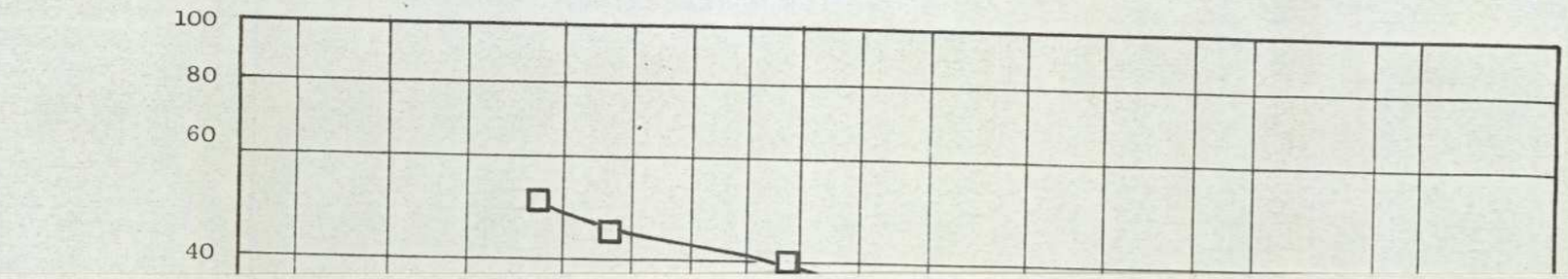
Figure 36



Ballotini

Glass dust

Particles used in the channel experiments



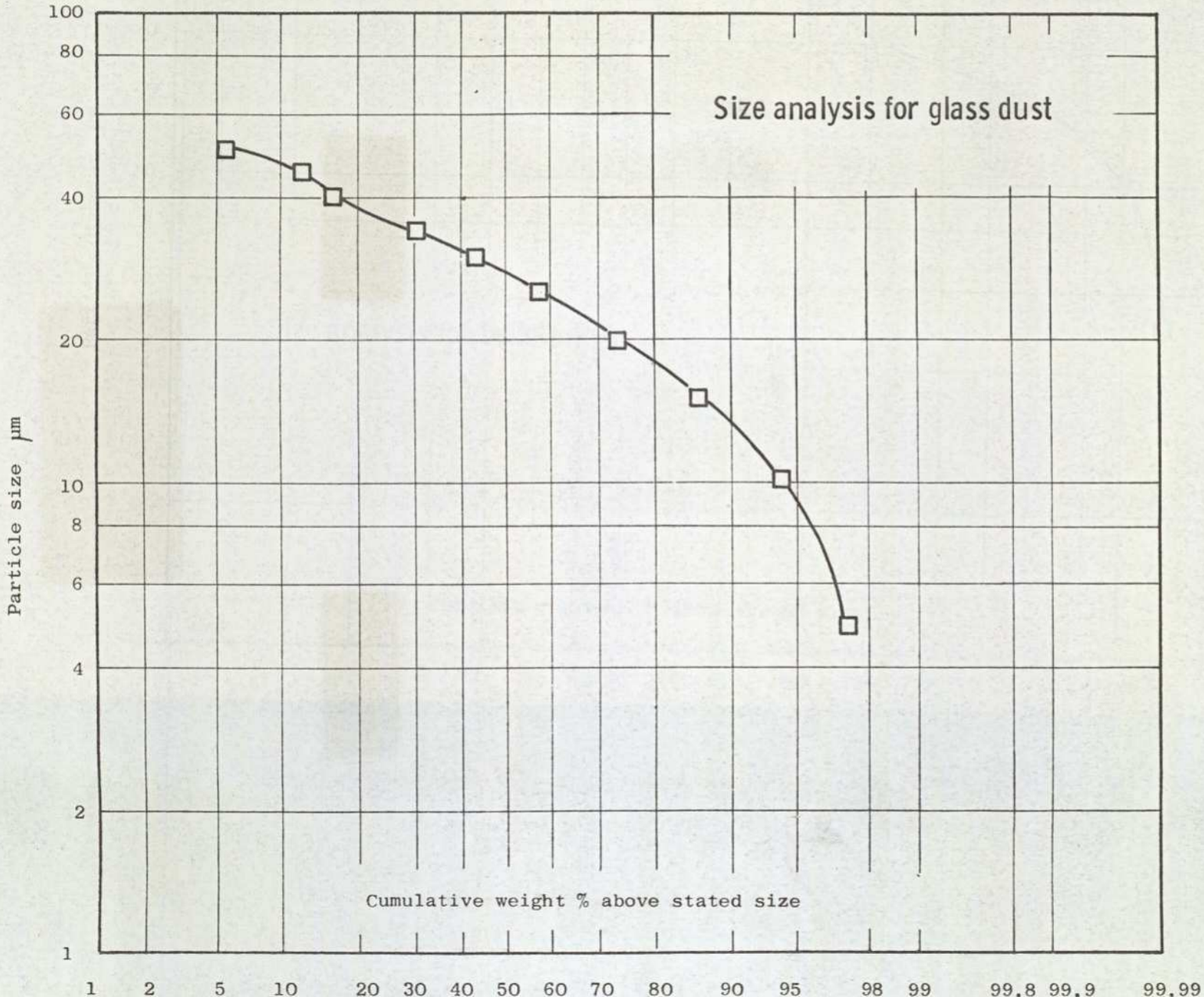

Size analysis for glass dust
Particle size μm
100
80
60
40
20
10
8
6
4
2
1
Cumulative weight % above stated size
1
2
5
10
20
30
40
50
60
70
80
90
95
98
99
99.8
99.9
99.99

Figure 37

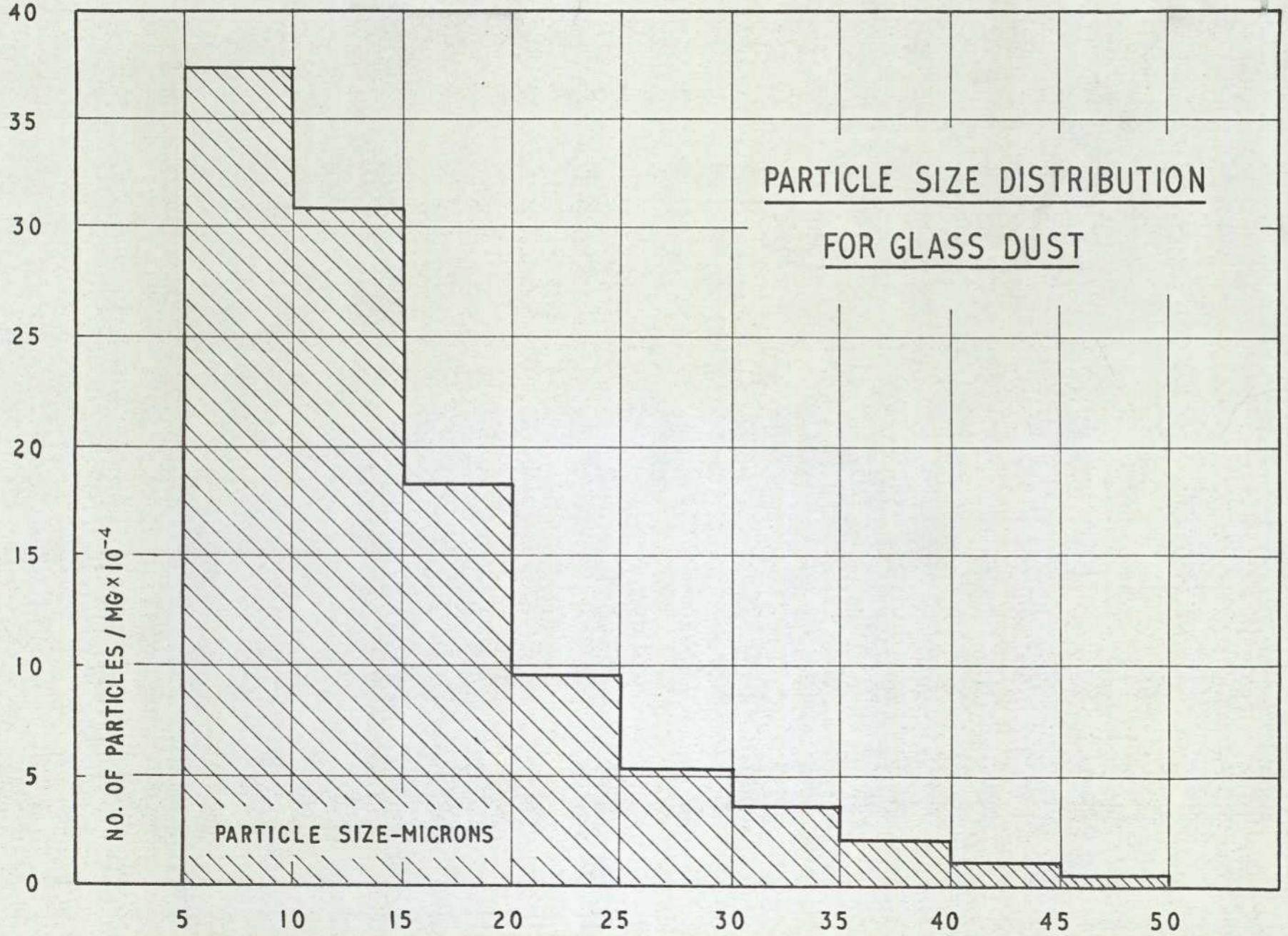

PARTICLE SIZE DISTRIBUTION
FOR GLASS DUST
NO. OF PARTICLES / MG × 10⁻⁴
PARTICLE SIZE-MICRONS
0
5
10
15
20
25
30
35
40
5
10
15
20
25
30
35
40
45
50

Figure 39

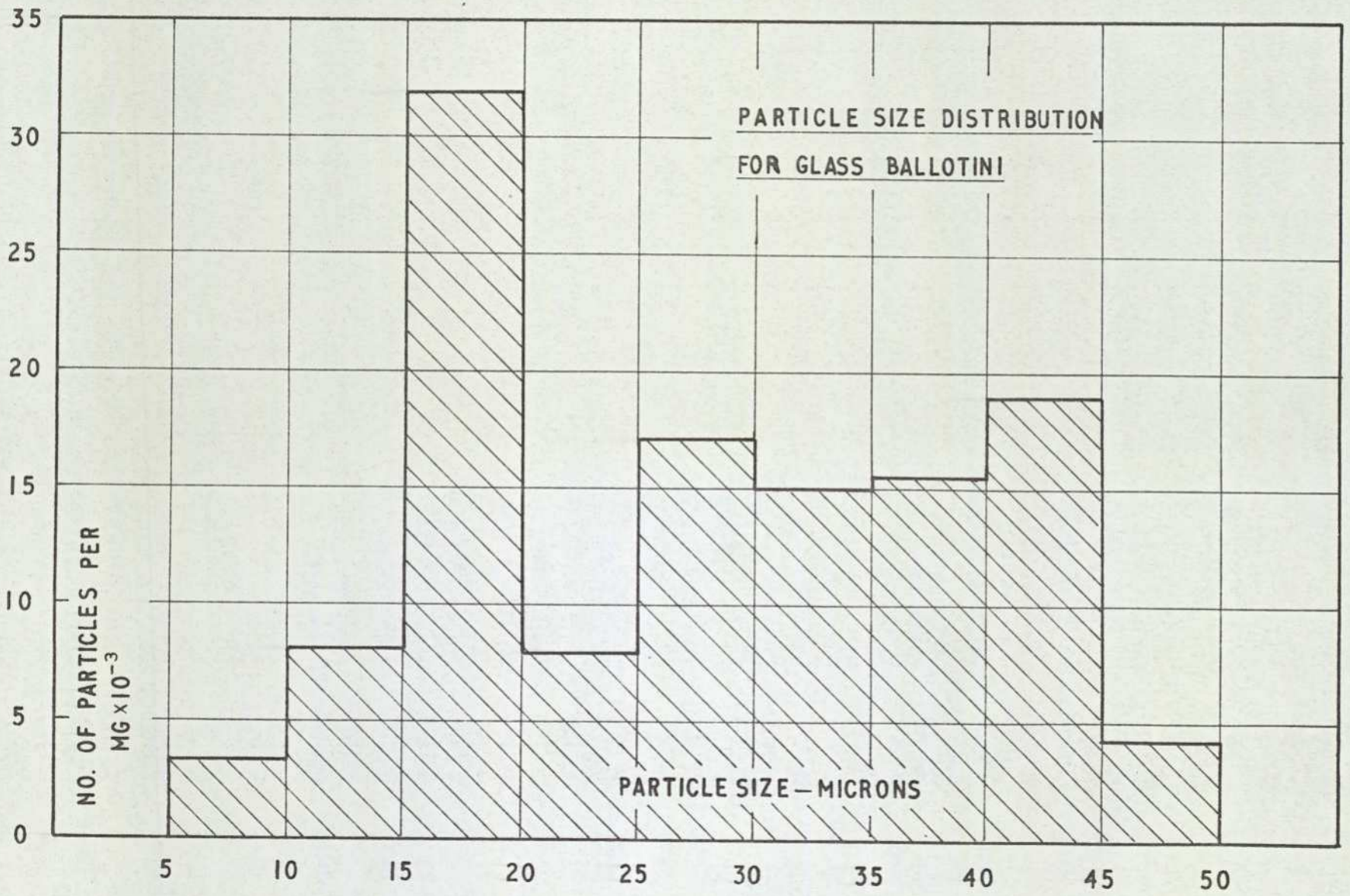
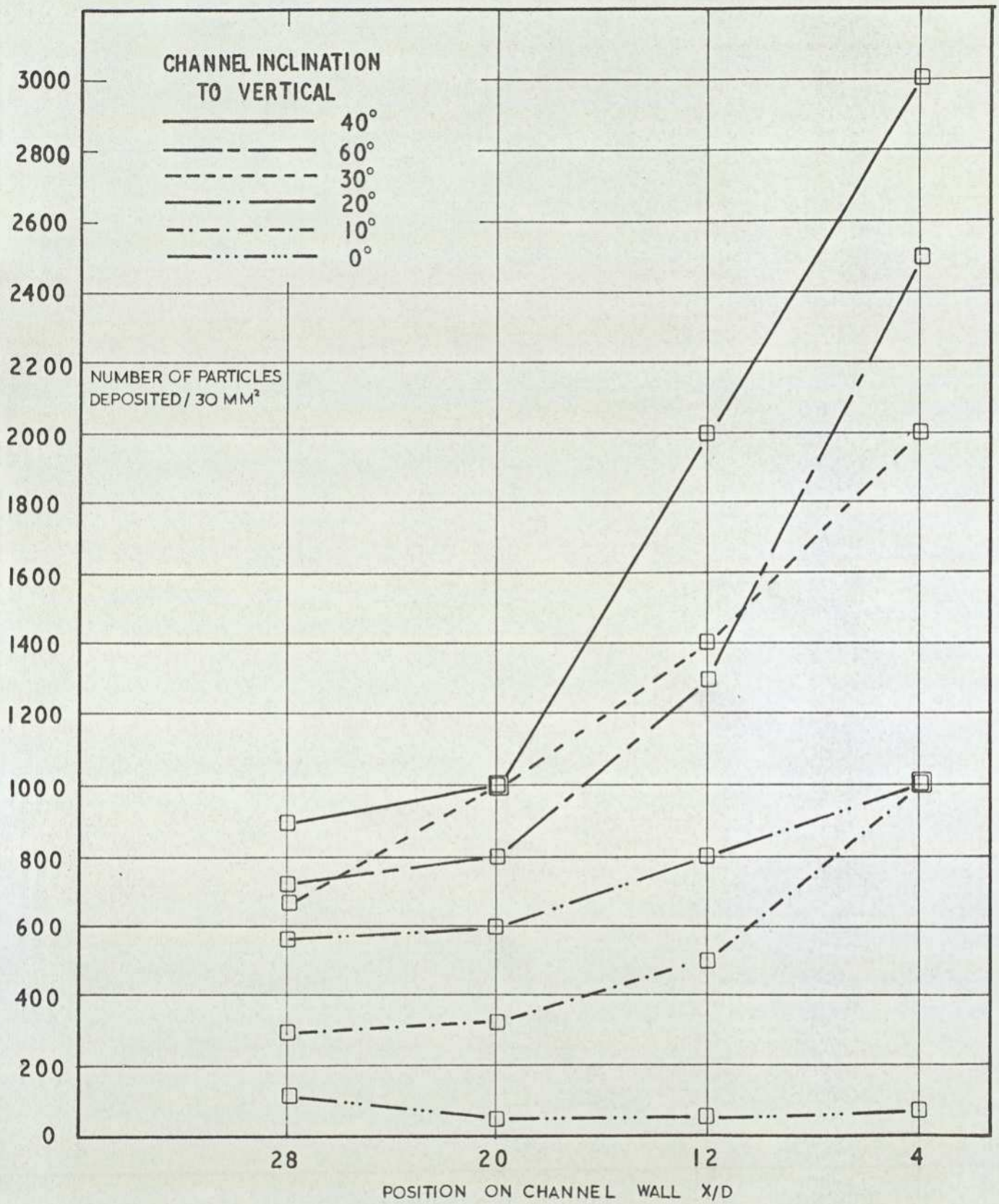
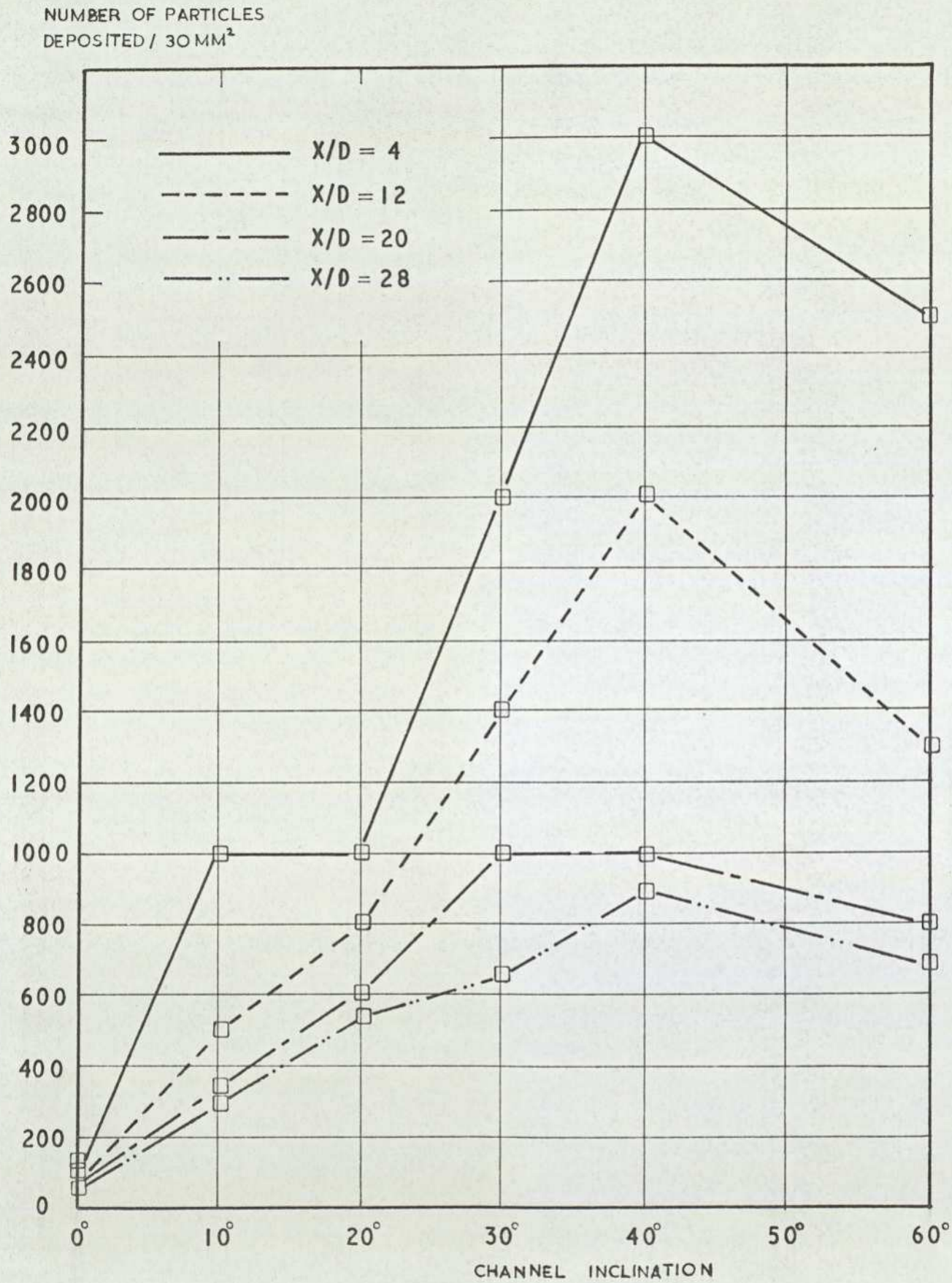

PARTICLE SIZE DISTRIBUTION
FOR GLASS BALLOTINI
NO. OF PARTICLES PER MG x10⁻³
PARTICLE SIZE – MICRONS
0
5
10
15
20
25
30
35
5
10
15
20
25
30
35
40
45
50

Figure 40



PARTICLE DEPOSITION ON THE BOTTOM CHANNEL WALL FOR VARIOUS ANGLES OF INCLINATION AT RE.=150



VARIATION OF DEPOSITION ON BOTTOM CHANNEL WALL WITH INCLINATION FOR VARIOUS VALUES OF X/D AT RE.=150

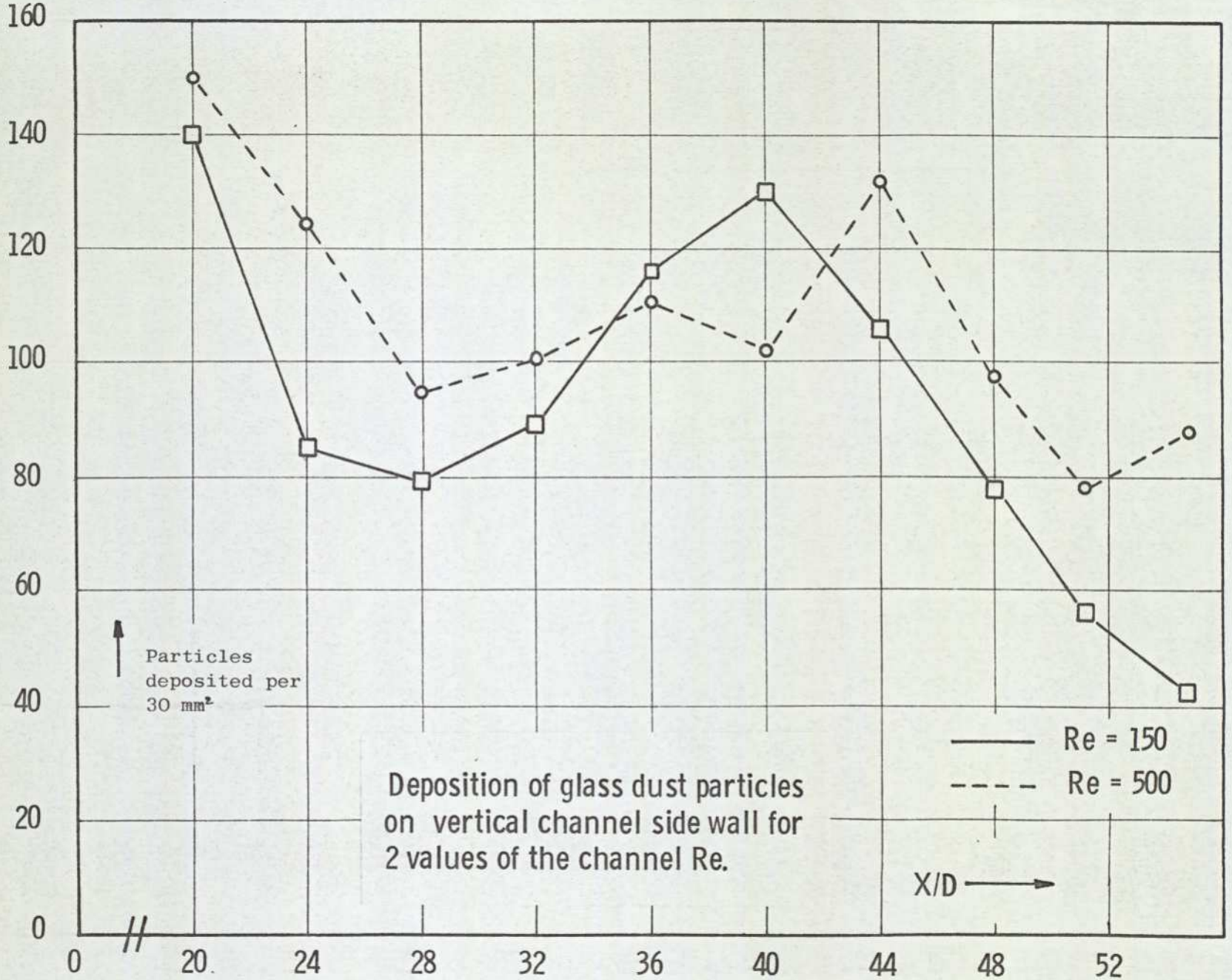
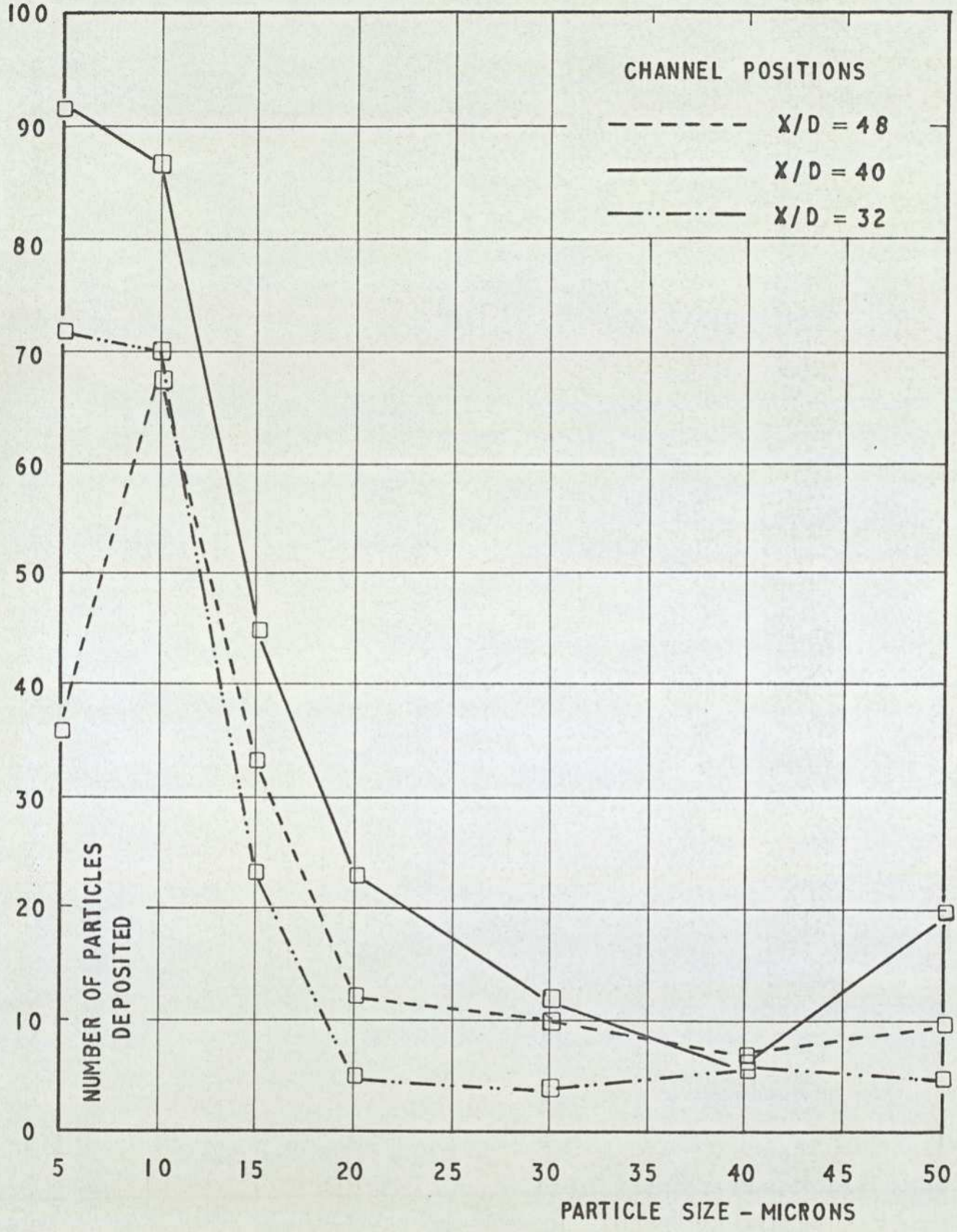

160
140
120
100
80
60
40
20
0
0
20
24
28
32
36
40
44
48
52
Particles deposited per 30 mm²
Re = 150
Re = 500
X/D
Deposition of glass dust particles on vertical channel side wall for 2 values of the channel Re.

Figure 43



SIZE DISTRIBUTION OF DEPOSITED PARTICLES FOR 3 VALUES OF X/D IN VERTICAL CHANNEL AT RE.=140

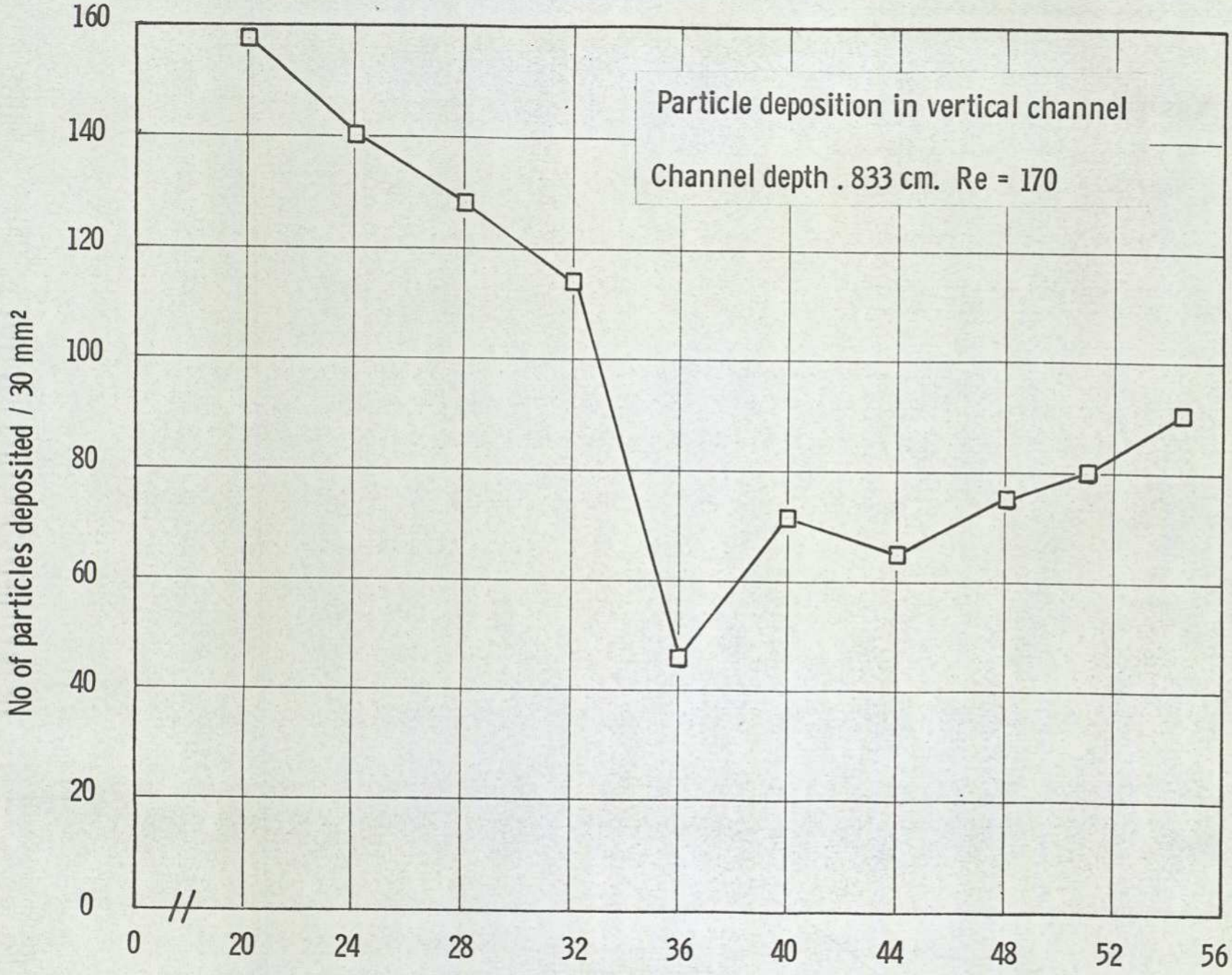

Particle deposition in vertical channel
Channel depth . 833 cm. Re = 170
No of particles deposited / 30 mm²
160
140
120
100
80
60
40
20
0
0
20
24
28
32
36
40
44
48
52
56
Position on channel
X/D

Figure 45

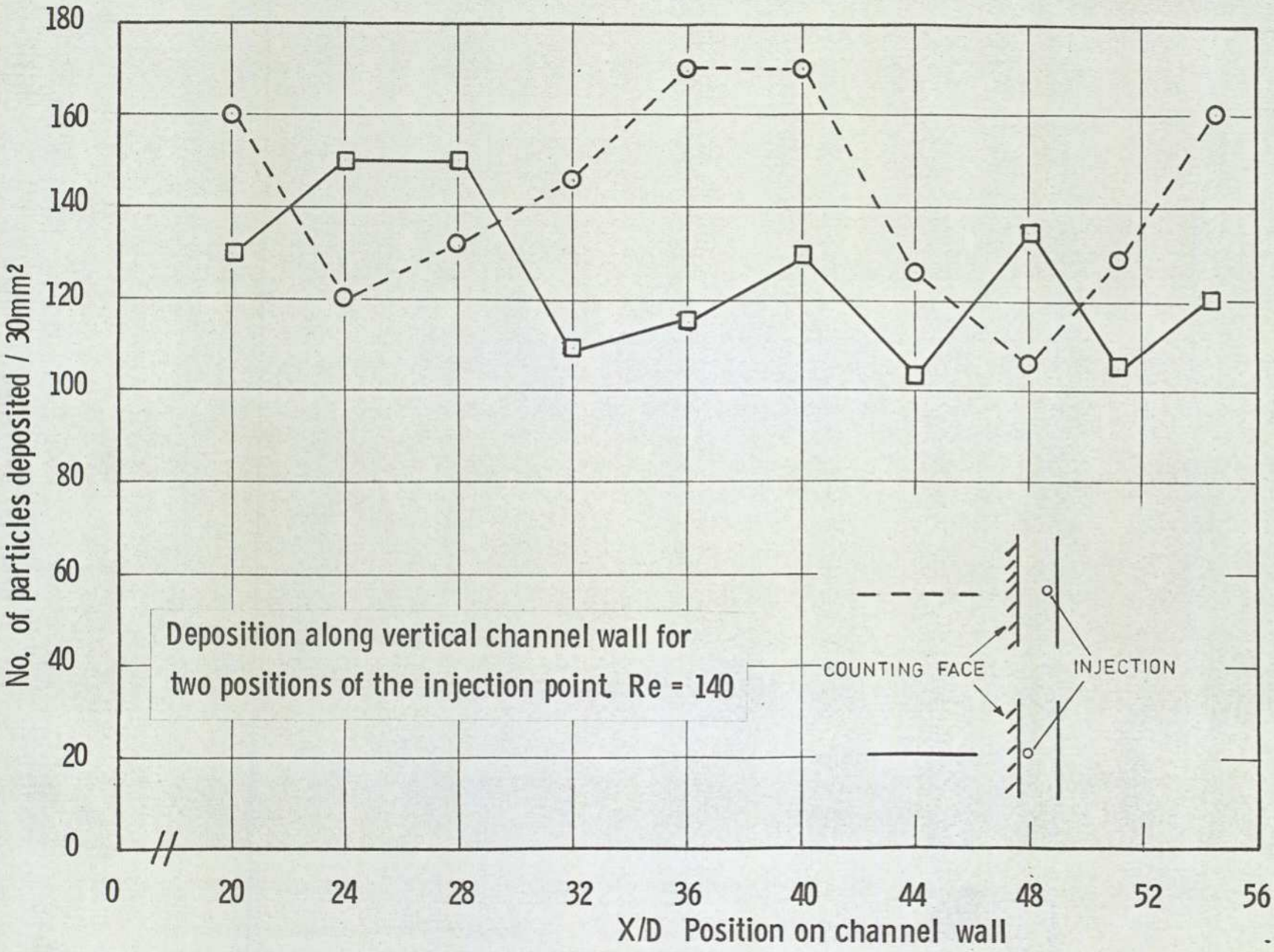

180
160
140
120
100
80
60
40
20
0
No. of particles deposited / 30mm²
0
20
24
28
32
36
40
44
48
52
56
X/D Position on channel wall
Deposition along vertical channel wall for
two positions of the injection point. Re = 140
COUNTING FACE
INJECTION

Figure 46

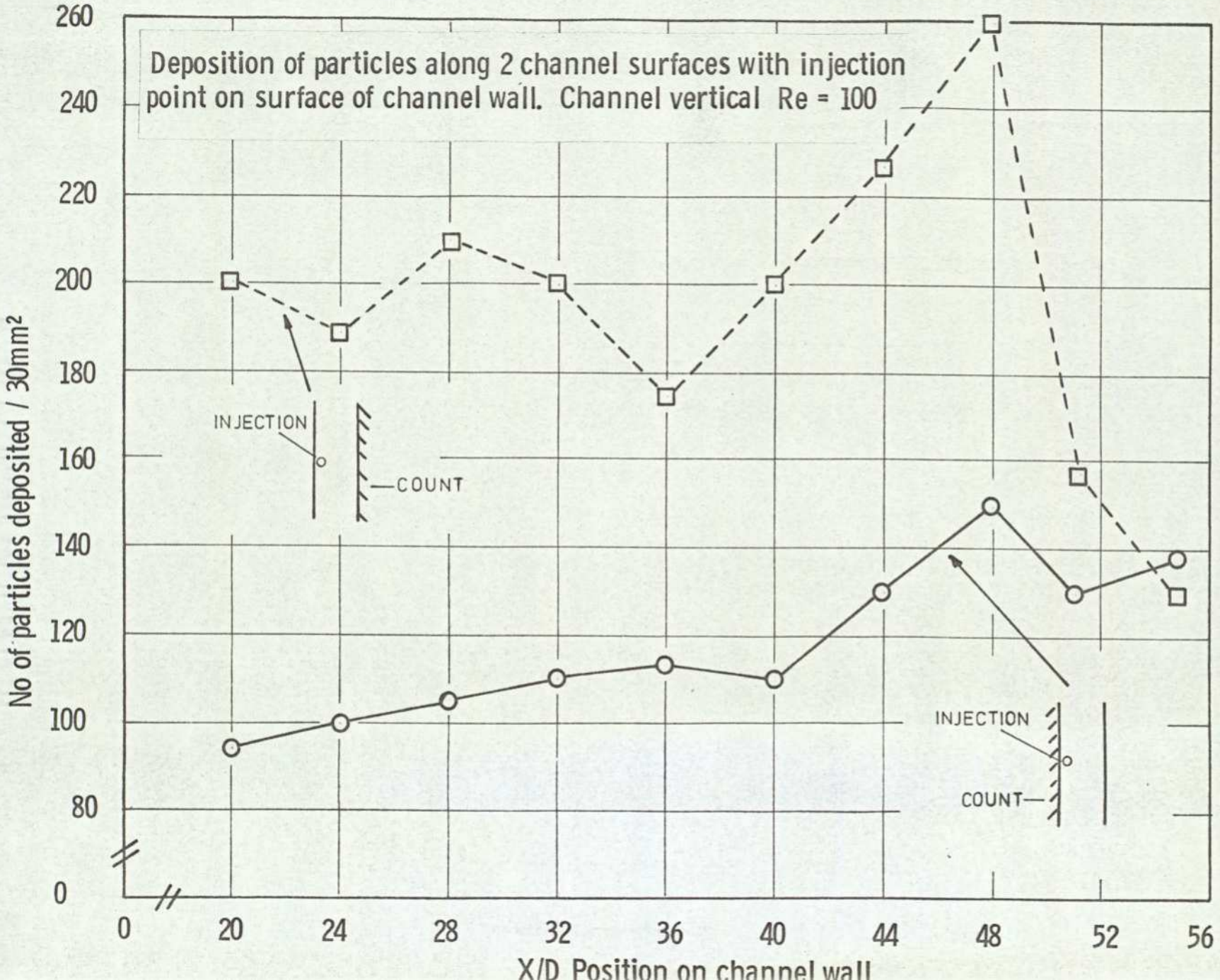

Deposition of particles along 2 channel surfaces with injection point on surface of channel wall. Channel vertical Re = 100
No of particles deposited / 30mm²
X/D Position on channel wall
INJECTION
COUNT
INJECTION
COUNT
260
240
220
200
180
160
140
120
100
80
0
0
20
24
28
32
36
40
44
48
52
56

Figure 47

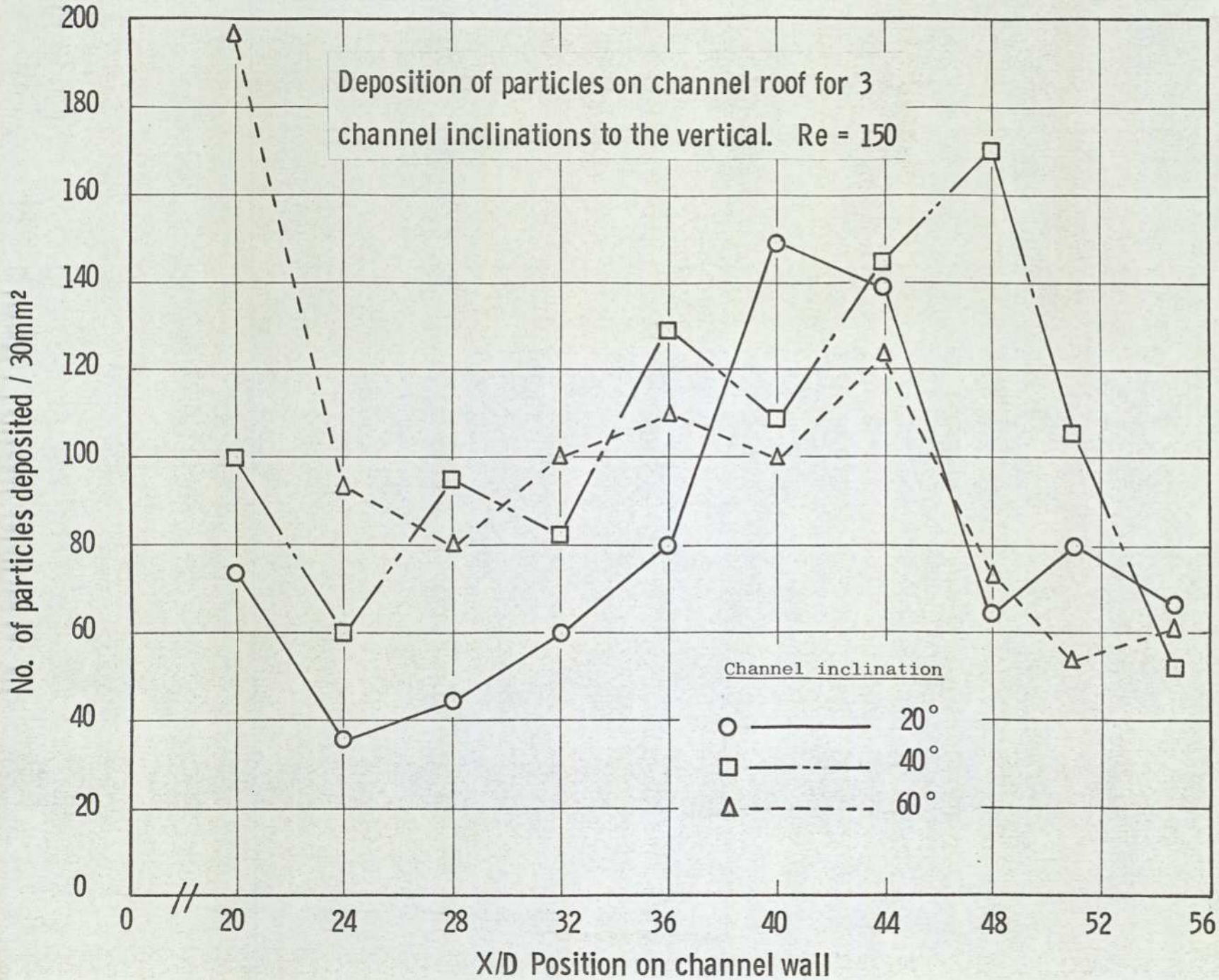
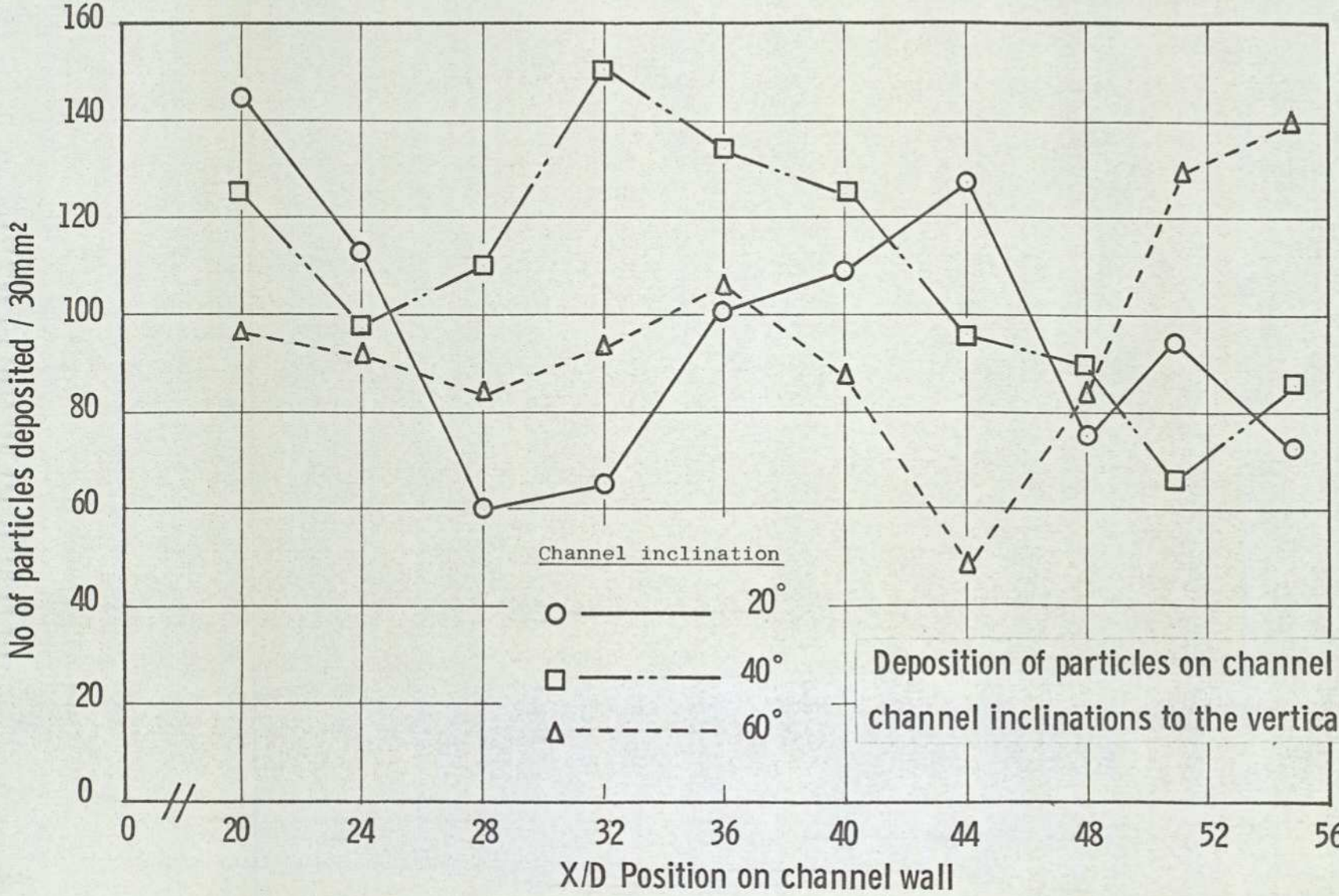
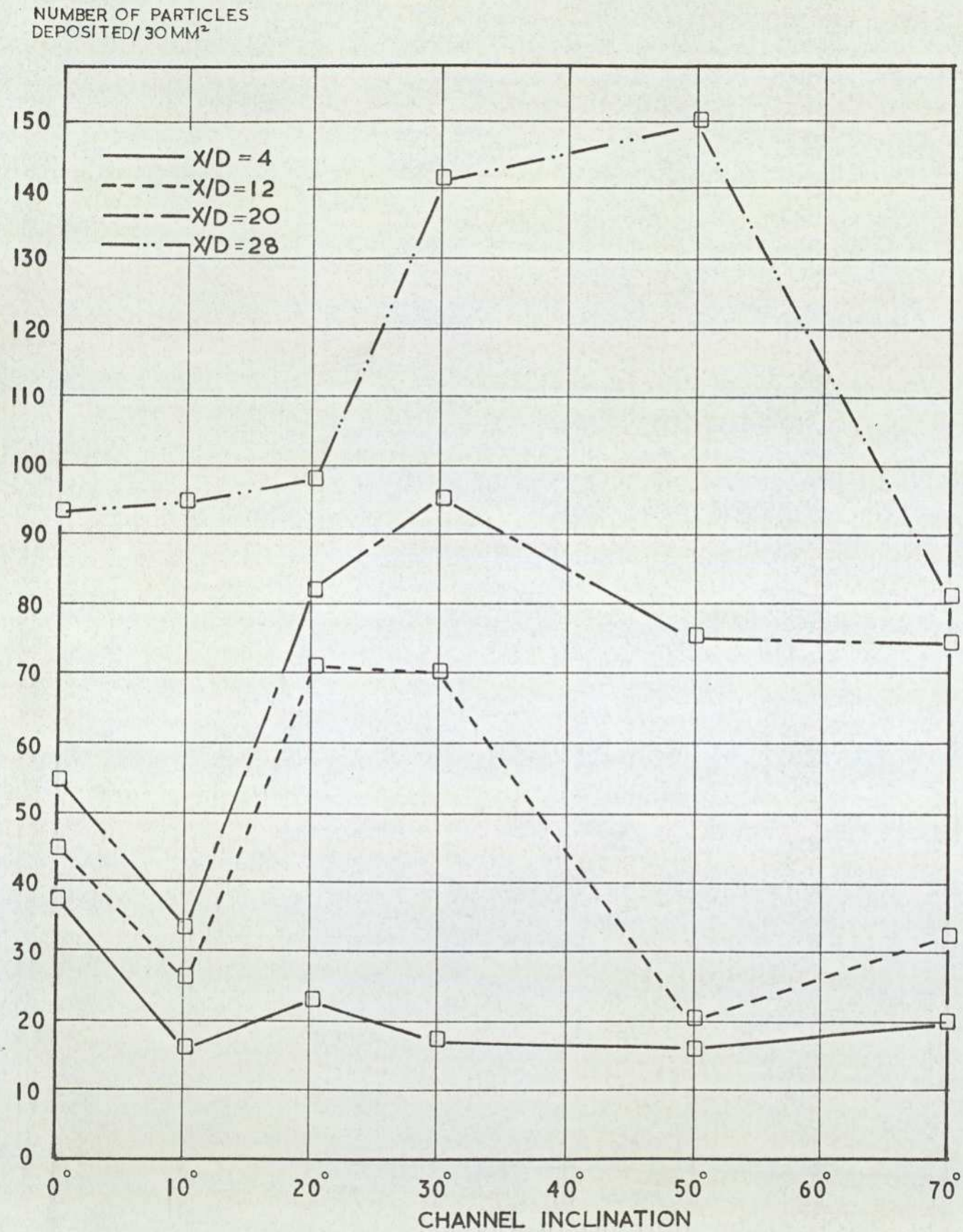

Deposition of particles on channel roof for 3 channel inclinations to the vertical. Re = 150
No. of particles deposited / 30mm²
X/D Position on channel wall
Channel inclination
20°
40°
60°
0
20
40
60
80
100
120
140
160
180
200
20
24
28
32
36
40
44
48
52
56

Figure 48



Deposition of particles on channel roof for 3 channel inclinations to the vertical. Re = 500

Figure 49



VARIATION OF DEPOSITION ON UPPER CHANNEL WALL WITH INCLINATION FOR VARIOUS VALUES OF X/D AT RE=150

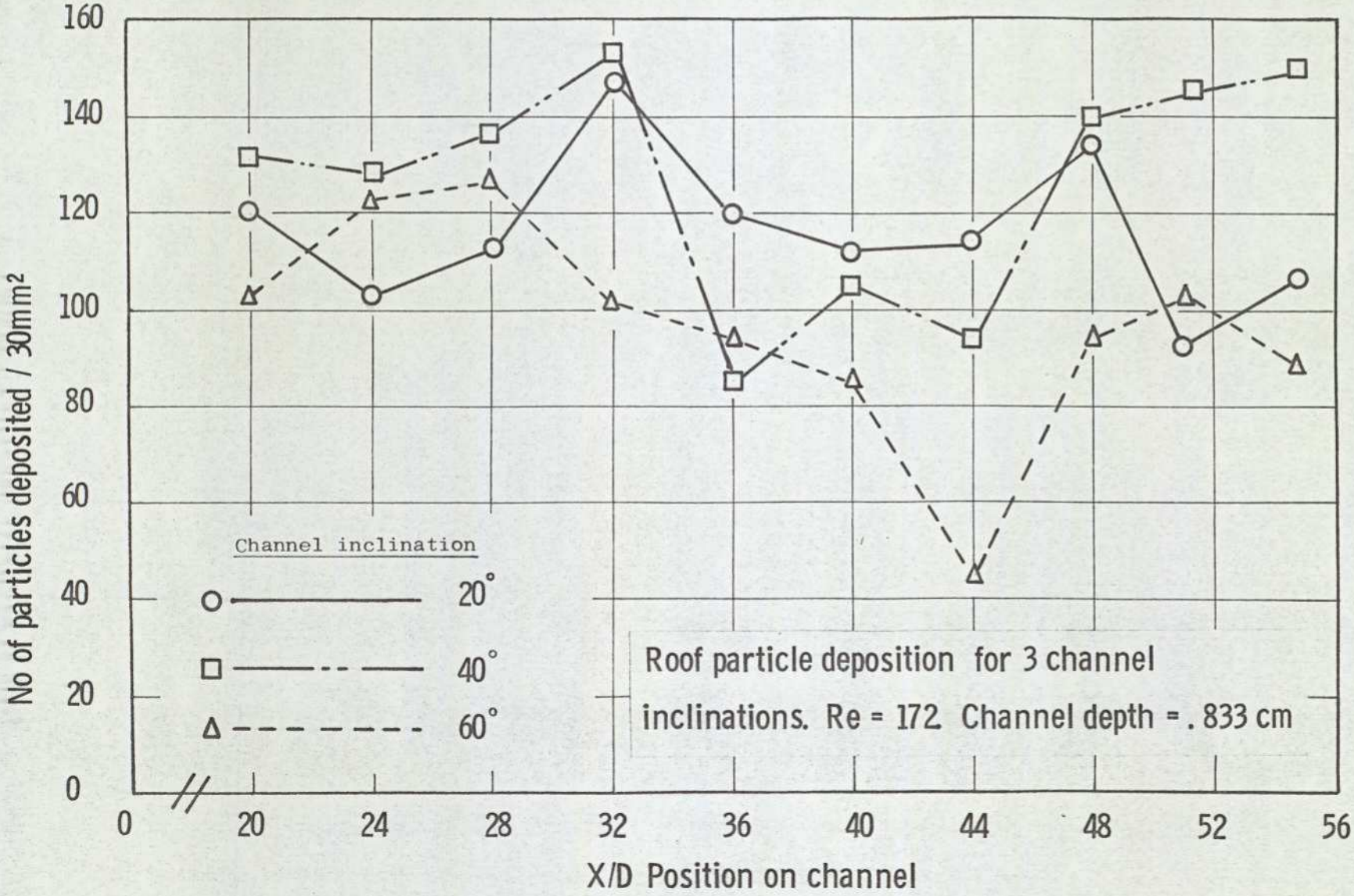

160
140
120
100
80
60
40
20
0
No of particles deposited / 30mm²
0
20
24
28
32
36
40
44
48
52
56
X/D Position on channel
Channel inclination
20°
40°
60°
Roof particle deposition for 3 channel
inclinations. Re = 172. Channel depth = .833 cm

Figure 51

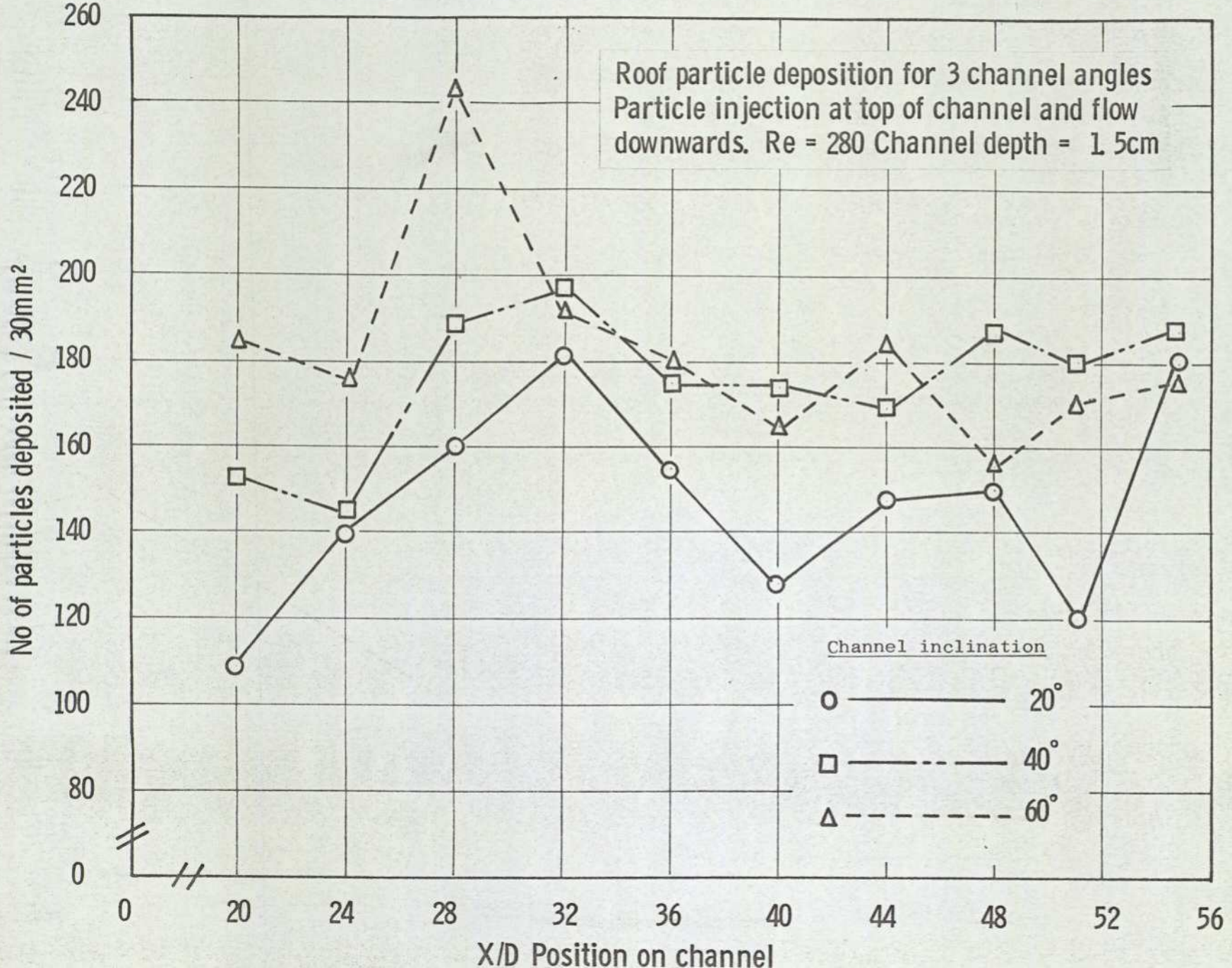

Roof particle deposition for 3 channel angles
Particle injection at top of channel and flow downwards. Re = 280 Channel depth = 1.5cm
No of particles deposited / 30mm²
X/D Position on channel
Channel inclination
20°
40°
60°
0
80
100
120
140
160
180
200
220
240
260
20
24
28
32
36
40
44
48
52
56

Figure 52

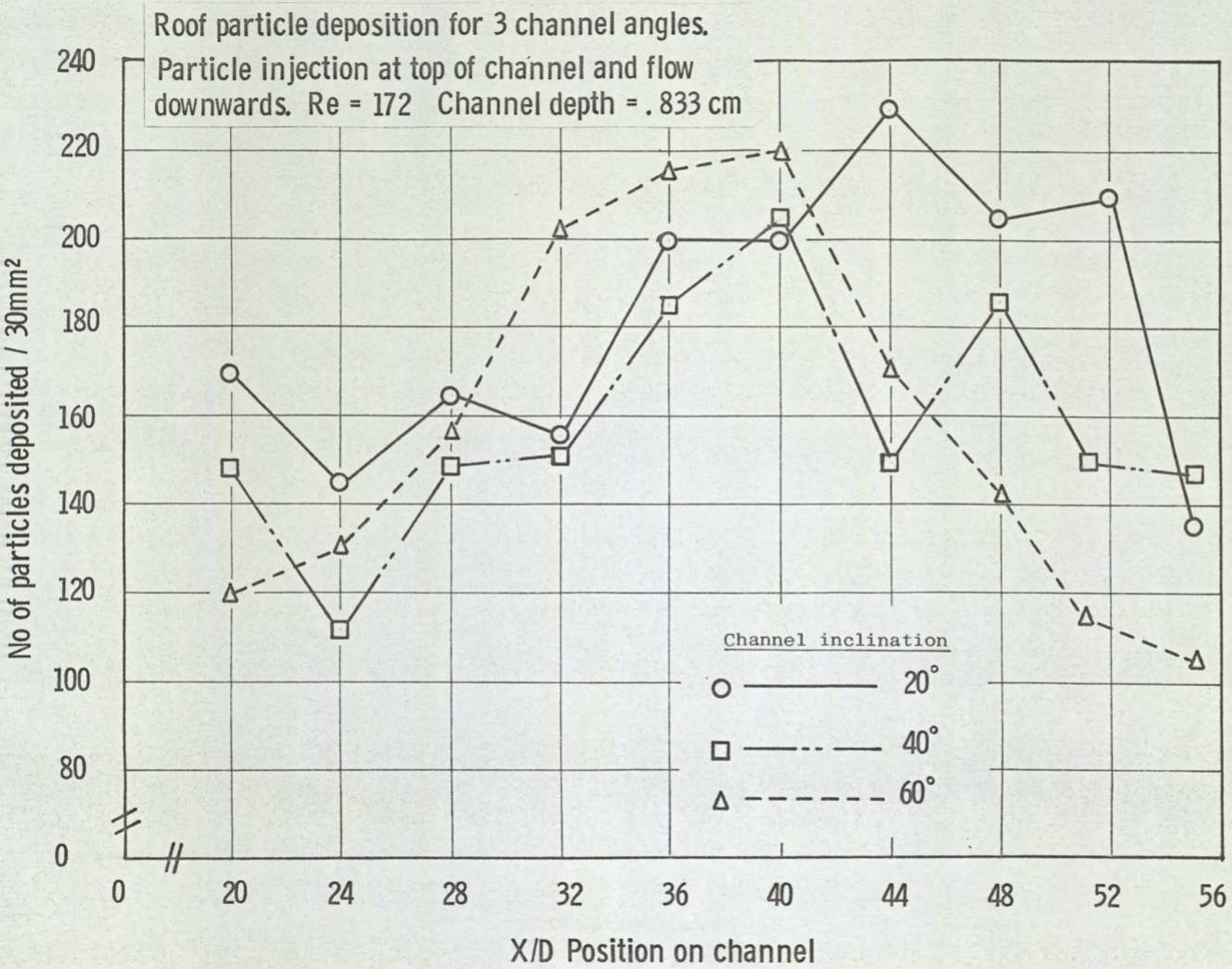

Roof particle deposition for 3 channel angles.
Particle injection at top of channel and flow downwards. Re = 172 Channel depth = .833 cm
No of particles deposited / 30mm²
240
220
200
180
160
140
120
100
80
0
0
20
24
28
32
36
40
44
48
52
56
X/D Position on channel
Channel inclination
20°
40°
60°

Figure 53

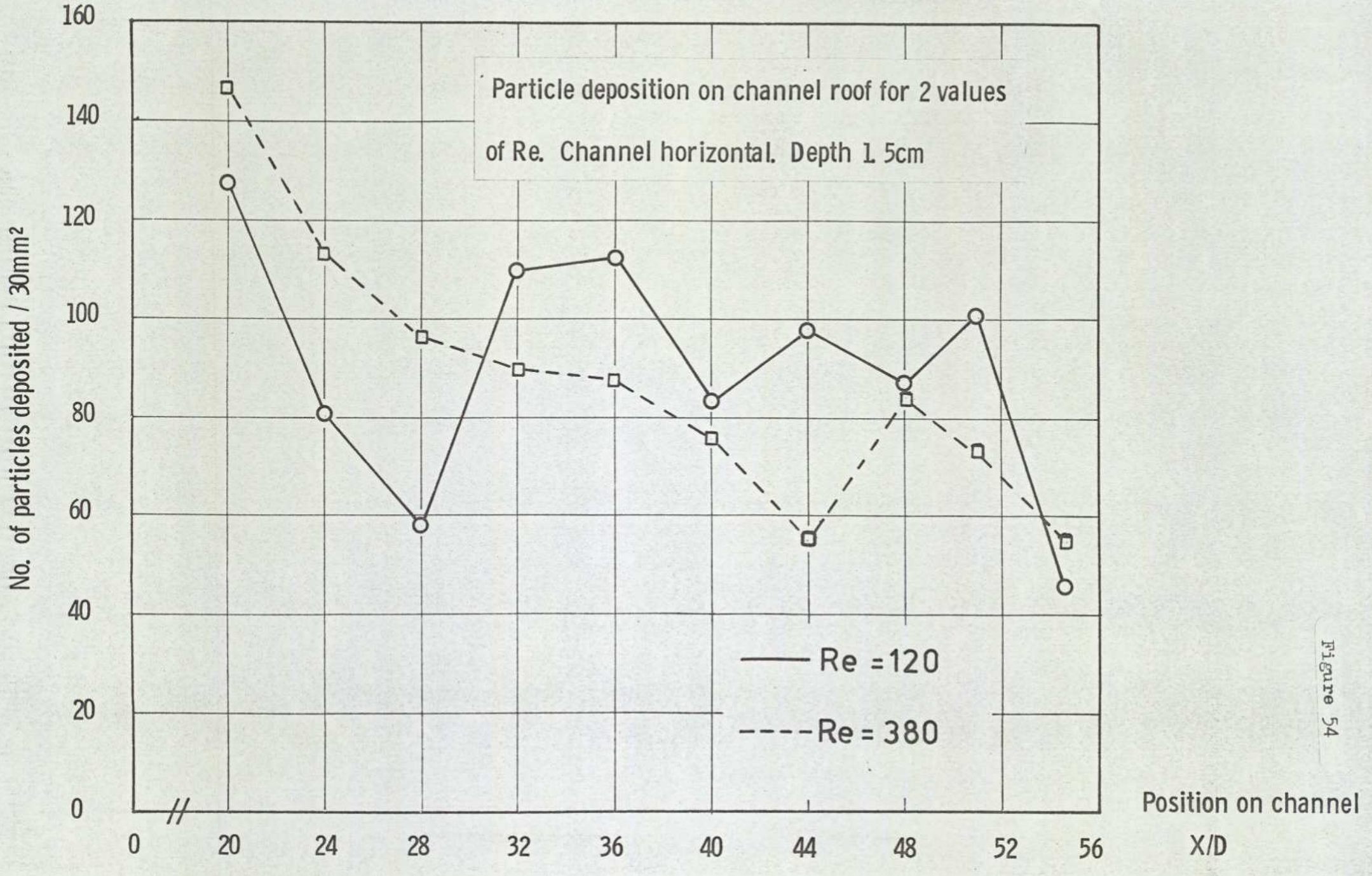

Particle deposition on channel roof for 2 values
of Re. Channel horizontal. Depth 1.5cm
No. of particles deposited / 30mm²
Position on channel
X/D
Re =120
Re = 380
0
20
40
60
80
100
120
140
160
0
20
24
28
32
36
40
44
48
52
56

Figure 54

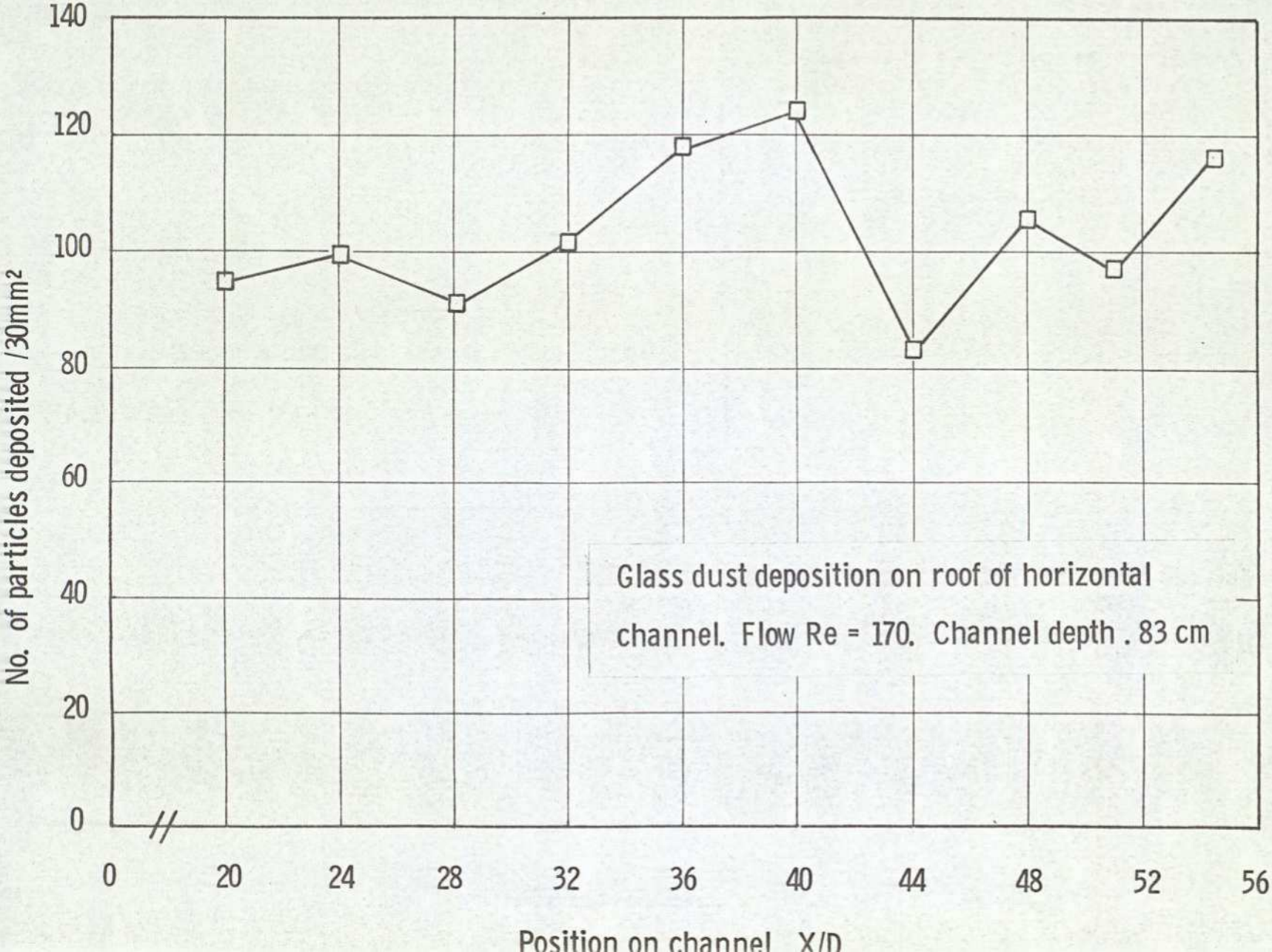

140
120
100
80
60
40
20
0
No. of particles deposited /30mm²
Glass dust deposition on roof of horizontal channel. Flow Re = 170. Channel depth . 83 cm
0
20
24
28
32
36
40
44
48
52
56
Position on channel X/D

Figure 55

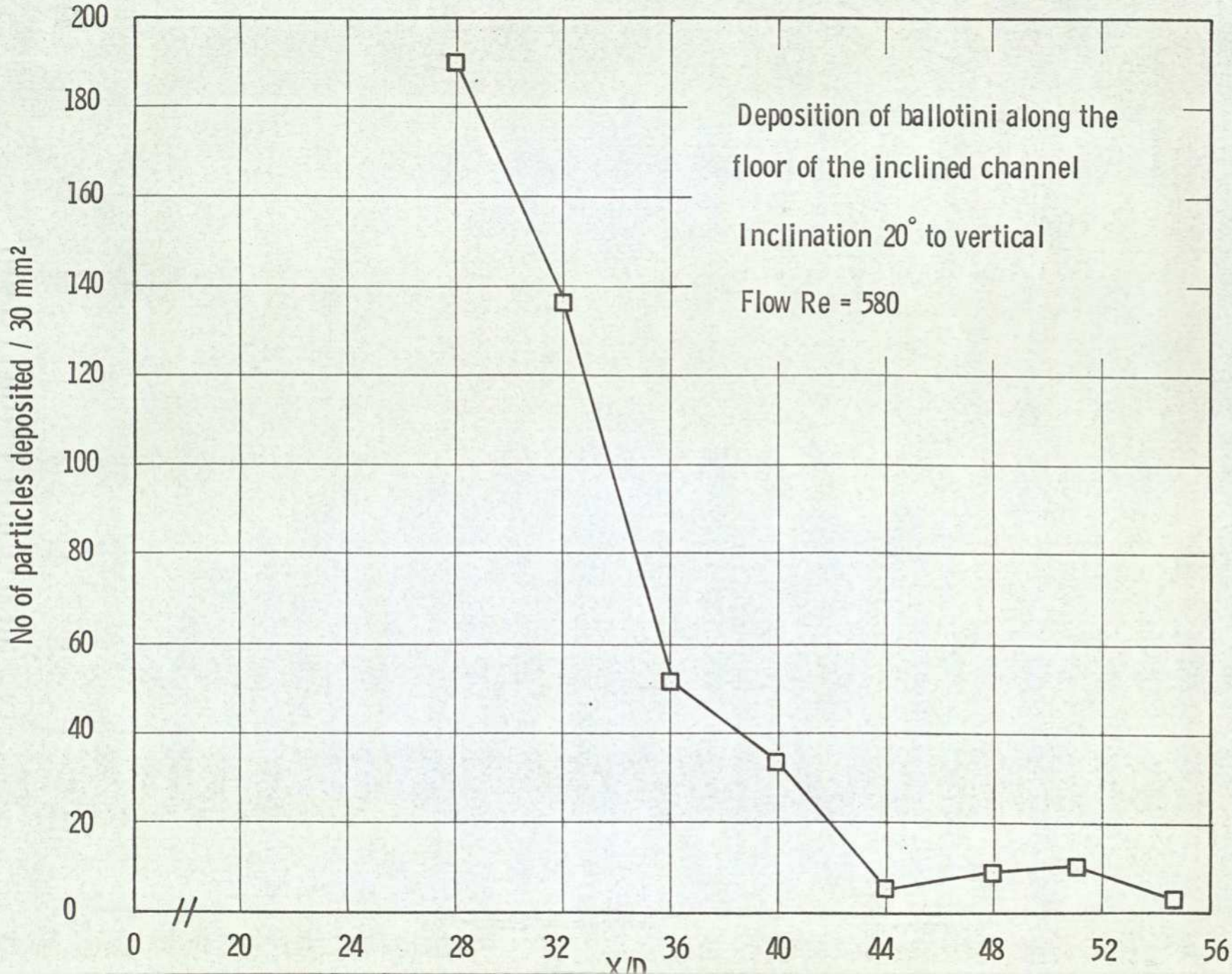

Deposition of ballotini along the floor of the inclined channel
Inclination 20° to vertical
Flow Re = 580
No of particles deposited / 30 mm²
200
180
160
140
120
100
80
60
40
20
0
0
20
24
28
32
36
40
44
48
52
56
X/D
Position on channel

Figure 56

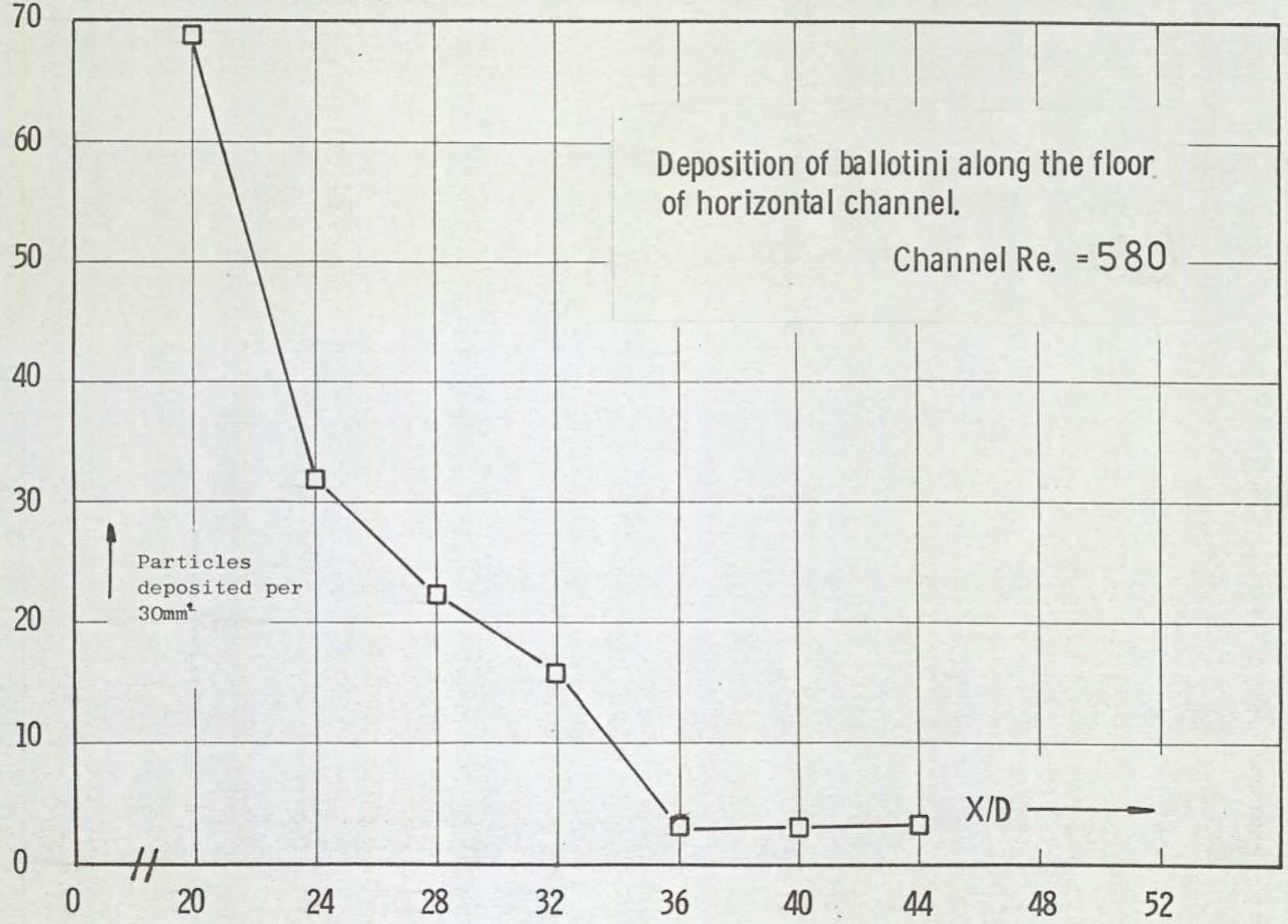

Deposition of ballotini along the floor of horizontal channel.
Channel Re. = 580
Particles deposited per 30mm²
X/D
70
60
50
40
30
20
10
0
0
20
24
28
32
36
40
44
48
52

Figure 57

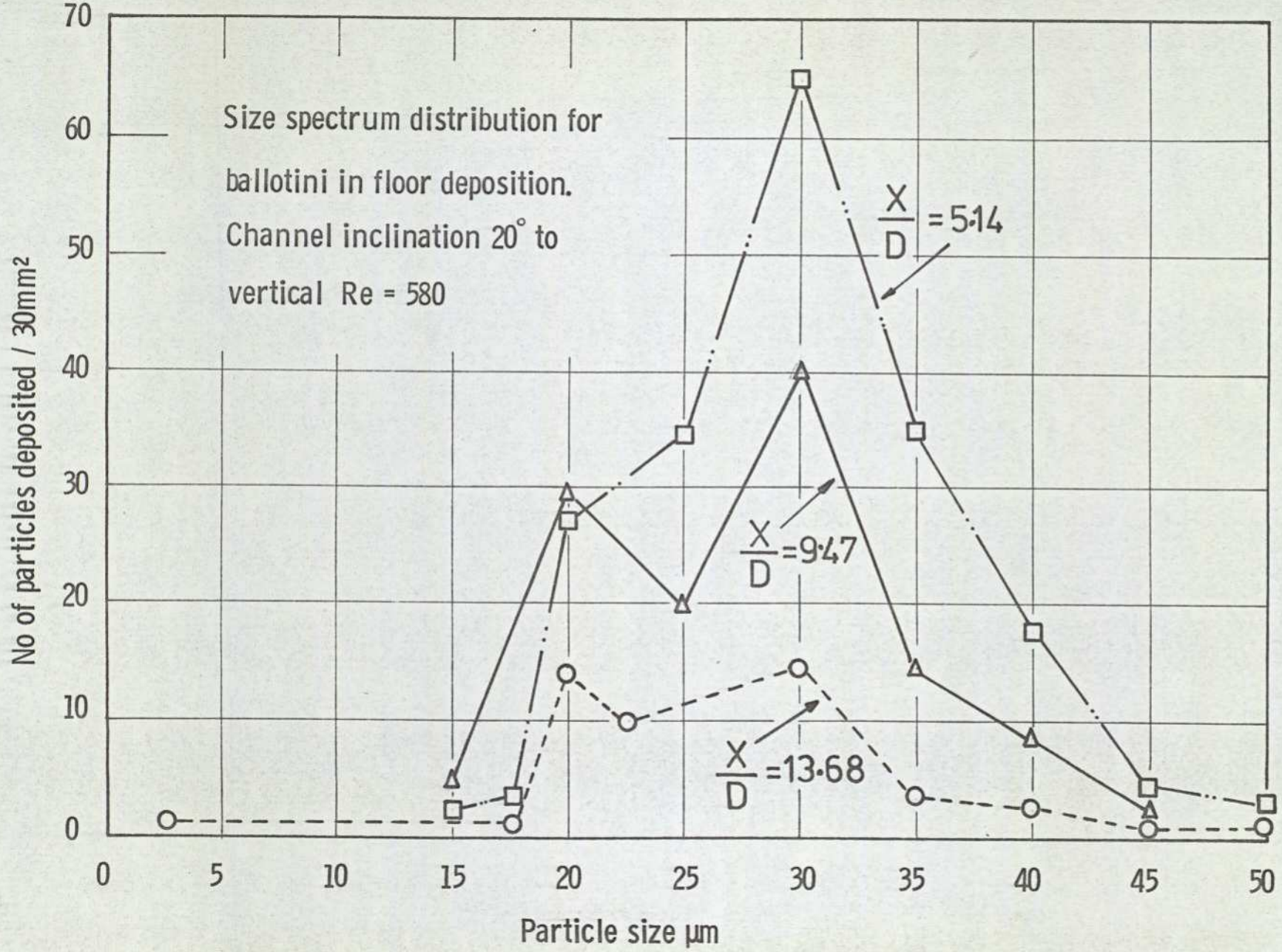
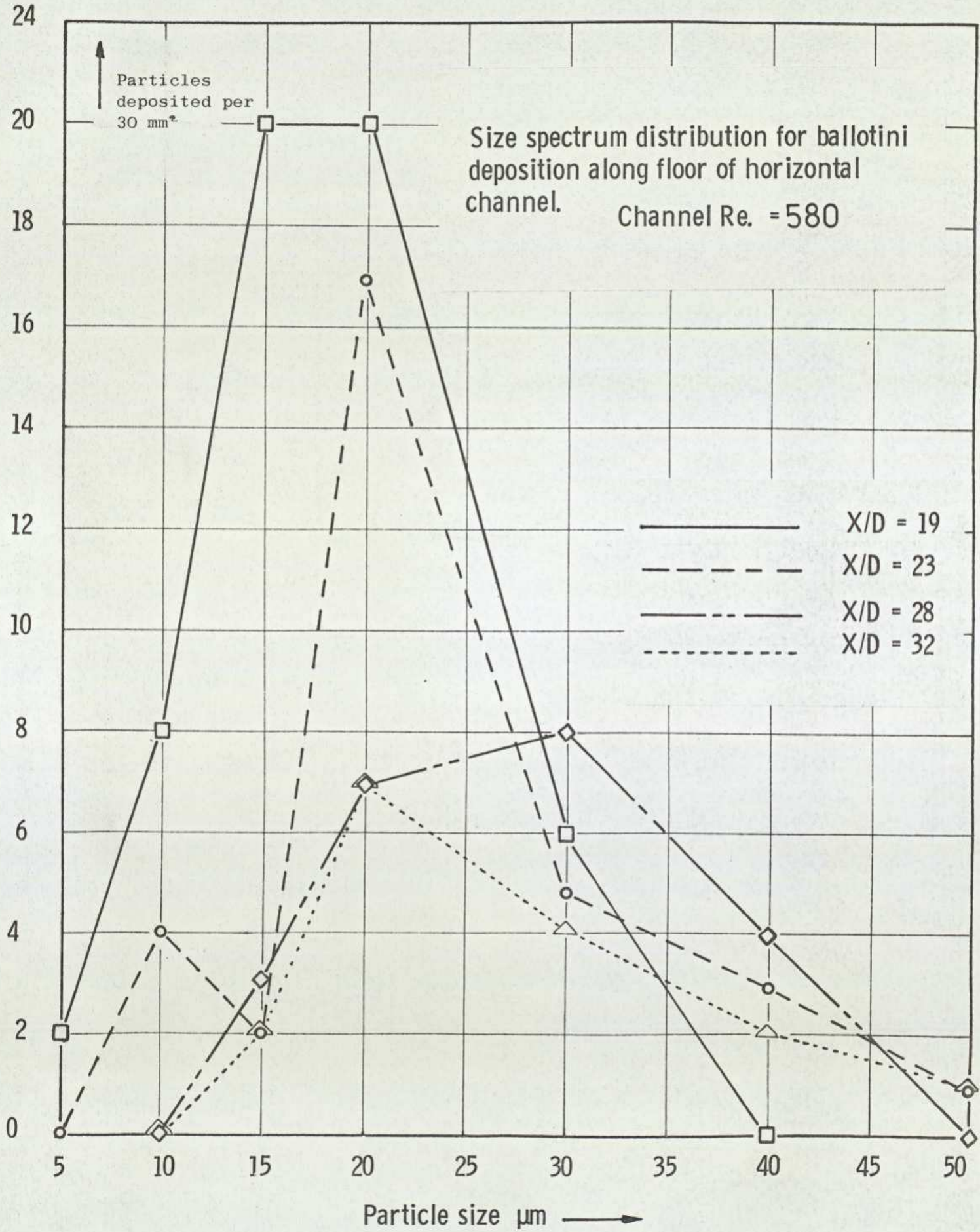

Size spectrum distribution for
ballotini in floor deposition.
Channel inclination 20° to
vertical Re = 580
X/D = 5·14
X/D = 9·47
X/D = 13·68
No of particles deposited / 30mm²
Particle size µm
0
10
20
30
40
50
60
70
0
5
10
15
20
25
30
35
40
45
50

Figure 58

Figure 59


Particles deposited per 30 mm²
Size spectrum distribution for ballotini deposition along floor of horizontal channel.
Channel Re. = 580
X/D = 19
X/D = 23
X/D = 28
X/D = 32
24
20
18
16
14
12
10
8
6
4
2
0
5
10
15
20
25
30
35
40
45
50
Particle size μm

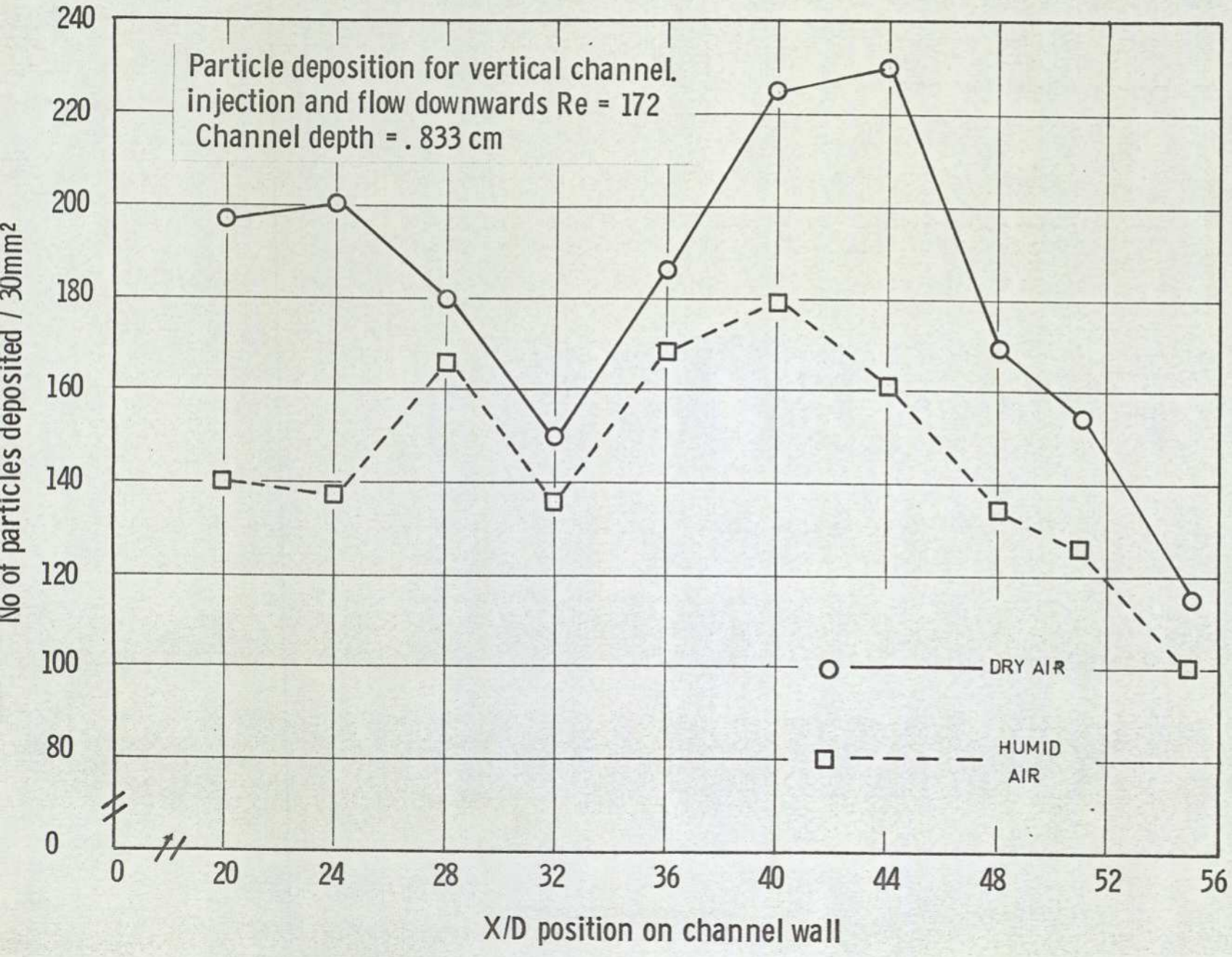

Particle deposition for vertical channel.
injection and flow downwards Re = 172
Channel depth = . 833 cm
No of particles deposited / 30mm²
240
220
200
180
160
140
120
100
80
0
0
20
24
28
32
36
40
44
48
52
56
X/D position on channel wall
DRY AIR
HUMID AIR

Figure 60

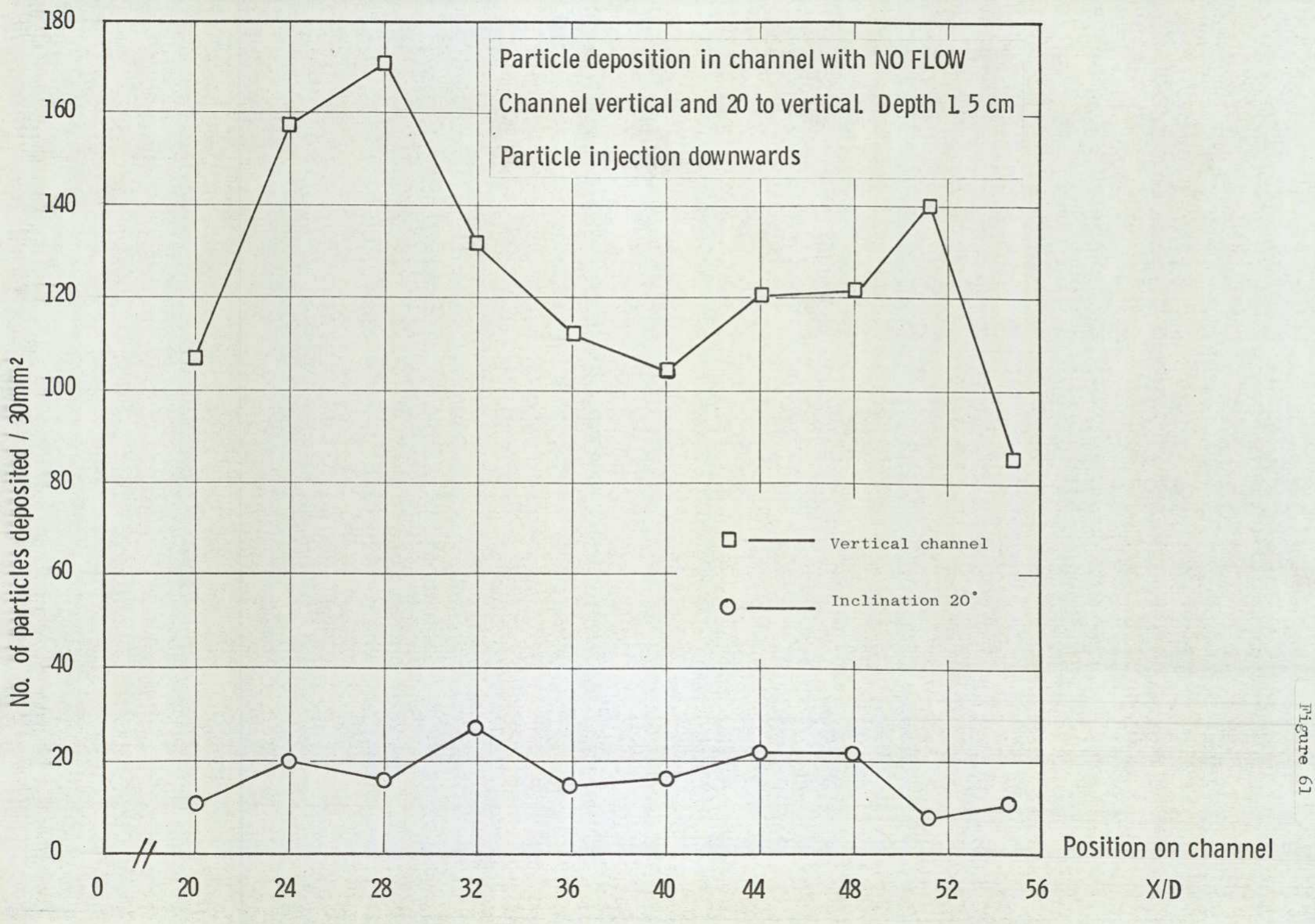

Particle deposition in channel with NO FLOW
Channel vertical and 20 to vertical. Depth 1.5 cm
Particle injection downwards
Vertical channel
Inclination 20°
No. of particles deposited / 30mm²
Position on channel
X/D
0
20
40
60
80
100
120
140
160
180
0
20
24
28
32
36
40
44
48
52
56

Figure 61

Effect of various wall materials on glass dust deposition in vertical channel flow. Re = 100

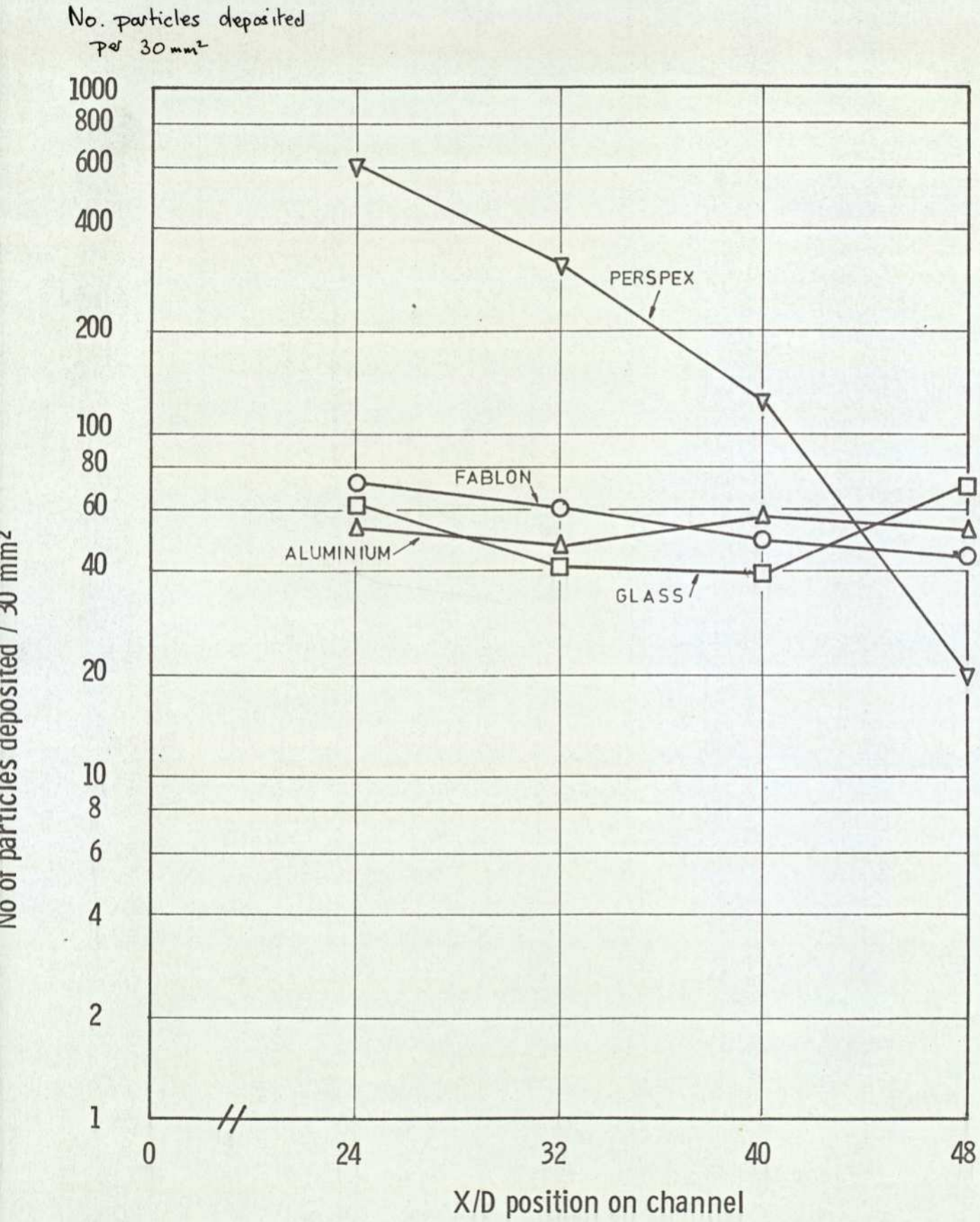


Figure 63

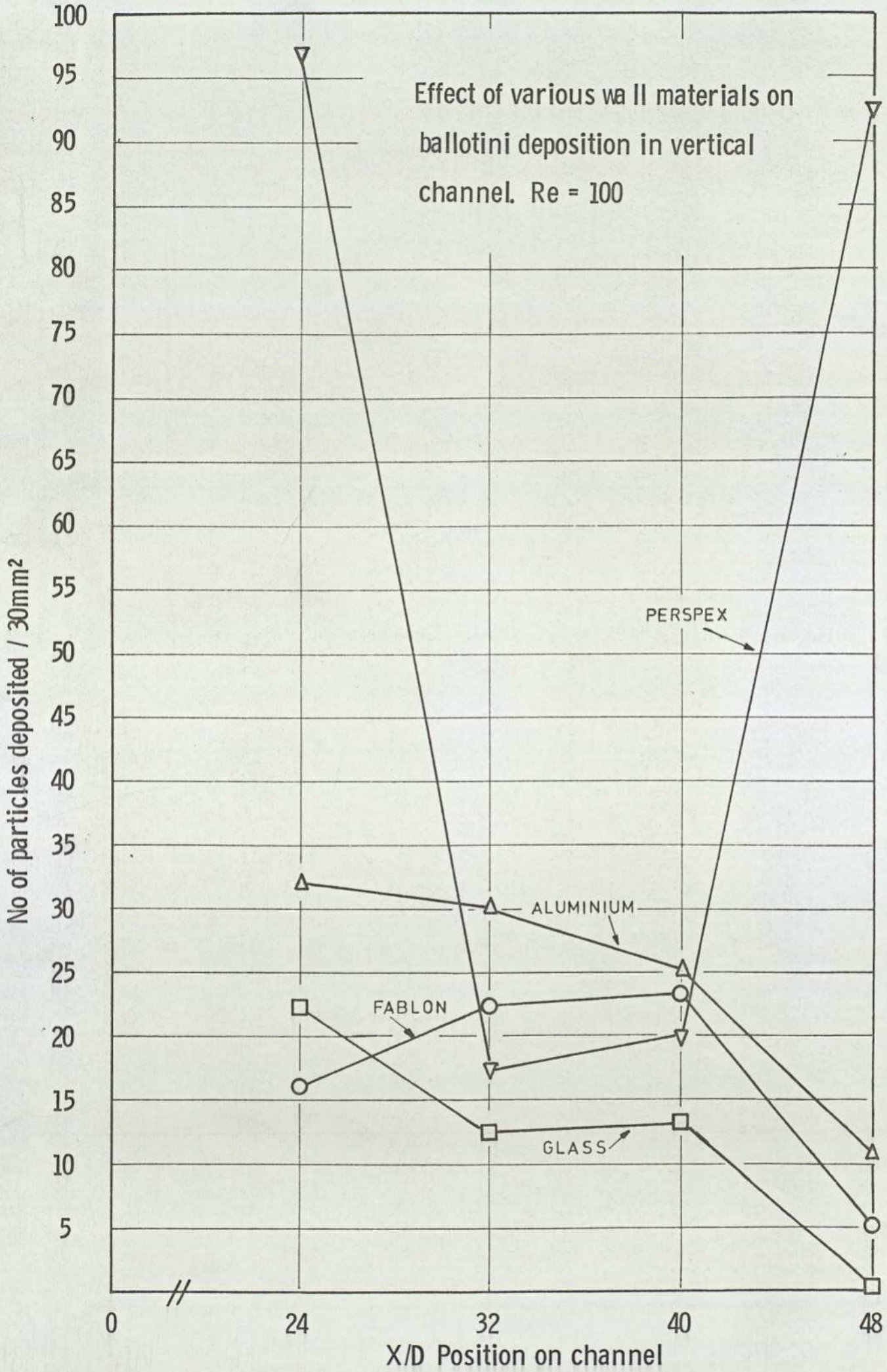
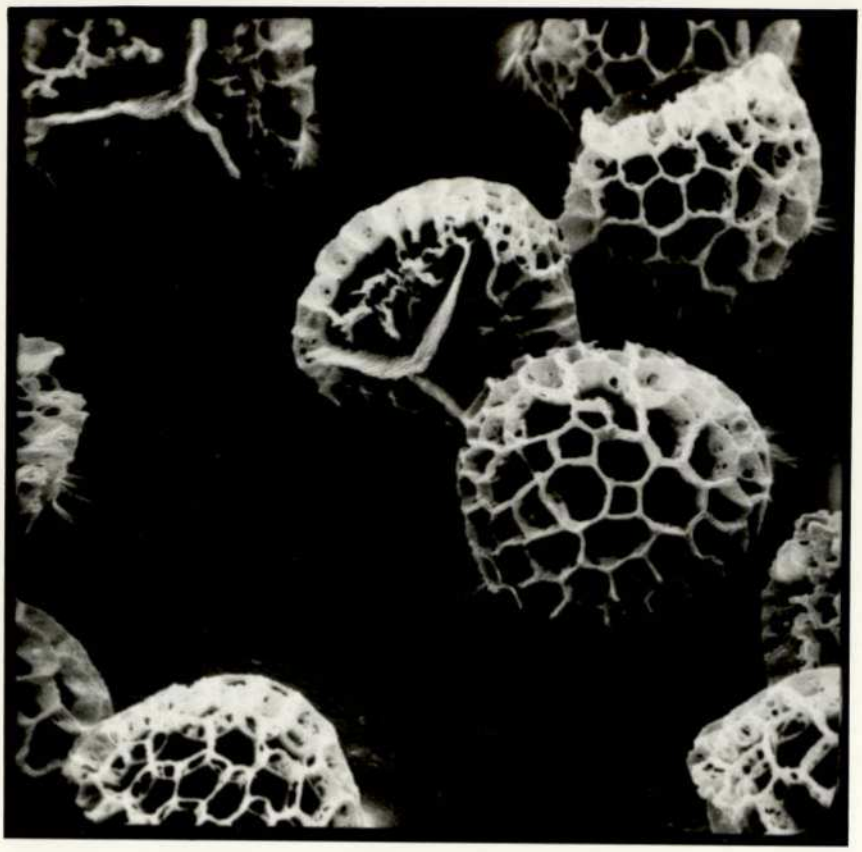

Effect of various wa ll materials on ballotini deposition in vertical channel. Re = 100
PERSPEX
ALUMINIUM
FABLON
GLASS
No of particles deposited / 30mm²
X/D Position on channel
100
95
90
85
80
75
70
65
60
55
50
45
40
35
30
25
20
15
10
5
0
24
32
40
48

Figure 64



Lycopodium

Figure 65

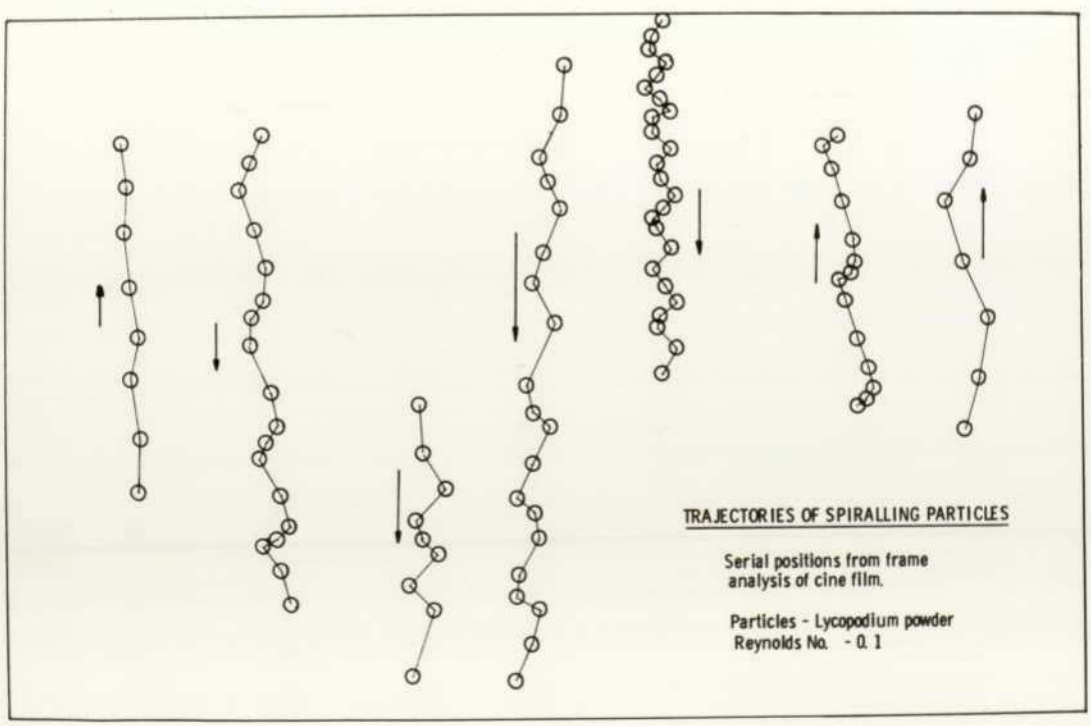
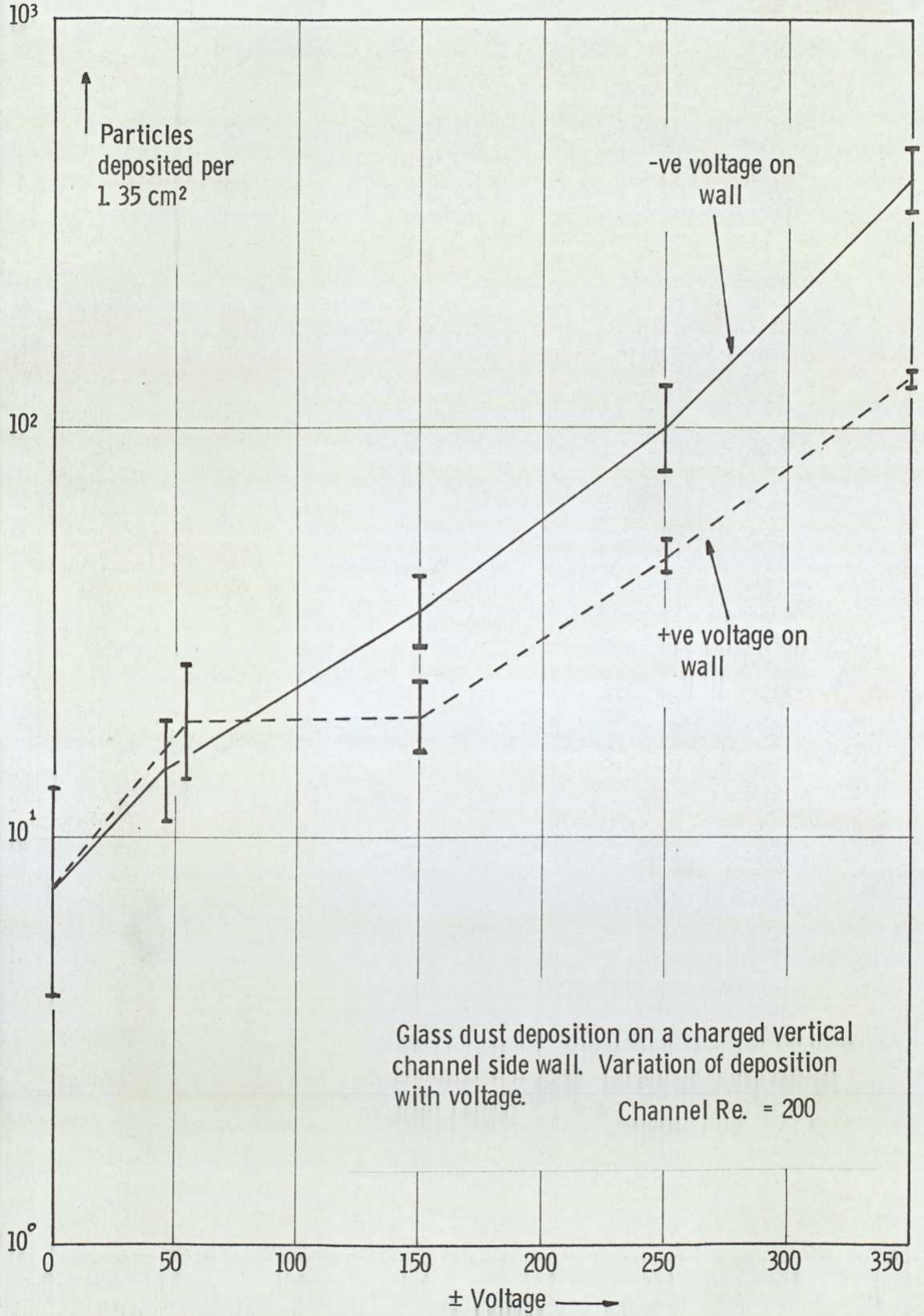
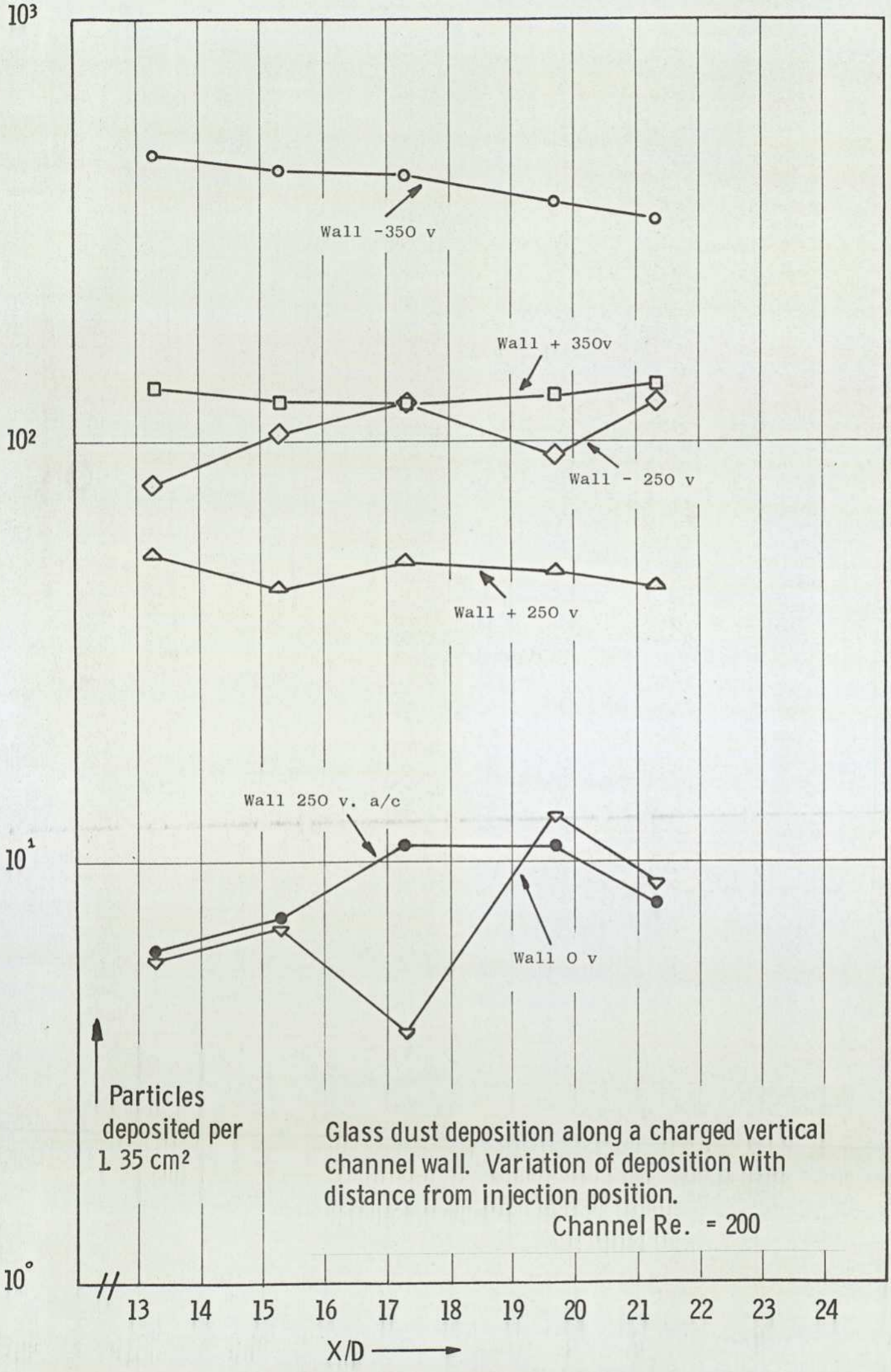


Figure 66



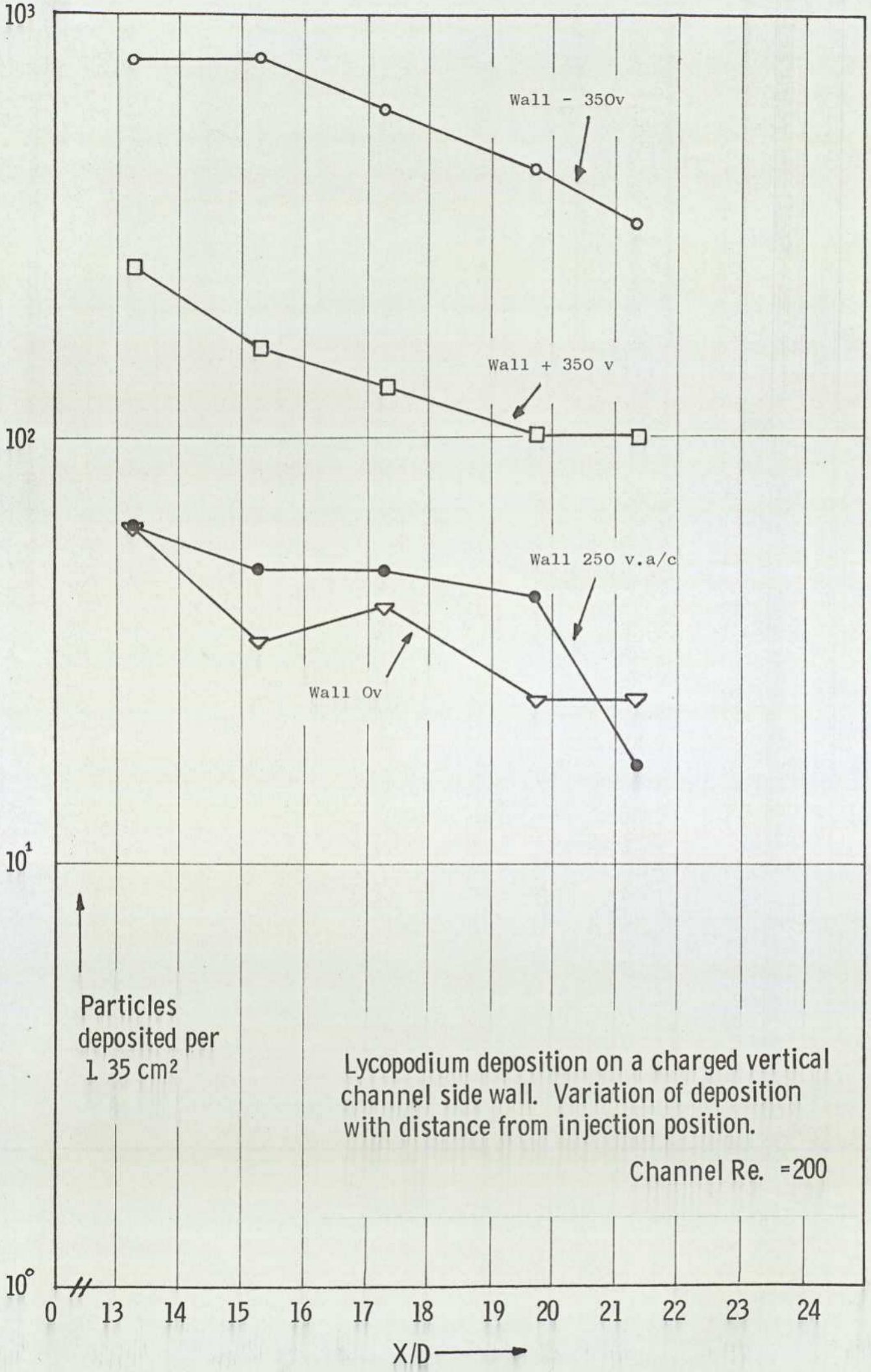
Glass dust deposition on a charged vertical channel side wall. Variation of deposition with voltage.

Channel Re. = 200



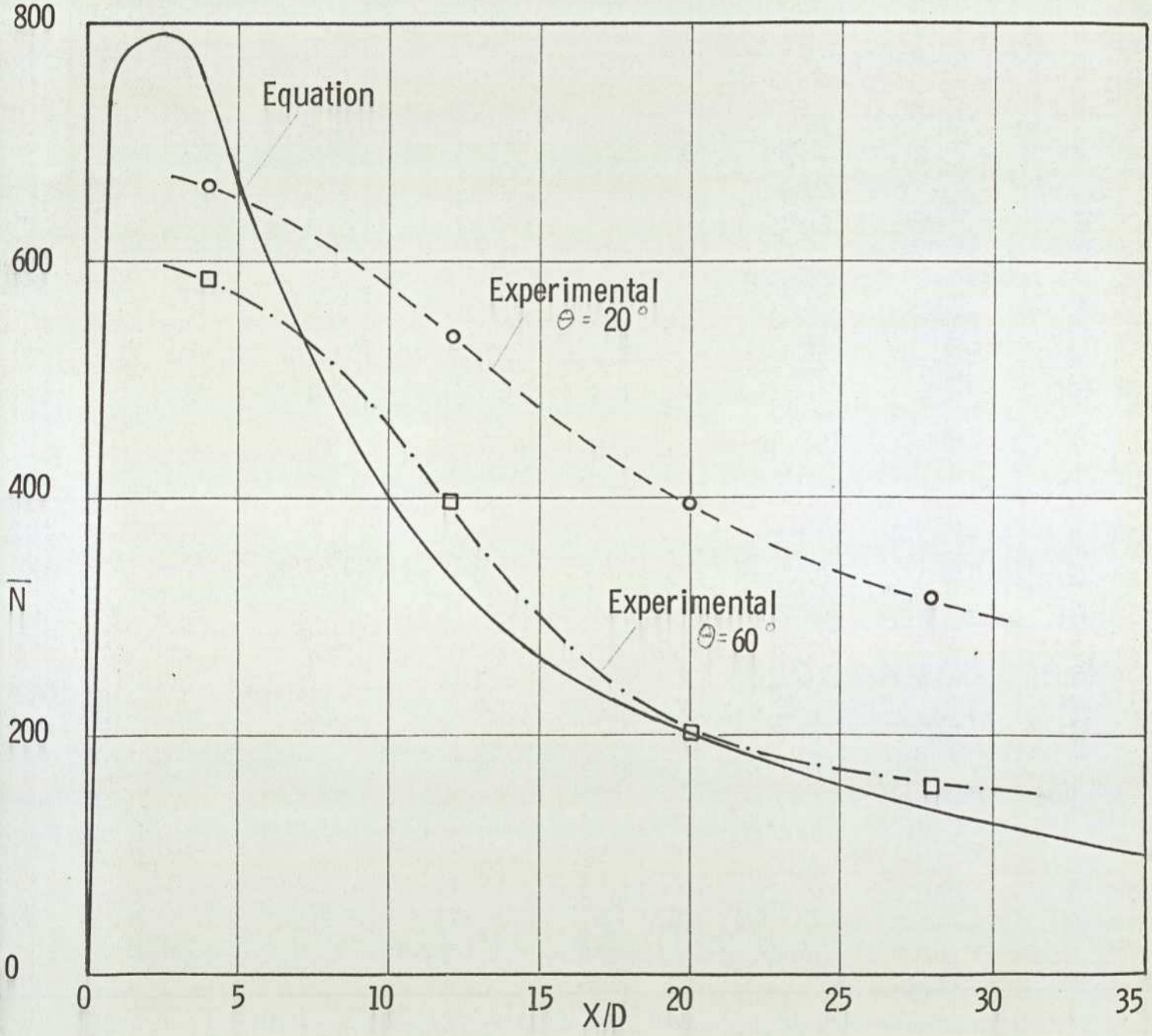
Glass dust deposition along a charged vertical channel wall. Variation of deposition with distance from injection position.

Channel Re. = 200



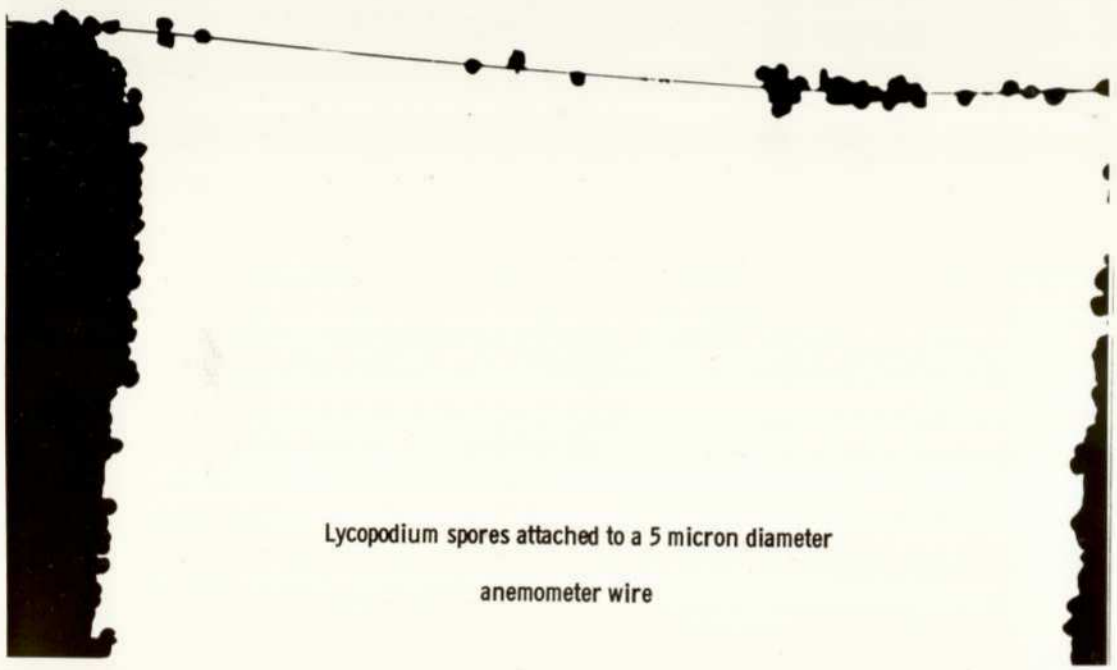
Lycopodium deposition on a charged vertical channel side wall. Variation of deposition with distance from injection position.

Channel Re. =200

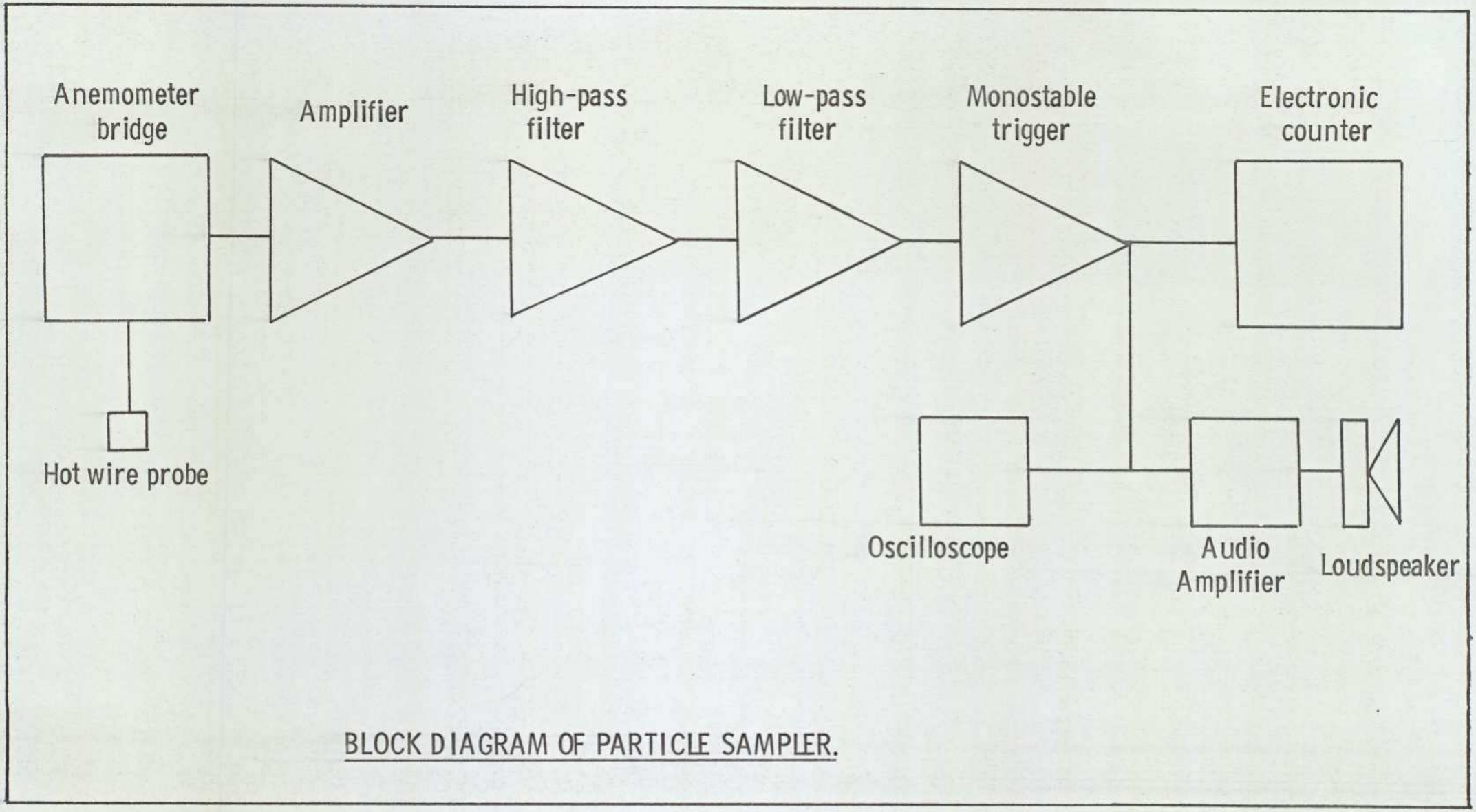


Channel floor deposition for channel inclination of 20° to vertical. Equation compared with experiment at 2 angles reduced to similar scale.

Figure 70



Lycopodium spores attached to a 5 micron diameter anemometer wire



BLOCK DIAGRAM OF PARTICLE SAMPLER.

Figure 71

CIRCUIT DIAGRAM OF PARTICLE SAMPLER

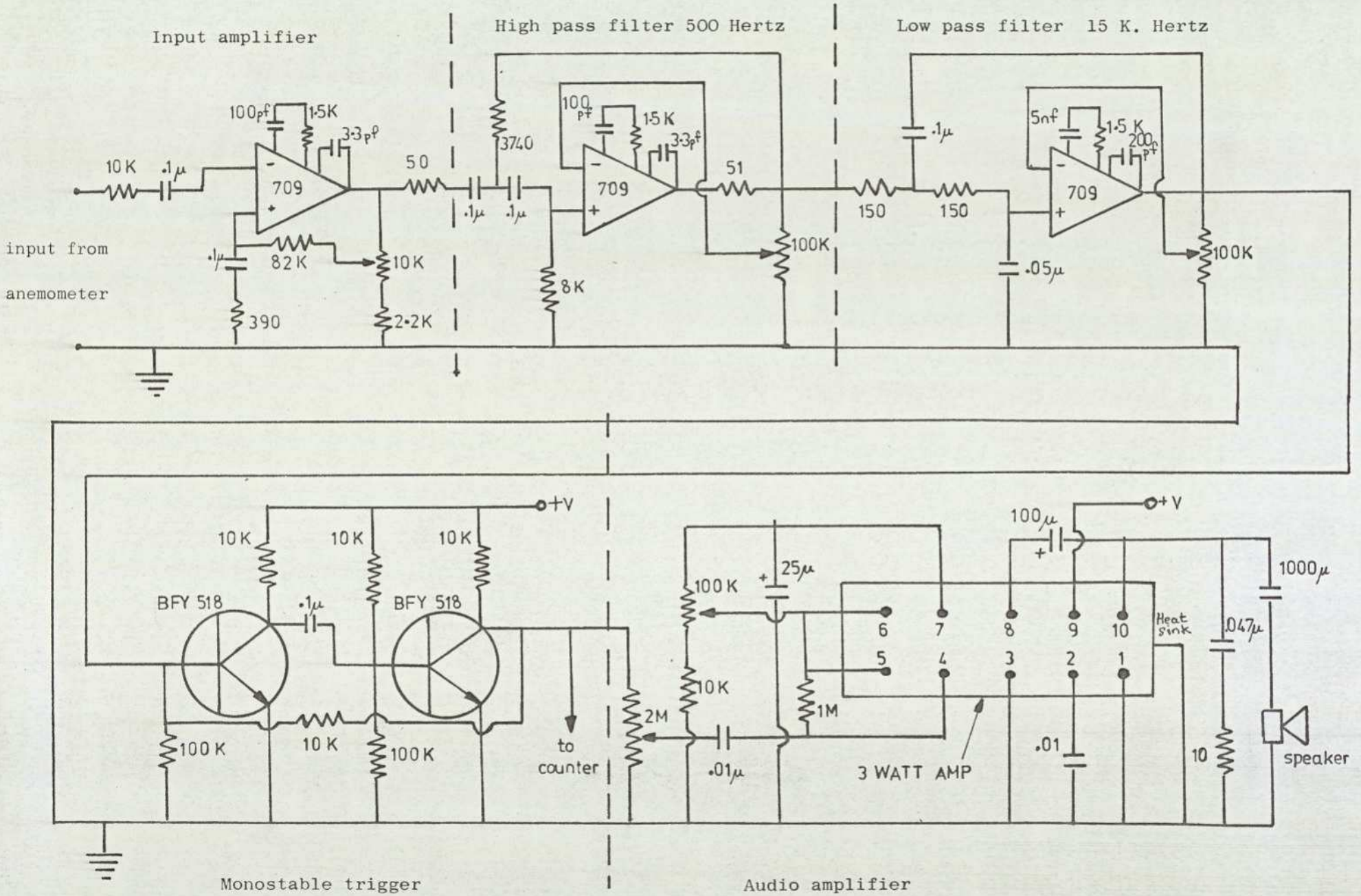
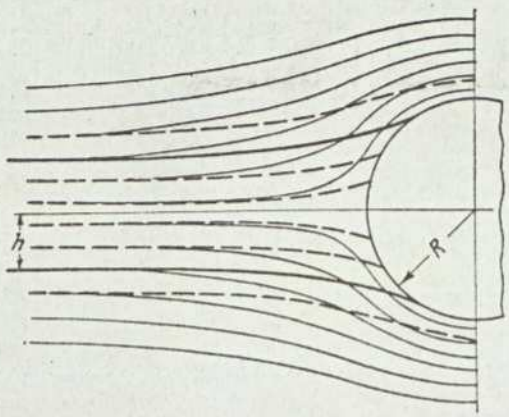
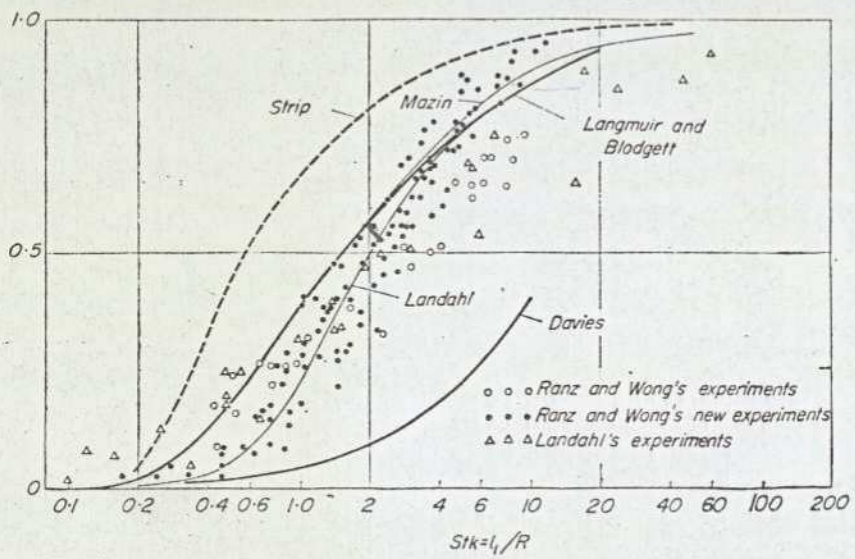


Figure 72

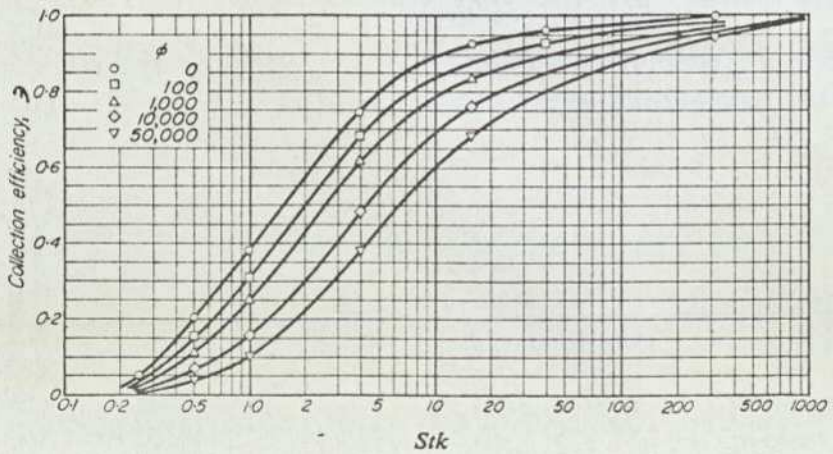
Figure 73



Inertial deposition of particles and the collection efficiency.

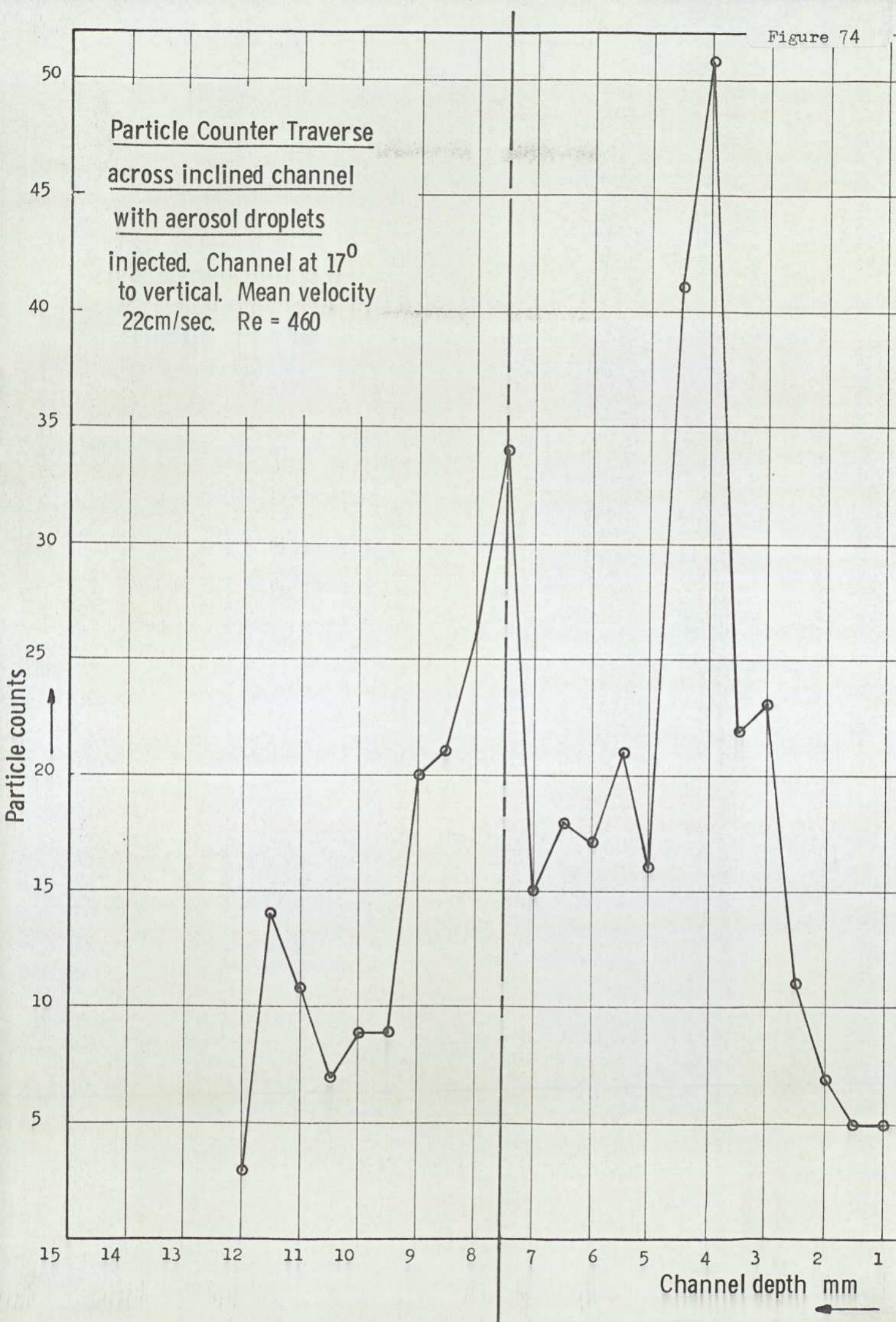


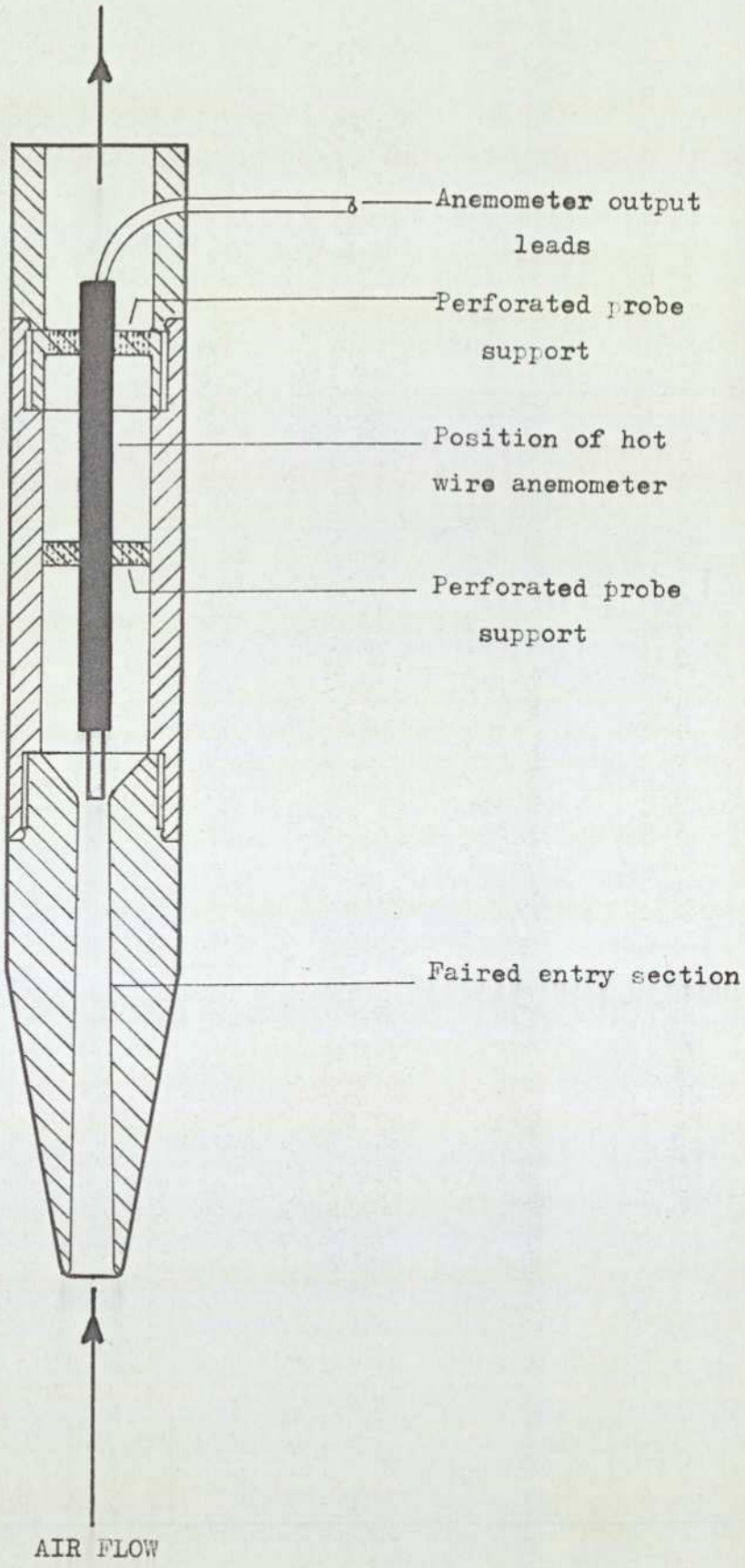
Efficiency of inertial deposition on a cylinder.



Inertial deposition of particles for potential flow past a cylinder.

Figure 74


Particle Counter Traverse
across inclined channel
with aerosol droplets
injected. Channel at 17° to vertical. Mean velocity 22cm/sec. Re = 460
Particle counts
50
45
40
35
30
25
20
15
10
5
15 14 13 12 11 10 9 8 7 6 5 4 3 2 1
Channel depth mm



Scale: full size

BOUNDARY LAYER SAMPLING NOZZLE INCORPORATING A HOT WIRE ANEMOMETER PROBE

Figure 76

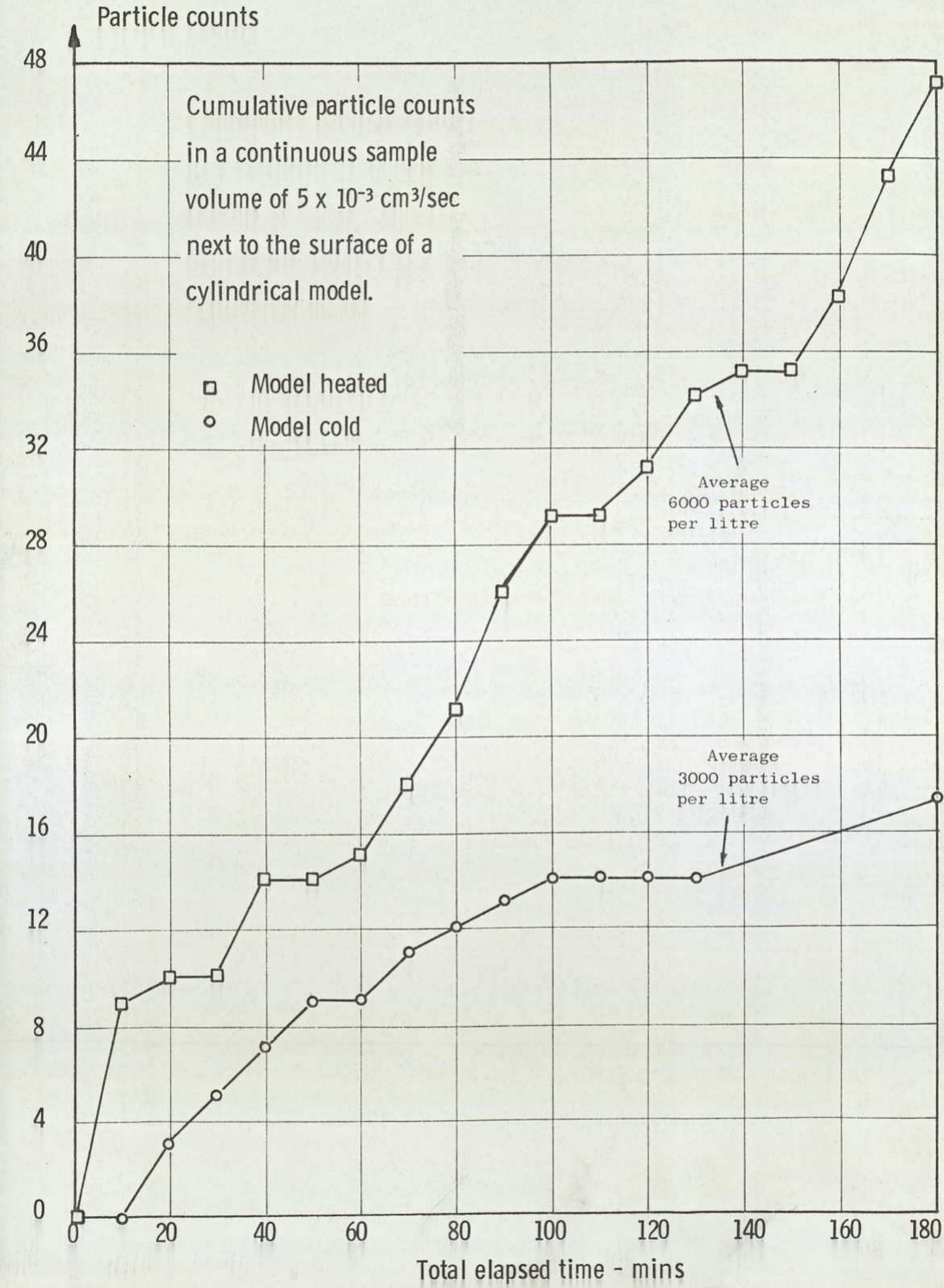

Particle counts
48
44
40
36
32
28
24
20
16
12
8
4
0
Cumulative particle counts
in a continuous sample
volume of 5 x 10⁻³ cm³/sec
next to the surface of a
cylindrical model.
Model heated
Model cold
Average
6000 particles
per litre
Average
3000 particles
per litre
0
20
40
60
80
100
120
140
160
180
Total elapsed time - mins

Figure 77

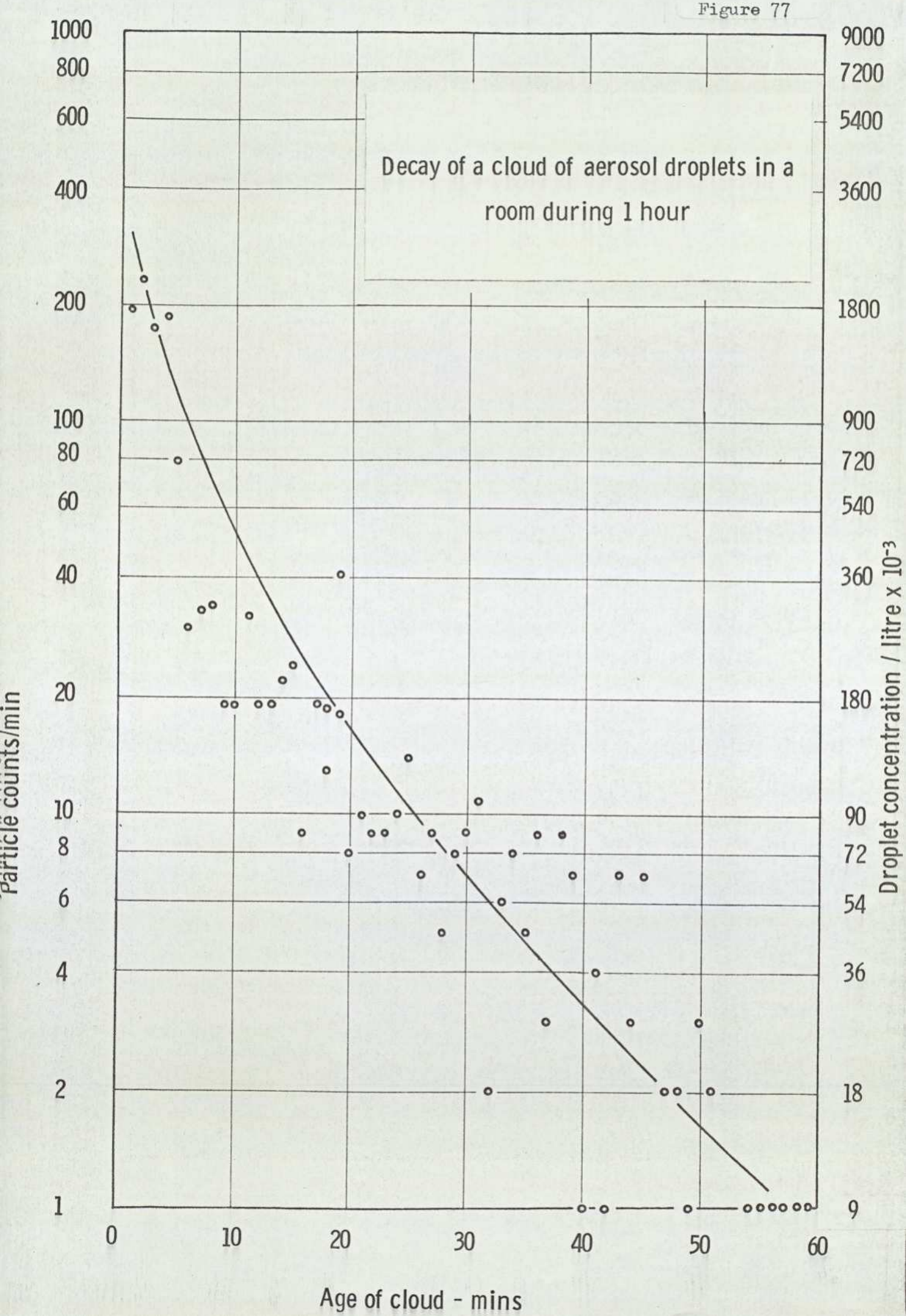

Decay of a cloud of aerosol droplets in a room during 1 hour
Particle counts/min
Droplet concentration / litre x 10^{-3}
Age of cloud - mins
1000
800
600
400
200
100
80
60
40
20
10
8
6
4
2
1
9000
7200
5400
3600
1800
900
720
540
360
180
90
72
54
36
18
9
0
10
20
30
40
50
60

Figure 78



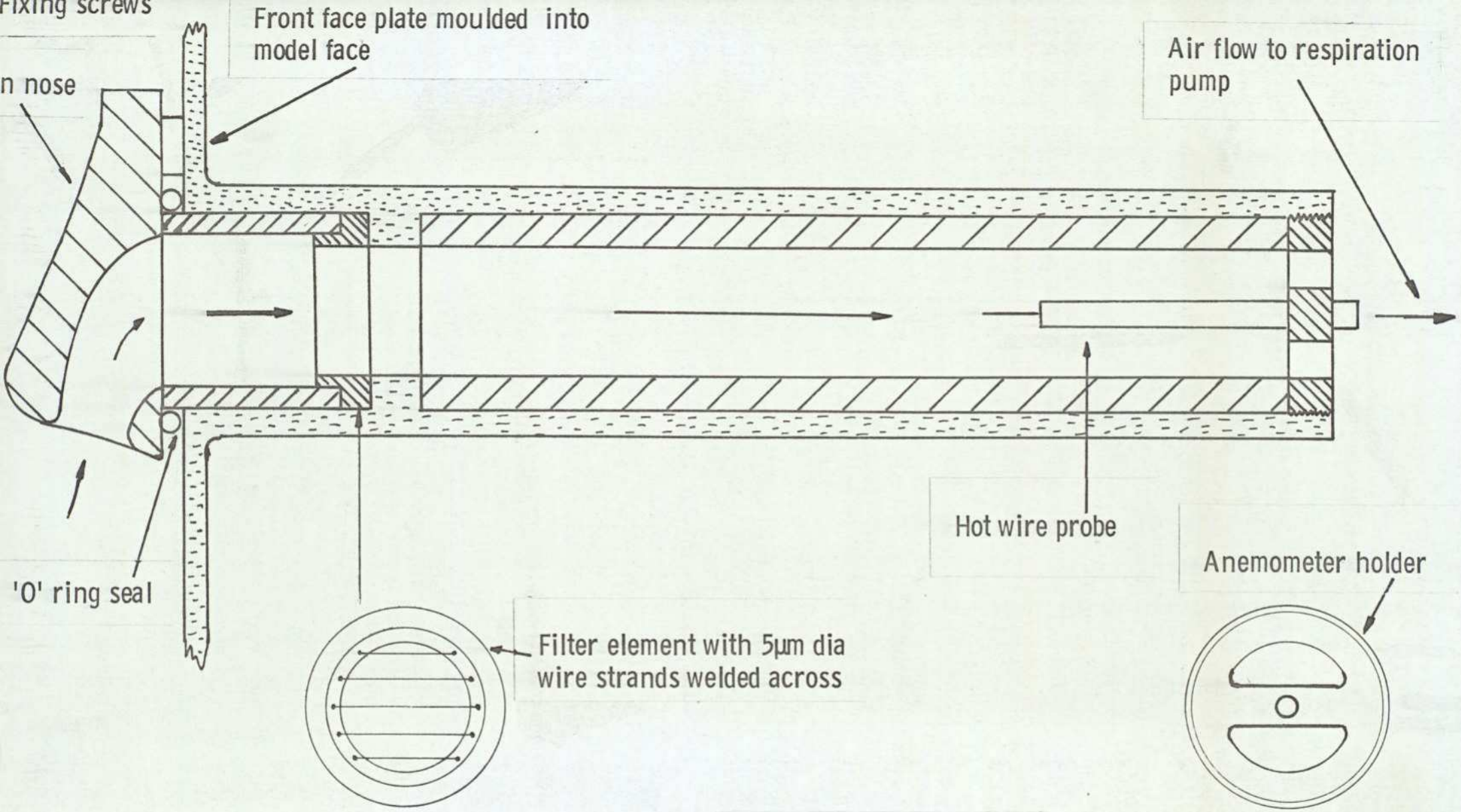
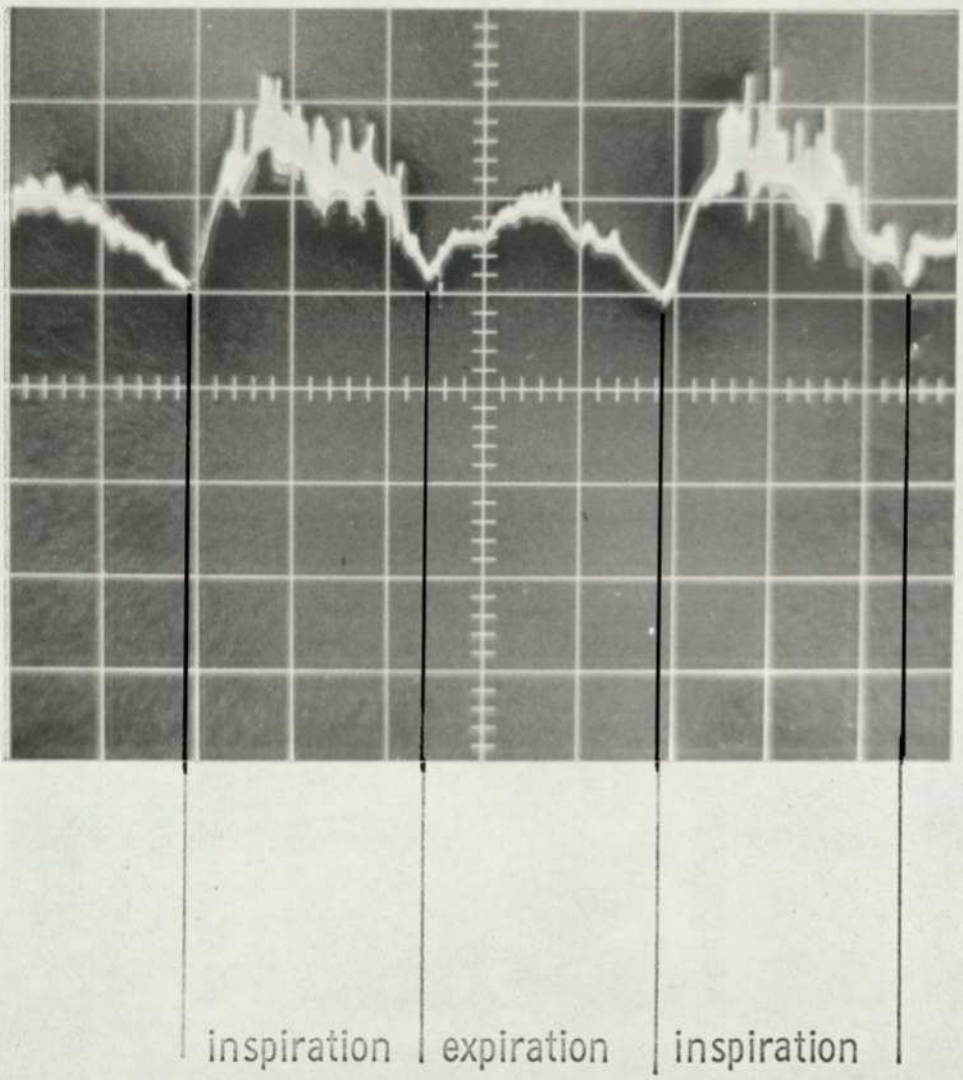
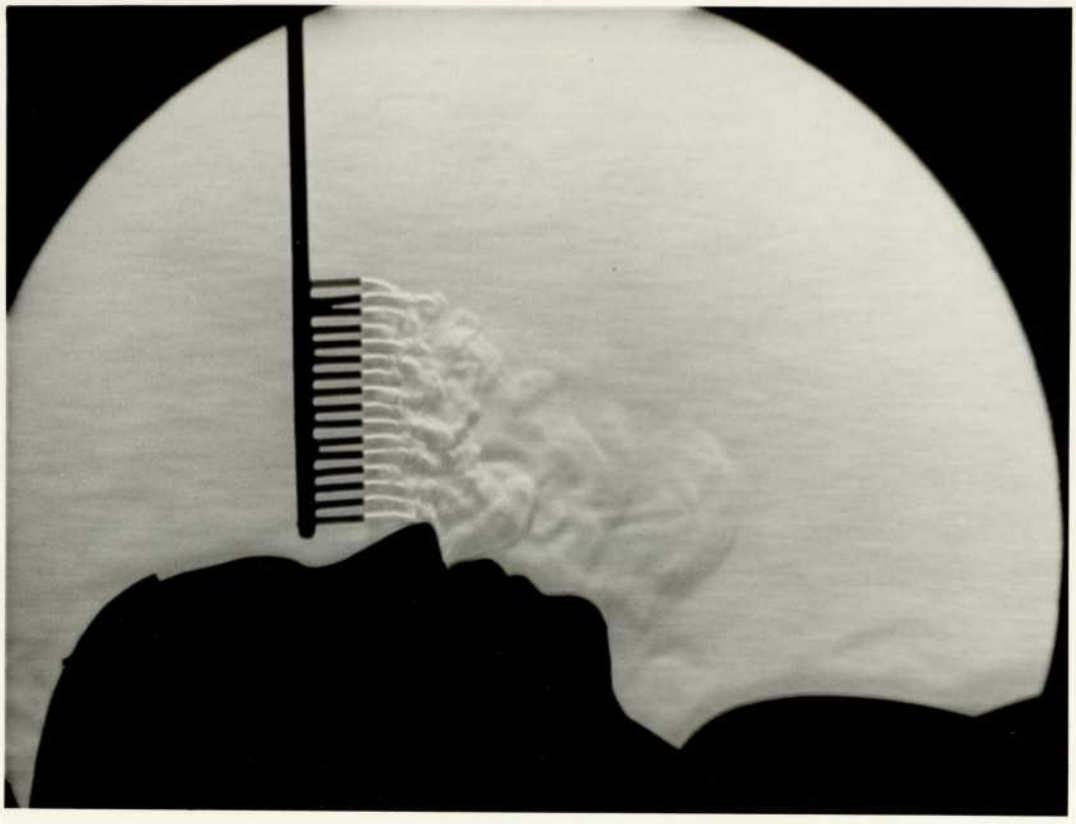


Diagram to show nose fixings and respiration tubes for model of the human form

Figure 79

Oscillograph trace of the output from the anemometer probe situated in the 'airways' of the heated model of the human form. "Breathing rate" in this trace - 18 cycles / min.





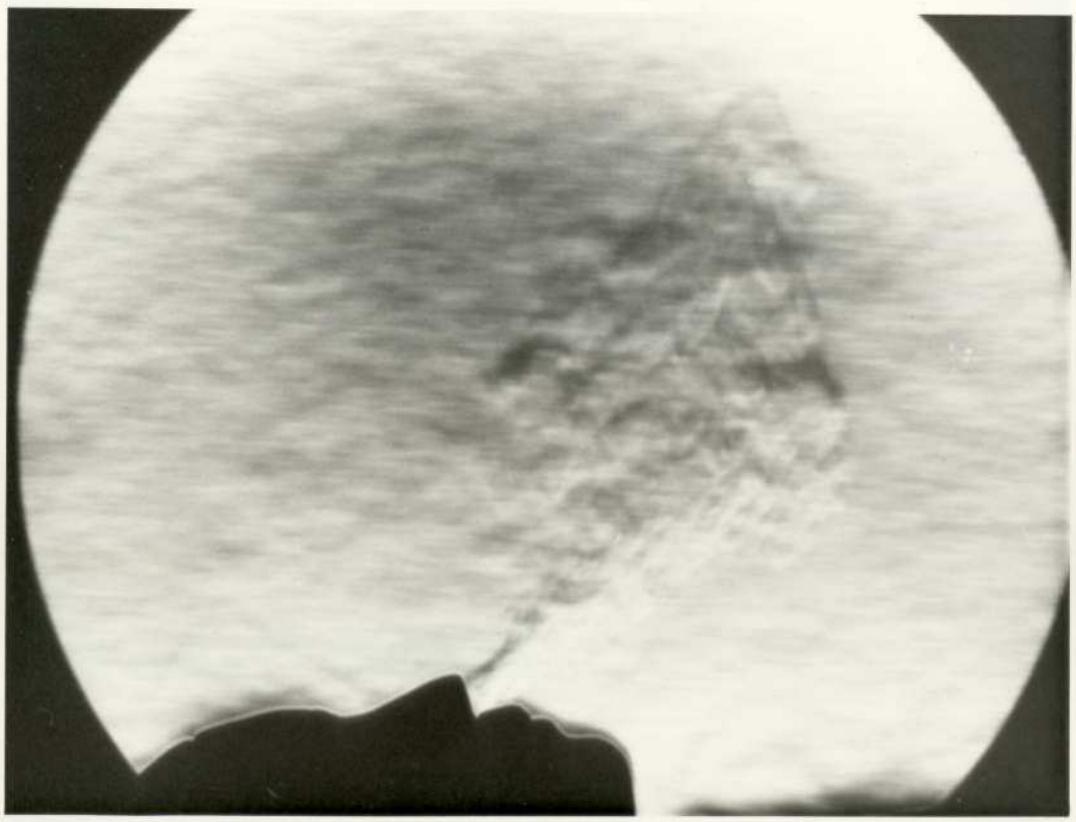


Figure 82

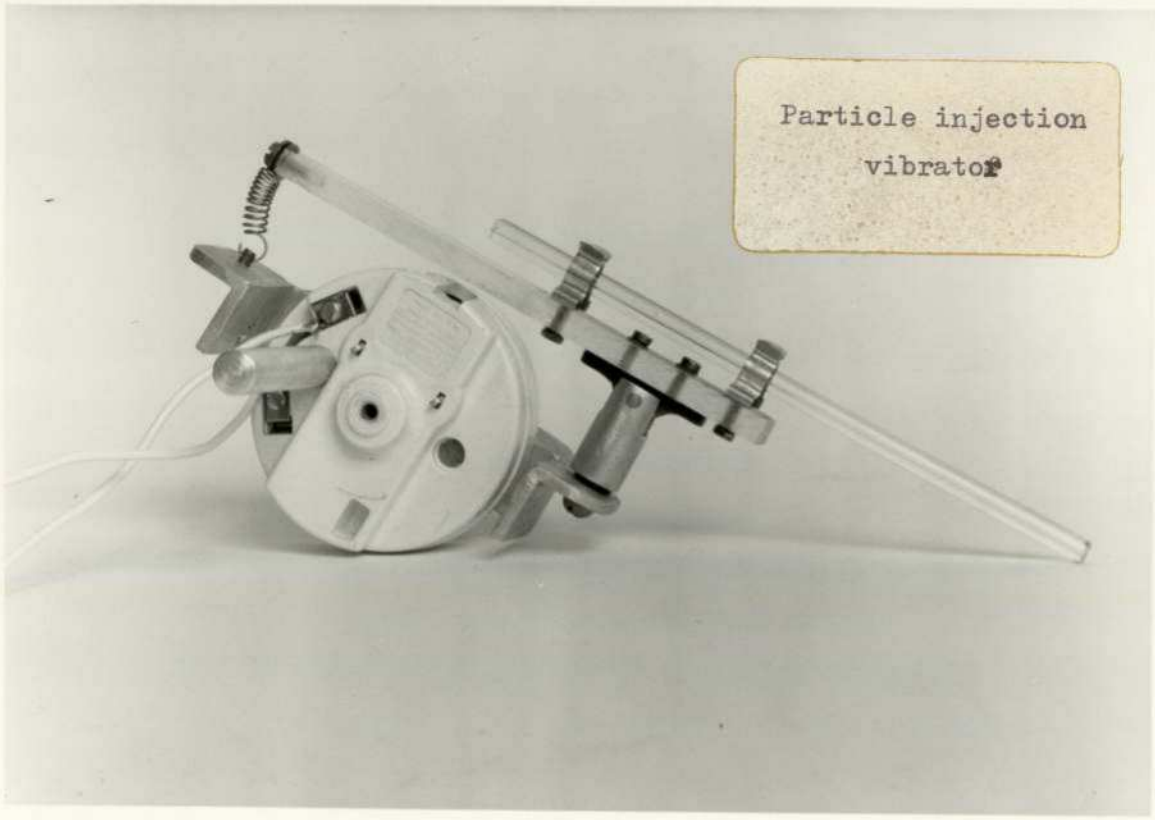
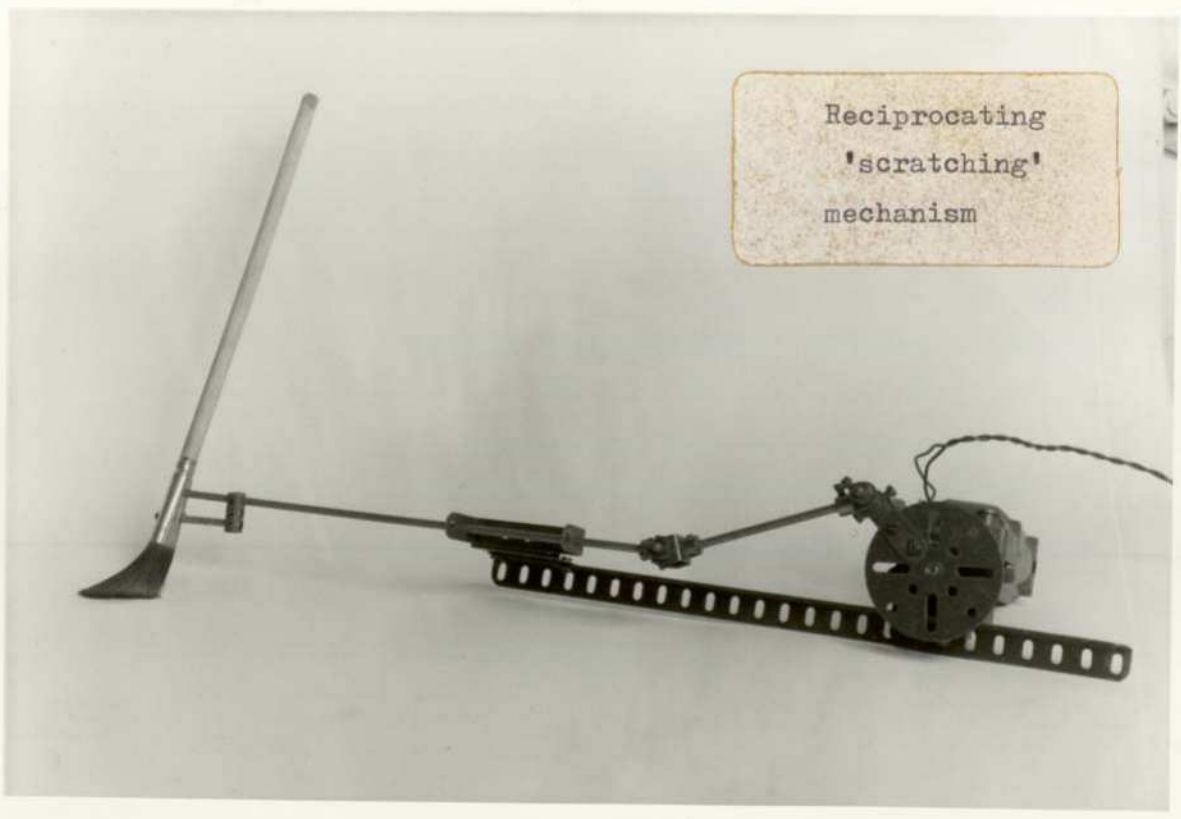
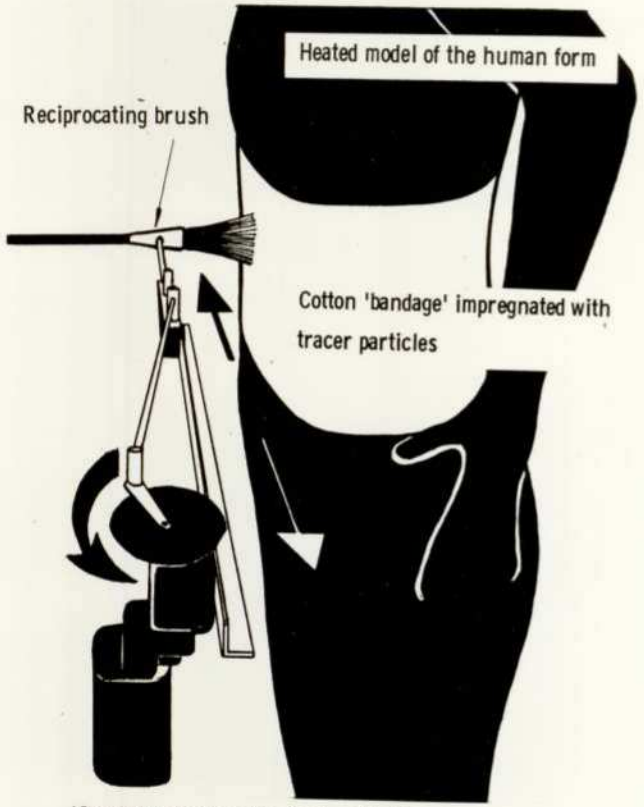


Figure 83





'Scratching' apparatus designed to liberate particles
from the model surface into the convective flow

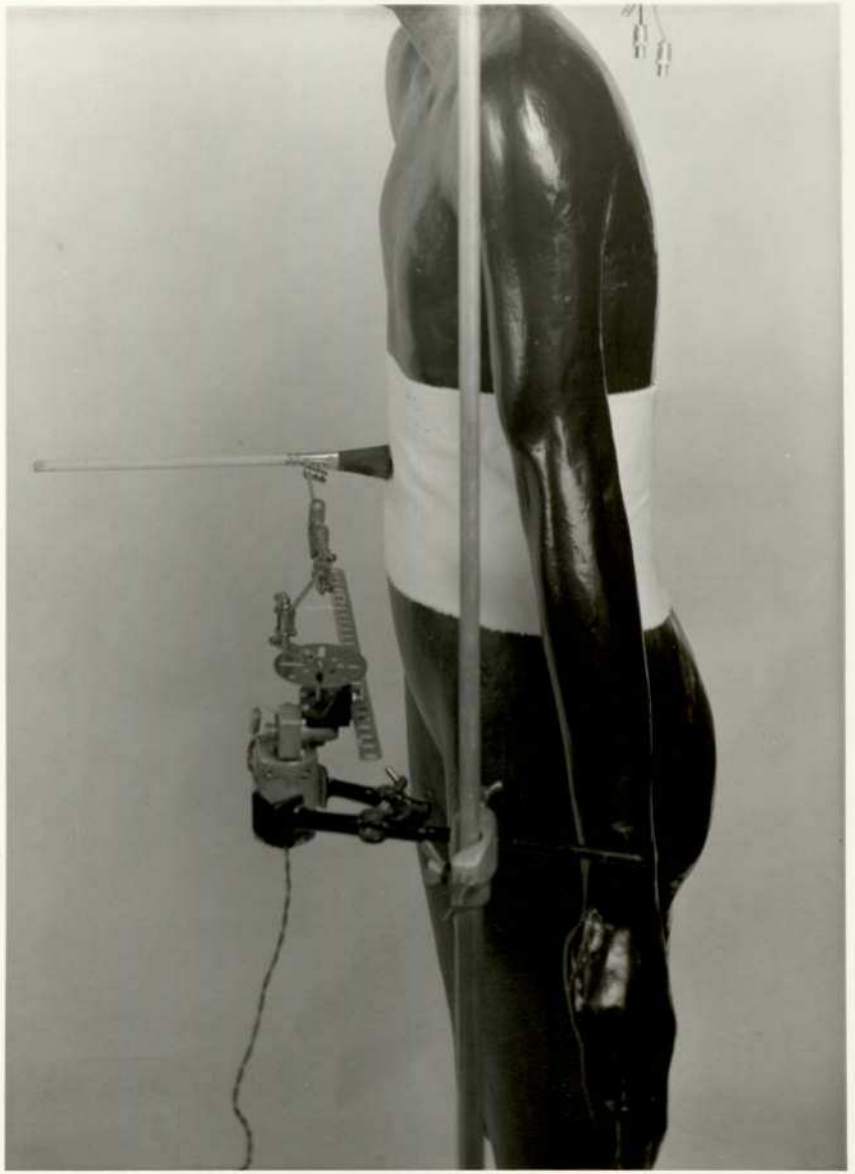
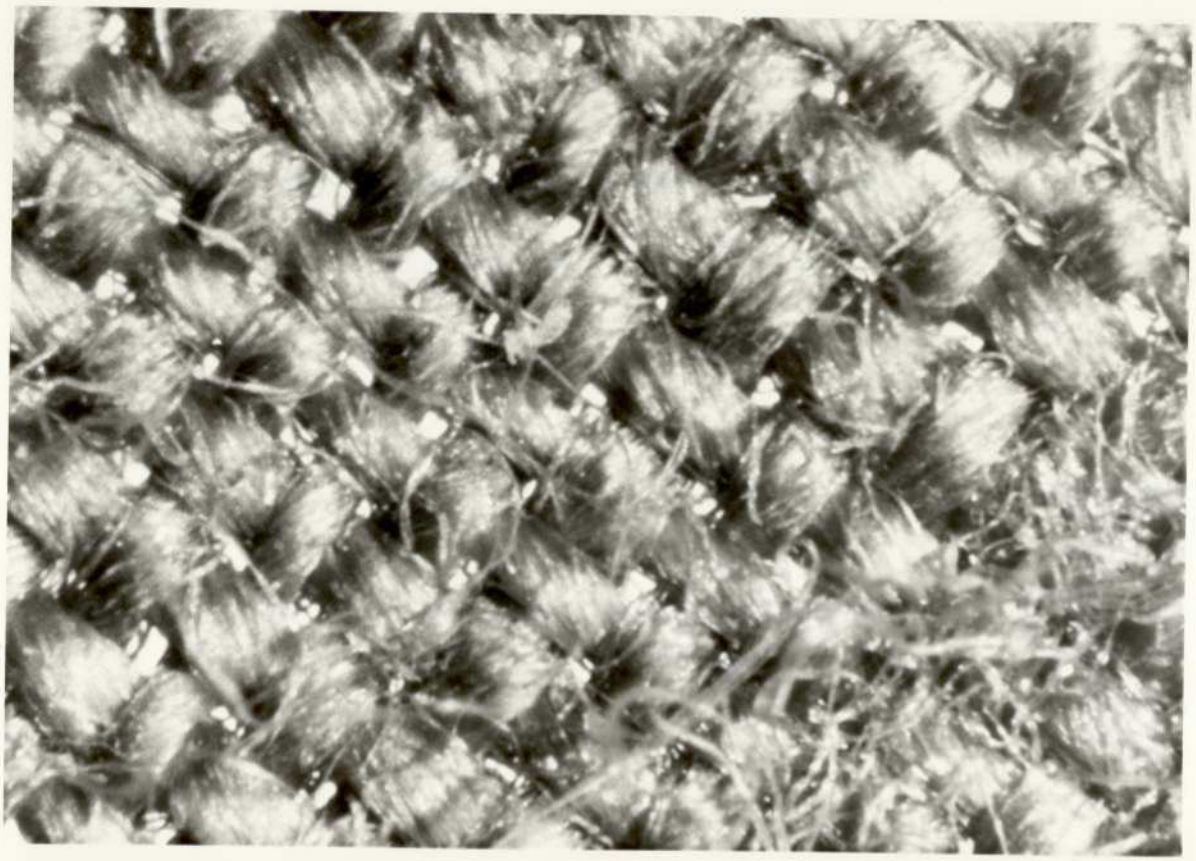


Figure 84

Figure 85

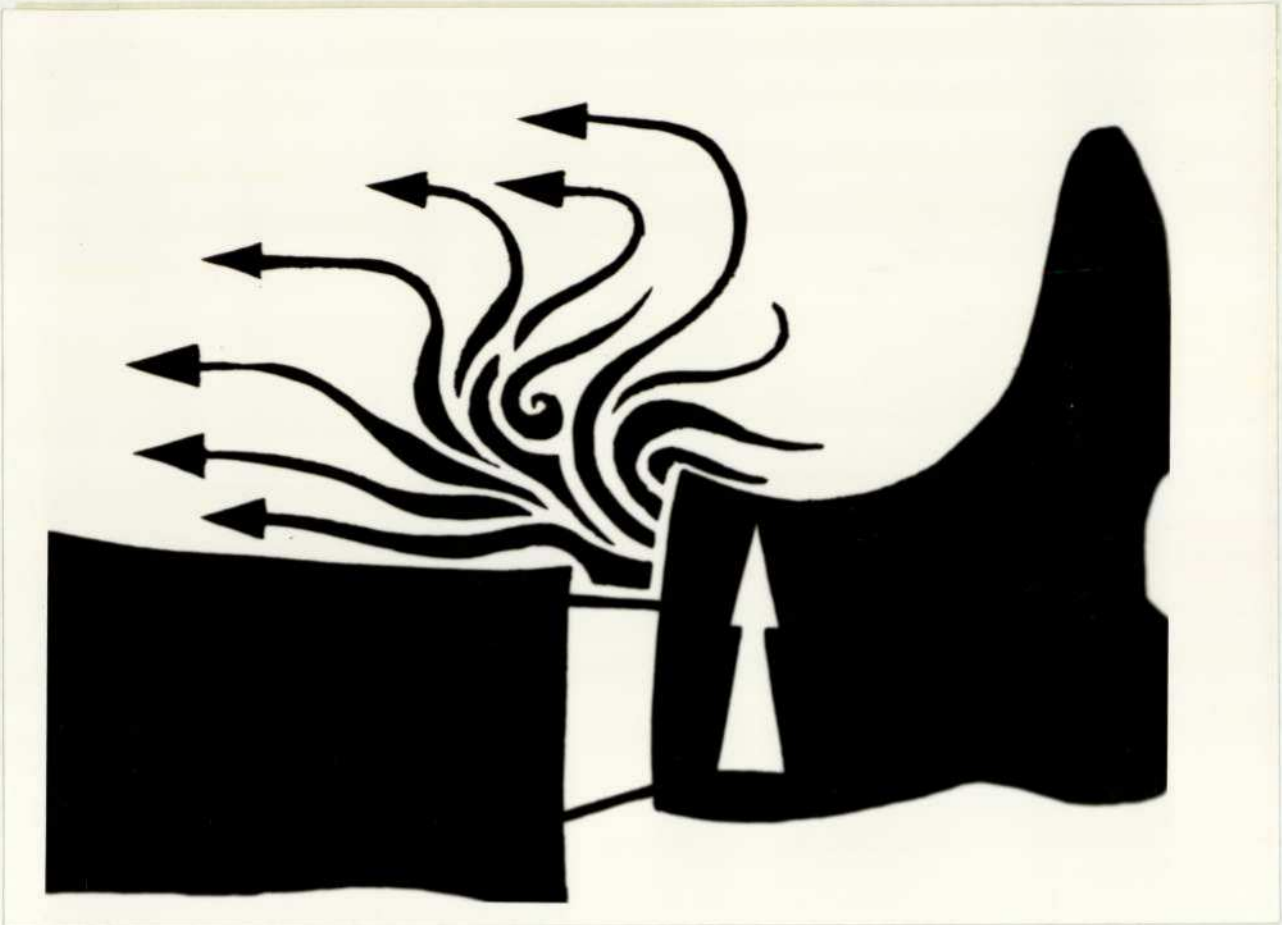


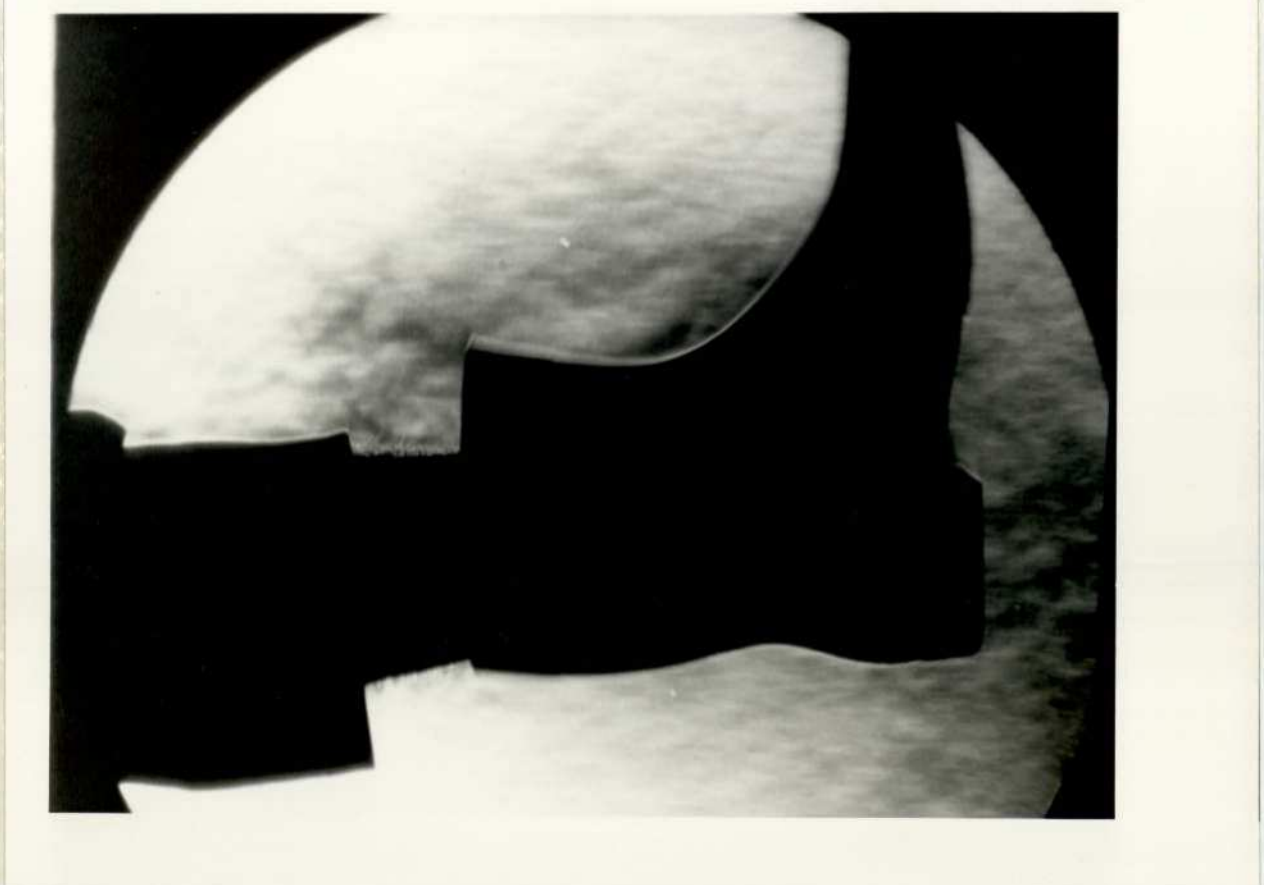
Cotton weave

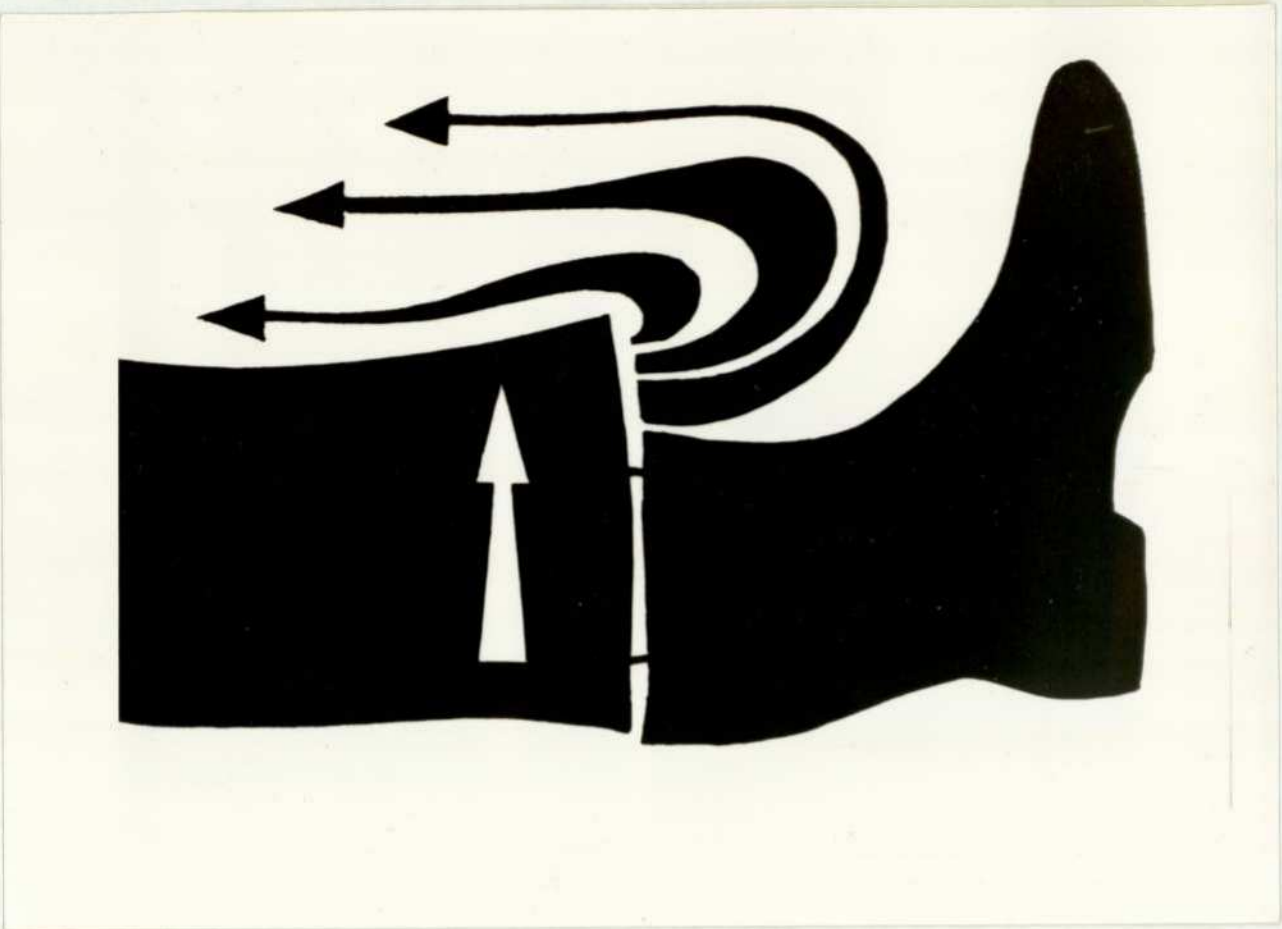
Figure 86











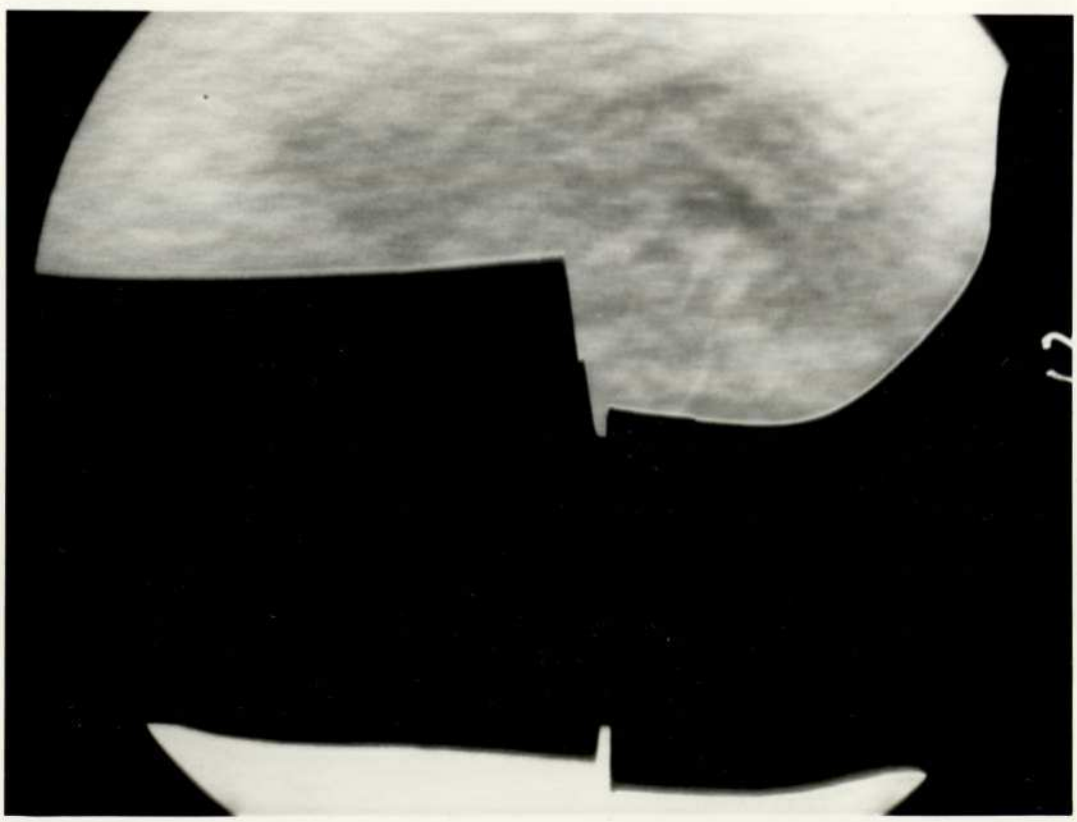


Figure 89



Figure 90

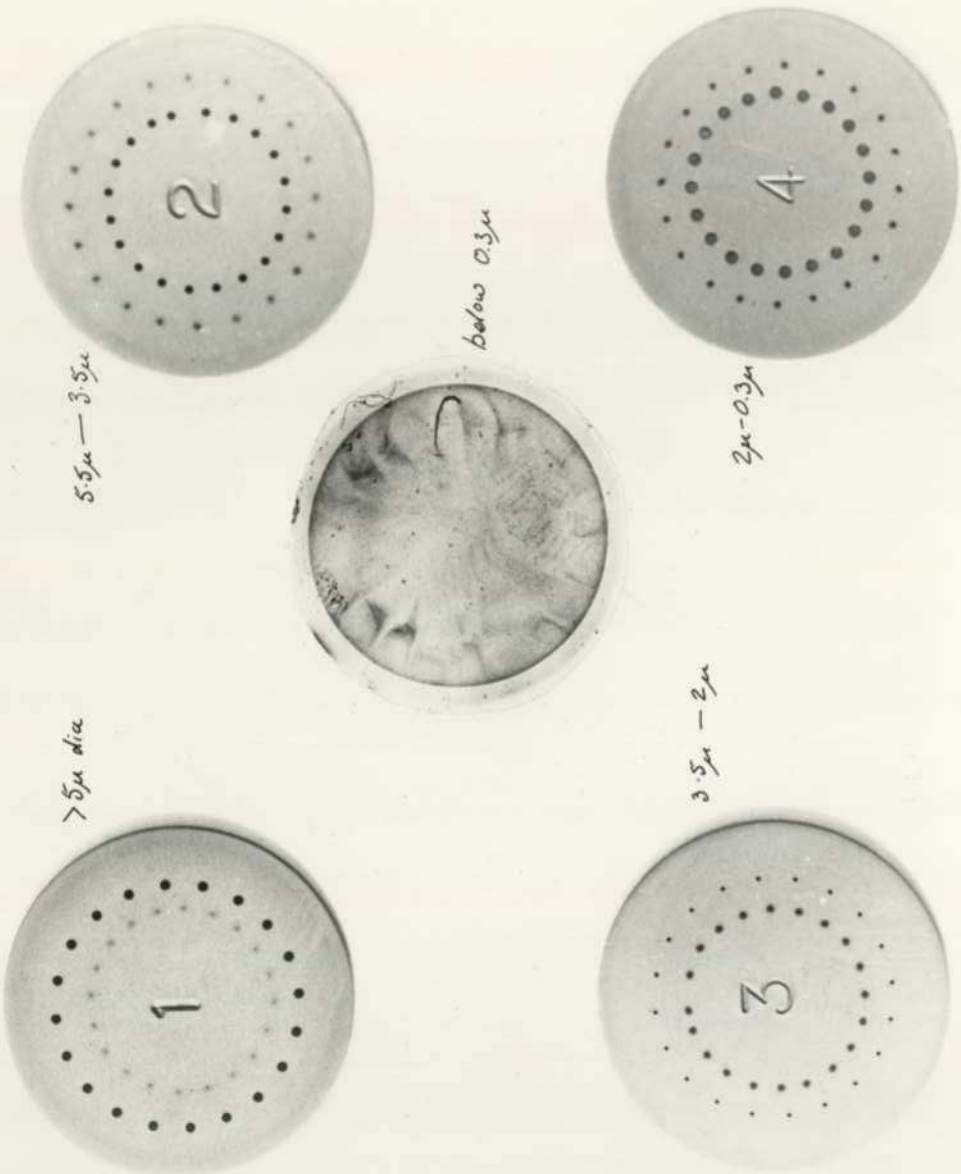




Anderson

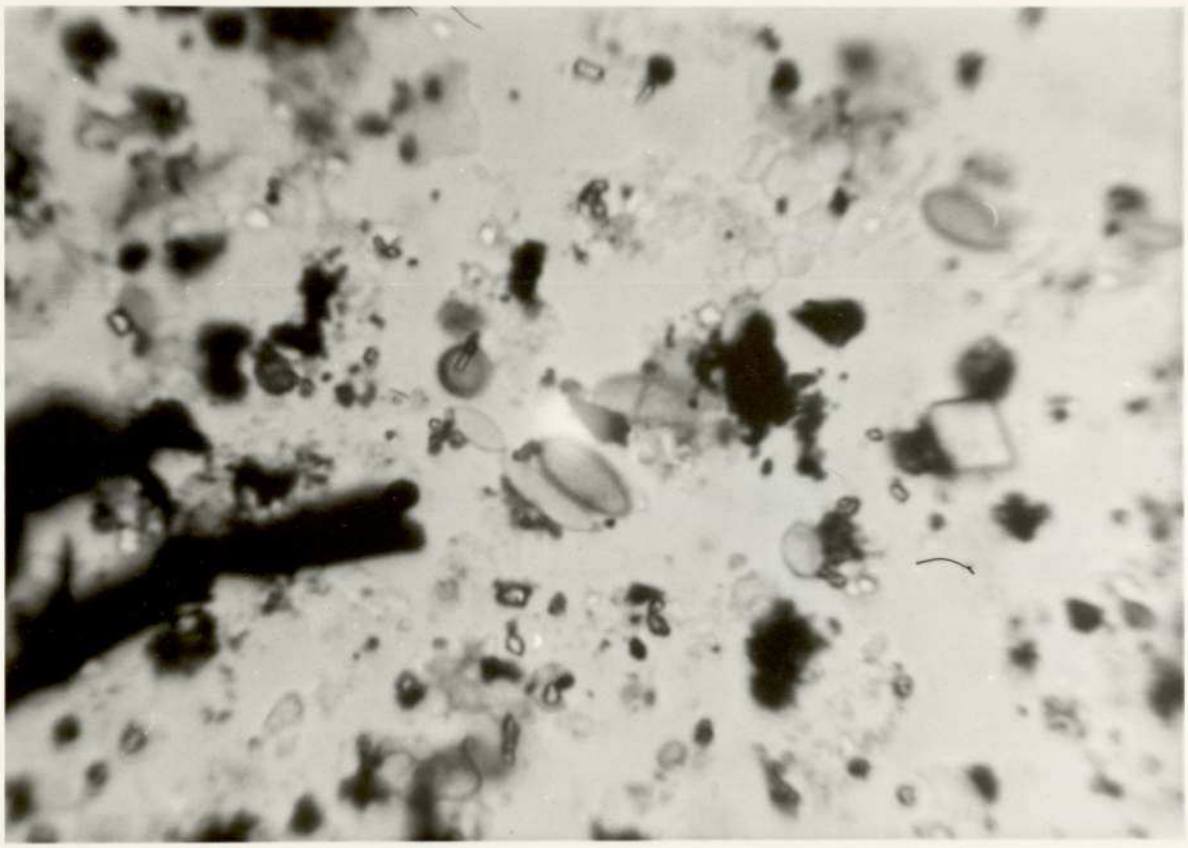
Mini sampler

Figure 91

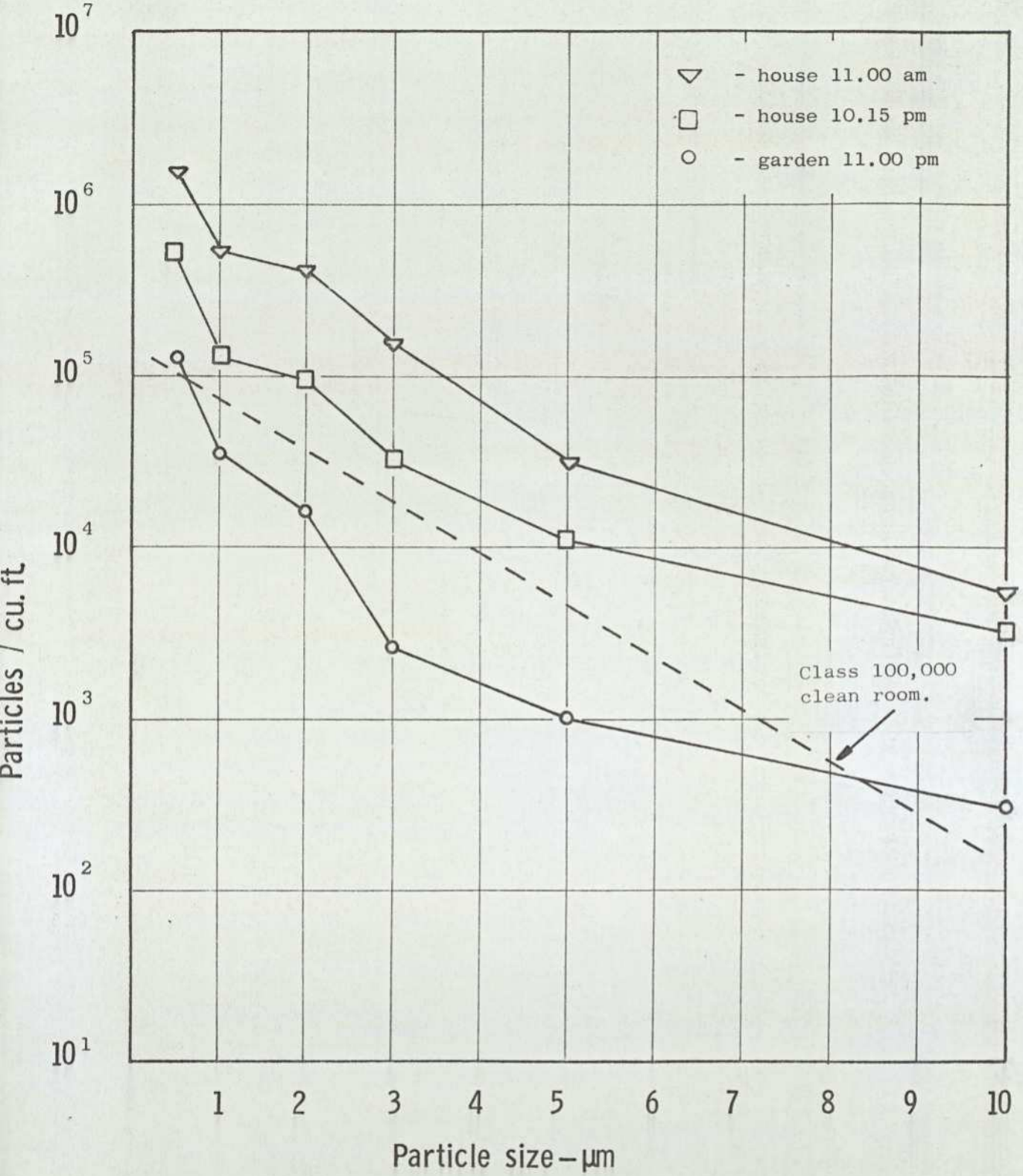


Dust samples from Northern Line
between Morden and Hampstead
June 21st 1971. Run time 1 hour
Flow 1 4 litres/min

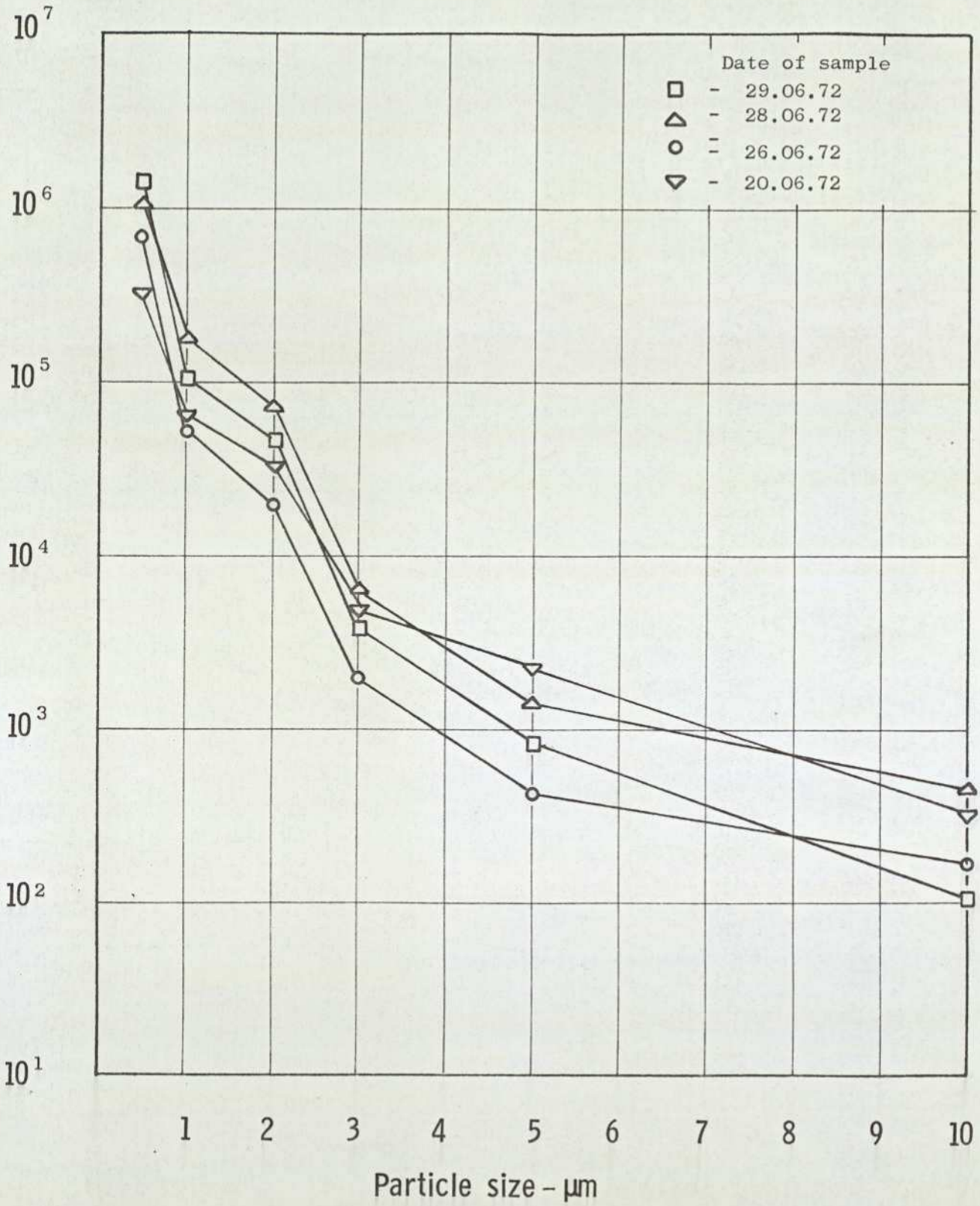
Figure 93



Garden sample

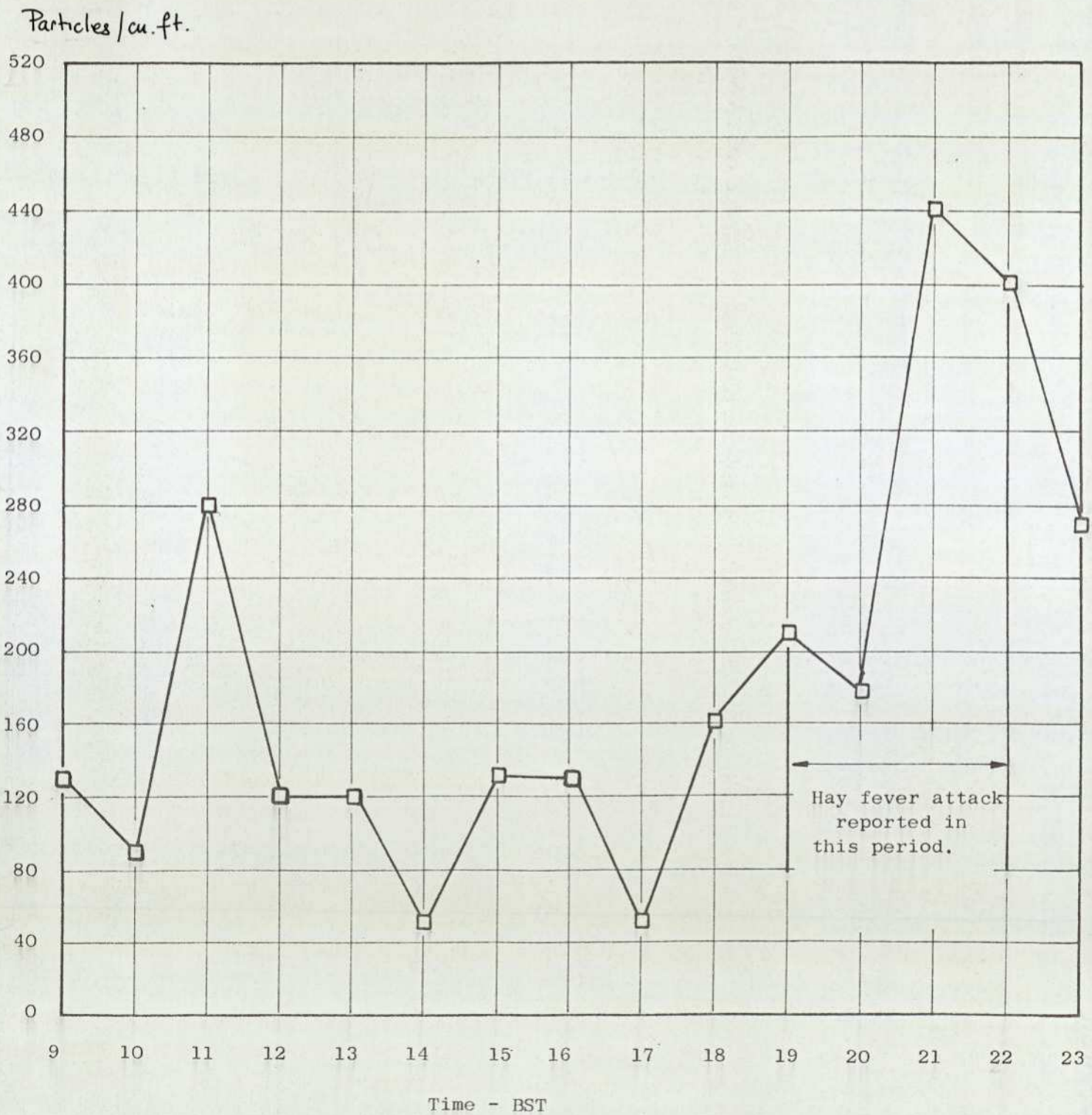


Particle concentration levels in a house and garden

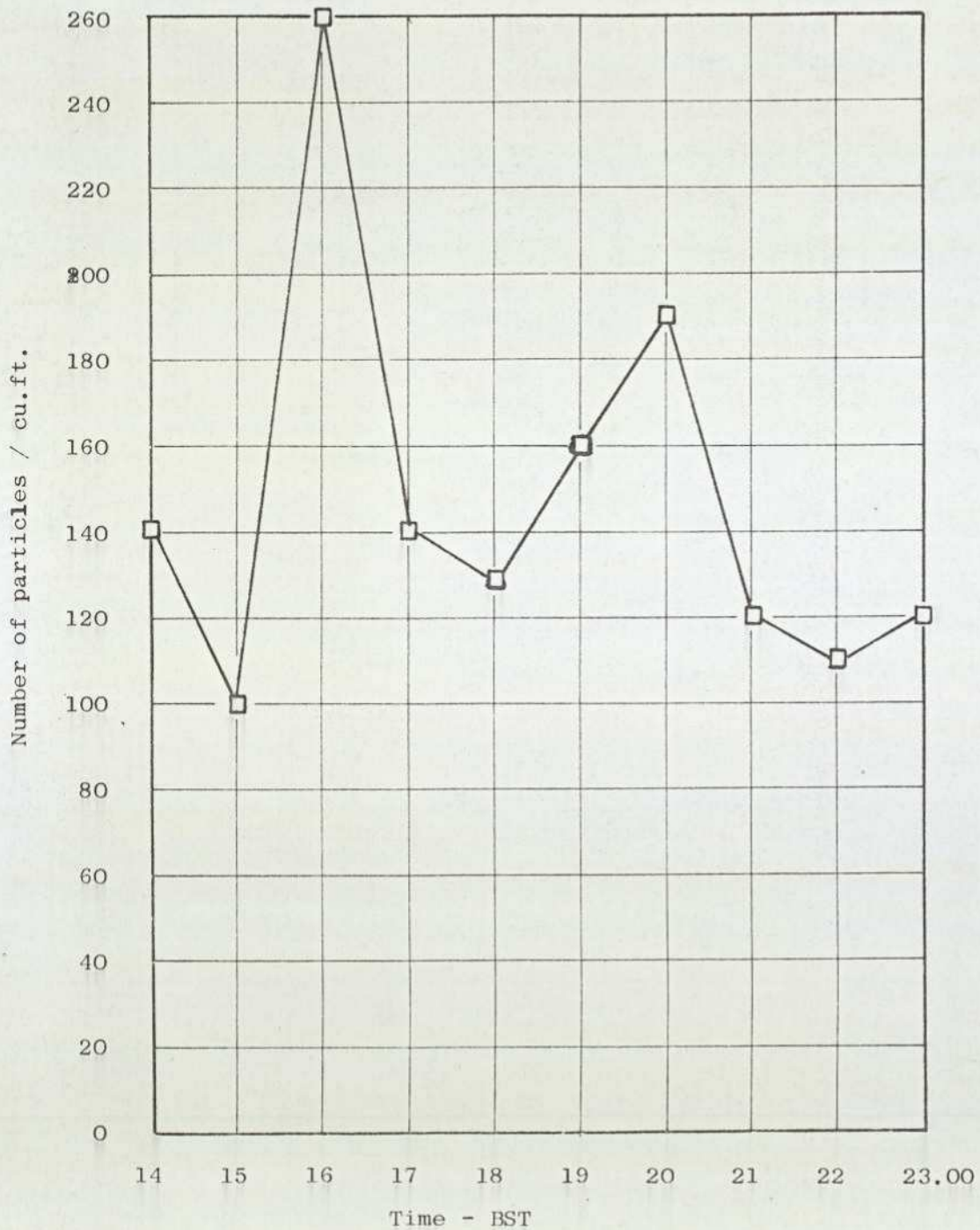


Particle concentration levels in a rural garden on 4 days

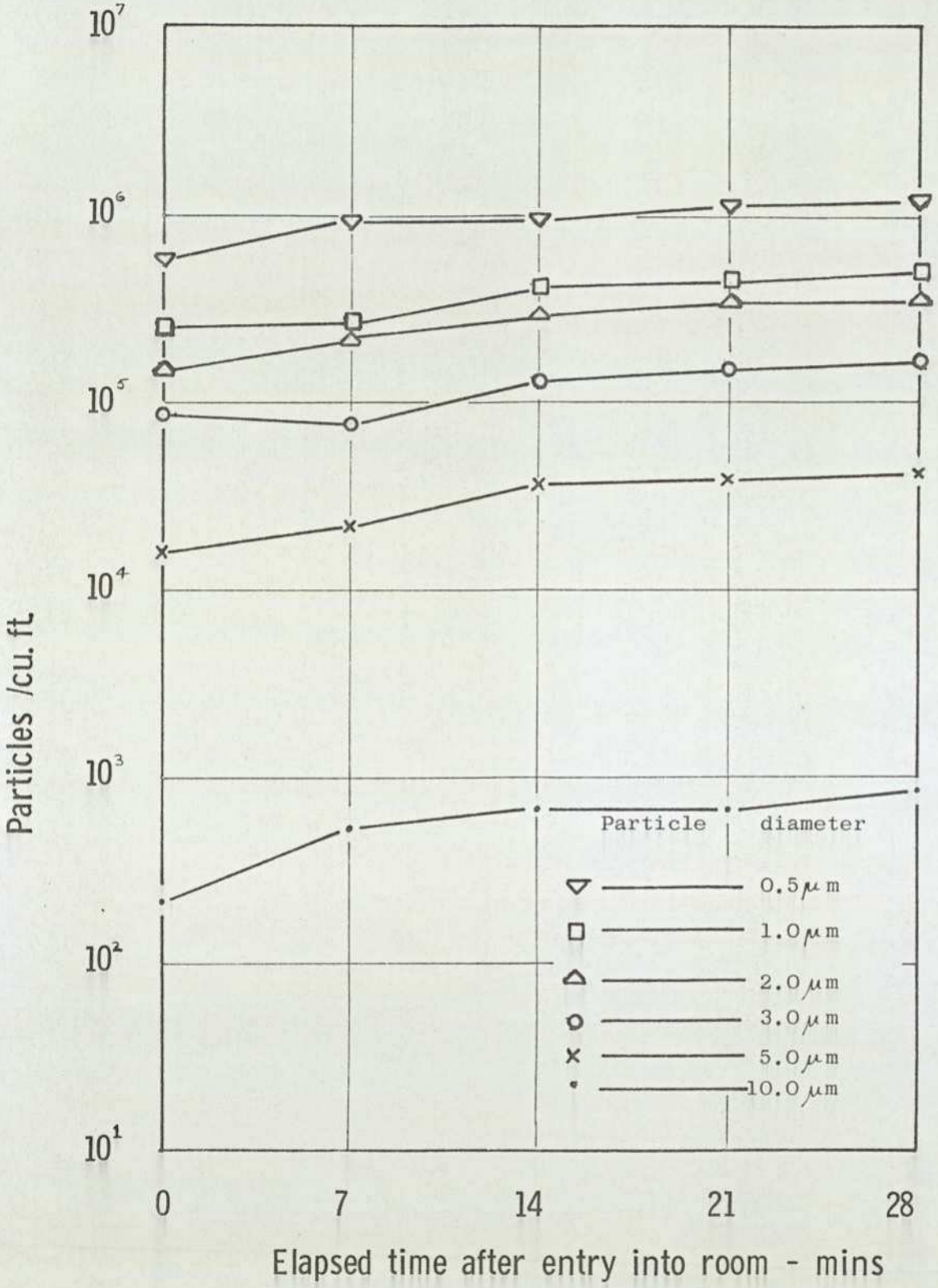
Concentration levels in garden air for particles greater than 5µm. dia. Date. - 28/06/72. Pollen count 250. Wind S.



Concentration levels in garden air for particles greater than 5µm. dia. Date 29/06/72. Pollen count 89 Wind S.

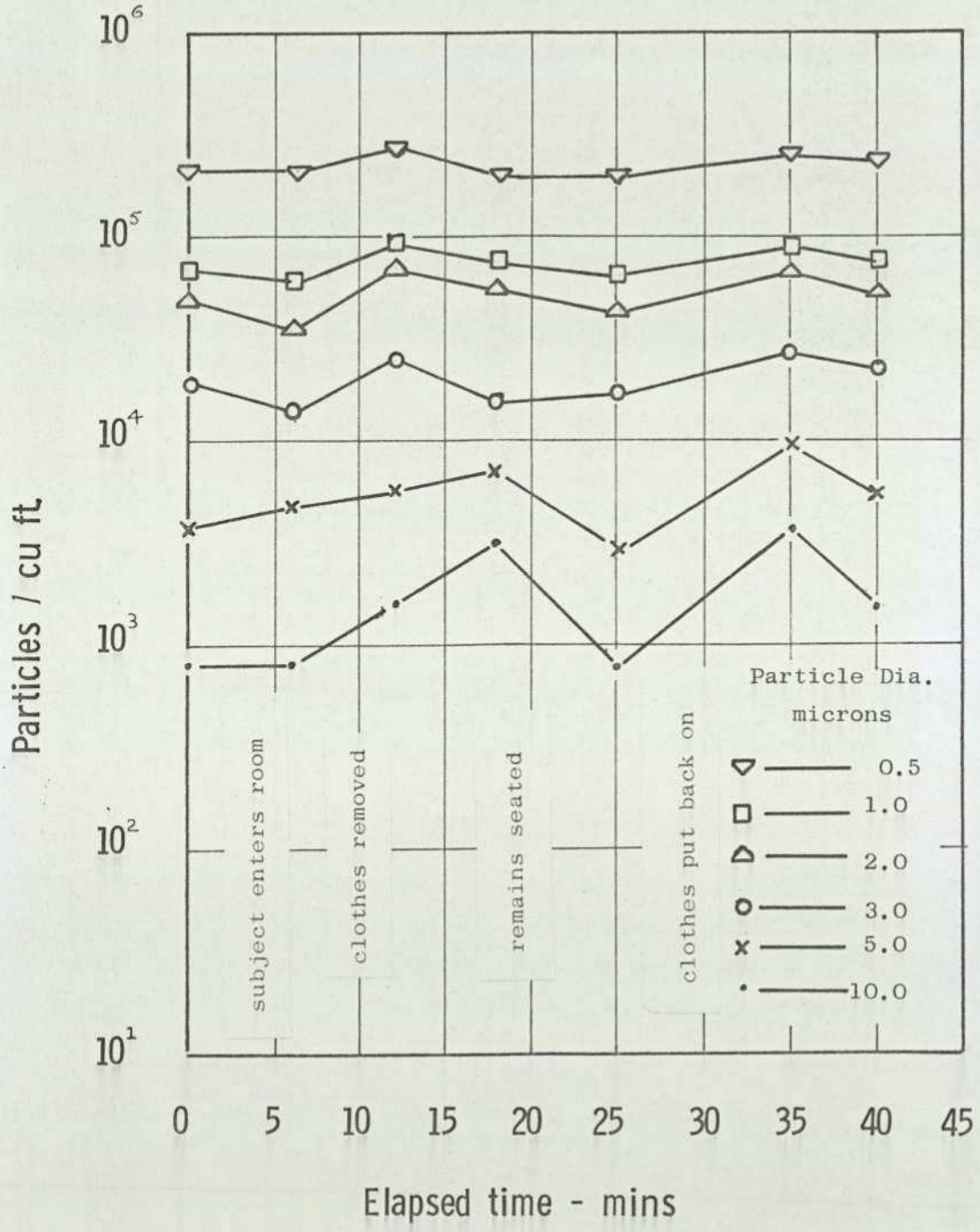


Particle concentration increase in a small room after subject enters and slowly walks around.



Room volume 450 cu. ft.

Variation of particle concentration levels during various activities in a small room. Vol. 450 cu. ft.



VARIATION OF $\frac{C_l}{C_d}$ WITH ANGLE OF INCIDENCE α FOR 2 VALUES OF RE

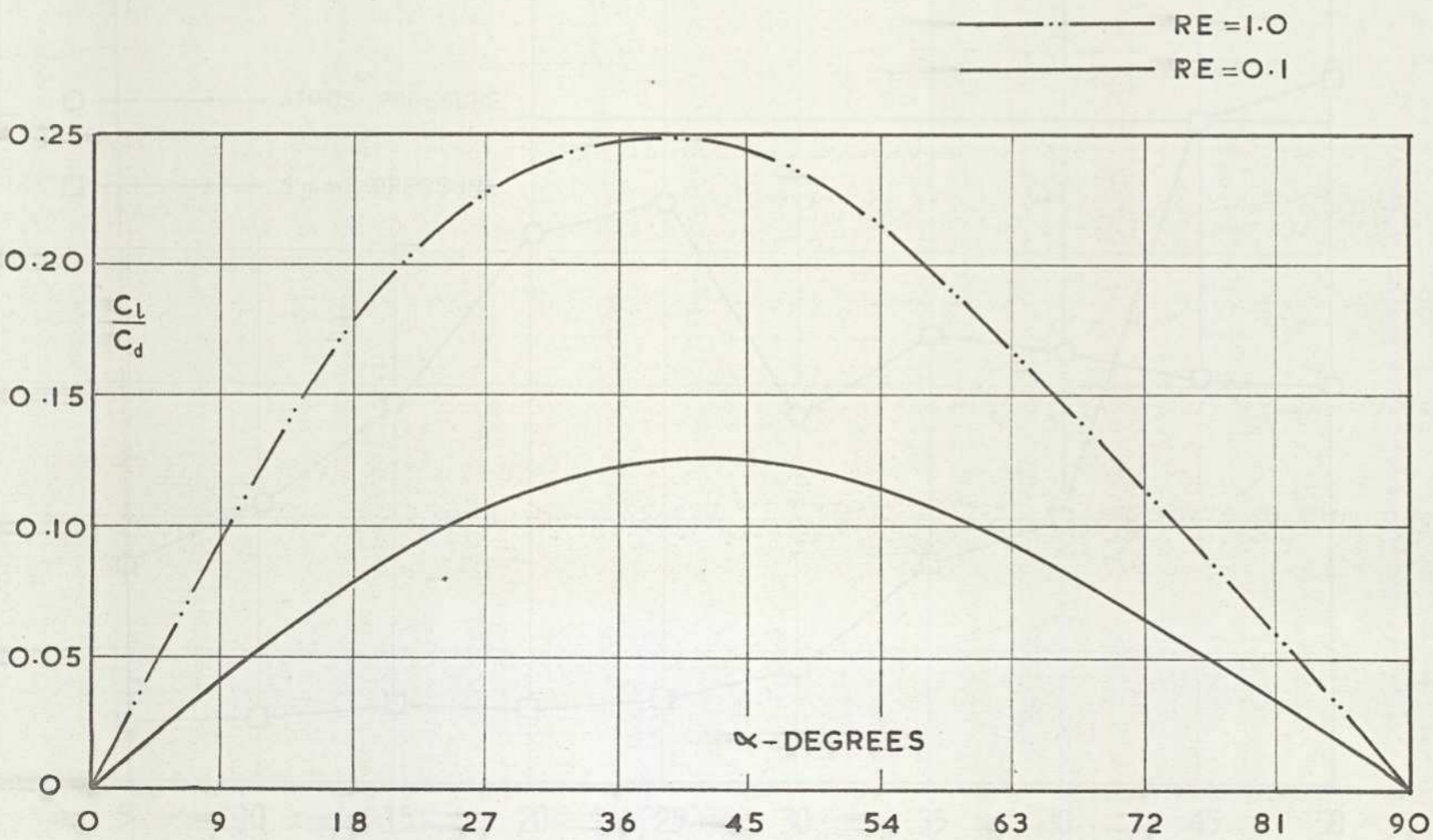


Figure 100

FROM IMAI

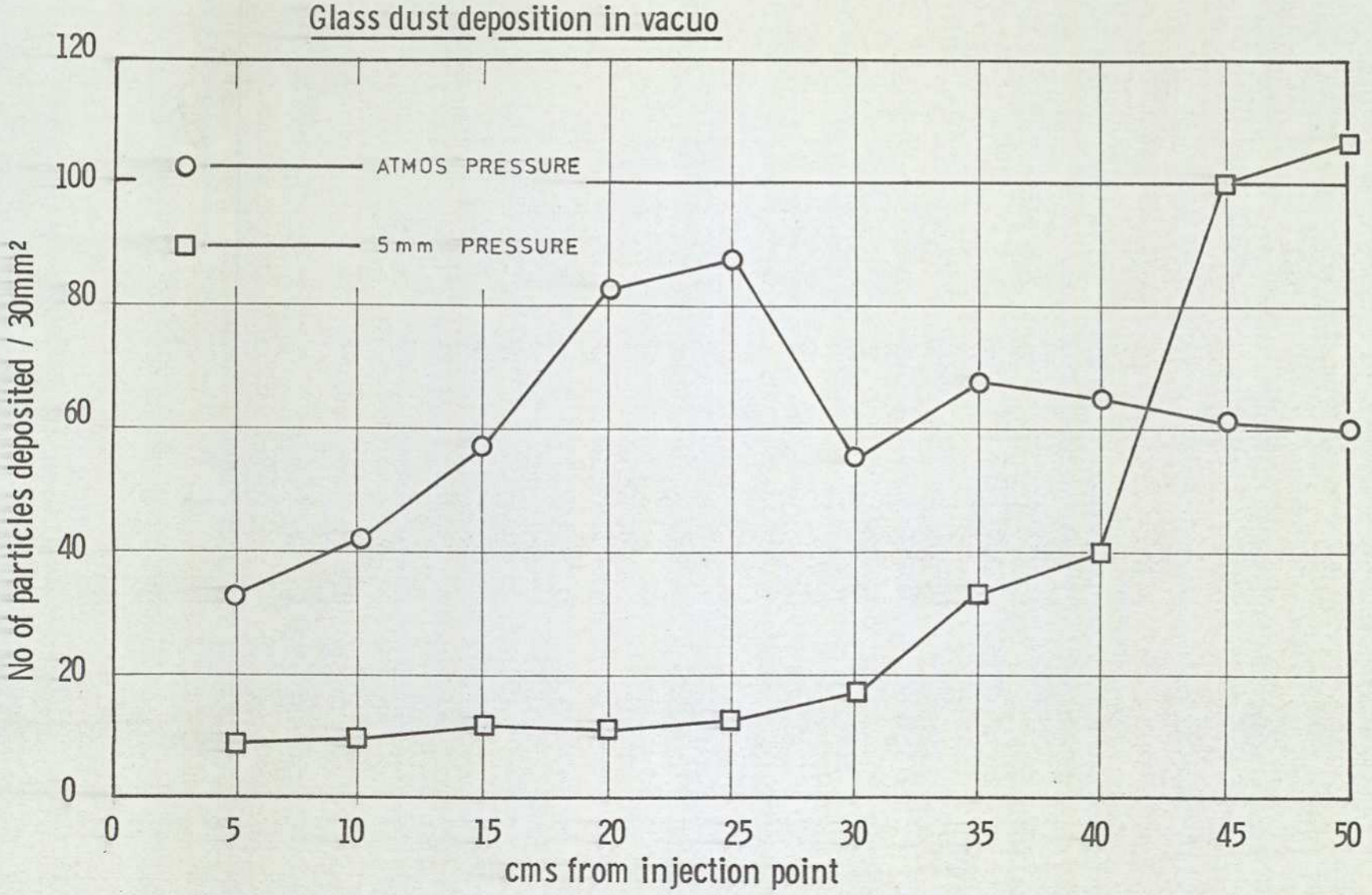
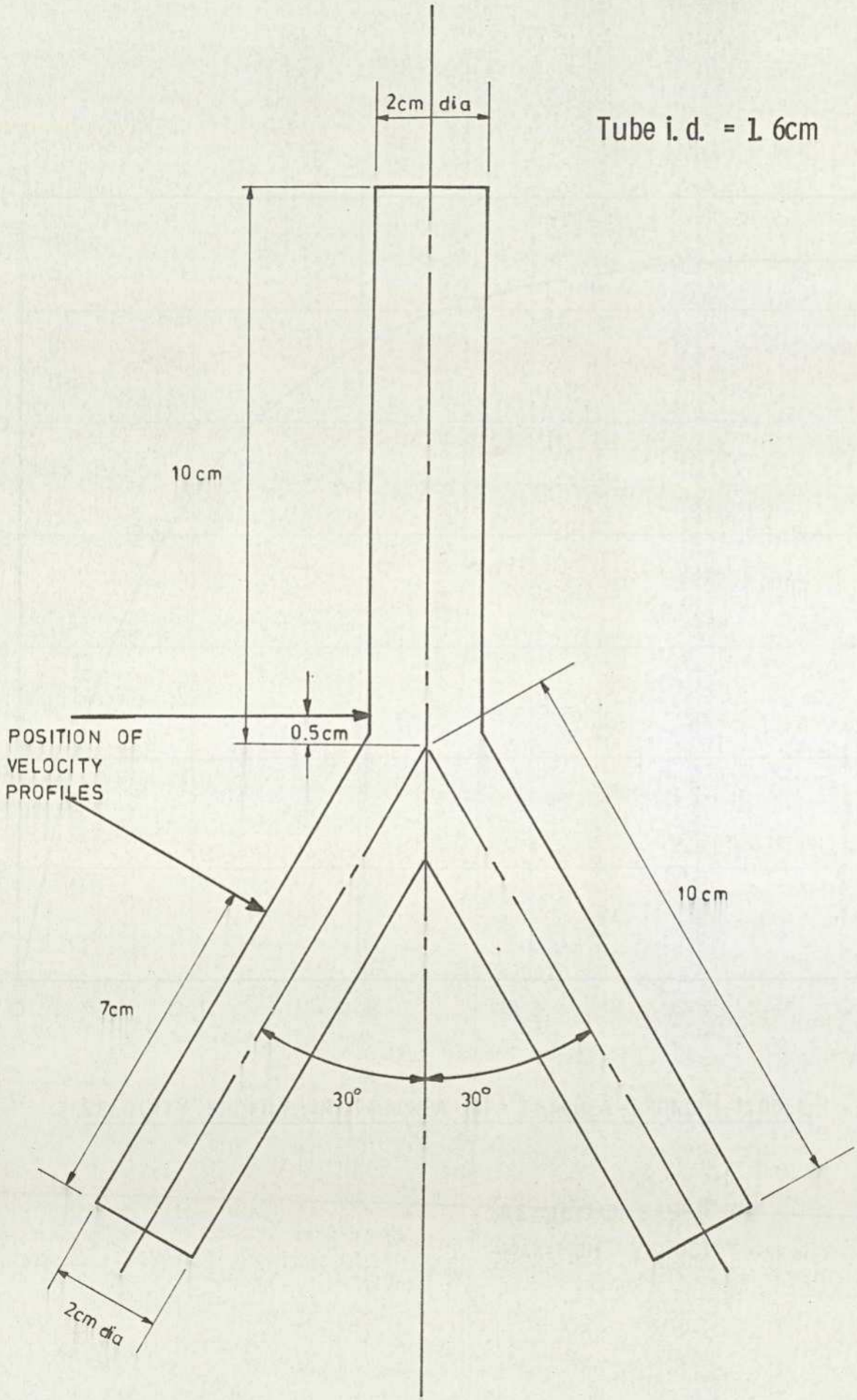

Glass dust deposition in vacuo
ATMOS PRESSURE
5 mm PRESSURE
No of particles deposited / 30mm²
cms from injection point
0
20
40
60
80
100
120
0
5
10
15
20
25
30
35
40
45
50

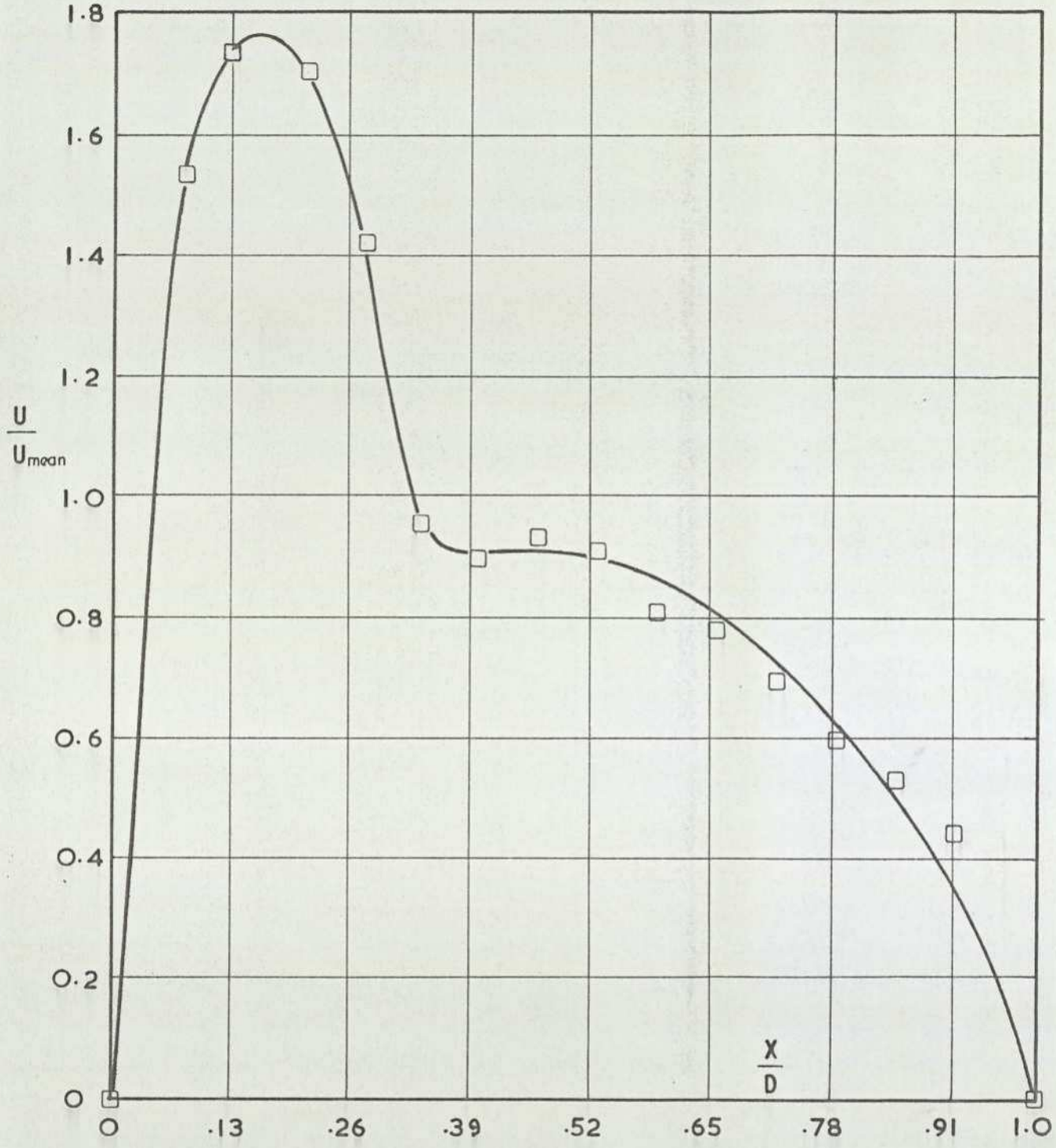
Figure 101

Figure 102

Glass model of trachea and bronchi

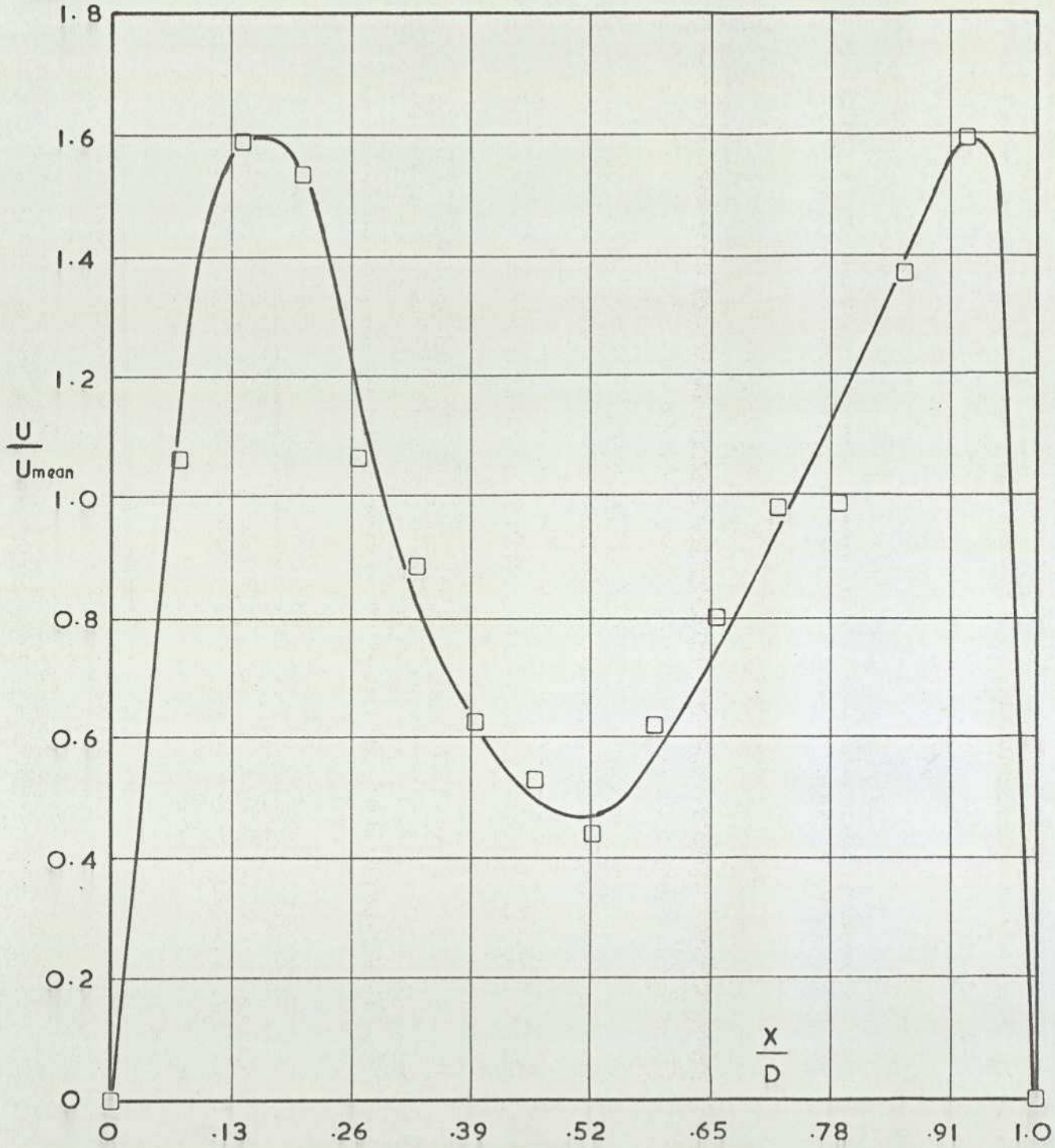
Scale - full size





VELOCITY PROFILE IN BRONCHI OF TRACHEA BRONCHI MODEL

RE = 820 BASED ON MAXIMUM
TRACHEA VELOCITY



VELOCITY PROFILE IN BRONCHI OF TRACHEA-BRONCHI MODEL

RE = 1044 BASED ON MAXIMUM
TRACHEA VELOCITY

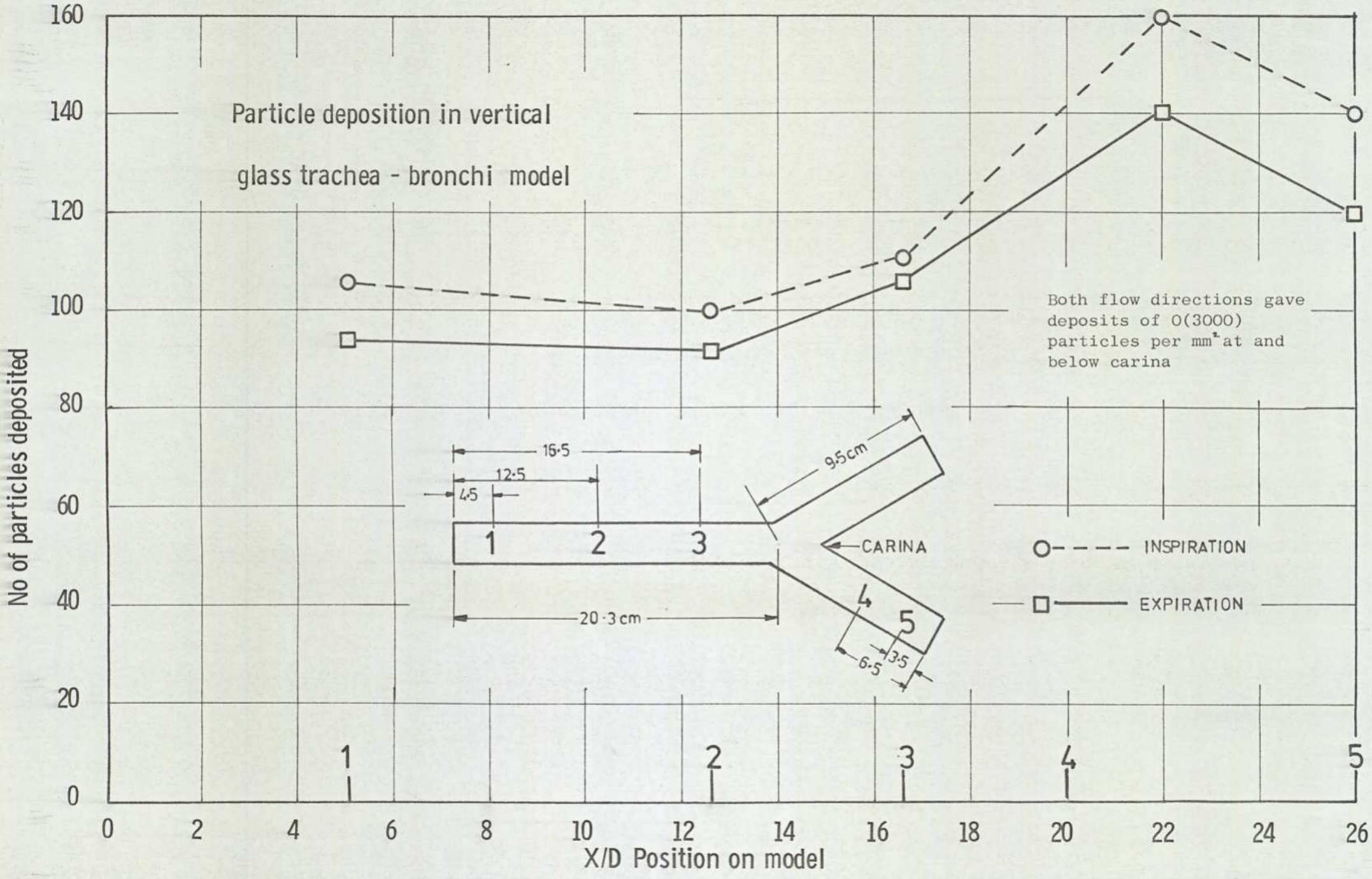

Particle deposition in vertical
glass trachea - bronchi model
Both flow directions gave deposits of O(3000) particles per mm² at and below carina
INSPIRATION
EXPIRATION
CARINA
16·5
12·5
4·5
9·5cm
20·3 cm
6·5
3·5
No of particles deposited
X/D Position on model
0
20
40
60
80
100
120
140
160
0
2
4
6
8
10
12
14
16
18
20
22
24
26
1
2
3
4
5

Figure 106

This content has been removed for copyright protection reasons

Clark, R.P., Cox, R.N. and Lewis, H.E. (1970) 'Particle transport within the human micro-environment', Journal of Physiology, 208(2), pp. 43P-45P.

Clark, R.P., Cox, R.N. and Lewis, H.E. (1971a) 'Particle detection in the human micro-environment', Journal of Physiology, 214, pp. 3P-4P.

Clark, R.P., Cox, R.N. and Lewis, H.E. (1971b) 'Deposition and dispersion of particles from the human micro-environment', Journal of Physiology, 216(1), pp. 19P-20P.

Clark, R.P., Cox, R.N. and Toy, N. (1972) 'A surface plate calorimeter for measuring local heat transfer in free and forced convection within the human micro-environment', Journal of Physiology, 223(1), pp. 10P-12P.

Cox, R.N. and Clark, R.P. (1969) 'The natural convection flow around the human body', Quest, 9, pp. 9-13.

Cox, R.N. and Clark, R.P. (1973) 'The natural convection flow about the human body', Revue Générale de Thermique, 12, pp. 11-19.

Lewis, H.E., Foster, A.R., Mullan, B.J., Cox, R.N. and Clark, R.P. (1969) 'Aerodynamics of the human microenvironment', The Lancet, 293(7609), pp. 1273-1277.